AD813456

BSD TR 66-372, Vol. XIII

Final Report

RADIATION DAMAGE STUDY (RADS)

Volume XIII — Dynamic Response of Beams, Plates, and Shells to Pulse Loads

By

G. R. ABRAHAMSON, A. L. FLORENCE, AND H. E. LINDBERG

Poulter Laboratories
Stanford Research Institute
Menlo Park, California

SRI Project FGU-5733

Under Subcontract To

AVCO MISSILES, SPACE AND ELECTRONICS GROUP
MISSILE SYSTEM DIVISION
201 Lowell Street
Wilmington, Massachusetts 01887

AVMSD-0339-66-RR, VOL. XIII
September 1966

Contract AF04(694)-824

Prepared for

BALLISTIC SYSTEMS DIVISION
DEPUTY FOR BALLISTIC MISSILE REENTRY SYSTEMS
AIR FORCE SYSTEMS COMMAND
Norton Air Force Base, California 92409

STANFORD RESEARCH INSTITUTE

MENLO PARK CALIFORNIA

BSD TR 66-372, Vol. XIII	Short Title Ref: AVMSD-0339-66-RR, Vol. XIII

Final Report

RADIATION DAMAGE STUDY (RADS)

Volume XIII — Dynamic Response of Beams, Plates, and Shells to Pulse Loads

Prepared for:

BALLISTIC SYSTEMS DIVISION
DEPUTY FOR BALLISTIC MISSILE REENTRY SYSTEMS
AIR FORCE SYSTEMS COMMAND
NORTON AIR FORCE BASE, CALIFORNIA 92409

CONTRACT AF04(694)-824

Under Subcontract to:

AVCO MISSILES, SPACE AND ELECTRONICS GROUP
MISSILE SYSTEMS DIVISION
201 LOWELL STREET
WILMINGTON, MASSACHUSETTS 01887

SUBCONTRACT NO. 159706

Prepared by: G. R. ABRAHAMSON, A. L. FLORENCE, AND H. E. LINDBERG
EXPLOSIVES ENGINEERING DIVISION
POULTER LABORATORIES
STANFORD RESEARCH INSTITUTE
MENLO PARK, CALIFORNIA 94025

SRI Project FGU-5733

Copy No. ....

FOREWORD

This is the second of two volumes prepared by Stanford Research Institute under subcontract to the Avco Corporation as part of the Radiation Damage Study (RADS) Program, Contract AF04(694)-824, sponsored by the Air Force Ballistic Systems Division. The two volumes contributed by SRI are designated Volumes XII and XIII of the RADS Final Report. Volume XII is classified and treats structural response of reentry vehicles to pulse loads. This volume (XIII) treats the response of bars, plates, and cylindrical shells, the basic elements found in reentry vehicles.

This program was administered under the direction of the Air Force Ballistic Systems Division, with Capt. John Rec as project officer. Messrs. T. S. Trybul and John Koehler of Aerospace Corporation served as principal technical monitors.

The complete RADS Final Report consists of the following volumes:

VOLUME	TITLE
I	Program Manager's Summary
II	Survey of X-Ray Phenomenology Prediction Techniques
III	Radiation Transport and Deposition
IV	One-Dimensional Material Response: The XIP Code
V	Materials Data Handbook
VI	Vehicle Response
VII	Vehicle Hardening
VIII	The OSCAR Code
IX	Simulation Test Techniques
X	Special Instrumentation Requirements
XI	Equation of State and One-Dimensional Characteristic Code Studies

VOLUME	TITLE
XII	Special Problems in Structural Response of Reentry Vehicles
XIII	Dynamic Response of Beams, Plates, and Shells to Pulse Loads
XIV	Pre-Test Analysis of Chaff
XV	UMBER Experiments
XVI	Nosetip Experiments

This technical report has been reviewed and approved for publication.

Approval Authority: J. R. Rec, Capt., BSYDV

PREFACE

The purpose of this volume is to present in an easily assimilated form the results of research on dynamic structural response which has been in progress at Stanford Research Institute since about 1959. Much of this information is available in published papers and reports, but some of these are not generally available and some contain a good deal of overlap. Also, the individual papers lack the overall viewpoint that can be developed only after many aspects of the problem have been examined.

Two areas of response are treated, dynamic plastic bending and dynamic pulse buckling. These are preceded by a general discussion in Chapter 1 of structural response from pulse loads and identification of peak pressure and impulse as the most significant load parameters affecting structural response. In Chapter 2 the fundamental theory of dynamic plastic bending is developed, using simply supported and clamped beams as examples. Pulse loads treated range from ideal (zero time) impulses to step loads with exponential, triangular, and rectangular time profiles. In Chapter 3 this theory is extended to circular plates. Since many problems are treated in Chapters 2 and 3, a certain amount of repetition has been allowed to enable the reader to start anywhere without excessive foraging. In Chapter 4 a development of the basic theory of dynamic elastic and plastic pulse buckling is given, again using a simple bar as an example to give the concepts in their simplest form. In Chapter 5 the analytical techniques are applied to cylindrical shells under lateral pressure pulses.

CONTENTS

CONTENTS (Continued)

CONTENTS (Concluded)

ILLUSTRATIONS

ILLUSTRATIONS (Continued)

ILLUSTRATIONS (Continued)

ILLUSTRATIONS (Continued)

ILLUSTRATIONS (Continued)

ILLUSTRATIONS (Continued)

ILLUSTRATIONS (Concluded)

TABLES

SUMMARY

S.1 Introduction

In this summary section the status of existing analyses is briefly given and areas for most fruitful future development are suggested. Buckling theories are discussed first because they bear more directly on the design of the external shell of operational structures. This is followed by a summary of theories for dynamic plastic bending of auxilliary beam and plate structures which are used in aft covers, stiffening, and in internal components. In the main text the order is reversed because bending theories are more familiar.

S.2 Pulse Buckling

S.2.1 Experimental Evidence of Buckling

One of the first modes of structural damage repeatedly observed to occur in structures under explosively induced loads is dynamic buckling. It is observed in simple metal shells and in the metal subshells of composite shells with a brittle outer layer (such as Micarta). Also, when the total thickness of the composite is small, both shells buckle as a unit and the brittle outer shell cracks into longitudinal strips of widths corresponding to the half-wavelength of the buckle pattern. In the HARTS* program, it was found that pulse buckling is a significant damage mode over the entire range of external pressure pulses from ideal (zero time) impulses to long duration blast loads.

S.2.2 Scope of Buckling Theories

These observations led to a basic investigation of pulse buckling, and three basic types of buckling have been identified: elastic, plastic flow, and visco-plastic. Elastic buckling occurs in

*Hardening Technology Studies, sponsored by the Air Force Ballistic Systems Division, Ref. 9, Ch. 5.

very long or thin structures in which the duration of compressive membrane stresses can be sufficiently long to allow significant buckling during elastic motion. In thicker structures the duration of possible elastic motion, before wave reflections or membrane stress reversal occurs, is so small compared to the buckling time that significant buckling motion occurs only if the stresses are large enough to induce membrane plastic flow. This is called plastic-flow buckling and the flexural stiffness is governed by the strain hardening modulus. In many engineering metals this modulus is about 1/100 the elastic modulus so resistance to buckling is greatly reduced. In some materials (e.g., mild steel) the strain hardening modulus is so small that the resistance to buckling must come from the increase in stress with strain rate. This is called visco-plastic buckling.

Theories of elastic and plastic-flow buckling have been worked out for bars, plates, rings, and cylindrical shells, and a visco-plastic theory has been worked out for rings and cylindrical shells. The scope of these theories and supporting experiments is summarized in Table S.1. The first three columns give the structures and loading conditions investigated, and the fourth and fifth columns indicate the available theoretical and experimental results. Equation numbers of buckling formulas derived in the present volume are given in the next column; if no number is given, the references, in the last column, must be consulted.

S.2.3 Sensitivity of Solutions to Structural Imperfections and Material Properties

The basic observation of both the experiments and the theory is that pulse buckling consists of rapid exponential growth of imperfections in structural shape, leading to large flexural deformations, permanent strains, and cracking. A convenient and useful theoretical buckling threshold is the load necessary to amplify the imperfections by, say, 1000. Where comparisons are available, this value gives theoretical loads which are within 30% of experimentally determined loads to produce first measurable permanent buckling deformation in aluminum shells.

Table 5.1

AVAILABLE ANALYSES AND EXPERIMENTAL RESULTS FOR DYNAMIC PULSE BUCKLING

Diagram	Structure	Loading	Types of Analyses	Experiments*	Buckling Formula (Equation No.)	References	
						Chapter	Number
	Bar	Axial (Impact)	E PF	E PF	4.91, 4.110, 4.129	4	17, 19
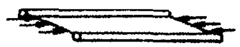	Plate	Axial (Impact)	E PF	E PF		4	20
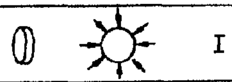	Ring	Radial Impulse	E PF VP	E PF VP	5.29	3	1, 2
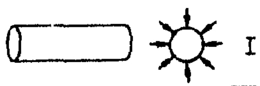	Cylindrical Shell	Radial Impulse	E PF VP	E PF VP Cracking	5.29	5	1, 2
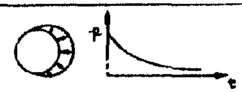	Cylindrical Shell	Blast	E PF	E PF	5.27 through 5.31	5	9
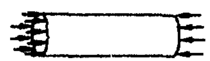	Cylindrical Shell	Axial (Impact)	E PF	E PF		5	12, 13
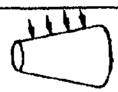	Cone	Blast, Impulse	Cyl. theory adequate except near tip	E PF	5.27 through 5.31	5	9
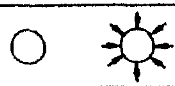	Sphere	Radial Impulse	In process	PF			

E Elastic; buckling takes place under elastic membrane stress.

PF Plastic-flow; plastic membrane strains, flexure resisted by strain-hardening modulus.

VP Visco-plastic; plastic strains, flexure resisted by strain-rate modulus.

*Most experiments are on simple metal structures, usually of aluminum or steel.

Calculated buckling threshold loads are relatively insensitive to changes in the magnitude of this amplification criterion. For example, increasing the amplification from 100 to 1000 for a cylindrical shell under radial impulse requires an increase in impulse of only 15%. Errors in estimating the magnitude of imperfections in shell shape are reflected in changes in the amplification to produce observable threshold buckling. Thus, in the above example, a decrease in imperfection amplitude by a factor of 10 would result in only a 15% increase in impulse. This indicates that, although little is known about the magnitude of imperfections, better specification will have a small effect on theoretical buckling loads.

The effect of material properties on buckling thresholds can be illustrated by the same example. The radial impulse I to produce threshold buckling in a simple metal shell is given by

$$I = \left(\frac{95}{K}\right)^{1/4} \left(\rho\sigma_y\right)^{1/2} a \left(\frac{h}{a}\right)^{3/2}$$

where

K = average slope beyond yield of $\sigma/(d\sigma/d\epsilon)$ vs. ϵ

σ = compressive hoop stress, ϵ = strain

ρ = density

σ_y = yield stress

a = radius

h = wall thickness

Since impulse increases as the square root of the yield stress, a 20% error in this material property gives an error in impulse of only 10%. Impulse is even less sensitive to changes in the strain-hardening parameter K. An increase in K of approximately 40% is required to give a 10% increase in impulse.

S.3 Bending of Beams and Plates

The principal beam and plate problems of interest that are solvable by elementary analytical methods are presented in Table S.2. The first four columns describe the problems which have been investigated. Blast loading refers to pulses having an instantaneous rise to a peak pressure followed by a decay to zero pressure in a rectangular, triangular, or exponential shape; pulse durations are arbitrary. In some of the problems the available solutions are limited to the rectangular pulse, and others are limited still further to ideal (zero time) impulses. These are so noted.

Column five (analyses) refers to the types of analyses which have either provided solutions or will readily lead to solutions. These are classified according to the idealized material properties used: linear-elastic (E), rigid-plastic (RP), and visco-plastic (VP). Linear-elastic theory is suitable for obtaining threshold loads to reach yield stresses in ductile materials or to reach fracture stresses in brittle materials. Rigid-plastic theory is suitable where the plastic work done during deformation considerably exceeds the elastic strain energy capacity. Visco-plastic theory is necessary for strain-rate sensitive materials. In the present report we utilize only the rigid-plastic theory, in its simplest form, i.e., neglecting elastic strain energy and vibrations, strain hardening, strain-rate sensitivity, and geometry changes. For impulsive loading these assumptions mean that the kinetic energy input is equal to the plastic work done. Comparable problems solved by the other theories are given in the references.

For impulsive loading, formulas giving the permanent central deflection δ_{rp} predicted by the simple rigid-plastic theory are listed and compared with corresponding experimental deflections δ_{ex} in the column labeled δ_{ex}/δ_{rp}. A similar comparison is not possible for blast loads because of the lack of data.

The next column indicates the range of applicability of the rigid-plastic theory. A lower limit is set by the ratio R of the kinetic energy input to strain energy capacity. For plates, an upper limit is

Table S.2

AVAILABLE ANALYSES AND EXPERIMENTAL RESULTS FOR BEAMS AND PLATES

Diagram	Structure	Supports	Theoretical Loading	Types of Analyses*	Experimental Loading	Permanent Deflection (Impulsive Load and RP Theory), δ_{rp}	δ_{ex}/δ_{rp}	Applicability Bounds Lower	Applicability Bounds Upper	References Chapter	References Number
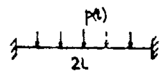	Beam	Clamped	Blast	RP E	Impulse	$\frac{1}{6}\frac{I^2L^2}{mM_o}$	0.72	$R > 3$		2	3, 4
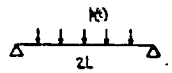	Beam	Pinned	Blast	RP E	Impulse	$\frac{1}{3}\frac{I^2L^2}{mM_o}$	0.68	$R > 3$		2	3, 4
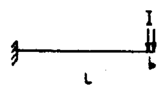	Cantilever†		Impulse	RP VP E	Impulse	$\frac{2}{3}\frac{I^2b^2}{mM_o}(1+4 \ln L/b)$	0.7	$R > 3$		2	5
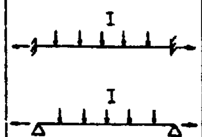	Beam Tie†	Clamped Pinned	Impulse	RP VP E	Impulse	Cubic in δ	~0.65	$R > 4$		2	8, 9
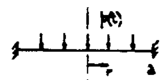	Circular Plate	Clamped	Rectangular Pulse	RP VP E	Impulse and Blast	$0.56\frac{I^2a^2}{8mM_o}$	~0.7	$R > 5$	$\frac{\delta_{rp}}{a} < 1/3$	3	3, 5, 11
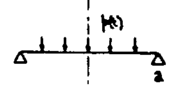	Circular Plate	Pinned	Rectangular Pulse	RP VP E	Impulse	$\frac{I^2a^2}{8mM_o}$	~0.7	$R > 5$	$\frac{\delta_{rp}}{a} < 1/3$	3	2, 4, 8
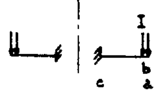	Annular† Plate	Clamped Inside Free Out.	Impulse	RP E	Impulse	$\frac{I^2b^2}{mM_o} f(a, b, c)$	~0.55	$R > 5$	$\frac{\delta_{rp}}{a} < 1/3$	3	7

*RP Rigid-plastic
VP Visco-plastic
E Elastic

†Not covered in this report. See references in last column.

a plate radius
b width of loading
L half-span
m mass/unit length or area
M_o plastic yield moment
R kinetic energy input/elastic strain energy capacity
δ_{ex} experimental permanent deflection
δ_{rp} theoretical permanent deflection

given by the deflection-to-radius ratio δ_{rp}/a at which membrane forces become significant.

Advantages of the simple rigid-plastic theory are that

1. Analyses and results are often simple.

2. Agreement with experimental results are adequate for many engineering applications (see δ_{ex}/δ_{rp} values in Table S.2).

3. Simple approximate extensions to include properties such as strain hardening is sometimes possible.

S.4 Future Work

Future development of the analytical approach to the response of reentry vehicle-type structures should consist of extending and improving the theories for damage mechanisms already examined, and devising new analytical models to explain other observed damage mechanisms.

Extension and improvement of existing theories should include:

1. A theory for laminar buckling of a metal subshell in the presence of a constraining (but not buckling) heat shield;

2. Buckling theories for more complex structures, for example foam and honeycomb sandwich shells and rib-stiffened shells;

3. More extensive experiments to compare predicted and observed damage thresholds;

4. Experiments and extended theories to compare response from symmetric (nose-on) and asymmetric (side-on) loads; and

5. Comparison of elastic bending theories to experimentally observed thresholds of permanent deformation and cracking.

New damage mechanisms which at present have no analytical explanation include:

1. Circumferential delamination of tape-wound heat shields both at hard points and throughout the span between end supports;

2. Longitudinal heat shield cracking under the peak of a side-on impulsive load;

3. Response of structures to thermal loads; and

4. Response of heated structures to impulsive loads.

CHAPTER 1

AMPLITUDE-IMPULSE CHARACTERIZATION OF CRITICAL PULSE LOADS IN STRUCTURAL DYNAMICS

by

G. R. Abrahamson and H. E. Lindberg

1.1 Introduction

The determination of critical loads is a central problem in structural dynamics. The method of characterizing critical loads is important because it can simplify or complicate analysis, and can facilitate or hinder the interpretation of theoretical results and comparison with experiments. The amplitude-impulse characterization of critical pulse loads is particularly significant because it is simple and useful and applies to all structures, including complex structures such as reentry vehicles. We begin with a discussion of critical pulse loads for a linear oscillator to demonstrate the ideas involved and then show that critical pulse loads for complex structures can be characterized in the same way. To facilitate the discussion, we henceforth refer to the amplitude-impulse (P,I) characterization as the π characterization.

1.2 π Characterization for a Linear Oscillator

The displacement of a linear oscillator having natural frequency ω is given in conventional notation by[1*]

$$x = (x_i + A)\cos \omega t + \left(\frac{\dot{x}_i}{\omega} + B\right) \sin \omega t \qquad (1.1)$$

*References are given at the end of each chapter.

where the subscript i denotes initial values and A and B are the integrals

$$A = -\frac{P}{\omega}\int p(t')\sin\omega t'dt'$$

$$B = \frac{P}{\omega}\int p(t')\cos\omega t'dt' \tag{1.2}$$

$p(t')$ being of unit amplitude, P the force amplitude per unit mass, and t time. To simplify the equations, we rewrite (1.1) as

$$x = \frac{P}{\omega^2} f \tag{1.3}$$

where

$$f = \frac{\omega^2}{P}\left[(x_i + A)\cos\omega t + \left(\frac{x_i}{\omega} + B\right)\sin\omega t\right] \tag{1.4}$$

For a static load the displacement is given by

$$x_o = \frac{P_o}{\omega^2} \tag{1.5}$$

where P_o is the static load (per unit mass). Taking the maximum of (1.3) and dividing by (1.5) yields

$$\frac{x_m}{x_o} = \frac{P}{P_o} f_{max} \tag{1.6}$$

To characterize critical loads in terms of amplitude and impulse we put $x_m/x_o = 1$ in (1.6) and obtain

$$\frac{P}{P_o} = f_{max}^{-1} \tag{1.7}$$

for the ratio of dynamic and static loads which produce the same maximum displacement. Impulse is given by the area under the force-time curve and can be written

$$I = Pq \tag{1.8}$$

where

$$q = \int p(t)dt \tag{1.9}$$

T being the load duration. For an ideal impulse (i.e., delivered in zero time), the maximum displacement is given by

$$I = \omega x_m \tag{1.10}$$

Identifying x_m with x_o of (1.5) yields

$$I_o = \frac{P_o}{\omega} \tag{1.11}$$

and from (1.11) and (1.8) we obtain

$$\frac{I}{I_o} = \frac{P}{P_o}\,\omega q \tag{1.12}$$

Equations (1.7) and (1.12) give the amplitude-impulse combinations which produce the same maximum displacement of a linear oscillator.

A plot of P/P_o and I/I_o from (1.7) and (1.12) is given in Fig. 1.1 for loads with a step rise and linear decay. Since this is a log-log plot, along lines of unit slope load duration is constant, and here is given in terms of the period τ. For loads of short duration ($t_2/\tau \lesssim 2/3\pi = 0.21$), the curve approaches the vertical asymptote $I/I_o = 1$. In this region the response is insensitive to load amplitude and depends mainly on impulse. For loads of long duration ($t_2/\tau \gtrsim 6/\pi = 1.9$), the curve approaches the horizontal asymptote $P/P_o = 0.5$. In this region the response is insensitive to impulse and depends mainly on amplitude. In the intermediate region, the response depends on both amplitude and impulse.

1.3 Comparison of the π Characterization with Response Spectrum*

For a linear oscillator, the π characterization is related to the response spectrum. The latter is defined as the maximum response of a linear oscillator to a given load, stated as a function of oscillator frequency.

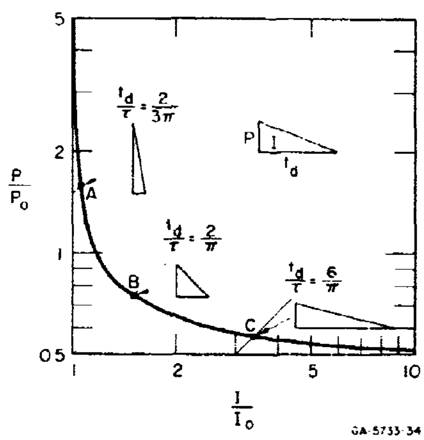

FIG. 1.1 π DIAGRAM FOR A LINEAR OSCILLATOR FOR LOADS WITH A STEP RISE AND LINEAR DECAY

To obtain the response spectrum R, we put $P/P_o = 1$ in (1.6) and get

$$R = \frac{x_m}{x_o} = f_{max} \qquad (1.13)$$

Hence, as can be seen from (1.7), R and P/P_o are reciprocals. A plot of R from (1.13) is given in Fig. 1.2 for loads with a step rise and linear decay. For long durations or high frequencies, R approaches 2, as is well known. For short durations or low frequencies, R approaches zero; hence, direct representation of impulsive loads is lost at the origin. In contrast, as shown in Fig.1.1, for the π characterization, loads of short duration correspond to $I/I_o = 1$, which is useful information.

For a single degree-of-freedom system, the essential difference between the π characterization and the response spectrum is that the π characterization prominently displays impulsive response while the response spectrum does not. For multi-degree-of-freedom systems, however, the two concepts represent basically different approaches to dynamic response. The response spectrum is fundamentally a description of the pulse--nothing need be said of the structure The π characterization

*Also called shock spectrum, amplification spectrum, dynamic load factor, etc.

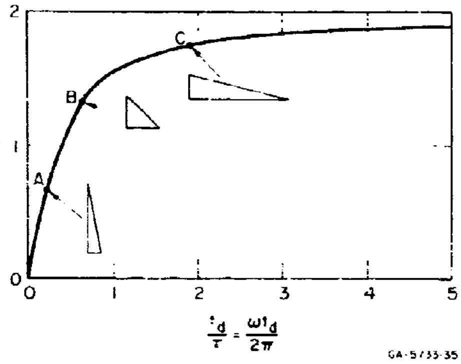

FIG. 1.2 RESPONSE SPECTRUM FOR LOADS WITH A STEP RISE AND LINEAR DECAY

is fundamentally a description of the strength (or susceptibility) of a given structure for pulse loads.

The response spectrum is used as an analytical tool to build up the response of a complex (linear) structure by superposition of the response of its normal modes. A key in this process is the superposition scheme. This usually involves some subjective decision on which modes to add algebraically and which to add arithmetically.

The π diagram is used as a systematic means for gathering and displaying theoretical and experimental response information, separating loads that cause damage from loads that do not. Since superposition is not required, the approach is valid for any type of response, including plastic deformations and buckling. Therein lies the advantage of the π diagram; these problems are beyond the scope of conventional shock and vibration theories. Further useful features of the π diagram are given later, after consideration of the effects of pulse shape and rise time for single-degree-of-freedom systems.

1.4 Effects of Pulse Shape and Rise Time

1.4.1 Effects of Pulse Shape

Figure 1.3 gives the π diagram for a linear oscillator under step-rise pulse loads with various types of decay. The ordinate is taken as half that of Fig. 1.1 to facilitate comparison below with corresponding curves for the rigid-plastic model. Except for the scale change, the curve for the triangular loads is the same as that of Fig. 1.1.

The curve for rectangular loads is below that for triangular loads and the curve for exponential loads is above it. The relative positions of the curves are related to the duration required

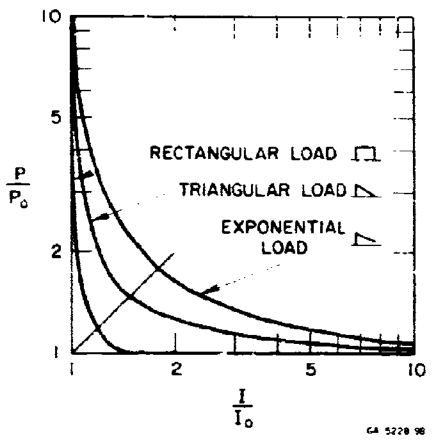

FIG. 1.3 COMPARISON OF LOADS REQUIRED TO PRODUCE THE SAME MAXIMUM DISPLACEMENT OF A LINEAR OSCILLATOR.
P_o is half the static load required to produce the given displacement and I_o is the ideal impulse required to produce the given displacement.

to impart a given impulse for a given amplitude. This is the least for rectangular loads and the greatest for exponential loads.

The curves have the same asymptotes and differ most in the knee region. Along the line of unit slope in Fig. 1.3, the values of P/P_o and I/I_o for the rectangular and exponential loads differ by about 40%, and for the triangular and exponential loads they differ by about 20%.

Figure 1.4 gives the π diagram for a one-degree-of-freedom, rigid-plastic system. The curves are similar in shape to those of Fig. 1.3, but are shifted outward from the origin. The relative positions of the curves for the different pulse shapes are unchanged. As for the linear oscillator, the curves have the same asymptotes and differ most in the knee region. Along the line of unit slope the values of P/P_o and I/I_o for the rectangular and exponential loads differ by about 30%, and for the triangular and exponential loads they differ by about 20%.

1.4.2 Effects of Rise Time

The effects of rise time on critical load curves for a linear oscillator can be illustrated using a load with a linear rise and linear decay. The critical load curves for such loads are given in Fig. 1.5. The heavy curve $t_r/\tau = 0$ is for loads with a step rise and is the same as that of Fig. 1.1. The curve $t_r = t_d$ is for loads with a linear rise and step decay. Since $t_r \le t_d$, the curves for t_r/τ = constant terminate at $t_r = t_d$. Curves for $t_r/\tau = 0.1$ to 0.5 extend below the step-rise curve, indicating a resonance effect. Curves for $t_r/\tau \ge 0.6$ lie above the step-rise curve. For $t_r/\tau = 1, 2, 3$, etc., the critical load curves lie on the horizontal line $P/P_o = 1$.

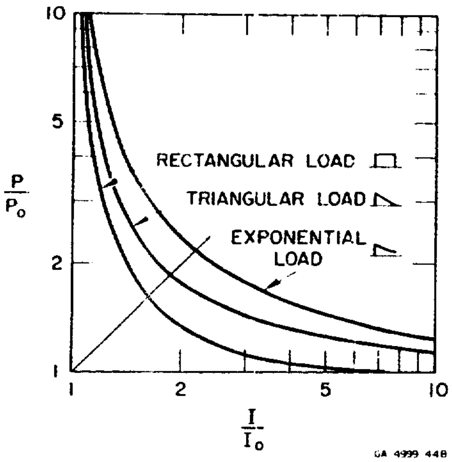

FIG. 1.4 COMPARISON OF LOADS REQUIRED TO PRODUCE THE SAME MAXIMUM DEFORMATION OF A ONE-DEGREE-OF-FREEDOM RIGID PLASTIC SYSTEM. P_o is the static yield load and I_o is the ideal impulse required to produce the given displacement.

Beyond the termination point of the critical load curve for $t_r/\tau = 1$ (on $t_r = t_d$), the numbers along the curve $t_r = t_d$ indicate the termination points of the corresponding critical load curves. The corresponding critical load curves are similar in shape to those shown for $t_r/\tau = 1.2$ and 1.4.

The curves of Fig. 1.5 for t_r/τ up to 0.5 are within about 20% of the step-rise curve $t_r/\tau = 0$. If such an error is acceptable, the curves for $0 \leq t_r/\tau \leq 0.5$ can be represented by the step-rise curve. If instead a central reference curve is used, the error would be only 10%.

1.5 Application of the π Characterization to Complex Structures

The real value of the π characterization of critical pulse loads is in its utility for complex structures. As a starting point for the discussion, we consider a structure with a load of a given space-time variation, for example a reentry vehicle with a load of cosine distribution on one side having a sharp rise and a linear decay.

For a given structure and type of load, we undertake a series of imaginary tests to determine the loads at which the structure fails. We first do a series of tests using long duration loads of increasing amplitude to determine the critical amplitude P_o at which failure occurs. This is indicated by the vertical column of points in Fig. 1.6. Next we do a series of tests using short duration loads of increasing impulse to determine the critical impulse I_o at which failure occurs. This is indicated by the horizontal row of points. For the given load distribution, P_o and I_o completely specify the critical loads of long and short duration.

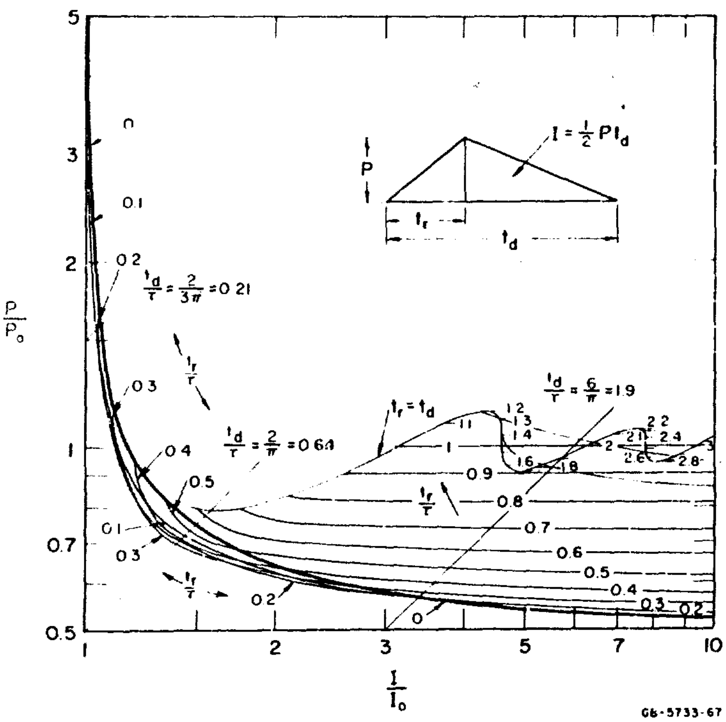

FIG. 1.5 π DIAGRAM FOR A LINEAR OSCILLATOR SHOWING EFFECTS OF RISE TIME

For loads of intermediate duration we consider a series of tests for constant load duration, corresponding, for example, to the line t_1 in Fig. 1.6. Since the load acts for a shorter time, we would expect the failure amplitude to be greater than P_o, as indicated. If the load duration is further reduced, say corresponding to the line t_2, we would expect that a further increase in amplitude would be required to produce failure. If the process of decreasing load duration were continued until the duration became short compared to response time, all combinations of amplitude and impulse which just produce failure would be established. For the particular structure and load space-time variation, the locus of such points completely describes the critical loads.

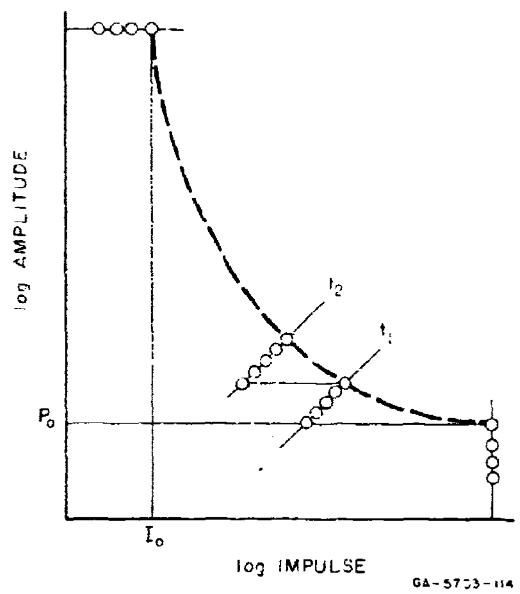

FIG. 1.6 EXPERIMENTAL DETERMINATION OF CRITICAL LOAD CURVE FOR A COMPLEX STRUCTURE

It is not necessary that the failure mode remain the same throughout the critical curve. In general, the failure mode will be different for different load durations. Thus, as shown in Fig. 1.7, the critical load curve obtained from the series of tests envisaged above would really be the envelope of the critical load curves for all the significant modes.

In principle, a different critical load curve is required for each space-time load variation. However, experience* shows that for a wide range of loads of smooth distribution (such as a cosine load over one side of a cylindrical shell) and with a decay similar to a linear or exponential decay, a single critical load curve is adequate for many applications.

A significant feature of the π characterization is that the damage gradient across the critical load curves is steep. For example, for cylindrical shells the maximum no-damage curve and the minimum severe-damage curve are always within a factor of two and often much less. This means that, for many applications, crude failure criteria are adequate. This is discussed more fully in Chapter 5 of Volume XII.

To build up critical load curves for a complex structure, we consider the possible failure modes and attempt to generate the corresponding critical load curves. Structural failure modes usually involve

*See Fig. 5.13, Chapter 5, this volume.

structural elements such as beams, plates, and shells. Critical load curves for these elements are given in the following chapters of this report.

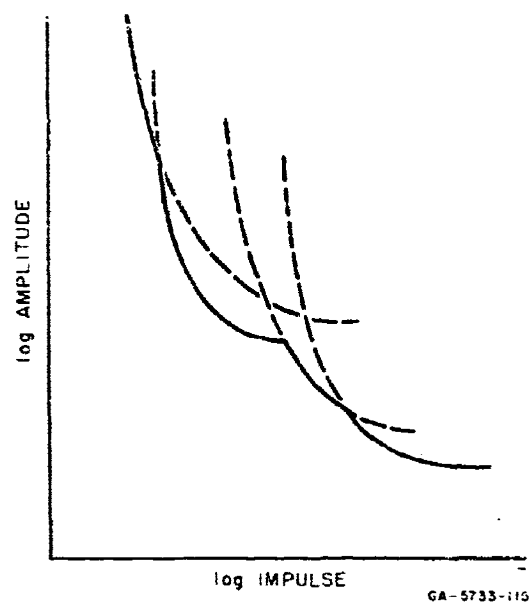

FIG. 1.7 π DIAGRAM SHOWING CRITICAL LOAD CURVE FOR A COMPLEX STRUCTURE AS THE ENVELOPE OF CRITICAL LOAD CURVES FOR SEVERAL MODES

REFERENCES

1. Timoshenko, S., and D. H. Young, Advanced Dynamics, McGraw-Hill Book Co., Inc. (1948).

CHAPTER 2

RIGID-PLASTIC BEAMS

by

A. L. Florence

2.1 Introduction

The response of a beam to a suddenly applied load which is large enough to cause plastic deformation is not easy to find even when the deflections are small enough to allow effects of geometry change to be neglected. This is primarily due to the nonlinearity of the stress-strain relationship. Further nonlinearity is introduced if the stress-strain relationship is sensitive to the rate of loading, but we shall not be concerned here with such a property.

To achieve some simplification, Lee and Symonds[1] introduced an idea to the dynamics of beams which has long been in use for finding collapse loads and mechanisms under static loading.[2] They idealized the properties of appropriate materials (e.g., aluminum alloys and steels) by neglecting elastic deformation and strain hardening; the resulting idealized material is called a rigid-perfectly plastic material (or, for brevity, rigid-plastic). Thus a beam under dynamic loading will remain rigid until the critical bending moment is reached at a sufficient number of sections where "plastic hinges" appear so that the beam moves as a mechanism. Depending on the problem, these plastic hinges either move along a beam with the critical moment or they are stationary as in static collapse. The above idealization of the material properties and the plastic hinge concept are described in Section 2.2, and the application to static collapse problems is outlined in Section 2.3.

Section 2.4 is devoted to a development of the dynamical theory of rigid-plastic beams. The treatment is similar to that given by Lee and Symonds,[1] but, to be closer to the objective of this report, the example of a clamped beam subjected to a uniformly distributed blast pulse is used to develop the theory.

Section 2.5 points out the similarity between the responses of simply supported and clamped beams. By using the results of Section 2.4 for general blast pulses, relationships among permanent central deflection, peak pressure, and impulse (area under pressure-time curve) are found in Sections 2.6 through 2.9 for exponential, triangular, and rectangular pulses.[3]

In Section 2.10 a theorem is proved concerning the effect of pulse shape on the deflection of a specified class of rigid-plastic structures. It states that among all pulses of equal peak pressure and impulse the rectangular pulse produces the maximum displacement. Although clamped and pinned beams subjected to uniformly distributed blast pulses do not fall into the specified class of structures when the peak pressures exceed three times the static collapse pressure, the theorem is extended to include these cases.

Section 2.11 discusses the "pressure-impulse" diagram and its usefulness in presenting the relationship between deflection, peak pressure, and impulse.

Finally, Section 2.12 presents the description and results of experiments on pinned and clamped beams subjected to uniformly distributed ideal impulses.[4] The final deformations are in close enough agreement with theoretical predictions to support use of the rigid-plastic theory for engineering applications.

Because of the lack of space, many important problems are not discussed such as those involving cantilevers and beams with axial constraints, but treatments can be found in Refs. 5 through 9.

2.2 Bending of Beams--Plastic Hinge

We are concerned here with beams subjected to transverse loading and with support constraints which give rise to a resistive bending moment and a shear force at each cross section (but no axial force). Specifically, we wish to find the distribution of normal stress over a beam cross section giving the resultant bending moment and then to use this distribution to find the moment-curvature relation for different basic types of material behavior. For simplicity of exposition, a beam of rectangular cross section is chosen.

Figure 2.1 shows a beam element of breadth b and depth h located a distance x along the beam from the origin. In Fig. 2.1a the element is in its original unstressed state. In Fig. 2.1b it is deformed by stresses having M and Q as resultant moment and shear force (the shear deformation is neglected); the neutral surface, denoted by NS, is given a radius of curvature R, and the end sections of the element, assumed to remain plane, subtend an angle $d\theta$. The fiber coordinate is z measured from the neutral surface or neutral axis (NA in Fig. 2.1c).

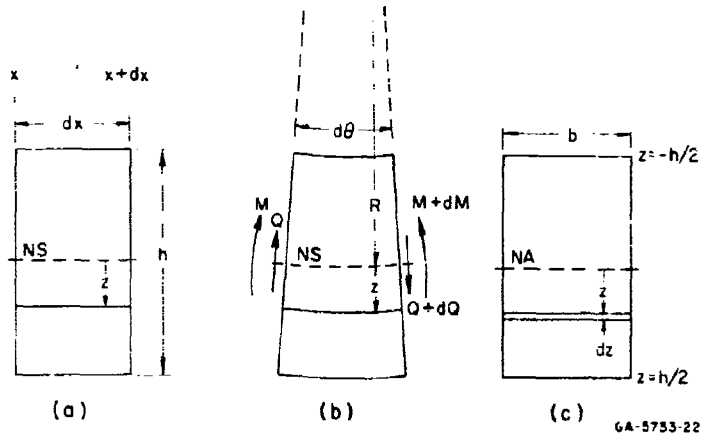

FIG. 2.1 BEAM ELEMENT. (a) Side view when unstressed, (b) Side view when stressed, (c) Cross section

Because of the bending action, the normal stresses acting on the element are compressive above and tensile below the neutral surface. New fiber lengths are given by $(R + z)d\theta$ with that at the neutral surface remaining unchanged as $dx = Rd\theta$. Thus at depth z a fiber has the strain

$$\varepsilon = \left[(R + z)d\theta - Rd\theta\right]/Rd\theta = z/R = \varkappa z \tag{2.1}$$

where $\varkappa$ is the curvature of the neutral surface.

Denoting the normal stress by σ, the bending moment M is found by integrating over the cross section:

$$M = b \int_{-h/2}^{h/2} z\sigma dz \tag{2.2}$$

If the stress is now given as a function of strain and the result $\varepsilon = \varkappa z$ from (2.1) is utilized, the integration of (2.2) provides the required moment-curvature relationship.

For an elastic material obeying Hooke's law with Young's modulus E, we have

$$\sigma = E\varepsilon = E\varkappa z \tag{2.3}$$

and hence (2.2) becomes

$$M = EI\varkappa \tag{2.4}$$

where $I = bh^3/12$ is the second moment of area of the beam cross section.

The linear stress distribution is shown in Fig. 2.2a. At the outermost fibers, $z = \pm h/2$, the maximum stress magnitudes σ_b occur. When $\sigma_b = \sigma_o$ (the yield stress), the maximum elastic bending moment M_e is being sustained by the beam cross section. From formulas (2.3) and (2.4), M_e and the corresponding curvature $\varkappa_e$ are

$$M_e = \sigma_o bh^2/6 \quad \text{and} \quad \varkappa_e = 2\sigma_o/Eh \tag{2.5}$$

The stress distribution is that of Fig. 2.2b.

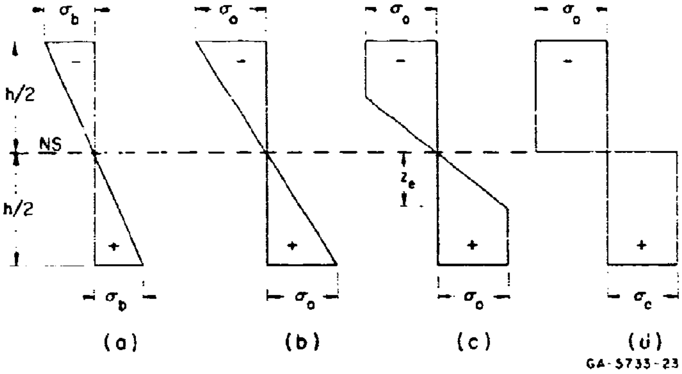

FIG. 2.2 DISTRIBUTIONS OF NORMAL STRESS ON BEAM CROSS SECTION. (a) Elastic, (b) Elastic at yielding, (c) Elastic-plastic, (d) Fully plastic.

An elastic-perfectly plastic material has the stress-strain relationship of Fig. 2.3a, in which the material behaves elastically until the yield stress σ_o at yield strain ϵ_e is reached. During further straining the stress remains constant at σ_o. For a beam of this material, bending beyond the maximum elastic moment M_e produces the stress distribution of Fig. 2.2c. At the two sections $z = \pm z_e$ the strain in the fibers is the yield strain. In the central region, $-z_2 < z < z_e$, the state is elastic with $\sigma = \sigma_o(z/z_e)$; outside this region it is plastic with a uniform normal stress σ_o. This stress distribution

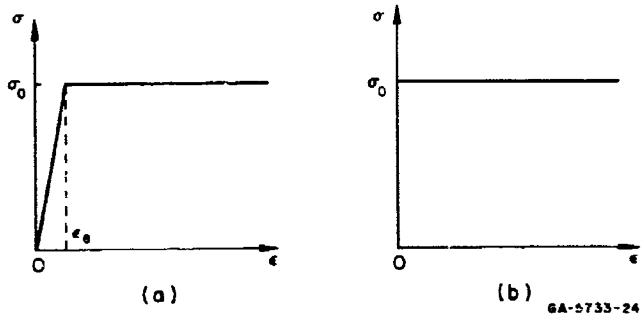

FIG. 2.3 STRESS-STRAIN RELATIONSHIPS. (a) Elastic-plastic, (b) Rigid-plastic.

substituted into the integral (2.2) gives for the bending moment

$$M = \sigma_o b(h^2/4 - z_e^2/3) \tag{2.6}$$

In the central region, $-z_e < z < z_e$, formula (2.3) applies so that z_e is determined by $z_e = \sigma_o/E\kappa$ which, when substituted in (2.6), gives the required moment-curvature relationship

$$M = \sigma_o(bh^2/4)[1 - (\kappa_e/\kappa)^2/3] \qquad \kappa \geq \kappa_e \tag{2.7}$$

As the bending moment increases the curvature increases and the coordinate z_e decreases, tending toward the limiting values $M = M_o$, $\kappa = \infty$, and $z_e = 0$ where

$$M_o = \sigma_o bh^2/4 \tag{2.8}$$

The stress distribution tends toward that of Fig. 2.2d. M_o is called the fully plastic moment. Formula (2.8) allows (2.7) to be written in the form

$$M = M_o\ [1 - (\kappa_e/\kappa)^2/3] \qquad \kappa \geq \kappa_e \tag{2.9}$$

This moment-curvature relationship is shown in Fig. 2.4 for the case of a 6061-T6 aluminum beam having a 1-inch-square cross section. The stress-strain curve was approximated by two straight lines representing an elastic-perfectly plastic behavior with $\sigma_o = 40,000\ lb/in^2$ and $E = 10^7\ lb/in^2$.

A rigid-perfectly plastic material has the stress-strain relationship of Fig. 2.3b. Strain is possible only when the stress is the yield stress σ_o. Figure 2.3b can be looked upon as the limiting case of the elastic-plastic behavior of Fig. 2.3a by letting the elastic modulus E tend to infinity. During this limiting process κ_e from (2.5) tends to zero and for $\kappa > \kappa_e$ formula (2.9) shows that M tends to M_o, the fully plastic moment. Thus for rigid-perfectly plastic materials we are led to the moment-curvature relationship $M = M_o (\kappa > o)$ as shown in Fig. 2.4. A consequence of this relationship is that curvature of a beam element is possible only when the bending moment there is the fully plastic moment. Furthermore, the curvature can become unbounded, providing a plastic hinge.

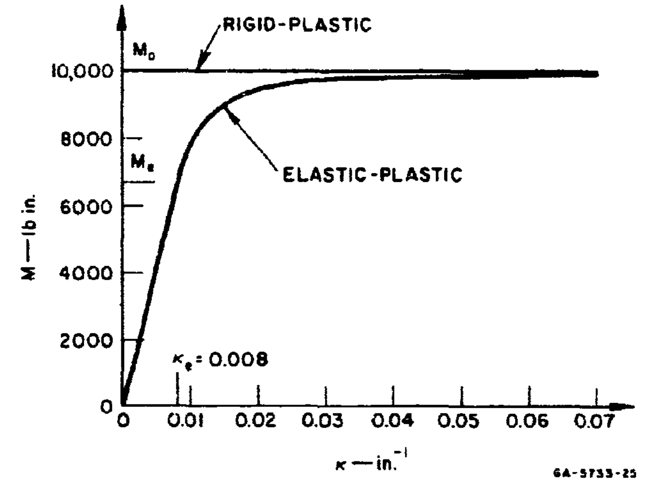

FIG. 2.4 MOMENT-CURVATURE RELATIONSHIPS FOR A BEAM OF 6061-T6 ALUMINUM WITH 1" × 1" CROSS SECTION (Elastic-plastic approximation uses σ_o = 40,000 lb/in.^{2} and E = 10^7 lb/in.^{2}; rigid-plastic approximation uses σ_o = 40,000 lb/in.^{2})

2.3 Collapse of Beams Under Static Loading

This discussion on the collapse of beams under static loading applies to beams of rigid-perfectly plastic material, the material of prime interest throughout this chapter. For brevity, it will be called a rigid-plastic material.

During gradual loading a rigid-plastic beam undergoes no deflection until a collapse mechanism forms consisting of rigid links between a sufficient number of hinges occurring both naturally (e.g., simple supports) and as plastic hinges each carrying the fully plastic moment and allowing large rotations. The load at which the mechanism appears is the static collapse load.

If the static collapse load is exceeded, the problem becomes dynamical with inertial forces coming into play. The static collapse mechanism is then used to describe the motion until the dynamic loading is large enough to cause violation of the yield condition, $M = M_o$, whereupon other mechanisms must be deduced. For loads slightly in excess of the static collapse load, it is reasonable to use the static collapse mechanism, because the inertial forces are still small.

Many structural problems are complicated enough to require the use of the theorems of limit analysis[2] to establish static collapse loads (or upper and lower bounds for these loads) and mechanisms. However, in this chapter each of the beam problems involving blast loads has a corresponding static problem with a simple exact solution. The beams are either clamped or simply supported with loading uniformly distributed over the entire length. In each of these symmetrical cases the static collapse mechanism has a hinge at each support and a hinge at midspan.

Before proceeding to these problems, let us consider a more general load distribution. Suppose we wish to find the dynamic response of a clamped rigid-plastic beam subjected to blast loading uniformly distributed from one support to midspan. We can first obtain the collapse pressure and mechanism for the corresponding static problem shown in Fig. 2.5a. Only the hinge locations at the supports are immediately obvious (from a qualitative knowledge of the elastic bending moment distribution for small enough values of the load p per unit length acting on an elastic beam). The third hinge required to form a mechanism is given the location $x = x_h$ as yet unknown. Each hinge supports a fully plastic moment of magnitude M_o. For distributed loading the shear force is continuous and for the present problem is

$$Q = \begin{cases} 3pL/8 - px & 0 \le x \le L/2 \\ 3pL/8 - pL/2 & L/2 \le x \le L \end{cases}$$

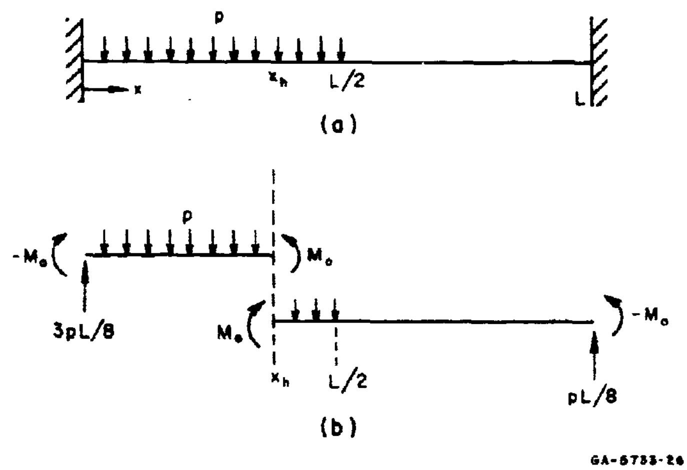

FIG. 2.5 STATIC COLLAPSE PROBLEM.
(a) Configuration, (b) Forces and moments.

Since $dM/dx = Q$, the moment M is also continuous. Thus to have a maximum $M = M_o$ at $x = x_h$ requires $Q = 0$ there. To have it otherwise would violate the yield condition in the neighborhood of $x = x_h$. With the aid of Fig. 2.5b we are now able to write the equilibrium equations for each link of our mechanism. By taking moments about each support, these equations are

$$2M_o = px_h^2/2 \qquad \text{and} \qquad 2M_o = p(L/2 - x_h)[L/2 + (L/2 + x_h)/2]$$

which provide the hinge location and static collapse pressure

$$x_h/L = (\sqrt{7} - 1)/4 \qquad p = 4M_o/x_h^2$$

These results would allow us to start the dynamic analysis by adopting the mechanism for pressures a little in excess of the static collapse pressure and taking into account the inertia forces.

2.4 Dynamic Response of Clamped Beams to Blast Loads

To present the method of finding the dynamic response of a rigid-plastic beam to blast loading, we shall treat fully the case of a clamped beam subjected to blast loading uniformly along its entire length (see Fig. 2.6a). A blast load is taken here to mean a pressure-time curve with an instantaneous rise to the peak pressure p_m followed by a monotonic decay as shown in Fig. 2.7. In later sections specific pressure-time curves are employed, including the rectangular pulse (constant pressure applied for a short time).

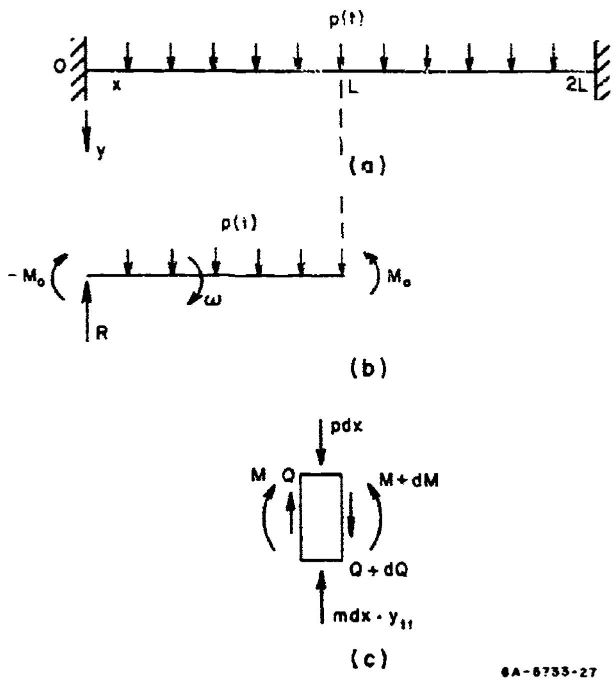

FIG. 2.6 CLAMPED BEAM IN MECHANISM 1 ($p_s < p_m < 3p_s$). (a) Configuration, (b) Dynamics of half-beam, (c) Beam element – notation

2.4.1 Mechanism 1

The static collapse mechanism has a plastic hinge at each support and at the beam center. Referring to Fig. 2.6b, which shows one-half of the beam with its attendant forces and moments, the sum of moments about the supports equated to zero gives the static collapse pressure

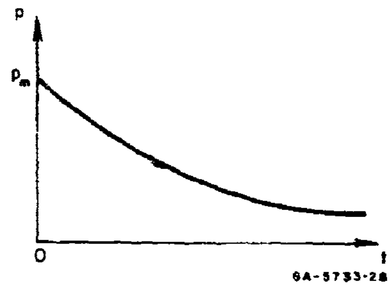

FIG. 2.7 TYPICAL BLAST LOAD

$$p_s = 4M_o/L^2 \qquad (2.10)$$

For peak pressures slightly in excess of p_s the inertia forces are small, so it is reasonable to use the static collapse mechanism to describe the motion. We shall call this mechanism 1. Let the velocity of the beam center be $V(t)$, where t represents time. The angular velocity ω of each half-beam is then

$$\omega = V/L \qquad (2.11)$$

The equation of angular motion about the support is

$$mL^3\dot{\omega}/3 = pL^2/2 - 2M_o \qquad (2.12)$$

where m is the beam mass per unit length and the dot denotes differentiation with respect to time.

From (2.12), (2.11), and (2.10) the acceleration of the beam center is

$$\dot{V} = 3(p - p_s)/2m \qquad (2.13)$$

With the beam initially at rest, integration of (2.13) gives

$$V = 3(I - p_s t)/2m \qquad (2.14)$$

where I is the impulse per unit length that has been applied at time t and is defined by

$$I(t) = \int_0^t p(\tau)d\tau \qquad (2.15)$$

The time t_2 at which motion ceases is found by setting $V = 0$ in (2.14) which, with $I_2 = I(t_2)$ defined by (2.15), gives

$$I_2 = p_s t_2 \qquad (2.16)$$

Interpreted geometrically, the result (2.16) requires the shaded areas in Fig. 2.8 to be equal. The angular momentum of a half-beam about a support is $mL^3\omega/3 = mL^2V/3 = (I - p_s t)L^2/2$, so the growth of the upper area shows how the angular momentum increases and the growth of the lower area shows how the angular momentum decreases until the beam comes to rest. At the intersection $p(t) = p_s$, the angular velocity is a maximum.

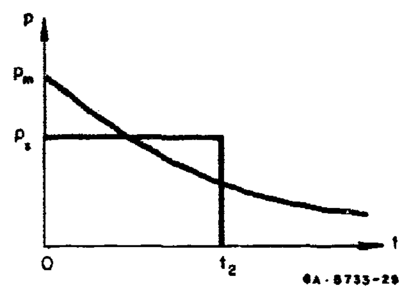

FIG. 2.8 GEOMETRICAL CONSTRUCTION FOR DURATION OF MOTION
(The two shaded areas are equal)

Knowing the duration of motion t_2, the final central deflection is calculated from

$$y(L,t_2) = \int_o^{t_2} V dt = \frac{3}{2m}\left[\int_o^{t_2} I dt - p_s t_2^2/2\right] \qquad (2.17)$$

To obtain the range of pressures for which mechanism 1 holds, it is necessary to establish the pressure at which the yield condition $M = M_o$ is violated. This pressure will now be found.

With the notation of Fig. 2.6c, the equations of motion of a beam element are

$$p + Q_x - my_{tt} = 0 \qquad (2.18)$$

$$Q - M_x = 0 \qquad (2.19)$$

where subscripts x and t denote partial differentiation. The rotary inertia of the beam element is neglected. When $y_{tt} = \dot{V}x/L$, with $\dot{V}$ from (2.13), is substituted in (2.18), we find that

$$Q_x/p_s = 3(\lambda - 1)\ \xi/2 - \lambda \qquad (2.20)$$

in which the convenient dimensionless qualities $\xi = x/L$ and $\lambda = p/p_s$ have been introduced. Expression (2.20) is linear in ξ and full lines corresponding to the values $\lambda = 1$, 2, and 3 are shown in Fig. 2.9a; a dashed line for $\lambda > 3$ is also shown (drawn for $\lambda = 5$). From (2.19), $Q_x = M_{xx}$, so (2.20) tells us that $M_{xx} < 0$ for $1 < \lambda < 3$, which means that the curvature of the bending moment diagram does not change sign as M increases from $-M_o$ at $\xi = 0$ to M_o at $\xi = 1$. Formula (2.20) also tells us that $Q_x = M_{xx} = 0$ at $\xi = 1$ when $\lambda = 3$ and that $Q_x = M_{xx} > 0$ in the neighborhood of $\xi = 1$ when $\lambda > 3$. Hence, when $\lambda > 3$, M_{xx} does change sign ($M_{xx}/p_s = -\lambda < 0$ at $\xi = 0$, $M_{xx}/p_s = (\lambda - 3)/2 > 0$ at $\xi = 1$).

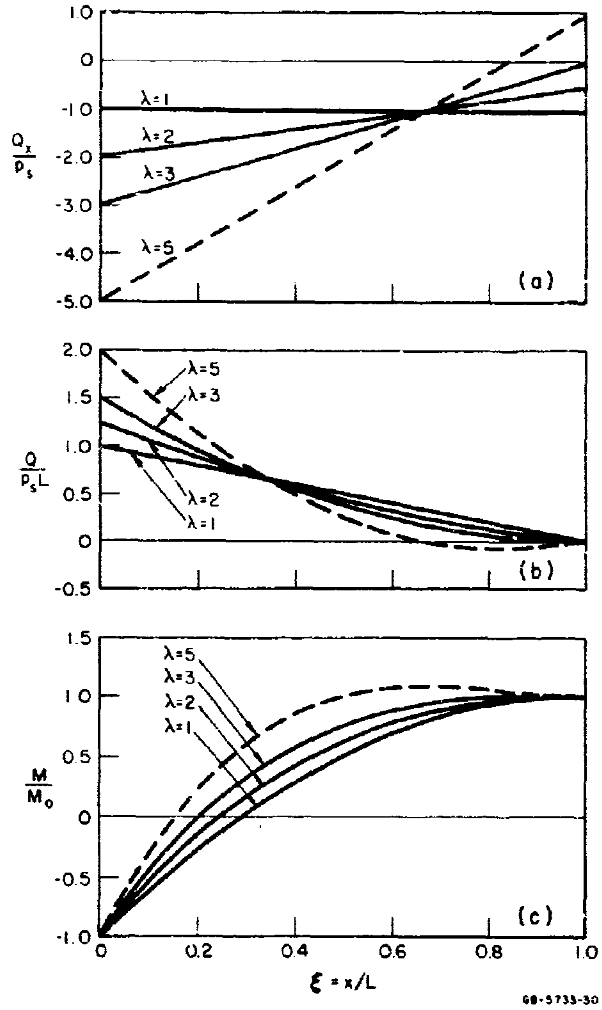

FIG. 2.9 DIAGRAMS FOR M_{xx}, M_x, AND M ASSOCIATED WITH MECHANISM I. (a) Q_x or M_{xx} diagram, (b) Shear force diagram ($Q = M_x$), (c) Bending moment diagram.

By integrating (2.20) we obtain for the shear force the expression

$$Q/p_s L = (1 - \xi)[\lambda + 3 - 3(\lambda - 1)\xi]/4 \qquad (2.21)$$

Shear force curves are shown in Fig. 2.9b. Note that $Q = M_x \geq 0$ for

$1 < \lambda < 3$ (equality at $\xi = 1$) but in the neighborhood of $\xi = 1$, $Q = M_x < 0$ for $\lambda > 3$. Now $M = M_o$, its maximum permissible value, at $\xi = 1$, so $M > M_o$ in the neighborhood of $\xi = 1$ for $\lambda > 3$. Thus the yield condition is violated when the pressure is greater than three times the static collapse pressure and mechanism 1 becomes invalid. For blast pulses as described by Fig. 2.7, the maximum or peak pressure p_m occurs immediately, so that if $p_s < p_m < 3p_s$ the entire deformation takes place by mechanism 1.

By integrating (2.21) we obtain for the bending moment the expression

$$M/M_o = 1 - (1 - \xi)^2 \left[2 - (\lambda - 1)\xi\right] \qquad (2.22)$$

Moment curves are shown in Fig. 2.9c. Note how the yield condition is violated for $\lambda > 3$. If $\lambda = 3 + \delta\lambda$, where $\delta\lambda$ is small and positive, and if $\xi = 1 - \delta\xi$, where $\delta\xi$ is likewise small and positive, the value of $\delta\xi$ giving $Q = 0$ (excepting $\delta\xi = 0$) is, from (2.21), $\delta\xi = 2\delta\lambda/3(2 + \delta\lambda)$. Using this result in (2.22), the maximum moment is approximately $M = M_o[1 + (\delta\lambda/3)^3] > M_o$.

2.4.2 Mechanism 2

The manner in which the yield moment is exceeded near the beam center when pressures are over three times the static collapse pressure suggests a new mechanism, "mechanism 2," consisting of a central part of variable length undergoing translatory motion connected at each end by a moving hinge to a part which rotates as a rigid body about a support (Fig. 2.10a). For the half-beam shown in Fig. 2.10b, it is assumed that each section between the hinge at $x = x_h(t)$ and the center is subjected to the fully plastic moment, but changes of curvature occur only at the hinge.

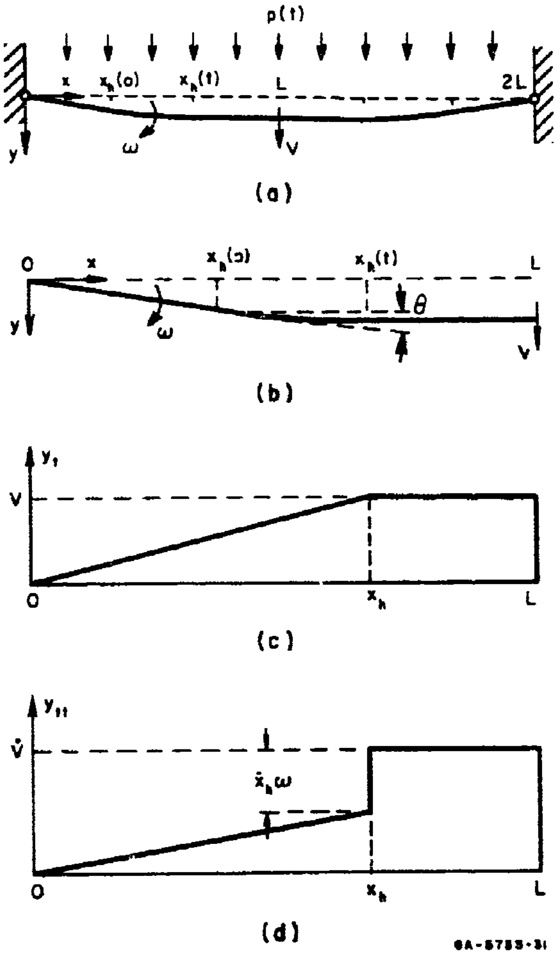

FIG. 2.10 CLAMPED BEAM IN MECHANISM 2 ($p_m > 3p_s$). (a) Mechanism 2, (b) Motion of half-beam, (c) Velocity distribution, (d) Acceleration distribution.

The displacement is continuous and is expressible as

$$y(x,t) = \begin{cases} y(L,t) - \int_x^{x_h(t)} \theta(x',t)dx' & 0 \le x \le x_h \\ y(L,t) & x_h \le x \le L \end{cases} \qquad (2.23)$$

in which θ is the slope or rotation of a beam element and for sufficiently small displacements $\theta = dy/dx$. As the plastic hinge travels along the beam from $x_h(0)$ to L, each section it passes is rotated an infinitesimal angle ωdt while x_h moves a distance $\dot{x}_h dt$. The hinge leaves behind it a deformed beam with a continuous slope θ and a curvature equal to $\omega/\dot{x}_h$.

Differentiation of (2.23) for the transverse velocity of the beam gives

$$y_t(x,t) = y_t(x_h^-,t) - (x_h - x)\omega - \theta(x_h,t)\dot{x}_h \qquad 0 \le x \le x_h \tag{2.24}$$

$$y_t(x,t) = y_t(x_h^+,t) = V \qquad x_h < x \le L \tag{2.25}$$

where x_h^- and x_h^+ signify points just to the left and right of x_h. By definition of the mechanism, the slope at the moving hinge is zero, that is, $\theta(x_h,t) = 0$. Hence (2.24) and (2.25) give the same velocity at x_h^- and x_h^+, proving that the velocity is continuous across the hinge at $x = x_h$, and consequently it is continuous along the whole beam. We thus have

$$y_t(x,t) = V - (x_h - x)\omega \qquad 0 \le x \le x_h \tag{2.26}$$

$$y_t(x,t) = V \qquad x_h \le x \le L \tag{2.27}$$

Differentiation of (2.26) and (2.27) for the acceleration gives

$$y_{tt}(x,t) = \dot{V} - (x_h - x)\dot{\omega} - \dot{x}_h\omega \qquad 0 \le x \le x_h \tag{2.28}$$

$$y_{tt}(x,t) = \dot{V} \qquad x_h \le x \le L \tag{2.29}$$

Hence at $x = x_h$ the acceleration has a discontinuity of magnitude $\dot{x}_h \omega$. Examples of velocity and acceleration distributions are shown in Figs. 2.10c and d.

One advantage of the theory of rigid-plastic beams is that the motion of a mechanism is governed by the equations of elementary rigid body dynamics. However, unlike mechanism 1, this mechanism has links which vary in length and thus it is not obvious that assuming fixed lengths at each instant is correct. The angular momentum about the support of the rigid portion between $x = 0$ and $x = x_h$ (Fig. 2.10) plus the element between $x = x_h$ and $x = x_h + \dot{x}_h \delta t$ at time t is

$$H = m x_h^3 \omega/3 + m\dot{x}_h \delta t \; V x_h$$

after neglecting powers of the increments higher than the first. Similarly, at time $t + \delta t$ the angular momentum is

$$H + \delta H = m x_h^3 (\omega + \delta\omega)/3 + m\dot{x}_h \delta t \; \omega x_h \cdot x_h$$

giving the momentum change

$$\delta H = m x_h^3 \delta\omega/3 + m\dot{x}_h \; \delta t x_h (\omega x_h - V)$$

But the velocity is continuous at $x = x_h$, that is, $\omega x_h = V$, so $\dot{H} = m x_h^3 \dot{\omega}/3$ holds whether the hinge is moving or stationary.

Before writing the equations of motion for each portion of the beam, we note that the shear force Q is zero at the traveling hinge. Integration of (2.18) with respect to x shows that Q, and hence, by (2.19), M_x, is continuous along the beam. Thus for $M = M_o$ to be a maximum at $x = x_h$ we have $M_x = Q = 0$ at $x = x_h$.

The equations of motion for the two portions of the half-beam are (see Fig. 2.11)

$$m\dot{V} = p \qquad x_h < x \le L \qquad (2.30)$$

$$m x_h^3 \dot{\omega}/3 = p x_h^2/2 - 2M_o \qquad 0 \le x < x_h \qquad (2.31)$$

and continuity of velocity requires

$$V = \omega x_h \qquad (2.32)$$

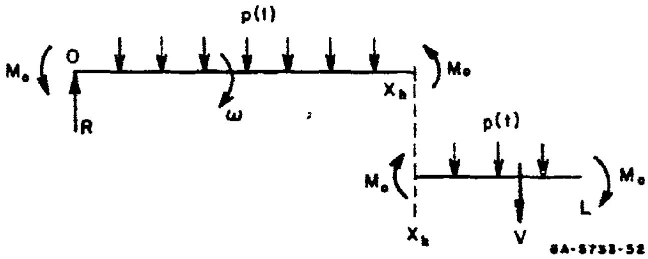

FIG. 2.11 HALF-BEAM IN MECHANISM 2

Equation (2.30) integrates immediately to give the velocity of the central portion of the beam as

$$V = I/m \qquad (2.33)$$

Thus from (2.32) $\omega = I/mx_h$ and when $\dot{\omega}$ is eliminated (2.31) is expressible in the form $(Ix_h^2)^{\cdot} = 12M_o$ giving for the hinge location

$$x_h^2 = 12M_o t/I \qquad (2.34)$$

and for the hinge velocity

$$x_h = 6M_o(I - pt)/I^2 x_h \qquad (2.35)$$

For a blast pulse with an instantaneous rise to its peak pressure p_m (see Fig. 2.7 or 2.8), the starting position of the plastic hinge is found by using in (2.34) the result: Lim $(I/t) = p_m$, $t \to 0$. This limiting process gives $x_h^2(0) = 12M_o/p_m$ or, in terms of $\lambda = p_m/p_s$ (whenever $\lambda > 3$), $x_h^2(0)/L^2 = 3/\lambda$. Again for a blast pulse we have $I > pt$, so that (2.35) predicts a positive hinge velocity. The monotonic decay of the blast pulse is more than enough to ensure that the hinge proceeds steadily toward the beam center. (Note that for a rectangular pulse we have $I = pt$ while the pulse is acting. Consequently $\dot{x}_h = 0$ and a stationary hinge exists at $x_h = 12M_o/p_m$.) Equation (2.34) also provides the time $t = t_1$ when the hinge arrives at the beam center as the solution to

$$I_1 = 12M_o t_1/L^2 = 3p_s t_1 \tag{2.36}$$

Equation (2.36) may be given a geometrical interpretation similar to that given for (2.16) which determines the duration of motion when it occurs entirely by mechanism 1. The horizontally shaded areas in Fig. 2.12 are equal.

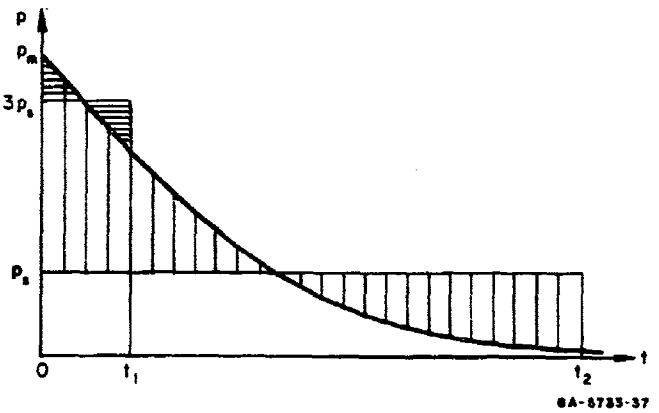

FIG. 2.12 GEOMETRICAL CONSTRUCTION FOR DURATION OF MOTION AND DURATION OF MECHANISM 2
(Areas shaded alike are equal)

At time $t = t_1$ the velocity of the beam center, from (2.33), is

$$V_1 = I_1/m \tag{2.37}$$

and the central deflection is

$$y(L,t_1) = \frac{1}{m}\int_0^{t_1} I\,dt \tag{2.38}$$

Motion now continues by mechanism 1 according to Eq. (2.12) or in terms of V instead of ω, according to Eq. (2.13). With the initial velocity condition (2.37), integration leads to

$$V = 3(I - p_s t)/2m \tag{2.39}$$

which is the same equation as (2.14). The total duration of motion t_2 is found by setting $V(t_2) = 0$ in (2.39). Hence

$$I_2 = p_s t_2 \tag{2.40}$$

Interpreted geometrically, this result states that the two vertically shaded areas in Fig. 2.12 are equal. The angular momentum of the half-beam about the support during deformation by mechanism 2 is $m(L^2 - x_h^2)/2 + mx_h^3\omega/3 = IL^2/2 - Ix_h^2/6 = (I - p_s t)L^2/2$ which is the same as that during deformation by mechanism 1. Thus the growth of the upper shaded area shows how the angular momentum increases and the growth of the lower shaded area shows how the angular momentum decreases until the beam comes to rest.

By integrating (2.39) the central deflection which occurs during deformation by mechanism 1 is

$$y(L,t_2) - y(L,t_1) = \frac{3}{2m}\left[\int_{t_1}^{t_2} I\,dt - \frac{p_s}{2}\left(t_2^2 - t_1^2\right)\right] \tag{2.41}$$

where $y(L,t_1)$ is given by (2.38).

To find the final shape of the half-beam, we consider it in the two regions $0 \le x \le x_h(0)$ and $x_h(0) \le x \le L$, where $x_h(0)$ is the initial position of the traveling hinge. The portion of the beam in the former region experiences only rigid-body rotation about the support so that

$$y(x,t_2) = \int_0^{t_2} \omega x dt \qquad 0 \le x \le x_h(0) \tag{2.42}$$

Now since $\omega = I/mx_h$ when $0 \le t \le t_1$ and $\omega = V/L = 3(I - pt)/2mL$ when $t_1 \le t \le t_2$, formula (2.42) becomes

$$y(x,t_2) = \frac{x}{m} \int_0^{t_1} \frac{I}{x_h} dt + \frac{3x}{2mL} \int_{t_1}^{t_2} (I - p_s t)dt$$
$$0 \le x \le x_h(0) \tag{2.43}$$

The times t_1 and t_2 are given by Eqs. (2.36) and (2.40). In the latter region $x_h(0) \le x \le L$ the traveling hinge passes through each beam section. Let $t = \tau$ be the time when the hinge arrives at section x. Then we have

$$y(x,t_2) = \int_0^{\tau(x)} V dt + \int_{\tau(x)}^{t_2} \omega x dt$$
$$x_h(0) \le x \le L \tag{2.44}$$

which, upon substituting $V = I/m$ and the above formulas for ω, becomes

$$y(x,t_2) = \frac{1}{m} \int_0^{\tau(x)} I dt + \frac{x}{m} \int_{\tau(x)}^{t_1} \frac{I}{x_h} dt + \frac{3x}{2mL} \int_{t_1}^{t_2} (I - p_s t)dt$$
$$x_h(0) \le x \le L \tag{2.45}$$

From (2.34), $\tau(x)$ is the solution of the equation $x^2 = 12M_o\tau/I(\tau)$ or of $(x/L)^2 = 3p_s\tau/I(\tau)$.

Turning now to the shear force and bending moment diagrams associated with mechanism 2, we first note that we have $M = M_o$ and hence $Q = 0$ in the region $x_h < x \le L$. We have already shown that at $x = x_h$, the location of the hinge, we have $M = M_o$ and $Q = 0$. It remains to describe M and Q in the region $0 \le x < x_h$.

From (2.18), the equation of motion of a beam element, the acceleration y_{tt} can be eliminated by using the relation $y_{tt} = \dot{\omega}x$ with $\dot{\omega}$ given by (2.31), the equation of motion about the support of the rigid portion of the half-beam. In this way we find that

$$Q_x = -[(I - pt)x/x_h + 2pt(1 - x/x_h)]$$

$$0 \le x < x_h \qquad (2.46)$$

which, since $I > pt$, is always negative no matter how large the pressure may be. Thus we also have $M_{xx} < 0$, which means that the curvature of the moment diagram is always negative. Note that at $x = x_h$ we have $Q_x = -(I - pt)/2t$, thereby giving the discontinuity there corresponding to the discontinuity $\dot{x}_h\omega$ of the acceleration.

By integrating (2.46) we obtain for the shear force

$$Q = x_h(1 - x/x_h)[I - pt)(1 + x/x_h) + 2pt(1 - x/x_h)]/4t$$

$$0 \le x \le x_h \qquad (2.47)$$

which shows that Q, and hence M_x, is always positive.

One further integration provides the following expression for the bending moment:

$$M/M_o = 1 - (1 - x/x_h)^2[(I - pt)(2 + x/x_h) + 2pt\ (1 - x/x_h)]/I$$

$$0 \le x \le x_h \qquad (2.48)$$

and because $Q = M_x$ is always positive, M increases monotonically from $-M_o$ at $x = 0$ to M_o at $x = x_h$. It is concluded therefore that no further mechanism need be sought.

The above observations are illustrated by Fig. 2.13 which shows the distributions along a half-beam of Q_x, Q, and M for a triangular blast pulse with $\lambda_m = p_m/p_s = 5$, $\lambda = p/p_s = 2$, and $x_h/L = (6/7)^{1/2}$.

2.4.3 Conservation of Energy

For a rigid-plastic beam initially at rest, the work done by the pressure equals the sum of the work done by plastic bending and the kinetic energy. Results follow which give the rate of work and rate of change of kinetic energy during deformation by mechanisms 1 and 2.

The rate of work done by the applied pressure is

$$\dot{W}_F = \int_o^L p y_t \, dx = \begin{cases} pV(L - x_h/2) & \text{mechanism 2} \\ pVL/2 & \text{mechanism 1} \end{cases}$$

and the rate of plastic work done in bending is

$$\dot{W}_P = 2M_o\omega = \begin{cases} 2M_oV/x_h & \text{mechanism 2} \\ 2M_oV/L & \text{mechanism 1} \end{cases}$$

while the rate of change of kinetic energy is

$$\dot{W}_K = \begin{cases} [mx_h^3\omega^2/6 + m(1 - x_h)V^2/2]^{\cdot} = pV(L - x_h/2) - 2M_oV/x_h & \text{mechanism 2} \\ [mL^3\omega^2/6]^{\cdot} = pVL/2 - 2M_oV/L & \text{mechanism 1} \end{cases}$$

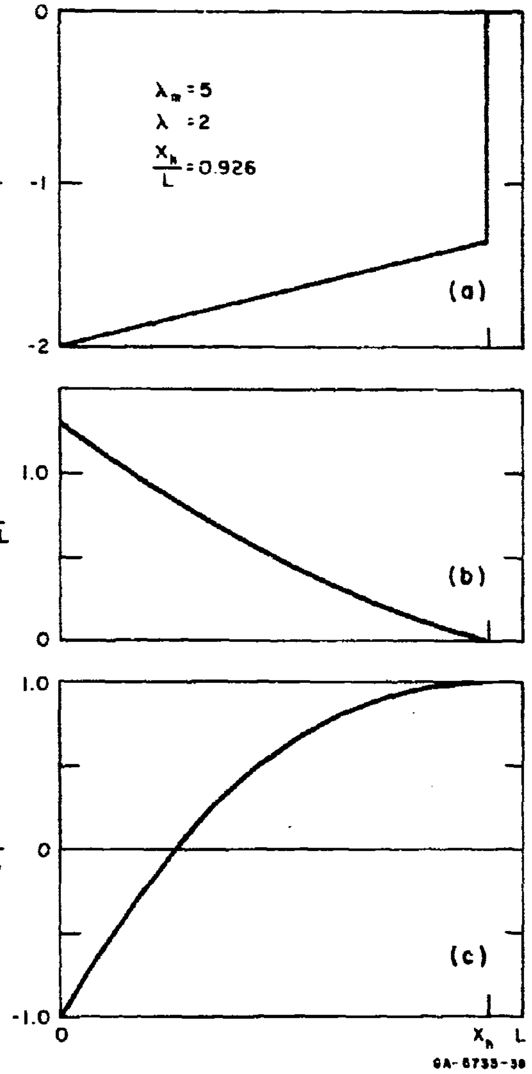

FIG. 2.13 DIAGRAMS FOR M_{xx}, M_x, AND M ASSOCIATED WITH MECHANISM 2. (a) Q_x or M_{xx} diagram, (b) Shear force diagram ($Q = M_x$), (c) Bending moment diagram.

It is readily seen that the results satisfy the conservation equation

$$\dot{W}_F = \dot{W}_P + \dot{W}_K$$

In the rather simple derivations, we use the relation $\omega = V/x_h$ (mechanism 2) or $\omega = V/L$ (mechanism 1) to eliminate ω, and the relations (2.34) and (2.35) for mechanism 2 to eliminate $\dot{x}_h$ and t. Making such an energy balance is often a useful check on the solution of the equations of motion.

2.5 Dynamic Response of Simply Supported Beams to Blast Loads

Since the dynmaic response of a simply supported beam to a uniformly distributed blast load is so similar to that of a clamped beam, we shall restrict ourselves to showing how the results of interest can be readily deduced from those in Section 2.4. Instead of a moment $M = -M_o$ due to a stationary plastic hinge at each support, we have the boundary condition $M = 0$ representing a pinned support. Consequently, the static collapse pressure is halved, and in the equations of angular motion of the rigid portion of a half-beam about its support, that is, in Eqs. (2.12) and (2.31) of mechanisms 1 and 2, the restoring moment is M_o from the traveling hinge instead of $2M_o$ from the traveling hinge plus the stationary hinge at the clamped support.

2.5.1 Mechanism 1

The static collapse mechanism is the same as that for the clamped beam, a hinge at each support and at the center. Since the only restoring moment acting on a half-beam is $M = M_o$ from the plastic hinge at the center, the equation of equilibrium gives a static collapse pressure of

$$p_s = 2M_o/L^2 \tag{2.49}$$

which is half of that required to cause collapse of a clamped beam.

For motion by mechanism 1 the governing equation, corresponding to (2.12), is

$$mL^3\dot{\omega}/3 = pL^2/2 - M_o$$

where $\omega = V/L$. Equations (2.13) to (2.21) hold provided that the value of p_s is given by (2.49) wherever it occurs. Because of the support condition $M = 0$, the bending moment expression (2.22) is replaced by

$$M/M_o = 1 - (1 - \xi)^2[2 - (\lambda - 1)\xi]/2$$

where $\xi = x/L$ and $\lambda = p/p_s$, with p_s again given by Eq. (2.49). Since Eqs. (2.20) and (2.21) still hold, the peak pressure of the blast pulse is restricted to the range $p_s < p_m < 3p_s$ (i.e., $1 < \lambda < 3$) in order not to violate the yield condition.

2.5.2 Mechanism 2

Whenever the peak pressure is greater than $3p_s$, the mechanism of deformation consists of a variable central length of beam undergoing translatory motion connected at each end by moving plastic hinges or interfaces to an outer portion of beam rotating as a rigid body about its support. In the central portion of beam the moment is $M = M_o$, but changes of curvature occur only at the ends. This mechanism is the same as that for clamped beams and is suggested by the trend of the shear force and bending moment distributions for mechanism 1 as pressures increase through $3p_s$. Although the miminum peak pressure activating mechanism 2 corresponds to $\lambda = p_m/p_s = 3$ as in the case of clamped beams, the actual minimum peak pressure is half of that for clamped beams because p_s is halved.

The equations of motion for mechanism 2 corresponding to (2.30) and (2.31) are

$$m\dot{V} = p \qquad\qquad x_h < x \le L$$

$$m x_h^3 \dot{\omega}/3 = p x_h^2/2 - M_o \qquad\qquad 0 \le x < x_h$$

where $\omega = V/x_h$. The solution giving the hinge location is found by using M_o instead of $2M_o$ in Eq. (2.34), so that

$$x_h^2 = 6M_o t/I \qquad \text{or} \qquad (x_h/L)^2 = 3p_s t/I \tag{2.50}$$

with p_s from Eq. (2.49). From Eq. (2.50) the initial position of the traveling hinge is given by

$$x_h^2(0) = 6M_o/p_m = 3/\lambda$$

and the hinge velocity is

$$\dot{x}_h = 3M_o(I - pt)/I^2 x_h$$

Provided we use formulas (2.49) and (2.50) for p_s and x_h whenever they occur, Eqs. (2.36) to (2.47) hold. Because of the support condition $M = 0$, the bending moment expression (2.48) is replaced by

$$M/M_o = 1 - (1 - x/x_h)^2[(I - pt)(2 + x/x_h) + 2pt(1 - x/x_h)]/2I$$

2.6 Clamped Beam Subjected to an Exponential Blast Load

We shall now find the relationship among the peak pressure, impulse, and final central deflection for a clamped rigid-plastic beam subjected to an exponential blast pulse uniformly distributed over its entire length. By an exponential blast pulse we mean a pulse with an instantaneous rise to its peak pressure p_m followed by an exponentially decaying pressure. It is represented by the pressure function

$$p = p_m e^{-kt} \tag{2.51}$$

where the constant $k = p_m/I_o$. The impulse I_o is the total area under the pressure-time curve. Corresponding to (2.51), we have the impulse function

$$I = I_o(1 - e^{-kt}) \tag{2.52}$$

The results we require are obtained by substituting Eq. (2.52) in the appropriate results of Section 2.4 for general blast pulses. It is convenient to express our results in terms of the dimensionless quantities

$$\lambda = p_m/p_s \qquad \tau = kt = p_m t/I_o \quad \text{and} \quad \nu = \delta/(I_o^2 L^2/mM_o) \tag{2.53}$$

where, for brevity, $\delta = y(L,t)$ is the central deflection.

2.6.1 Mechanism 1

For the peak pressure range $p_s < p_m < 3p_s$, where $p_s = 4M_o/L^2$ is the static collapse pressure, deformation starts by mechanism 1 (one plastic hinge at each support and one at midspan). The final central deflection is given by Eq. (2.17) in which t_2, the time when motion ceases, is the solution of Eq. (2.16). Inserting the impulse function (2.52) in (2.16) and converting to the dimensionless variables (2.53) yields for $\tau_2 = kt_2$ the equation

$$1 - e^{-\tau_2} = \tau_2/\lambda \qquad 1 < \lambda < 3 \tag{2.54}$$

Similarly from Eq. (2.17) the dimensionless final central deflection ν_2 (value of ν at time $t = t_2$ or when $\tau = \tau_2$) is

$$\nu_2 = 3[2(\lambda - 1) - \tau_2]\tau_2/16\lambda^2 \qquad 1 < \lambda < 3 \tag{2.55}$$

2.6.2 Mechanism 2

Whenever $p_m > 3p_s$, deformation starts by mechanism 2, which is described in Section 2.4.2. The central deflection at time t_1, when mechanism 2 changes to mechanism 1, is given by Eq. (2.38), t_1 being the solution of Eq. (2.36). With the impulse function (2.52) and the variables (2.53), these equations become

$$1 - e^{-\tau_1} = 3\tau_1/\lambda \qquad \lambda > 3 \tag{2.56}$$

$$\nu_1 = (\lambda - 3)\tau_1/4\lambda^2 \qquad \lambda > 3 \tag{2.57}$$

Motion continues by mechanism 1 until it ends at time t_2, the solution of (2.40), and the additional central deflection acquired is given by (2.41). With the impulse function (2.52), these equations become

$$1 - e^{-\tau_2} = \tau_2/\lambda \qquad \lambda > 3 \tag{2.58}$$

$$\nu_2 - \nu_1 = 3[2(\lambda - 1)\tau_2 - 2(\lambda - 3)\tau_1 - (\tau_2^2 - \tau_1^2)]/16\lambda^2$$
$$\lambda > 3 \tag{2.59}$$

2.6.3 Peak Pressure, Impulse, and Deflection Relationship

Equations (2.54) through (2.59) represent the required relationship among the peak pressure, impulse, and permanent central deflection. Note that for the exponential pulse the values of τ_1 and τ_2 are solutions of transcendental equations and have to be found numerically for each value of λ. The relationship is therefore best presented graphically as shown by the curve in Fig. 2.14. For a constant impulse I_o the curve shows that the central deflection increases with increasing peak pressure and tends asymptotically to a value corresponding to $\nu = 1/6$ for the ideal impulse. This can be seen by the following limiting process. As p_m and hence λ tend to infinity, the constant $k = p_m/I_o$ tends to infinity when I_o is held constant. Since the left-hand sides of Eqs. (2.56) and (2.58) are bounded ($0 < 1 - e^{-\tau} < 1$), the right-hand sides indicate that τ_1 and τ_2 also tend to infinity with λ. This behavior allows the approximations $e^{-\tau_1} \approx 0$ and $\epsilon^{-\tau_2} \approx 0$ so that, for large enough λ, τ_1 and τ_2 can be given the values $\tau_1 = \lambda/3$ and $\tau_2 = \lambda$. Substituting these values in (2.57) and (2.59) leads to $\nu_1 = 1/12$ and $\nu_2 = 1/6$, the latter being the value at the vertical asymptote in Fig. 2.14.

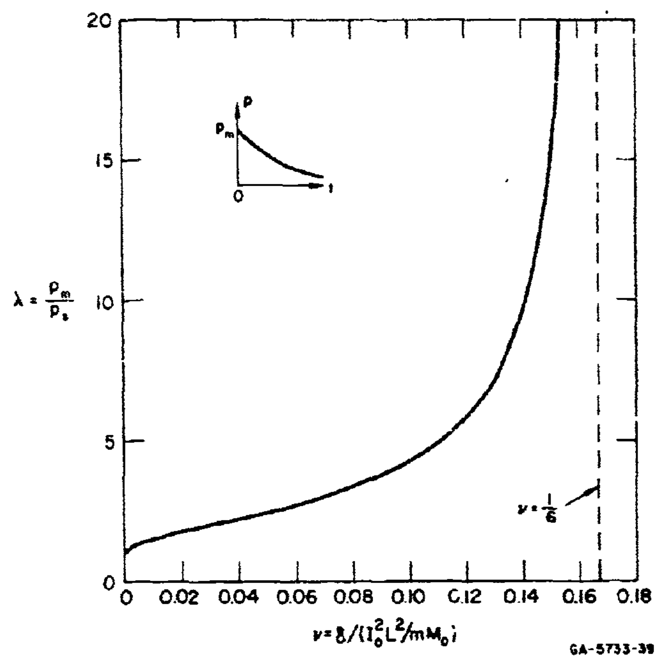

FIG. 2.14 PEAK PRESSURE, IMPULSE, CENTRAL DEFLECTION RELATIONSHIP FOR A CLAMPED BEAM SUBJECTED TO AN EXPONENTIAL PULSE

2.7 Clamped Beam Subjected to a Triangular Blast Load

We shall now find the relationship among the peak pressure, impulse, and permanent central deflection for a clamped rigid-plastic beam subjected to a triangular blast pulse uniformly distributed along its entire length. By a triangular blast pulse we mean a pulse with an instantaneous rise to its peak pressure p_m followed by a linearly decaying pressure. With t_o as the duration, the pulse is represented by the pressure function

$$p = \begin{cases} p_m(1 - t/t_o) & 0 \le t/t_o \le 1 \\ 0 & t/t_o \ge 1 \end{cases} \qquad (2.60)$$

The impulse $I_o = p_m t_o/2$ is the total area under the pressure-time curve. Corresponding to the pressure function (2.60) is the impulse function

$$I = \begin{cases} I_o(t/t_o)\,(2 - t/t_o) & 0 \le t/t_o \le 1 \\ I_o & t/t_o \ge 1 \end{cases} \qquad (2.61)$$

We shall follow the procedure of Section 2.6 for the exponential load by using the impulse function (2.61) in conjunction with the appropriate formulas derived in Section 2.4 for the general blast load. However, since the triangular pulse is of finite duration, attention has to be paid to the relationship of the time t_o, when the pulse ends, to the times t_1 and t_2, when mechanisms 2 and 1 end. As will be seen, this slight complication amounts to considering peak pressure values within four ranges instead of two as in the case of exponential pulses. On the other hand, the central deflection formulas turn out to be entirely explicit, unlike the exponential case which involves the solution of transcendental equations for the times t_1 and t_2.

Again it is convenient to express our results in terms of dimensionless quantities as follows:

$$\lambda = p_m/p_s \qquad \tau = t/t_o \qquad \text{and} \qquad \nu = \delta/(I_o^2 L^2/mM_o) \tag{2.62}$$

where, for brevity, $\delta = y(L,t)$ is used to denote the central deflection.

2.7.1 Mechanism 1

For the peak pressure range $p_s < p_m < 3p_s$, where $p_s = 4M_o/L^2$ is the static collapse pressure, deformation starts by mechanism 1 (described in Section 2.4.1). Assuming that deformation is still in progress at time t_o when the pulse ends, Eq. (2.14) predicts a velocity at midspan of

$$V(t_o) = 3I_o(1 - 2/\lambda)/2m \tag{2.63}$$

But (2.63) shows that $V(t_o)$ is positive only when λ lies in the range $2 < \lambda \le 3$. In other words, the beam is still moving at the termination of all pulses with peak pressures such that $2 < \lambda \le 3$, whereas motion ceases before the termination of pulses with peak pressures such that $1 < \lambda < 2$. These two cases are now considered separately.

Case 1: $2 \le \lambda \le 3$. Motion ceases at a time $t_2 \ge t_o$ given by $p_m t_o/2 = p_s t_2$, which is (2.16) with $I_2 = I(t_2) = I_o = p_m t_o/2$. Hence, in terms of λ and τ, we have $\tau_2 = \lambda/2$. With this value of τ_2 and the impulse function (2.61), Eq. (2.17) leads to the final dimensionless central deflection

$$\nu_2 = (3\lambda - 4)/16\lambda \qquad 2 \le \lambda \le 3 \tag{2.64}$$

Case 2: $1 < \lambda \le 2$. Motion ceases at a time $t_2 \le t_o$ given by (2.16) with $I_2 = I_o\tau_2(2 - \tau_2)$. Solving for τ_2 in terms of

λ. we find that $\tau_2 = 2 - 2/\tau$. With this value of τ_2 and the impulse function (2.61), Eq. (2.17) leads to

$$\nu_2 = (\lambda - 1)^3/\lambda^4 \qquad 1 \le \lambda \le 2 \qquad (2.65)$$

2.7.2 Mechanism 2

Whenever $p_m > 3p_s$, deformation starts by mechanism 2 (described in Section 2.4.2). Three possibilities arise: either the pulse ends during mechanism 2 motion or during mechanism 1 motion, or the pulse is still acting when motion ceases. We shall now show that the first two possibilities exist but the last does not. Assuming the pulse ends in mechanism 2, that is $t_o < t_1$ or $\tau > 1$, Eq. (2.36) ($I_1 = 3p_s t_1$) becomes $\tau_1 = \lambda/6$ because $I_1 = I_o$. Hence $\tau_1 > 1$ is possible if $\lambda > 6$. Assuming the pulse ends in mechanism 1, that is $t_o > t_1$ or $\tau_1 < 1$, Eq. (2.36) becomes $\tau_1 = 2 - 6/\lambda$ because $I_1 = I_o\tau_1(2 - \tau_1)$. Hence $\tau_1 < 1$ is possible if $3 < \lambda < 6$, and thus the whole range of $\lambda > 3$ is accounted for. A pulse with a duration exceeding the duration of motion t_2 has to satisfy Eq. (2.40) ($I_2 = p_s t$) which becomes $\tau_2 = 2(1 - 1/\lambda)$ because $I_2 = I_o\tau_2(2 - \tau_2)$. Hence for no $\lambda < 3$ is $\tau_2 < 1$, and so the pulse duration cannot exceed the motion duration. The two possible cases will now be treated separately.

Case 1: $3 < \lambda < 6$. Equation (2.36) with $I_1 = I_o\tau_1(2 - \tau_1)$ gives the dimensionless time when mechanism 2 ends as $\tau_1 = 2 - 6\lambda$. With this value of τ_1 and the impulse function (2.61) substituted in the central deflection Eq. (2.38), we have

$$\nu_1 = 2(\lambda - 3)^2(\lambda + 6)/3\lambda^4 \qquad 3 \le \lambda \le 6 \qquad (2.66)$$

The pressure is still being applied during part of the remaining mechanism 1 motion. After the pulse ends, the velocity is that of (2.39) with $I = I_o$, and thus (2.40), giving the time when motion ceases, becomes $I_o = p_s t_2$ which, in terms of τ_2 and λ, is $\tau_2 = \lambda/2$.

Substituting τ_1, τ_2, and I in (2.41), we obtain for the central deflection occurring during motion by mechanism 1

$$\nu_2 - \nu_1 = (3\lambda - 4)/16\lambda - (\lambda - 3)^2(\lambda + 3)/\lambda^4$$

which, upon substituting ν_1 from (2.66), becomes

$$\nu_2 = (3\lambda - 4)/16\lambda - (\lambda - 3)^3/3\lambda^4 \qquad 3 \le \lambda \le 6 \qquad (2.67)$$

Case 2: $\lambda > 6$. We have shown that whenever $\lambda > 6$ the pulse ends during motion by mechanism 2. Hence in (2.36) we can set $I_1 = I_o$ to give $\tau_1 = \lambda/6$. With this value of τ_1 and the impulse function (2.61) substituted in (2.38), we find that the dimensionless central deflection at the end of mechanism 2 is

$$\nu_1 = (\lambda - 2)/12\lambda \qquad (2.68)$$

No pressure is being applied during mechanism 1 motion. Setting $I_2 = I_o$ in (2.40) yields $\tau_2 = \lambda/2$ for determining the time when motion ceases and the newly found formulas for τ_1 and τ_2, along with the impulse $I = I_o$, substituted in (2.41) give

$$\nu_2 - \nu_1 = 1/12 \qquad (2.69)$$

for determining the central deflection acquired during motion by mechanism 1. By using (2.68) to remove ν_1 from (2.69), we obtain

$$\nu_2 = (\lambda - 1)/6\lambda \qquad \lambda \ge 6 \qquad (2.70)$$

2.7.3 Peak Pressure, Impulse, and Deflection Relationship

Equations (2.64), (2.65), (2.67), and (2.70) represent explicitly the required relationship among peak pressure, impulse, and permanent central deflection for all values of λ. In Fig. 2.15 the curve shows how the final dimensionless central deflection ν varies with λ. For a constant impulse I_o the central deflection δ increases monotonically with peak pressure and tends to a finite limiting value as $\lambda \to \infty$. This limiting value corresponds to an ideal impulse and is represented by the asymptote in Fig. 2.15. The value of ν at the asymptote, found by letting $\lambda \to \infty$ in (2.70), is $\nu = 1/6$, the same as that found in Section 2.6.3 for the limiting case of the exponential pulse, as expected.

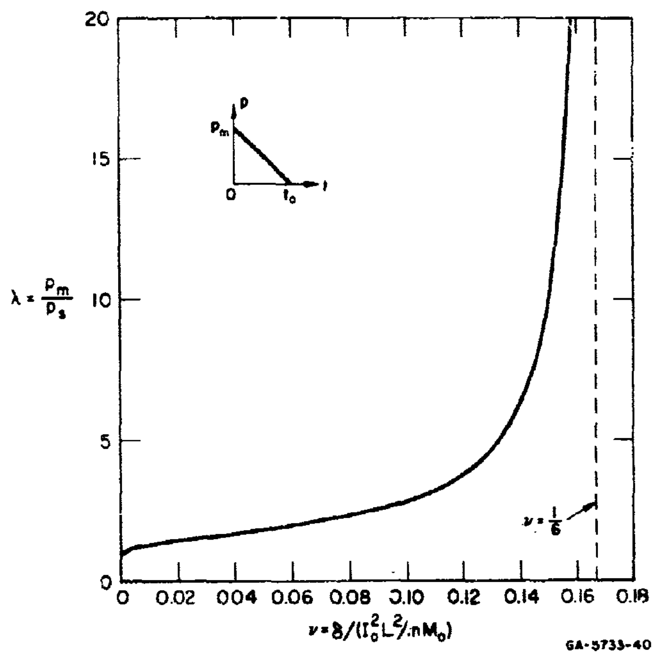

FIG. 2.15 PEAK PRESSURE, IMPULSE, CENTRAL DEFLECTION RELATIONSHIP FOR A CLAMPED BEAM SUBJECTED TO A TRIANGULAR PULSE

2.8 Clamped Beam Subjected to a Rectangular Blast Load

We shall now find the relationship among the pressure, impulse, and final central deflection for a clamped rigid-plastic beam subjected to a rectangular pulse uniformly distributed along its entire length. By a rectangular pulse we mean a pulse with an instantaneous rise to a pressure p_m which is then held constant until a time t_o when the pressure instantaneously falls to zero. The pressure and impulse functions meeting this description are

$$p = \begin{cases} p_m & 0 \le t < t_o \\ 0 & t > t_o \end{cases} \tag{2.71}$$

$$I = \begin{cases} p_m t = I_o(t/t_o) & 0 \le t \le t_o \\ p_m t_o = I_o & t \ge t_o \end{cases} \tag{2.72}$$

Again the results we require are found by substituting the impulse function (2.72) into the appropriate results of Section 2.4 for general blast pulses. A unique property of a rectangular pulse with $p_m > 3p_s$ is that the two hinges which appear within the span to form mechanism 2 remain stationary during the entire time the pulse is acting. This property ensures that the pulse is always over before mechanism 2 ends. Whenever $p_s < p_m < 3p_s$, motion is entirely by mechanism 1 with the velocity increasing while the constant pressure is being applied so again the pulse is always over before mechanism 1 ends. Thus the whole of a rectangular pulse is used to cause deformation which, of course, is never the case with an exponential pulse and is not the case with a triangular pulse whenever $p_s < p_m < 2p_s$.

Again it is convenient to express our results in terms of the dimensionless variables

$$\lambda = p_m/p_s \qquad \tau = t/t_o \qquad \text{and} \qquad \nu = \delta/(I_o^2 L^2/mM_o) \tag{2.73}$$

where, for brevity, $\delta = y(L,t)$ is the central deflection.

2.8.1 Mechanism 1

For the peak pressure range $p_s < p_m < 3p_s$, where $p_s = 4M_o/L^2$ is the static collapse pressure, motion starts by mechanism 1 (see Section 2.4.1). At time t_o Eq. (2.14) predicts a midspan velocity of

$$\ldots t_o) = 3I_o(1 - 1/\lambda)/2m$$

which is positive for λ in the whole range $1 < \lambda \leq 3$ under consideration. Motion thus ends at some time t_2 such that $t_2 > t_o$ or $\tau_2 > 1$. In terms of τ_2 and λ, this time, from (2.16) with $I_2 = I_o$, is $\tau_2 = 1/\lambda$. In terms of ν_2 and λ, from (2.17) with the impulse function (2.72) and with $\tau_2 = 1/\lambda$, the central deflection is

$$\nu_2 = 3(1 - 1/\lambda)/16 \qquad 1 \leq \lambda \leq 3 \tag{2.74}$$

2.8.2 Mechanism 2

Whenever $p_m > 3p_s$, motion starts by mechanism 2 (see Section 2.4.2). Equation (2.34), which is $x_h^2 = 12M_o t/I$, becomes $x_h^2 = 12M_o/p_m$ when the pulse is acting, showing that the hinge is stationary. After the pulse has ended the equation becomes $x_h^2 = 12M_o t/I_o$, and hence the time t_1 when mechanism 2 ends is given by (2.36) with $I_1 = I_o$. Thus $\tau_1 = \lambda/3$, and from (2.38) with the impulse function (2.72), we obtain

$$\nu_1 = 1/12 - 1/8\lambda$$

Motion is completed by mechanism 1 at a time t_2 determined by (2.40) with $I_2 = I_o$. Thus $\tau_2 = \lambda$ and (2.41) with $I = I_o$ gives

$$\nu_2 - \nu_1 = 1/12$$

Elimination of ν_1 then yields the required central deflection formula

$$\nu_2 = 1/6 - 1/8\lambda \qquad \lambda \geq 3 \tag{2.75}$$

2.8.3 Peak Pressure, Impulse, and Deflection Relationship

The required relationship among peak pressure, impulse, and permanent central deflection is represented explicitly by (2.74) and (2.75). From the equations the curve of λ versus ν in Fig. 2.16 was drawn. For a constant impulse I_o the central deflection δ increases

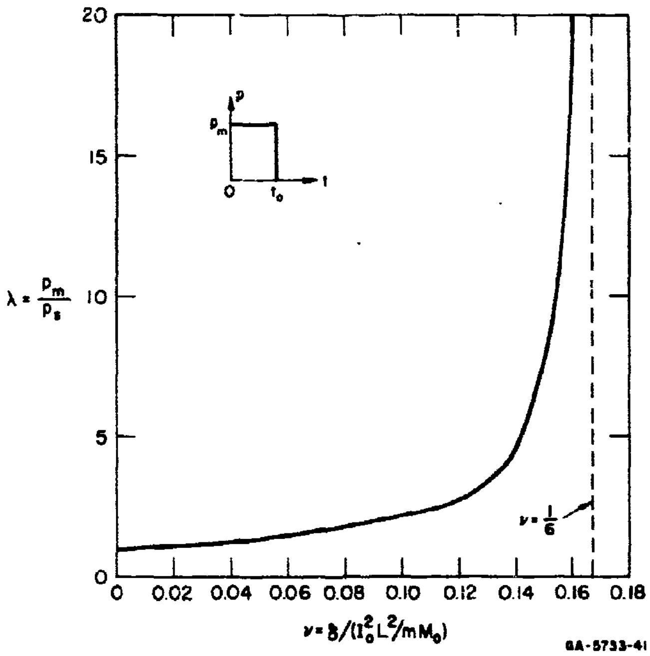

FIG. 2.16 PRESSURE, IMPULSE, CENTRAL DEFLECTION RELATIONSHIP FOR A CLAMPED BEAM SUBJECTED TO A RECTANGULAR PULSE

monotonically with peak pressure and tends to a finite limiting value as $\lambda \to \infty$. This limiting value corresponds to an ideal impulse and is represented by the asymptote in Fig. 2.16. The value of ν at the asymptote, found by letting $\lambda \to \infty$ in (2.75), is $\nu = 1/6$, the same as that found in Sections 2.6.3 and 2.7.3 for the limiting cases of exponential and triangular pulses, as it should be.

2.9 Simply Supported Beams Subjected to Specific Blast Loads

In this section we shall present formulas representing the relationship among peak pressure, impulse, and permanent central deflection for a simply supported rigid-plastic beam subjected to a specific blast load uniformly distributed along its entire length. The specific pulses which concern us here have exponential, triangular, and rectangular pressure-time curves, and we can write the formulas simply by doubling the right-hand sides of those for clamped beams in Sections 2.6, 2.7, and 2.8. The reason for this simple doubling process is basically that the restoring moment acting on the rigid portion of a beam as it rotates about a simple support is half of that acting when the support is clamped. It was shown in Section 2.5 that, with the exception of the bending moment distribution, the results of Section 2.4 for clamped beams under general blast loading are applicable to simply supported beams provided the appropriate static collapse load is taken, that is, $p_s = 2M_o/L^2$ instead of $p_s = 4M_o/L^2$. When the deflection formulas are being converted into the dimensionless form $\nu = \nu(\lambda)$, where

$$\lambda = p_m/p_s \qquad \nu = \delta/(I_o^2L^2/mM_o) \tag{2.76}$$

a factor $1/p_s$ appears on the right-hand side, thereby accounting for the doubling process. In (2.76) p_m denotes peak pressure, I_o the total area under the pressure-time curve, and δ denotes permanent mid-span deflection.

The results are given below in terms of the dimensionless variables λ and ν of (2.76) and the λ versus ν relationship for each pulse shape is shown in Fig. 2.17.

Exponential Pulse:

$$\nu = \begin{cases} 3[2(\lambda - 1) - \tau_2]\, \tau_2/8\lambda^2 & 1 \le \lambda \le 3 \\ [6(\lambda - 1)\, \tau_2 - 2(\lambda - 3)\, \tau_1 - 3(\tau_2^2 - \tau_1^2)]/8\lambda^2 & \lambda \ge 3 \end{cases}$$

where

$$(1 - 3^{-\tau_1}) = 3\tau_1/\lambda \quad \text{and} \quad (1 - e^{-\tau_2}) = \tau_2/\lambda$$

Triangular Pulse:

$$\nu = \begin{cases} 2(\lambda - 1)^3/\lambda^4 & 1 \le \lambda \le 2 \\ (3\lambda - 4)/8\lambda & 2 \le \lambda \le 3 \\ (3\lambda - 4)/8\lambda - 2(\lambda - 3)^3/3\lambda^4 & 3 \le \lambda \le 6 \\ (\lambda - 1)/3\lambda & \lambda \ge 6 \end{cases}$$

Rectangular Pulse:

$$\nu = \begin{cases} 3(\lambda - 1)/8\lambda & 1 \le \lambda \le 3 \\ (4\lambda - 3)/12\lambda & \lambda \ge 3 \end{cases}$$

Ideal Impulse:

$$\nu = 1/3 \qquad \lambda = \infty$$

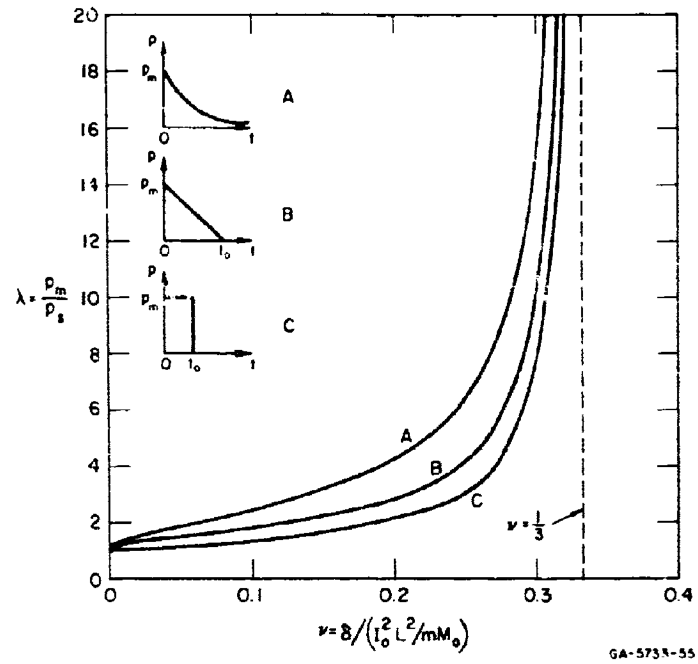

FIG. 2.17 PEAK PRESSURE, IMPULSE, CENTRAL DEFLECTION RELATIONSHIP FOR SIMPLY SUPPORTED BEAMS

An interesting feature of Fig. 2.17 is the spacing between the curves, which shows how the central deflection δ from pulses of equal peak pressure p_m and equal impulse I_o depends on the pulse shape. Any horizontal line $(\lambda > 1)$ intersects the curves to give three deflection values. The greatest of these is from the rectangular pulse and the smallest is from the exponential pulse. At low peak pressures the deflection values are significantly different from each other. As the peak pressure tends to infinity, the differences tend to zero, because each pulse tends to an ideal impulse. Figure 2.18 also illustrates these observations by showing the variation with λ of the ratios δ_B/δ_C and δ_A/δ_C of the central deflections from triangular and exponential pulses to those from rectangular pulses, all pulses having the same impulse I_o. The dependence of central deflection upon pulse shape is discussed more fully in the next section.

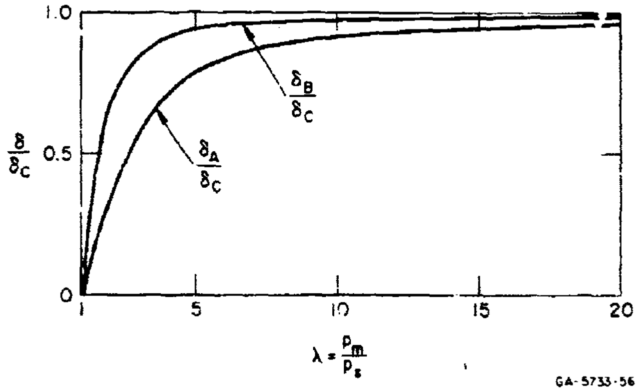

FIG. 2.18 VARIATION OF CENTRAL DEFLECTION RATIOS WITH PEAK PRESSURE FOR PINNED AND CLAMPED BEAMS (δ_A, δ_B, δ_C are central deflections caused by exponential, triangular, and rectangular pulses)

2.10 Pulse Shape which gives Maximum Deflection

Our main purpose is to prove that the permanent central deflection of a simply supported or clamped rigid-plastic beam due to a uniformly distributed blast pulse of given peak pressure and impulse is greatest when the pulse is rectangular. This result is also true for more general structures as will be shown by examples.

2.10.1 Simplest Rigid-Plastic System

We shall find the dependence on pulse shape of the maximum displacement of the simple system shown in Fig. 2.19. A pressure $p(t)$ acts on a mass m per unit area having a constant resisting pressure p_s. Whenever $p(t)$ becomes larger than p_s the mass is set in motion according to the equation

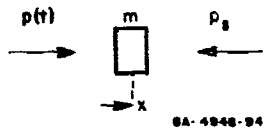

FIG. 2.19 SIMPLEST RIGID-PLASTIC SYSTEM

$$p(t) - p_s = m\ddot{x} \qquad (2.77)$$

where x is the displacement from the initial at-rest position. With the initial conditions

$x(0) = \dot{x}(0) = 0$, successive integrations of (2.77) give

$$I(t) - p_s t = m\dot{x} \tag{2.78}$$

$$A(t) - p_s t^2/2 = mx \tag{2.79}$$

where $I(t)$, the impulse, is the area under the pressure-time curve at time t, and $A(t)$ is the area under the impulse-time curve at time t. For convenience, but without loss of generality, we shall consider pulses with an initial pressure greater than p_s, i.e., $p(0) > p_s$.

Let the mass come to rest at time $t = t_2$. Then (2.78) with $\dot{x}(t_2) = 0$ gives $t_2 = I_2/p_s$ where $I_2 = I(t_2)$. Substituting this result for t_2 in (2.79) gives for the final displacement

$$mx_2 = A_2 - I_2 t_2/2 \tag{2.80}$$

in which $A_2 = A(t_2)$.

By means of expression (2.80), the deflections x_2 due to pulses of equal peak pressure p_m and impulse I_o are compared with the deflection due to a rectangular pulse of pressure p_m and impulse I_o. Note that I_o is the total area under the pressure-time curve, whereas I_2 is the area at time $t = t_2$. Thus two cases arise, depending on whether $I_o = I_2$ or $I_o > I_2$; in the former case the whole pulse is used in moving the mass, while in the latter it is not.

Case 1: $I_o = I_2$. If the pulse ends at time $t = t_o$, then $t_o \le t_2$ and, since $t_2 = I_2/p_s = I_o/p_s$, the duration of motion is the same for all pulses. Also, (2.80) becomes

$$mx_2 = A_2 - I_o t_2/2 \tag{2.81}$$

and, since the term $I_o t_2/2 = I_o^2/p_s$ is the same for all pulses, it remains to study the function A_2.

Among all pulses of equal impulse I_o and maximum pressure p_m, the minimum of the duration times t_o is possessed by a rectangular pulse. Let this minimum duration time be t_o'. Then when $t = t_o'$ the pulses satisfy $I \le p_m t_o'$ and $A \le p_m t_o'^2/2$ with equality only for the rectangular pulse. When $t = t_2$ $(t_2 \ge t_o > t_o')$,

$$A_2 = \int_0^{t_o'} I(\tau)d\tau + \int_{t_o'}^{t_2} I(\tau)d\tau \le p_m t_o'^2/2 + I_o(t_2 - t_o') \qquad (2.82)$$

again with equality only for the rectangular pulse, so that A_2 and hence x_2, from (2.81), are maximum when the pulse is rectangular.

This result can be illustrated in the impulse-time plane of Fig. 2.20. For a rectangular pulse, A_2 is the area under $OO'F$, whereas for more general pulses A_2 is the area under the curved line OO_1F. The triangular area under OF is $I_2t_2/2$. Thus, according to (2.80), the final displacement x_2 is $1/m$ times the difference between the two areas A_2 and $I_2t_2/2$. For a rectangular pulse this difference is the triangular area $OO'F$ and, for other pulses, it is the shaded area. The maximum slope of the curve OO_1 is that of the line OO' and is the maximum pressure p_m; therefore the curve lies wholly in triangle $OO'F$. Note that the slope of the line OF is p_s and if the curve intersects OF the mass comes to rest because, according to (2.78), $I = p_s t$ requires $\dot{x} = 0$. This, however, is case 2.

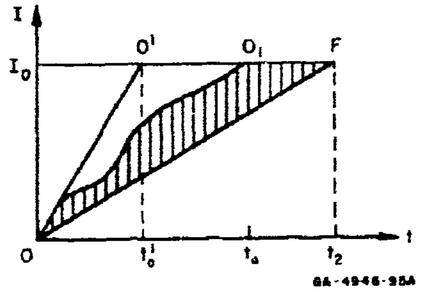

FIG. 2.20 IMPULSE-TIME DIAGRAM

Case 2: $I_2 < I_o$. In this case pressure is still being applied when motion ceases. Again let t_o' be the duration of a rectangular pulse of peak pressure p_m and impulse I_o and let the duration of motion when this rectangular pulse is applied be t_2'. The time t_2' equals the common duration of motion of case 1. In case 2, however,

t'_2 exceeds the duration of motion because $t'_2 = I_o/p_s > I_2/p_s = t_2$. Since $I_2 < I_o$, we have for A_2, instead of (2.82), the inequality

$$A_2 < p_m t_o'^2/2 + I_o(t_2 - t'_o)$$

Thus (2.80) for the maximum displacement becomes

$$mx_2 < I_o t'_o/2 + I_o(t_2 - t'_o) - I_2 t_2/2 \qquad (2.83)$$

In order to compare the displacement with that caused by a rectangular pulse, we add to the right-hand side of (2.83) the positive quantity $I_o(t'_2 - t_2) - (I_o t'_2 - I_2 t_2)/2$. That it is positive follows from an algebraic proof that it equals $I_o t'_2(1 - t_2/t'_2)^2/2$. In this way we obtain the inequality

$$mx_2 < I_o t'_o/2 + I_o(t'_2 - t'_o) - I_o t'_2/2 \qquad (2.84)$$

which states that whenever $I_2 < I_o$ the pulses cause displacements which are always less than that caused by a rectangular pulse with the same peak pressure and total impulse.

An illustration of this result can be seen in the impulse-time diagram of Fig. 2.21. Since $I_2/t_2 = p_s$, the point G lies on the line OF which is the same as OF in Fig. 2.20. The area under the curve OG is A_2 and the triangular area under OG is $I_2 t_2/2$. Their difference, shown shaded, is $1/m$ times the displacement x_2, while the triangular area OO′F is $1/m$ times the displacement due to a rectangular pulse. The inequality (2.84) states that the shaded area is less than the area of triangle OO′F.

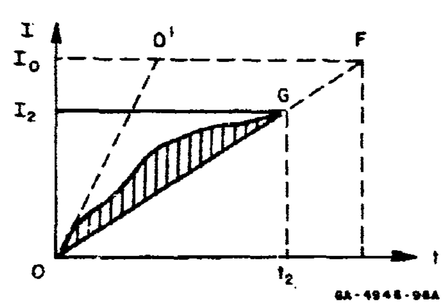

FIG. 2.21 IMPULSE-TIME DIAGRAM

From the above, the following theorem can be stated.

Theorem: Among all pulses of equal peak pressure and impulse, the rectangular pulse causes the maximum permanent deformation of a rigid-plastic structure that is representable by a mass with a constant resisting force.

2.10.2 Applications of the Theorem

We shall now give a few examples of simple rigid-plastic structures which are representable by a mass and a constant resisting force during deformation caused by blast loads.

(a) Beams: A simply supported or clamped rigid-plastic beam subjected to a blast pulse uniformly distributed along its entire length undergoes deformation by a three-hinged mechanism (one at each support and at midspan as described by mechanism 1 in Sections 2.4 and 2.5) whenever the peak pressure p_m lies in the range $p_s < p_m < 3p_s$ where $p_s = 2M_o/L^2$ and $p_s = 4M_o/L^2$ are, respectively, the static collapse pressures for the simply supported and clamped beams. For both types of support the equation of motion is

$$p(t) - p_s = (2m/3)\ddot{\delta} \qquad p_s < p_m < 3p_s$$

where δ is the central deflection. Thus these structures are representable by means of a mass $2m/3$ with a constant resisting force p_s and the theorem applies.

(b) Rings: Assuming that no buckling occurs, a rigid-plastic ring subjected to a blast pulse applied uniformly around the outside moves inward according to the equation

$$p(t) - \sigma_o h/a = m\ddot{w}$$

where σ_o is the yield stress, m the mass per unit length of circumference, h the thickness, a the radius, and w the inward displacement. Since the static collapse pressure is $p_s = \sigma_o h/a$, we have the required representation for the theorem

$$p(t) - p_s = m\ddot{w} \tag{2.85}$$

(c) Spherical Shell: The spherical shell problem analogous to the ring problem results in Eq. (2.85) with $p_s = 2\sigma_o h/a$.

(d) Circular Plate: It can be shown (see Section 3.7.1) that whenever the peak pressure p_m lies in the range $p_s < p_m < 2p_s$ a simply supported circular rigid-plastic plate subjected to a blast pulse uniformly distributed over the entire area is set in motion according to the equation

$$p(t) - p_s = (m/2)\ddot{\delta} \qquad p_s < p_m < 3p_s$$

where δ is the central deflection, m the mass per unit area, and $p_s = 6M_o/a^2$ is the static collapse pressure, M_o being the fully plastic moment per unit arc length and a the plate radius.

2.10.3 Clamped and Simply Supported Beams

It will now be proved that the permanent central deflection of a clamped or simply supported rigid-plastic beam caused by a uniformly distributed blast pulse of any peak pressure p_m and impulse I_o is greatest when the pulse is rectangular.

We have already proved this for peak pressures in the range $p_s < p_m < 3p_s$ by showing that the beam is representable by a mass and a constant resisting force and applying the theorem of Section 2.10.1. Whenever $p_m > 3p_s$, deformation starts by mechanism 2, which, as described in Sections 2.4.2 and 2.5.2, has two plastic hinges traveling toward each other while the central shortening portion of beam between the hinges undergoes translatory motion according to the equation $m\ddot{\delta} = p$. After the hinges meet at time $t = t_1$, deformation continues by mechanism 1 as described in Sections 2.4.1 and 2.5.1 until motion ceases at time $t = t_2$.

During this second phase of deformation the equation of motion is $m\ddot{\delta} = 3(p - p_s)/2$. Although the representation for the theorem is met in each of the two phases, they differ from each other and the theorem cannot be applied directly.

We shall use (2.36) and (2.40) for the times t_1 and t_2 and (2.38) and (2.41) for the central deflections (see Section 2.4.2). With the central deflections, impulses, and areas under the impulse-time curves at times t_1 and t_2 denoted by δ_1, δ_2, I_1, I_2, A_1, and A_2 these equations give

$$m\delta_2 = \begin{cases} (3A_2 - A_1)/2 - (3I_o t_2 - I_o t_1)/4 & 0 < t_o < t_1 \\ (3A_2 - A_1)/2 - (3I_o t_2 - I_1 t_1)/4 & t_1 < t_o < t_2 \\ (3A_2 - A_1)/2 - (3I_2 t_2 - I_1 t_1)/4 & t_2 < t_o \end{cases} \qquad (2.86)$$

where t_o is the pulse duration. In the first two expressions of (2.86) we have $3t_1 = t_2 = I_o/p_s$ and in the last we have $3t_1 = I_1/p_s$ and $t_2 = I_2/p_s$. Whenever the pulse ends during motion by mechanism 1, i.e., $o < t_o < t_1$, the central displacement and velocity according to (2.38) and (2.39) are $\delta_1 = A_1/m$ and $\dot{\delta}_1 = I_o/m$. Since A_1 is a maximum for a rectangular pulse (see proof of theorem in Section 2.10.1), the beam commences mechanism 1 with a maximum displacement for this pulse and with the same velocity as all other pulses having $t_o < t_1$. Thus the rectangular pulse produces the maximum final central deflection whenever $t_o < t_1$.

Expressions (2.86) are compared with the expression for a rectangular pulse, which is embedded in the first of (2.86), by means of areas in the impulse-time planes of Fig. 2.22. For this purpose it is convenient to rearrange (2.86) into the form

$$m\delta_2 = \begin{cases} (A_2 - I_o t_2/2) + [(A_2 - I_o t_2/2) - (A_1 - I_o t_1/2)]/2 & 0 < t_o < t_1 \\ (A_2 - I_o t_2/2) + [(A_2 - I_o t_2/2) - (A_1 - I_1 t_1/2)]/2 & t_1 < t_o < t_2 \\ (A_2 - I_2 t_2/2) + [(A_2 - I_2 t_2/2) - (A_1 - I_1 t_1/2)]/2 & t_2 < t_o \end{cases} \tag{2.87}$$

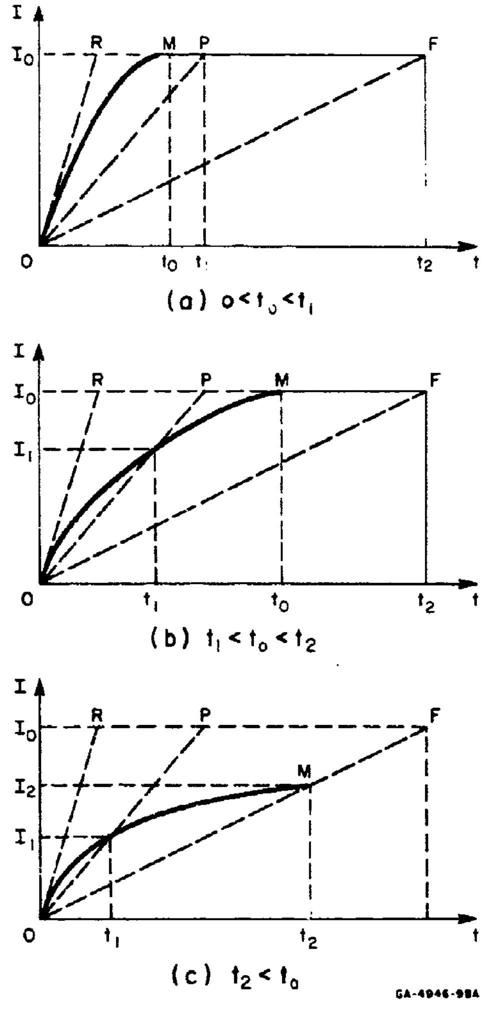

FIG. 2.22 IMPULSE-TIME DIAGRAMS FOR BEAMS ($p_m > 3p_s$). (a) $0 < t_o < t_1$, (b) $t_1 < t_o < t_2$, (c) $t_2 < t_o$

In each of the three diagrams the straight lines OR, OP, and OF are the same, having slopes p_m, $3p_s$, and p_s. Line OR is the path taken by a rectangular pulse, and the curve OM is the path taken by any other pulse with the same peak pressure p_m and impulse I_o. Each diagram corresponds to one case of (2.87). Since we are concerned with blast pulses only, the peak pressures all occur at $t = 0$, so that at the origin in each diagram the curve OM is tangential to OR. Apart from the case of a rectangular pulse, the curves OM all lie to the right of OR.

By algebraically adding the areas represented by the individual terms in each of (2.87) it can be seen that the sum is bounded by the triangle ORF plus one-half of triangle OPF, which corresponds to a rectangular pulse. Thus the rectangular pulse causes the greatest central deflection.

2.11 The Pressure-Impulse Diagram

A useful method of describing the behavior of structures subjected to blast pulses is to construct a pressure-impulse diagram. For all pulses of the same basic shape it shows how the peak pressure and impulse must be varied in order to maintain a prescribed permanent deflection. The ordinate of the diagram is the ratio $\lambda = p_m/p_s$ of the peak pressure to the static collapse pressure and the abscissa is the ratio I_o/I_1 of the impulse (total area under pressure-time curve) to the ideal impulse (zero duration) required to produce the same permanent deflection.

Such a diagram, applicable to both simply supported and clamped beams subjected to uniformly distributed blast pulses, is shown in Fig. 2.23. Each curve corresponds to a fixed pulse shape and gives the relationship between the peak pressure and impulse required to keep the central deflection at some prescribed value. The curves are obtained as follows: The central deflection due to a blast pulse is $\delta_o = (I_o^2 L^2/mM_o)$ $\nu(\lambda)$, where $\nu(\lambda)$ is a known function of λ, and the central deflection due to an ideal impulse is $\delta_1 = (I_1^2 L^2/mM_o)\nu(\infty)$. Since I_1 is to be the ideal impulse producing the same deflection as each pulse, we equate δ_o and δ_1 to give the required relationship, $I_o/I_1 = [\nu(\infty)/\nu(\lambda)]^{1/2}$.

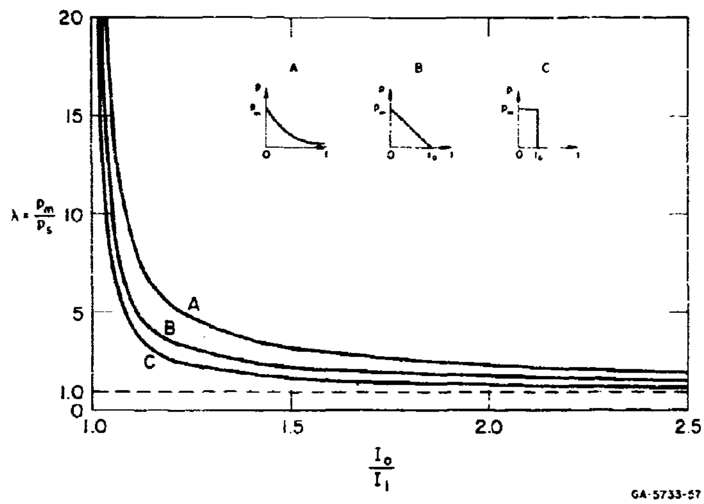

FIG. 2.23 PRESSURE-IMPULSE DIAGRAM
FOR PINNED AND CLAMPED BEAMS

For a clamped beam subjected to a rectangular pulse we have

$$\nu(\lambda) = \begin{cases} 3(\lambda - 1)/16\lambda & 1 \le \lambda \le 3 \\ (4\lambda - 3)/24\lambda & \lambda \ge 3 \end{cases}$$

and

$$\nu(\infty) = 1/6$$

so that

$$(I_o/I_1)^2 = \begin{cases} 8\lambda/9(\lambda - 1) & 1 \le \lambda \le 3 \\ 4\lambda/(4\lambda - 3) & \lambda \ge 3 \end{cases}$$

Each curve has the asymptotes $I_o/I_1 = 1$ and $\lambda = 1$ corresponding to an ideal impulse and a static collapse load. Keeping the deflection constant, small changes in I_o cause large changes in λ near the asymptote $I_o/I_1 = 1$, and small changes in λ cause large changes in I_o near the asymptote $\lambda = 1$.

It is interesting that a rectangular pulse with a pressure greater than eight times the static collapse pressure ($\lambda > 8$) requires less than a 5% increase in impulse over an ideal impulse to provide the same permanent central deflection; when $\lambda < 8$ the impulse increments required increase rapidly as λ decreases. The triangular and exponential pulses exhibit a similar behavior.

To produce the same deflection, the ratio of peak pressures of exponential and rectangular pulses with the same impulses is less than 2 whenever $I_o/I_1 > 1.2$; for pulses with the same peak pressure the ratio of impulses is less than 1.25 whenever $\lambda > 3.5$. Comparing exponential and triangular pulses giving the same deflection, the ratio of peak pressures is less than 1.5 whenever $I_o/I_1 > 1.2$; the ratio of impulses is less than 1.2 whenever $\lambda > 3.5$. This suggests that in certain ranges of peak pressure and impulse, pulse shape has a secondary effect ($\lambda > 3.5$, $I_o/I_1 > 1.2$).

2.12 Response of Beams to Uniformly Distributed Impulses: Comparison of Theory and Experiment

We have seen that the use of rigid-plastic theory allows a simple solution to the problem of finding the response of a clamped or simply supported beam to blast loading. Consequently the solution could possibly be useful and convenient for engineering applications. Unfortunately there are no experimental results with which to compare theoretical predictions except for a few in which beams are subjected to extremely short pulses with large peak pressures. Hence our attempts to establish the usefulness of the rigid-plastic theory are necessarily confined to ideal impulses.

The rigid-plastic theory can be expected to provide reasonable predictions only if the plastic work done is sufficiently greater than the elastic strain energy involved. To give some measure of this we introduce R, the ratio of kinetic energy input to elastic bending strain energy capacity. A consequence of the assumptions of rigid-plastic theory is that the kinetic energy input equals the plastic work done when the applied impulse is ideal. If I and m are the impulse and mass per unit length, the kinetic energy input is $I^2/2m$. If the maximum elastic bending moment that can be sustained by the beam cross section is M_e, the bending strain energy capacity per unit length is $M_e^2/2D$, where D is the flexural rigidity. Hence $R = I^2D/mM_e^2$.

The descriptions and results of the experiments which follow are for pinned and clamped beams, each of which is subjected to an impulse uniformly distributed over its entire span. By comparing experimental and theoretical permanent central deflections, we shall see that the rigid-plastic theory gives reasonable predictions whenever R is greater than about 2. An experiment for testing the assumed mechanisms of deformation is described and discussed. Because the theory for an ideal impulse is much simpler than the theory in Sections 2.4 and 2.5 for general blast pulses, it is given here in full before discussing the experiments.

2.12.1 Theory for Pinned Beams

The deformation is assumed to occur in two phases. In the first, a plastic hinge originates at each support and travels toward midspan. The two traveling hinges divide the beam into three parts which behave as rigid bodies, the decreasing center part undergoing translatory motion at its initial velocity until the hinges meet at midspan while each outer part rotates about its support. In the second phase, a stationary plastic hinge occupies the midspan section and each half-beam rotates about its support as a rigid body until motion ceases.

The mechanisms of deformation are those called mechanisms 2 and 1 in Section 2.5 for the treatment of the response of pinned beams to uniformly distributed blast loading. There it was shown that pulses with peak pressures p_m greater than three times the static collapse pressure p_s started the motion by mechanism 2 with the initial position of each traveling hinge given by $x_h^2(0)/L^2 = 3/\lambda$ where $\lambda = p_m/p_s$, L is the halfspan, and $x_h(0)$, the initial position, is measured from the nearer support. In the limiting process, $p_m \to \infty$ or $\lambda \to \infty$, we approach an ideal impulse and we have $x_h(0) \to 0$ so that our assumption of a traveling hinge originating at each support is consistent with the ideal impulse considered as the limiting case of a blast pulse.

We shall now derive the required deformation formulas. We refer to Fig. 2.24 for nomenclature and an illustration of mechanism 2.

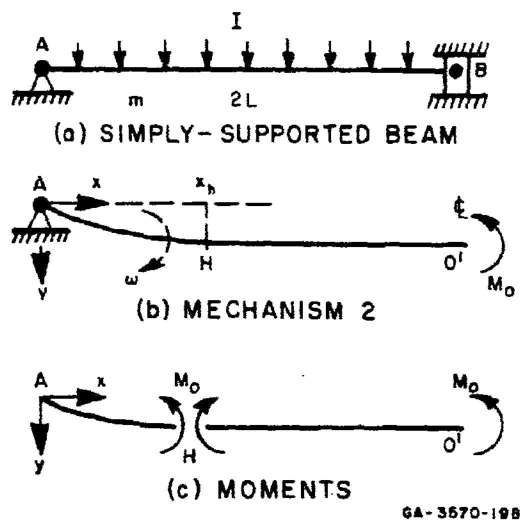

FIG. 2.24 SIMPLY SUPPORTED BEAMS UNDER A UNIFORMLY DISTRIBUTED IMPULSE
(a) Simply supported beam, (b) Mechanism 2, (c) Moments

The equation of motion of the rigid portion of length x_h rotating about the support with an angular velocity ω is

$$m x_h^3 \dot{\omega}/3 = -M_o \tag{2.88}$$

where M_o is the fully plastic moment. Note that in order not to violate the yield condition ($|M| \le M_o$) there is no shear force ($dM/dx = 0$) at the moving hinge (see Section 2.4).

The portion between moving hinges is undergoing translatory motion at a velocity $V = I/m$. At the hinge, continuity of velocity requires

$$\omega x_h = V = I/m \tag{2.89}$$

Eliminating ω from (2.88) and (2.89) leads to the following simple differential equation for the hinge location:

$$(x_h^2)^{\cdot} = 6M_o/I \tag{2.90}$$

which, with the initial condition $x_h(0) = 0$, integrates readily to give

$$x_h^2 = 6M_o t/I \tag{2.91}$$

Phase 1 ends when $x_h = L$ which, according to (2.91), occurs at $t_1 = IL^2/6M_o$. Each element of the half-beam at time t_1 has undergone a rotation

$$\theta(x,t_1) = \int_{\tau}^{t_1} \omega dt = \frac{I}{m} \int_{x}^{L} \frac{dx_h}{x_h \dot{x}_h} \tag{2.92}$$

where τ is the time when the hinge arrives at section x (the second integral indicates how the evaluation may readily be performed). The use of (2.90) in the second integral of (2.92) gives

$$\theta(x,t_1) = (I^2/3mM_o)(L - x) \tag{2.93}$$

With the approximation $\theta = dy/dx$ the shape of the beam at time t_1 is

$$y(x,t_1) = (I^2/6mM_o)(2L - x)\,x \tag{2.94}$$

Motion is now completed by mechanism 1 (Fig. 2.25) according to the equation

$$mL^3\,\dot{\omega}/3 = -M_o \tag{2.95}$$

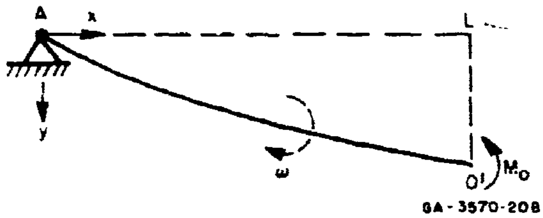

FIG. 2.25 MECHANISM I

At time t_1 the angular velocity has the value $\omega(t_1) = V/L = I/mL$ and if t_2 is the time when motion ceases, $\omega(t_2) = 0$. Hence, by integrating (2.95), we find that $t_2 = IL^2/2M_o = 3t_1$. During this phase of the motion all elements of each half-beam undergo the same rotation

$$\theta(x,t_2) - \theta(x,t_1) = \int_{t_1}^{t_2} \omega dt = \frac{mL^3}{3M_o} \int_{o}^{I/mL} \omega d\omega = I^2L/6mM_o \qquad (2.96)$$

By combining (2.93) and (2.96), we obtain for the final rotations

$$\theta(x,t_2) = (I^2/6mM_o)(3L - 2x) \qquad (2.97)$$

and by introducing the approximation $dy/dx = \theta$ and integrating, we obtain for the final shape of the half-beam

$$y(x,t_2) = (I^2/6mM_o)(3L - x)\, x \qquad (2.98)$$

Thus, the final shape of the entire beam consists of two parabolic arcs intersecting at a finite slope at the center $x = L$. From (2.97) and (2.98) the slope $\theta = \theta(o,t_2)$ at the support and the central deflection $\delta = y(L,t_2)$ are

$$\theta = I^2L/2mM_o \qquad (2.99)$$

$$\delta = I^2L^2/3mM_o \qquad (2.100)$$

Formulas (2.98), (2.99), and (2.100) will be used for comparison with experimental results.

2.12.2 Theory for Clamped Beams

The results for clamped beams can be written directly from (2.98), (2.99), and (2.100) merely by replacing M_o by $2M_o$. This is because clamping the supports introduces there fully plastic moments, which double the resisting moments acting on the rotating parts of the beam. Thus the plastic hinge location in phase 1, the final beam shape, the slope at the support, and the deflection at the center are given by

$$x_h^2 = 12M_o t/I \quad (2.101)$$

$$y(x,t_2) = (I^2/12mM_o)(3L - x)\,x \quad (2.102)$$

$$\theta = I^2L/4mM_o \quad (2.103)$$

$$\delta = I^2L^2/6mM_o \quad (2.104)$$

2.12.3 Description of Experiments

The experiments were performed with beams of 2024-T4 aluminum, 6061-T6 aluminum, 1018 cold-rolled steel, and annealed 1018 steel. They were nominally 1-inch wide and 1/4-inch deep with spans of 18 inches. Figure 2.26 shows the experimental arrangement for pinned beams. It shows in particular two different ways of providing pinned ends. For the steel beams 1/4-inch-diameter steel pins were required to withstand the shearing forces; the pins were supported by steel bearing blocks to reduce the contact pressure on the sliding surface. For the aluminum beams 1/8-inch-diameter steel pins through the ends of the beams were strong enough. The span of the pinned beams decreased during initial deformation. End conditions for clamped beams were provided by placing each end in a close-fitting tunnel so that during deformation the material flowed into the span which was maintained constant while end rotation was prevented.

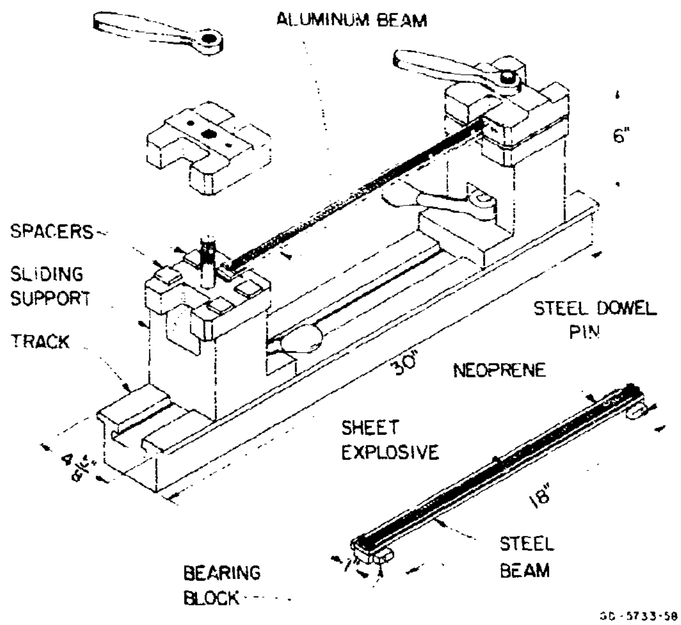

FIG. 2.26 EXPERIMENTAL ARRANGEMENT

The impulse was generated by sheet explosive in the form of a 1/2-inch-wide strip placed centrally over a 1-inch-wide by 1/8-inch-thick solid neoprene attenuator laid on the beam as shown in Fig. 2.26. The attenuator is a convenient minimum required to prevent spalling of the beams. A five-grain mild detonating fuze was used to detonate the explosive at the center of the beam. Central initiation is preferred to end initiation, because the initial transverse velocity distribution imparted to the beam is more uniform and the delivery time of the impulse is halved.[10] For a halfspan of 9 inches, the total detonation time is about 32 μsec. That the imparted velocity is uniformly distributed along the beam is primarily due to the detonation velocity of the explosive (0.28 inch/μsec) being sufficiently supersonic relative to the maximum wave velocity (0.2 inch/μsec).

For the explosive-attenuator-target configuration just described, the initial velocities of four aluminum and four steel beams were obtained by means of a rotating mirror streak camera trained on the center of each beam. From these experiments it was found that for each beam material the impulse imparted to the beam was proportional to the explosive thickness in the range of interest. A common parameter for describing the calibration of sheet explosive for an explosive-attenuator-target configuration is the impulse I_o per unit volume (dyne-sec/cm^3) of explosive. I_o is often a constant over a wide range of explosive thickness as it was found to be in the above calibration experiments. Once I_o is known, the impulse I per unit length of beam is simply calculated from the product of I_o, the explosive thickness, and the explosive width. Two values of I_o are listed in Table 2.1, one value for the aluminum beams and the other for the steel beams.

Table 2.1

BEAM PROPERTIES

Material	E (psi)	c_o (lb/in.)	ρ (lb sec^2/in.^{4})	b (inch)	d (inch)	L (inches)	I_o (dyne-sec/cm^3)
Al 2024-T4	10×10^6	52,000	0.000258	1.0	0.251	9.0	2.9×10^5
Al 6061-T6	10×10^6	40,000	0.000253	1.0	0.245	9.0	2.9×10^5
CR 1018 steel	30×10^6	84,000	0.000732	1.0	0.248	9.0	3.25×10^5
Annealed 1018 steel	30×10^6	43,000	0.000732	1.0	0.248	9.0	3.25×10^5

A high-impulse test (experiment CA2) was performed to see if longitudinal extension occurred and so to assess the effects of unavoidable frictional forces at the supports. The beam was suitably scribed on its side, and measurements before and after deformation were compared. No permanent extension of the neutral surface was observed. This technique was also used to find the strain of the outer fibers at midspan and resulted in a value of 4%.

Several of the experiments were photographed with a Beckman and Whitley (Model 189) framing camera to provide a qualitative justification of the mechanisms assumed in the rigid-plastic theory. Figure 2.27 is a photograph of experiment with frames at 83.3 μsec intervals (only alternate frames are shown). The observed deformation follows the assumed mechanisms; the plastic hinge velocity obtained from these photographs is later compared with the velocity predicted by the rigid-plastic theory.

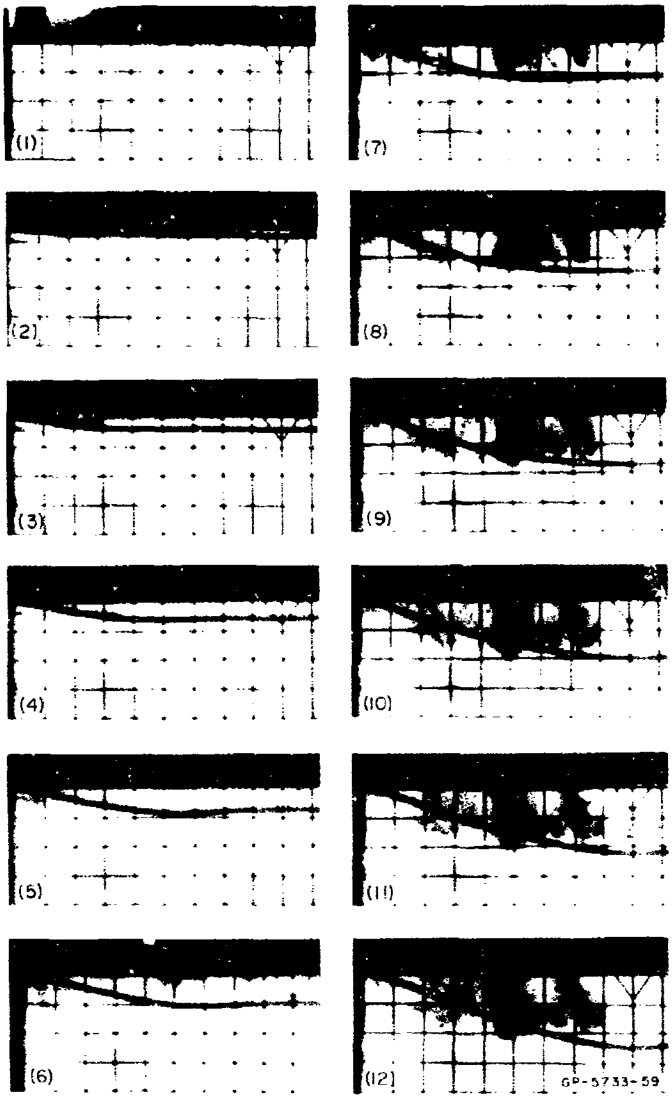

FIG. 2.27 FRAMING CAMERA RECORD FOR EXPERIMENT CA3

Almost all of the observations are terminal and consist of the central deflection, the maximum slope, and, in some cases, the entire deformed shape of the beam.

2.12.4 Experimental Results and Observations

Table 2.1 shows the beam materials and properties along with the impulse constants I_o obtained from the calibration experiments. The yield stress σ_o is the average from tensile tests. Instead of the conventional yield stress, we use here the stress at the point of intersection of a bilinear fit of that part of a stress-strain curve up to 4% strain. Tables 2.2 and 2.3 give the experimental and theoretical results for pinned and clamped beams.

Table 2.2

EXPERIMENTAL AND THEORETICAL RESULTS FOR PINNED BEAMS

Experiment No.	I (lb.sec.in^{-1})	R	δ_{ex}/L	θ_{ex}	δ_{th}/L	θ_{th}	δ_{ex}/δ_{th}	θ_{ex}/θ_{th}
PA 1	0.124	4.639	0.564	0.766	0.865	1.298	0.652	0.590
2	0.098	2.896	0.350	0.500	0.540	0.810	0.648	0.617
3	0.095	2.739	0.349	0.477	0.511	0.766	0.683	0.623
4	0.090	2.473	0.321	0.404	0.461	0.692	0.696	0.584
5	0.088	2.325	0.302	0.393	0.434	0.650	0.697	0.604
6	0.087	2.301	0.302	0.387	0.429	0.643	0.705	0.601
7	0.087	2.288	0.300	0.387	0.427	0.640	0.703	0.605
8	0.086	2.230	0.252	0.333	0.416	0.624	0.607	0.534
9	0.086	2.219	0.256	0.334	0.414	0.621	0.619	0.538
10	0.084	2.140	0.289	0.370	0.399	0.598	0.724	0.618
11	0.066	1.337	0.116	0.149	0.249	0.374	0.463	0.398
12	0.065	1.299	0.117	0.152	0.242	0.363	0.682	0.418
13	0.064	1.239	0.105	0.137	0.231	0.347	0.457	0.395
14	0.062	1.162	0.081	0.110	0.217	0.325	0.376	0.339
15	0.060	1.108	0.083	0.107	0.207	0.310	0.402	0.345
PB 1	0.091	4.495	0.413	0.548	0.660	0.991	0.625	0.553
2	0.076	3.142	0.282	0.375	0.462	0.693	0.612	0.542
3	0.075	3.069	0.259	0.326	0.451	0.676	0.574	0.482
4	0.060	2.007	0.124	0.165	0.295	0.442	0.419	0.373
5	0.059	1.916	0.134	0.167	0.281	0.422	0.475	0.396
6	0.047	1.208	0.055	0.101	0.178	0.266	0.312	0.379
7	0.045	1.087	0.046	0.057	0.160	0.240	0.288	0.238
PS 1	0.191	4.571	0.314	0.415	0.464	0.697	0.677	0.596
2	0.190	4.524	0.333	0.443	0.460	0.689	0.725	0.643
3	0.188	4.463	0.317	0.399	0.453	0.680	0.698	0.587
4	0.161	3.254	0.231	0.297	0.331	0.496	0.699	0.599
5	0.160	3.225	0.232	0.302	0.328	0.492	0.709	0.614
6	0.160	3.225	0.226	0.293	0.328	0.492	0.688	0.596
7	0.147	2.704	0.193	0.237	0.275	0.412	0.704	0.575
8	0.144	2.611	0.214	0.268	0.265	0.398	0.808	0.674
9	0.139	2.425	0.141	0.188	0.246	0.370	0.573	0.509
10	0.137	2.374	0.144	0.183	0.241	0.362	0.599	0.506
11	0.134	2.251	0.178	0.227	0.229	0.343	0.777	0.662
12	0.131	2.160	0.148	0.190	0.219	0.329	0.673	0.577
13	0.129	2.103	0.133	0.172	0.214	0.321	0.624	0.537
14	0.127	2.029	0.141	0.178	0.206	0.309	0.684	0.575
15	0.125	1.968	0.151	0.197	0.200	0.300	0.756	0.657
16	0.102	1.308	0.067	0.083	0.133	0.199	0.502	0.416
17	0.102	1.298	0.058	0.075	0.132	0.198	0.438	0.379
18	0.101	1.296	0.062	0.076	0.132	0.198	0.473	0.385
19	0.064	0.511	0.015	0.025	0.052	0.078	0.283	0.321
20	0.044	0.239	0.003	0.006	0.024	0.036	0.137	0.165
PSA 1	0.124	7.473	0.312	0.403	0.389	0.583	0.803	0.691
2	0.124	7.379	0.296	0.368	0.384	0.576	0.770	0.639
3	0.082	4.081	0.162	0.208	0.212	0.318	0.764	0.653
4	0.082	4.055	0.171	0.209	0.211	0.316	0.811	0.661
5	0.081	3.966	0.144	0.192	0.206	0.309	0.700	0.620

PA = pinned 2024-T4 aluminum PS = pinned cold-rolled 1018 steel

PB = pinned 6061-T6 aluminum PSA = pinned annealed 1018 steel

Table 2.3

EXPERIMENTAL AND THEORETICAL RESULTS FOR CLAMPED BEAMS

Experiment No.	I (lb.sec.in.$^{-1}$)	R	δ_{ex}/L	θ_{ex}	δ_{th}/L	θ_{th}	δ_{ex}/δ_{th}	θ_{ex}/θ_{th}
CA 1	0.146	6.469	0.453	0.567	0.603	0.905	0.752	0.627
2	0.146	6.437	0.433	0.510	0.600	0.900	0.722	0.567
3	0.146	6.412	0.466	0.530	0.598	0.897	0.779	0.591
4	0.144	6.236	0.409	0.490	0.581	0.872	0.703	0.562
5	0.143	6.191	0.462	0.509	0.577	0.866	0.801	0.588
6	0.141	6.018	0.433	0.529	0.561	0.842	0.772	0.629
7	0.129	5.002	0.280	0.334	0.466	0.699	0.600	0.478
8	0.128	4.964	0.304	0.362	0.463	0.694	0.658	0.522
9	0.101	3.060	0.204	0.247	0.285	0.428	0.717	0.577
10	0.101	3.057	0.183	0.221	0.285	0.427	0.643	0.517
11	0.100	3.004	0.176	0.217	0.280	0.420	0.627	0.517
12	0.089	2.386	0.161	0.194	0.223	0.334	0.724	0.581
13	0.074	1.666	0.087	0.112	0.155	0.233	0.558	0.481
14	0.072	1.572	0.080	0.093	0.147	0.220	0.546	0.423
15	0.058	1.014	0.049	0.057	0.095	0.142	0.517	0.402
CS 1	0.221	6.216	0.231	0.271	0.317	0.476	0.729	0.570
2	0.220	6.154	0.230	0.270	0.314	0.471	0.733	0.573
3	0.198	4.997	0.178	0.206	0.255	0.382	0.697	0.539
4	0.196	4.895	0.187	0.226	0.250	0.375	0.748	0.603
5	0.166	3.519	0.124	0.146	0.180	0.269	0.693	0.542
6	0.165	3.461	0.130	0.152	0.177	0.265	0.736	0.574
7	0.115	1.695	0.050	0.059	0.086	0.130	0.578	0.455
8	0.114	1.663	0.051	0.060	0.085	0.127	0.602	0.472
9	0.071	0.638	0.017	0.018	0.033	0.049	0.512	0.368

CA = clamped 2024-T4 aluminum

CS = clamped cold-rolled 1018 steel

The subscripts "ex" and "th" stand for experimental and theoretical respectively. Symbols δ and θ represent permanent central deflections and slopes at or near the supports. For the pinned beams in Table 2.2, the theoretical values are obtained from formulas (2.99) and (2.100); those for the clamped beams in Table 2.3 are obtained from formulas (2.103) and (2.104). Table 2.4 contains the averages of the deflection ratios δ_{ex}/δ_{th} and the slope ratios θ_{ex}/θ_{th} for all cases of the series PA, PS, PSA, CA, and CS in which $R > 2$, where $R = I^2D/M_e^2$ is the ratio of the kinetic energy input to the elastic strain energy capacity.

The central deflection results in Tables 2.2 and 2.3 are plotted in Figs. 2.28 and 2.29. Several of the beams were measured along their entire lengths, and the resulting profiles are shown in Figs. 2.30 through 2.33 along with the theoretical shapes as predicted by either (2.98) or (2.102).

Table 2.4

AVERAGE DEFLECTION AND
SLOPE RATIOS ($R > 2$)

Experiment No.	δ_{ex}/δ_{th}	θ_{ex}/θ_{th}
PA 1-10	0.673	0.591
PS 1-15	0.693	0.593
PSA 1-5	0.770	0.653
CA 1-12	0.716	0.563
CS 1-6	0.723	0.567

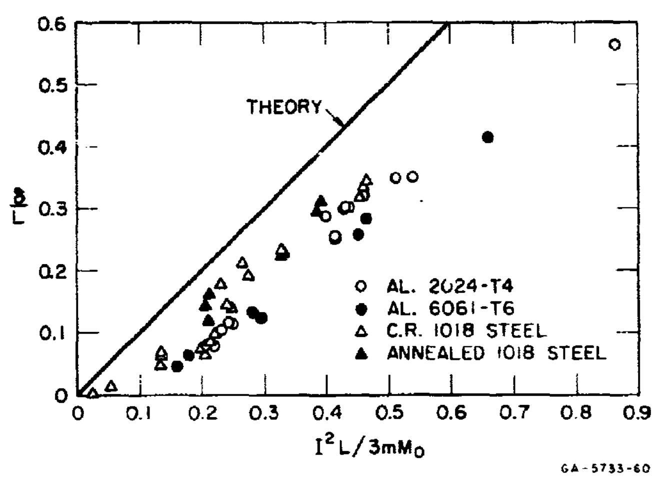

FIG. 2.28 THEORETICAL AND EXPERIMENTAL CENTRAL DEFLECTIONS FOR PINNED BEAMS

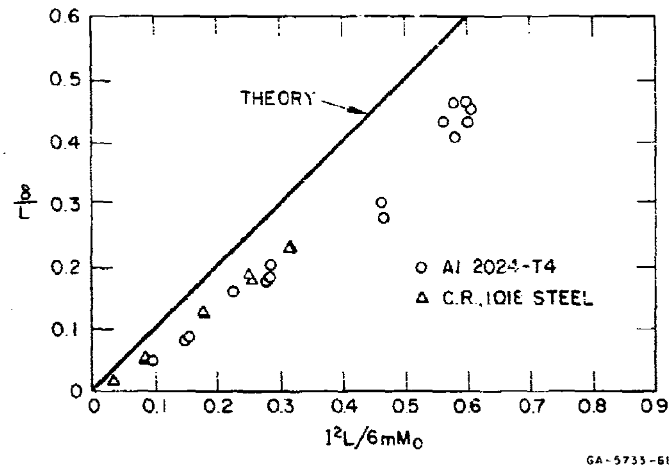

FIG. 2.29 THEORETICAL AND EXPERIMENTAL CENTRAL DEFLECTIONS FOR CLAMPED BEAMS

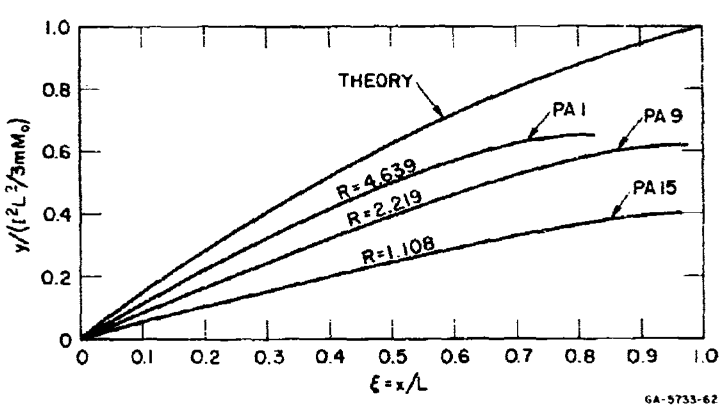

FIG. 2.30 THEORETICAL AND EXPERIMENTAL SHAPES FOR PINNED BEAMS OF 2024-T4 ALUMINUM

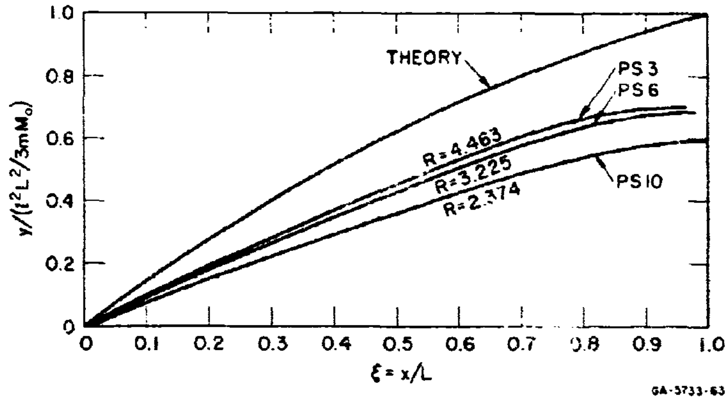

FIG. 2.31 THEORETICAL AND EXPERIMENTAL SHAPES FOR PINNED BEAMS OF C.R. 1018 STEEL

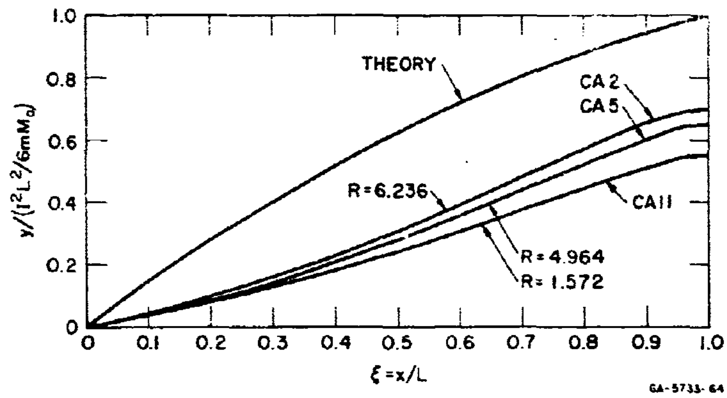

FIG. 2.32 THEORETICAL AND EXPERIMENTAL SHAPES FOR CLAMPED BEAMS OF 2024-T4 ALUMINUM

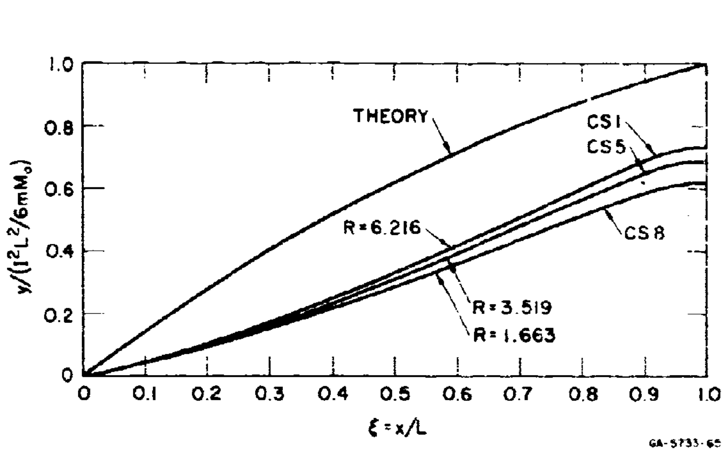

FIG. 2.33 THEORETICAL AND EXPERIMENTAL SHAPES FOR CLAMPED BEAMS OF C.R. 1018 STEEL

From the results in Tables 2.2 and 2.3 (and Figs. 2.28 and 2.29), it is clear that the central deflection or support slope predictions are good for engineering applications. In the present series of experiments no significant improvement of correlation occurs as R is increased beyond 2. Table 2.4 shows that for the PA, PS, PSA, CA, and CS series the average deflection ratios lie between 0.67 and 0.77 and the average slope ratios are between 0.56 and 0.66.

From the deformed shapes shown in Figs. 2.30 through 2.33 we make the following observations.

1. Except in the central region, the experimental curvature appears to be smaller than the theoretical curvature, especially for the pinned steel (PS) beams in Fig. 2.31. This indicates that the traveling hinge model of mechanism 2 overestimates curvature; this could be attributed to elastic effects and, in the case of cold-rolled steel, to strain-rate effects. At the center, the deformation by mechanism 1 predicts a slope discontinuity because of the ideal nature of a stationary plastic hinge; a continuous slope at the center would be provided by including elastic effects, the knee of the stress-strain curve in the case of the aluminum, and strain-rate or strain-hardening effects.

2. The theoretically predicted curvature of the clamped beams is $\kappa = y_{xx} = - I^2/6mM_o$, which is a constant, whereas the shapes in Fig. 2.32 and 2.33 exhibit reverse curvatures adjacent to the support. This criticism of the theory is not entirely valid, because experimental design difficulties prevent a true comparison; keeping the span constant requires that beam material be fed into the span region, thereby spreading the stationary hinge at the support over a finite length of beam. (An experiment providing clamping against rotation but allowing the span to shorten as in the case of the pinned beam experiments introduces longitudinal inertial forces.)

We have already mentioned that Fig. 2.27 provides a qualitative justification of the mechanisms assumed in the rigid-plastic theory. However, it does illustrate that elastic modes of vibration can interfer with the smooth action of the mechanisms. This effect can be seen by constructing from the framing camera record of Fig. 2.27 an x-t plot of the traveling hinge. This is shown in Fig. 2.34. A smooth curve could be obtained for 5 inches of the 9-inch half-span due to the interaction with the elastic mode. The effect was to arrest the progress of the hinge for about 100 μsec after which the mechanisms continued to operate. The half amplitude of the vibration was comparable to the beam depth.

Returning to Fig. 2.34, the theoretical x-t plot from $x_h = (12M_o t/I_1)^{1/2}$ is shown for comparison with the experimental x-t plot. Except during initial motion, when the theory exhibits the singular behavior $\dot{x}_h \sim t^{-1/2}$, the actual hinge velocity is greater than predicted. However, the trends are similar and, except for the interaction mentioned above, do give confidence in the use of the rigid-plastic model and its mechanisms.

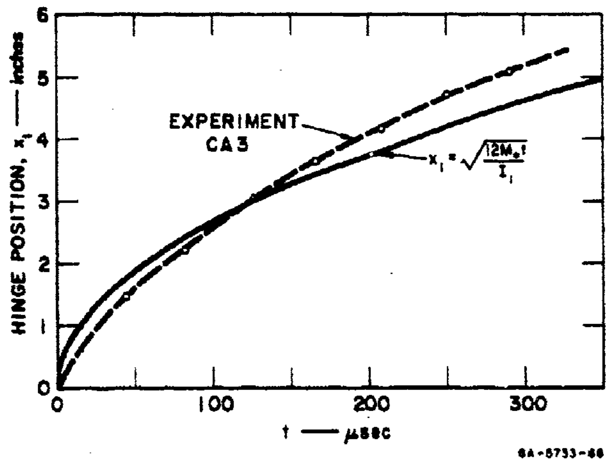

FIG. 2.34 THEORETICAL AND EXPERIMENTAL x-t PLOTS OF TRAVELING HINGE

REFERENCES

1. Lee, E. H. and P. S. Symonds, "Large Plastic Deformations of Beams under Transverse Impact," J. Appl. Mech. 19, 308, 1952.

2. Hodge, P. G., Jr., Plastic Analysis of Structures, McGraw-Hill Book Co., Inc., New York (1959).

3. Symonds, P. S., "Large Plastic Deformations of Beams under Blast-Type Loading," Proc. Second U.S. Natl. Congress of Appl. Mech., p. 505, 1954.

4. Florence, A. L. and R. D. Firth, "Rigid-Plastic Beams under Uniformly Distributed Impulses," J. Appl. Mech. 32, 481-488, 1965.

5. Symonds, P. S. and S. R. Bodner, "Experimental and Theoretical Investigations of the Plastic Deformation of Cantilever Beams Subjected to Impulsive Loading," J. Appl. Mech. 29, 719-728, 1962.

6. Ting, T. C. T., "The Plastic Deformation of a Cantilever Beam with Strain-Rate Sensitivity under Impulsive Loading," J. Appl. Mech. 31, 38-42, 1964.

7. Ting, T. C. T., "Large Deformation of a Rigid, Ideally Plastic Cantilever Beam," J. Appl. Mech. 32, 295-302, 1965.

8. Symonds, P. S. and P. S. Mentel, "Impulsive Loading of Plastic Beams with Axial Constraints," J. Mech. and Phys. of Solids 6, 186-202, 1958.

9. Humphreys, J. S., "Plastic Deformation of Impulsively Loaded Straight Clamped Beams," J. Appl. Mech. 32, 7-10, 1965.

10. Florence, A. L., "Traveling Force on a Timoshenko Beam," J. Appl. Mech. 32, 351-358, 1965.

CHAPTER 3

RIGID-PLASTIC CIRCULAR PLATES

by

A. L. Florence

3.1 Introduction

In the introduction to Chapter 2 we stated that it is difficult to find the response of a beam to a suddenly applied load which is large enough to cause plastic deformation even when geometry changes are neglected. This is true a fortiori for circular plates even under axisymmetric conditions. Not only is the stress-strain state nonlinear, it is also biaxial.

In order to render plate problems tractable to analysis, an idealization of the stress-strain relationship similar to that in beam analysis was introduced by Hopkins and Prager.[1] For appropriate materials (e.g., aluminum alloys and steels) it is assumed that the material remains rigid until a yield condition is satisfied, and only when it is satisfied is plastic deformation possible; such a material is called a rigid-perfectly plastic material. With this idealization Hopkins and Prager[1] found the static collapse loads of circular plates. Later[2] they developed the dynamical theory of rigid-perfectly plastic circular plates and found the response of a simply supported circular plate to a uniformly distributed rectangular load pulse.

Throughout this chapter the treatment is restricted to circular plates of material insensitive to strain rate. Membrane forces are neglected, and the yield condition which is expressed in terms of bending moments is that of Tresca. Problems related to those treated in this chapter can be found in Refs. 3 through 8.

Section 3.2 discusses the Tresca yield condition and associated flow law. A development of the dynamical theory of rigid-plastic plates is contained in Sections 3.3 and 3.4 covering such topics as plastic regimes, hinge circles, continuity requirements at regime boundaries, equilibrium equations, and the analytical approach.

Sections 3.5 and 3.6 are devoted to finding the static collapse pressures of simply supported and clamped plates.[9,10]

In Section 3.7 the relationship among central deflection, pressure, and impulse (area under pressure-time curve) is found for uniformly distributed rectangular pulses acting on simply supported circular plates.[1] Finally, a similar relationship is found in Section 3.8 for clamped circular plates.[11]

3.2 Tresca Yield Condition and Flow Rule

We are now concerned with circular plates under axisymmetric loads, so the stress components σ_r, σ_θ, and σ_z in the radial, circumferential, and axial directions in the cylindrical coordinate system (r, θ, z) are the principal stresses. The plate is assumed to be thin enough to allow the usual assumption that the stress normal to the middle plane is negligible. Accordingly, we shall assume $\sigma_z = 0$.

In a simple uniaxial tensile test on an elastic-perfectly plastic material,plastic deformation can occur only when the yield stress σ_o is reached. Similarly, in a biaxial state of stress, plastic deformation is possible only if a certain yield condition is fulfilled. The two most common yield conditions are those of von Mises and Tresca* which, in terms of σ_r and σ_θ, can be written as

$$\sigma_r^2 - \sigma_r\sigma_\theta + \sigma_\theta^2 = \sigma_o^2 \qquad (3.1)$$

and

$$\max\left(|\sigma_r|\ ,\ |\sigma_\theta|\ ,\ |\sigma_r - \sigma_\theta|\right) = \sigma_o \qquad (3.2)$$

where again σ_o is the yield stress obtained from a uniaxial tensile test. The yield stress σ_o is regarded throughout as a positive quantity.

*See Ref. 9 for a more complete discussion of these yield conditions.

The conditions (3.1) and (3.2) can be looked upon as equations of an ellipse and a hexagon when plotted in two-dimensional stress space as shown in Fig. 3.1.

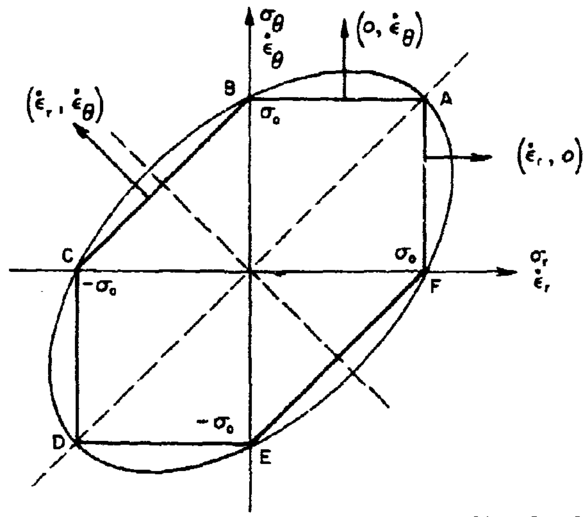

FIG. 3.1 von MISES YIELD ELLIPSE AND TRESCA YIELD HEXAGON

From this point on we shall confine our attention to rigid-perfectly plastic materials (which, for brevity, we shall call rigid-plastic) obeying the Tresca yield condition. For stress states within the hexagon of Fig. 3.1 the material is rigid; plastic deformation is possible only when the stress state lies on the hexagon. Stress states outside the hexagon do not exist. Note that since we have restricted ourselves to rigid-plastic materials the yield hexagon retains its size, shape, and position throughout deformation.

The flow rule states that the strain-rate vector $(\dot{\varepsilon}_r, \dot{\varepsilon}_\theta)$ is an outward normal to the yield hexagon when drawn in a strain-rate space superposed on the stress space of σ_r and σ_θ. ($\dot{\varepsilon}_r$ and $\dot{\varepsilon}_\theta$ axes superposed in the same sense on the σ_r and σ_θ axes, respectively.) The vector is drawn from the point on the yield hexagon describing the existing stress state. By way of illustration, we see that along the sides

FA, AB, and BC, the strain-rate vectors are $(\dot{\epsilon}_r, o)$, $(o, \dot{\epsilon}_\theta)$, and $(\dot{\epsilon}_r, \dot{\epsilon}_\theta)$, and $(\dot{\epsilon}_r, \dot{\epsilon}_\theta)$, with $-\dot{\epsilon}_r = \dot{\epsilon}_\theta$ in the last. At a corner, the strain-rate vector can take on any direction between the outward normals of the two sides forming the corner. Note that the flow rule is concerned only with the ratio of $\dot{\epsilon}_r$ and $\dot{\epsilon}_\theta$ and alone says nothing about magnitudes.

Figure 3.2 shows a plate element and serves to establish the sign convention adopted for the bending moments M_r and M_θ and for the shear force Q. Positive deflections w(r, t) are taken in the direction of the positive z axis (downward) so that positive moments cause tension below the midplane and compression above the midplane. Thus the moments per unit arc length of a plate of thickness h are

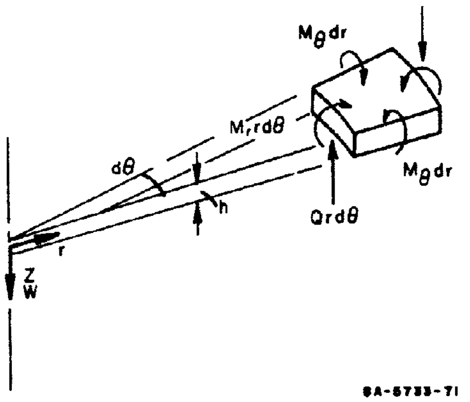

FIG. 3.2 PLATE ELEMENT — NOTATION

$$M_r = \int_{-h/2}^{h/2} \sigma_r z dz \qquad M_\theta = \int_{-h/2}^{h/2} \sigma_\theta z dz \tag{3.3}$$

It will now be shown that whenever plastic bending is possible these moments take on particularly simple forms which allow the Tresca yield hexagon in stress space to be transformed into a hexagon in moment space. Also, the flow rule stating the normality of the strain-rate vector $(\dot{\epsilon}_r, \dot{\epsilon}_\theta)$ to the stress hexagon transforms to the flow rule stating the normality of the curvature-rate vector $(\dot{\kappa}_r, \dot{\kappa}_\theta)$ to the moment hexagon.

We shall now make use of a second assumption of plate theory; plate elements normal to the midsurface remain normal during deformation. The kinematic consequence of this assumption is that $\dot{\epsilon}_r = z\dot{\kappa}_r$ and $\dot{\epsilon}_\theta = z\dot{\kappa}_\theta$, and hence $\dot{\epsilon}_r/\dot{\epsilon}_\theta = \dot{\kappa}_r/\dot{\kappa}_\theta$, where, in terms of the transverse velocity $v = \partial w/\partial t$, the principal curvature rates are

$$\dot{\kappa}_r = -\frac{\partial^2 v}{\partial r^2} \qquad\qquad \dot{\kappa}_\theta = -\frac{1}{r}\frac{\partial v}{\partial r}$$

Since the ratio $\dot{\epsilon}_r/\dot{\epsilon}_\theta$ is independent of z, the strain-rate vector has the same slope for each level z in the element, but the direction of the vector above the midsurface is opposite that below the midsurface. For a von Mises yield ellipse the slope and direction of the strain-rate vector as an outward normal uniquely determines the stress distribution on the sides of the plate element. For a Tresca yield hexagon a unique stress distribution can be justified if we regard each straight side of the hexagon as the limit of a curve. Figure 3.3 shows a stress distribution for a stress state on side AB of the hexagon in Fig. 3.1.

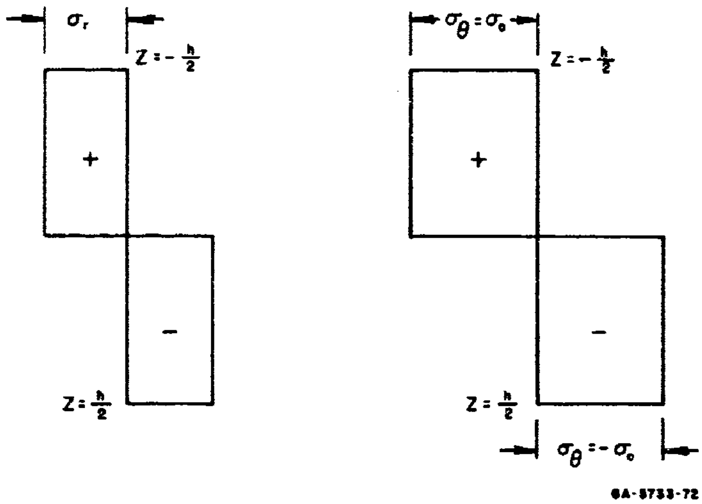

FIG. 3.3 STRESS DISTRIBUTION ON PLATE ELEMENT
(Shown for stress point on AB of Fig. 3.1 — note that $\xi_r = 0$)

We have shown then that σ_r and σ_θ, acting on the sides of the upper half of a plate element, are constant (independent of z), and similarly, they are constant on the lower half but opposite in sign. This simple stress distribution substituted into (3.3) for the bending moments gives

$$M_r = \sigma_r h^2/4 \qquad M_\theta = \sigma_\theta h^2/4 \tag{3.4}$$

Thus, in terms of the moments, the Tresca yield condition becomes

$$\max\left(|M_r| \; , \; |M_\theta| \; , \; |M_r - M_\theta| \right) = M_o$$

where $M_o = \sigma_o h^2/4$ is the fully plastic moment per unit length. Furthermore, with $\dot{\epsilon}_r/\dot{\epsilon}_\theta = \dot{\kappa}_r/\dot{\kappa}_\theta$ the flow law states that the curvature-rate vector $(\dot{\kappa}_r, \dot{\kappa}_\theta)$ is normal to the moment hexagon when the $\dot{\kappa}_r, \dot{\kappa}_\theta$ plane is superposed on the M_r, M_θ plane. The integrated or plate form of the Tresca yield condition and associated flow law shown in Fig. 3.4 is the form we shall use in solving rigid-plastic plate problems.

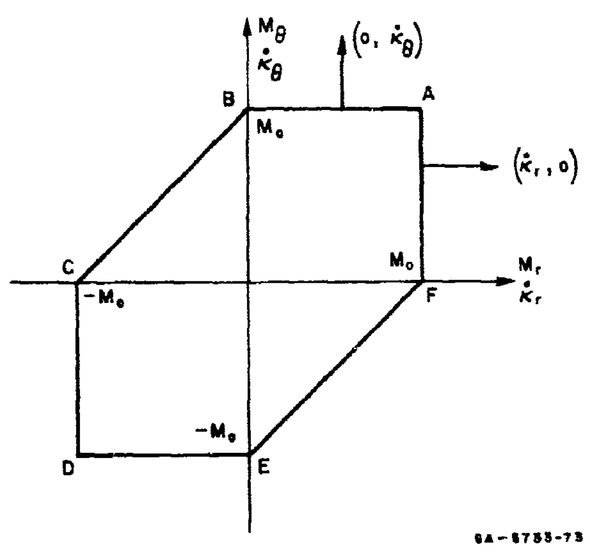

FIG. 3.4 TRESCA YIELD HEXAGON FOR A PLATE

3.3 Plastic Regimes, Hinge Circles, and Continuity Requirements

3.3.1 Plastic Regimes

By a plastic regime we mean the plastic bending moments M_r and M_θ together with the curvature rates $\dot{\kappa}_r$ and $\dot{\kappa}_\theta$ associated with a corner or a side of the Tresca yield hexagon (Fig. 3.4). During plastic deformation due to axisymmetric loading, a circular plate is generally divided into a central region and one or more annular regions, each with a certain plastic regime. In dynamics problems the circles separating the regimes can have radii which are functions of time, and even the numer of regimes can vary. Let us first look at the regimes in Fig. 3.4 to see what can readily be deduced to assist in the solution of plate problems.

It is sufficient to consider the regimes FA, A, AB, B, BC, and C forming one-half of the perimeter of the hexagon in Fig. 3.4. From the Tresca yield condition, the flow rule, and the curvature-rate formulas

$$\dot{\kappa}_r = - \frac{\partial^2 v}{\partial r^2} \qquad \dot{\kappa}_\theta = - \frac{1}{r} \frac{\partial v}{\partial r}$$

the results of Table 3.1 are readily deduced. For brevity, a subscript r is attached to the velocity v to denote partial differentiation. The quantities a and b signify functions of time. It can be seen that for the regimes FA, AB, and BC the r-dependency of the velocity fields has been obtained.

Table 3.1

TRESCA PLASTIC REGIMES

Regime (Fig. 3.4)	Bending Moments	Curvature Rates	Velocity Fields
FA	$M_r = M_o$ $\quad 0 < M_\theta < M_o$	$\dot{\kappa}_r \geq 0$ $\quad \dot{\kappa}_\theta = 0$	$v = a$
A	$M_r = M_\theta = 0$	$\dot{\kappa}_r \geq 0$ $\quad \dot{\kappa}_\theta \geq 0$	$v_{rr} \leq 0$ $\quad v_r \leq 0$
AB	$0 < M_r < M_o$ $\quad M_\theta = M_o$	$\dot{\kappa}_r = 0$ $\quad \dot{\kappa}_\theta \geq 0$	$v = ar + b$
B	$M_r = 0$ $\quad M_\theta = M_o$	$- \dot{\kappa}_\theta \leq \dot{\kappa}_r \leq 0$	$0 \leq v_{rr} \leq - v_r/r$
BC	$M_\theta - M_r = M_o$	$0 \leq \dot{\kappa}_\theta = - \dot{\kappa}_r$	$v = a \ln r + b$ $\quad a \leq 0$
C	$M_r = - M_o$ $\quad M_\theta = 0$	$- \dot{\kappa}_\theta \leq \dot{\kappa}_r \leq 0$	$0 \leq v_{rr} \leq - v_r/r$

3.3.2 Hinge Circles

If during deformation of a circular plate there is a circle C across which the curvature rate $\dot{\kappa}_r$ and hence $\partial v/\partial r$ is discontinuous, C is called a "hinge circle;" it corresponds to a plastic hinge in a rigid-plastic beam and, like a plastic hinge, need not be stationary. Like the plastic hinge, the hinge circle may be regarded as the limiting case of bending as an elastic-plastic material tends to a rigid-plastic material (see Section 2.2). At the hinge circle the curvature rate $\dot{\kappa}_r$ is infinite in the limit and, if the hinge circle is stationary, the curvature κ_r is also infinite in the limit (and the curvature and slope are discontinuous across C). Referring to Fig. 3.4 or Table 3.1, the plastic regimes at hinge circles can be FA, A, and C on the half of the hexagon under consideration, because an infinite ratio $\dot{\kappa}_r/\dot{\kappa}_\theta$ is possible in these regimes.

3.3.3 Continuity Requirements

In order to discuss the continuity requirements at a hinge circle, we shall treat a specific case which arises when a simply supported circular plate is subjected to a blast pulse with a sufficiently high peak pressure, or to an impulse uniformly distributed over the whole plate area. This should assist the physical interpretation of the results. A more general treatment is given by Hopkins and Prager.[2]

Consider then Fig. 3.5, which shows a plate radius at an instant early in a plastic deformation process according to the assumed plastic regimes indicated (see Fig. 3.4 for the plastic regimes of the Tresca hexagon). A moving plastic hinge circle with a regime A exists at a radius $r = r_h(t)$ which is assumed to be decreasing. The situation is similar to the corresponding clamped beam mechanism 2 treated in Section 2.4.2. The central circular area $0 \le r \le r_h(t)$ is undergoing translatory motion at a velocity $V(t)$ while the elemental section in $r_h(t) \le r \le a$ is undergoing rotatory motion about the support at an angular velocity $\omega(t)$. The deformed portion of the radius outside the hinge circle does not deform further because the plastic regime AB requires $\dot{\kappa}_r = 0$.

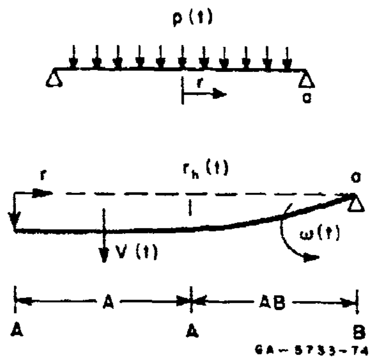

FIG. 3.5 SIMPLY SUPPORTED PLATE — DEFORMATION AND PLASTIC REGIMES

The displacement is continuous and is given by

$$w(r,\ t) = \begin{cases} \displaystyle\int_o^t V dt & 0 \le r \le r_h(t) \\[2ex] \displaystyle\int_o^t V dt - \int_{r_h(t)}^{r} \theta(r,\ t) dr & r_h(t) \le r \le a \end{cases} \tag{3.5}$$

in which $\theta(r,\ t) = \partial w/\partial r$ is the slope or rotation of an element of the radius at time t.

By time differentiation of expressions (3.5), the velocity distribution is

$$\frac{\partial w}{\partial t} = \begin{cases} V & 0 \le r < r_h(t) \\[1ex] V - \omega(r - r_h) + \theta(r_h, t)\dot{r}_h & r_h(t) < r \le a \end{cases} \tag{3.6}$$

As the radius of the plastic hinge circle decreases, each element of radius which it passes is rotated an infinitesimal angle. This angle is ωdt as the hinge circle radius changes by $\dot{r}_h dt$; thus the hinge circle leaves behind it a deformed radius with a continuous slope θ

and a curvature $\kappa_r = \omega/\dot{r}_h$. In our example, $\theta(r_h, t)$ of (3.6) is infinitesimal and in the limit $\theta(r_h, t) = 0$, so that

$$\frac{\partial w}{\partial t} = \begin{cases} V & 0 \le r \le r_h(t) \\ V - \omega(r - r_h) & r_h(t) \le r \le a \end{cases} \tag{3.7}$$

and the velocity is continuous at $r = r_h(t)$. Note that if the hinge circle were stationary, a case which arises with a rectangular pulse of sufficiently high peak pressure, $\theta(r_h, t)$ would be finite but $\dot{r}_h = 0$. Hence (3.7) again applies.

By time differentiation of (3.7), the acceleration distribution is

$$\frac{\partial^2 w}{\partial t^2} = \begin{cases} \dot{V} & 0 \le r < r_h(t) \\ \dot{V} - \dot{\omega}(r - r_h) + \omega\dot{r}_h & r_h(t) < r \le a \end{cases} \tag{3.8}$$

and we see that a discontinuity of acceleration equal to $\omega\dot{r}_h$ exists at the hinge circle. Across a stationary hinge circle, the acceleration is continuous ($\dot{r}_h = 0$).

From (3.5) the slopes are

$$\frac{\partial w}{\partial r} = \begin{cases} 0 & 0 \le r \le r_h(t) \\ -\theta(r, t) & r_h(t) < r \le a \end{cases} \tag{3.9}$$

and, since $\theta(r_h, t) = 0$ when the hinge circle is moving, the slope is continuous across the hinge circle. For a stationary hinge circle $\theta(r_h, t) \neq 0$ and the slope is discontinuous. Since $\kappa_\theta = -\partial w/r\partial r$, these results show that the circumferential component of curvature is continuous across a moving hinge circle and discontinuous across a stationary one.

The radial component of curvature $\kappa_r = -\partial^2 w/\partial r^2$ is discontinuous across the moving hinge circle. On the inside $\kappa_r = 0$, and on the outside, as we have shown, the hinge circle leaves behind it a curvature $\kappa_r = \omega/\dot{r}_h$. Across a stationary hinge circle κ_r can be either continuous or discontinuous. In our example with a rectangular pulse of sufficiently high pressure, $\kappa_r = 0$ on either side of the hinge circle and is therefore continuous.

Differentiation of (3.7) with respect to r or (3.9) with respect to t gives

$$\frac{\partial^3 w}{\partial t \partial^2 r} = \begin{cases} 0 & 0 \le r < r_h(t) \\ -\dot{\omega} & r_h(t) < r \le a \end{cases} \tag{3.10}$$

which shows that the curvature rate $\dot{\kappa}_r = -\partial^3 w/\partial t \partial r^2$ is discontinuous across a stationary of nonstationary hinge circle unless the angular velocity ω is constant.

Finally, we shall find the continuity conditions at a hinge circle which apply to the bending moments and shear force. Figure 3.6 shows two plate elements, one on either side of a hinge circle

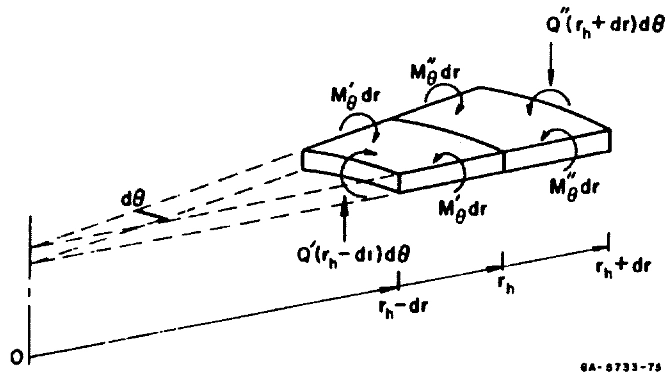

FIG. 3.6 PLATE ELEMENTS NEXT TO HINGE CIRCLE

or regime boundary of radius $r = r_h$. With the forces and moments shown, vertical equilibrium requires

$$Q''(r_h + dr) - Q'(r_h - dr) + (p'' - mw''_{tt})r_h\, dr + (p' - mw'_{tt})r_h\, dr = 0$$

where w_{tt} is the acceleration. Letting dr become zero leaves $Q' = Q''$ so that the shear force is continuous. Moment equilibrium about $r = r_h$ requires

$$M''_r(r_h + dr) - M'_r(r_h - dr) - (Q' + Q'')r_h\, dr - (M'_\theta + M''_\theta)dr = 0$$

and, by again letting dr become zero, we have $M'_r = M''_r$ so that the radial bending moment is continuous. Since the circumferential moments M'_θ and M''_θ are independently in equilibrium, they need not be related to each other and may have a discontinuity across $r = r_h$.

3.4 Analytical Approach: Equilibrium Equations

The motion of a rigid-plastic beam takes place by means of mechanisms consisting of finite rigid portions of beam joined by natural or plastic hinges; the motion can be conveniently analyzed by using the equations of rigid body dynamics. The motion of a plate, on the other hand, involves yielding, not just at the hinge circle but throughout finite regions of the plate. Nevertheless, by regarding an elemental section as a tapered beam with moments M_θ distributed along its sides, a mechanism approach is possible. However, in view of the complicated "beam" shape (being triangular or trapezoidal in plan) and its loading, one is forced to start from the equilibrium equations of a plate element bounded by the polar coordinate lines. The concept of a mechanism applied to an elemental sector of plate is still useful for an understanding of the deformation process.

With the aid of Fig. 3.7 the equations of equilibrium or motion of a plate element are readily found to be

$$\frac{\partial}{\partial r}(Qr) + \left(p - m\frac{\partial^2 w}{\partial t^2}\right)r = 0$$

$$\frac{\partial}{\partial t}(M_r r) - M_\theta - Qr = 0$$

where p and m are the applied pressure and mass per unit area of plate. Since the shear force is zero at the plate center, these equations can be written in the form

$$\frac{\partial}{\partial r}(M_r r) - M_\theta = Qr = -\int_0^r \left(p - m\frac{\partial^2 w}{\partial t^2}\right)r\,dr \qquad (3.12)$$

To find the initial motion, a distribution of plastic regimes is chosen consistent with the center and support conditions. At the plate center $M_r = M_\theta = M_o$, so that the regime there is A in Fig. 3.4. At a simple support $M_r = 0$, giving regime B; at a clamped support $M_r = -M_o$, suggesting regime C. Regime boundaries must provide continuous radial moments M_r. The flow rule of these regimes suggest velocity fields.

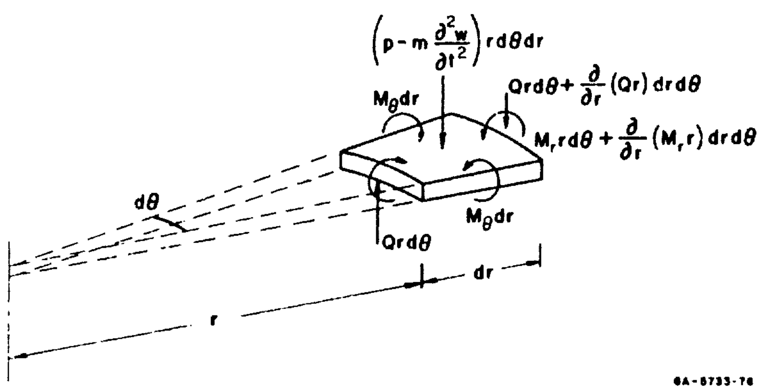

FIG. 3.7 PLATE ELEMENT — FORCES AND MOMENTS

They have to be consis 'nt with the boundary conditions and give a velocity distribution ntinuous in r. The velocity fields and moments are then substituted n (3.12). These procedures will be applied to dynamic problems, bu first we shall devote the next two sections to establishing static collapse pressures and mechanisms for simply supported and clamped circular plates.

3.5 Static Collapse Pressure of a Simply Supported Plate

The uniformly distributed pressure which just causes collapse of a rigid-plastic simply supported circular plate will now be found. Setting the inertia term equal to zero in (3.12) and treating the pressure as a constant gives

$$\begin{aligned} Q &= -pr/2 \\ \frac{\partial}{\partial r}(M_r r) - M_\theta &= -pr^2/2 \end{aligned} \qquad (3.13)$$

We shall assume that at collapse the entire plate is plastic so that at each element a plastic regime exists. Then, at the center $M_r = M_\theta = M_o$, and at the support $M_r = 0$. Now M_r must vary continuously from $M_r = 0$ at the support to $M_r = M_o$ at the center. Consequently, the plastic regimes governing the plate deformation are A, AB, and B in Fig. 3.8, with A at the center and B at the support. This means that throughout the plate $M_\theta = M_o$ and (3.13) can be integrated to give $M_r = M_o - pr^2/6$. Using the boundary condition $M_r(a) = 0$, where a is the plate radius, gives a static collapse pressure

$$p_s = 6M_o/a^2 \qquad (3.14)$$

Before (3.14) can be said to be the actual collapse and not merely a lower bound,[9,10] we must prove that the velocity field stemming from the flow law is admissible. Along AB of Fig. 3.8, $\dot{\kappa}_r = -d^2v/dr^2 = 0$, so that the velocity fields are of the form $v = \alpha r + \beta$, where α and β are constants. Now the boundary condition $v(a) = 0$ demands that

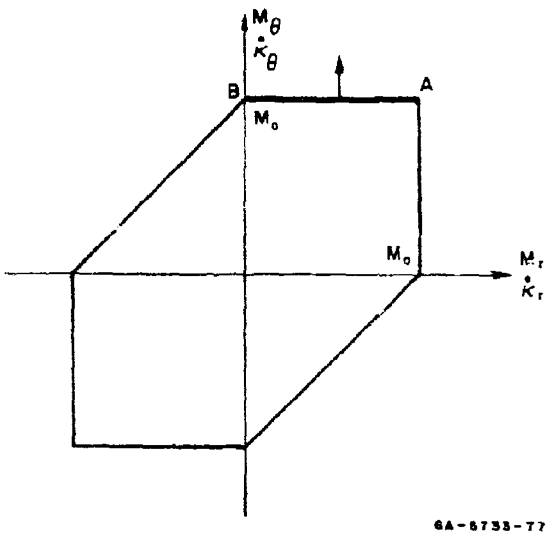

FIG. 3.8 TRESCA YIELD HEXAGON — REGIMES FOR SIMPLY SUPPORTED PLATE

$\beta = -a\alpha$ and the velocity field becomes

$$v = v_o(1 - r/a) \qquad (3.15)$$

where v_o is the indeterminate velocity of the plate center at collapse. The plate therefore collapses into a cone with a concentrated hinge circle at the center, where the plastic regime B, being a corner of the yield hexagon, allows a discontinuity of slope. The velocity distribution (3.15) gives the mechanism applicable to an elemental plate sector. Each radius remains straight and rotates as a "rigid body" about the support. Since the velocity field satisfies all conditions, (3.14) gives the static collapse pressure.

3.6 Static Collapse Pressure of a Clamped Plate

We shall now find the uniform pressure which just causes collapse of a rigid-plastic clamped circular plate. By setting the inertia term equal to zero and by treating the pressure as a constant, equations (3.12) become

$$\left.\begin{aligned} Q &= -pr/2 \\ \frac{\partial}{\partial r}(M_r r) - M_\theta &= -pr^2/2 \end{aligned}\right\} \qquad (3.16)$$

At collapse, the entire plate is assumed to be plastic so that at each plate element a plastic regime exists. Then, as for simply supported plates, we have $M_r = M_\theta = M_o$ in plastic regime A at the center (see Fig. 3.9). At a clamped support either the slope $dw/dr = 0$ (which gives $\dot{\kappa}_\theta = -dv/rdr = 0$) or a hinge circle exists there. To find

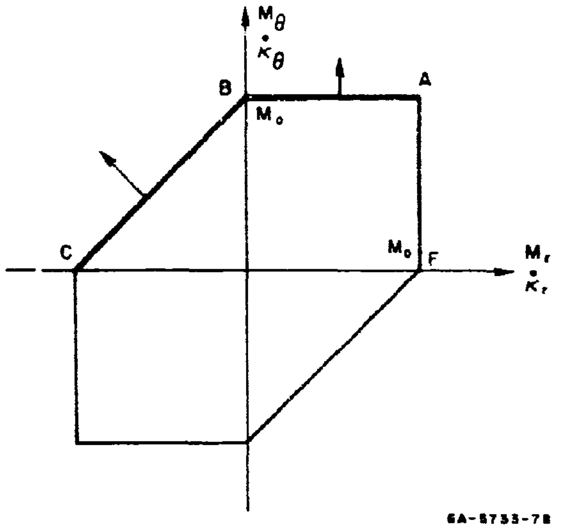

SA-5733-78

FIG. 3.9 TRESCA YIELD HEXAGON — REGIMES FOR CLAMPED PLATE

which condition actually occurs at the support, let us work outward from the center of the plate, determining plastic regimes as we proceed. For continuity of M_r, the regime for the area of plate surrounding the center is either A, AF, or AB. It cannot be $A(M_r = M_\theta = M_o)$ or $AF(M_r = M_o,\ 0 < M_\theta < M_o)$ because $M_r = M_o$ substituted in (3.16) gives $M_\theta = M_o + pr^2/2$, which is incompatible with $M_\theta = M_o$ for A and $0 < M_\theta < M_o$ for AF. Thus, in the vicinity of the center, the regime is AB $(M_\theta = M_o,\ 0 < M_r < M_o)$, which is compatible with (3.16). The corresponding velocity field, from the flow law $\dot{\kappa}_r = -d^2v/dr^2 = 0$, is of the form $v = \alpha r + \beta$. For this regime to extend to the support at radius a, we have $v = -\alpha(a - r)$. Thus zero slope is not possible at the support and, since the alternative is a plastic hinge circle with $M_r = -M_o$, the plastic regime AB does not reach the support. We therefore let B be the regime at an interior circle of radius $r = r_b$; outside this circle the regime is BC, since M_r must be continuous throughout the plate. Regime BC has the yield condition $M_\theta - M_r = M_o$ and the flow law $\dot{\kappa}_\theta + \dot{\kappa}_r = 0$, the latter demanding velocity fields of the form $v = \gamma \ln r + \delta$, where γ and δ are constants. With the support condition $v(a) = 0$, the velocity becomes $v = -\gamma \ln(a/r)$ giving at the support $\dot{\kappa}_\theta = -\gamma/a^2$, which is not zero. Hence the support is a hinge circle with plastic regime C, and we have $M_r = -M_o$. We now proceed to find the collapse pressure using the deduced distribution of plastic regimes, A at $r = 0$, AB in $0 < r < r_b$, B at $r = r_b$, BC in $r_b < r < a$, and C at $r = a$.

In the region $0 < r < r_b$ with plastic regime AB, we have $M_\theta = M_o$ so that (3.16) gives for M_r the expression $M_r = M_o - pr^2/6$. At the as yet unknown radius $r = r_b$ the plastic regime is B with $M_r = 0$ so that the static collapse pressure is

$$p_s = 6M_o/r_b^2 \tag{3.17}$$

provided the velocity field satisfies all its requirements. To find r_b we first note that the region $r_b < r < a$ is governed by regime BC with the yield condition $M_\theta = M_o + M_r$ which when substituted in (3.16) gives $M_r = M_o \ln(r/r_b) - p(r^2 - r_b^2)/4$. Then with the support condition $M_r(a) = -M_o$ we have the equation for $(r_b/a)^2$

$$5 + \ln(a/r_b)^2 = 3(a/r_b)^2$$

with the solution $r_b/a = 0.730$. Thus the static collapse load of (3.17) becomes

$$p_s = 11.26\ M_o/a^2 \tag{3.18}$$

This value must be regarded as a lower bound until it is established that the velocity field satisfies all requirements.

The velocity distribution from the flow rule of regimes AB and BC is

$$v = \begin{cases} \alpha r + \beta & 0 < r < r_b \\ \gamma \ln r + \delta & r_b < r < a \end{cases} \tag{3.19}$$

Eliminating from (3.19) the constants γ and δ by ensuring continuity of v and dv/dr (no hinge circle with regime B) at $r = r_b$ and eliminating β by satisfying the support condition $v(a) = 0$ leads to

$$v = v_o \begin{cases} \rho_b - \rho + \rho_b \ln(1/\rho_b) & 0 \le \rho \le \rho_b \\ \rho_b \ln(1/\rho) & \rho_b \le \rho \le 1 \end{cases} \tag{3.20}$$

where $v_o = -\dot{\alpha}a$, $\rho = r/a$, and $\rho_b = r_b/a$. The portion of the plate within $r = r_b$ becomes a cone with a concentrated hinge circle at the center where the plastic regime is A. At $r = r_b$, where the plastic regime is B, continuity of velocity and slope is assured. At the support where the plastic regime is C, the velocity is zero and a hinge circle exists. All requirements are met by the velocity field, and (3.18) is the static collapse load.

3.7 Simply Supported Plate Subjected to a Rectangular Pulse

We shall now find the relationship among the peak pressure, impulse, and final central deflection for a simply supported circular rigid-plastic plate subjected to a rectangular pulse uniformly distributed over its entire area. As shown in Fig. 3.10, the pulse has an instantaneous rise to a pressure p_m which remains constant until a time t_o when it instantaneously falls to zero. The pressure and impulse functions meeting this description are

$$p = \begin{cases} p_m & 0 \le t < t_o \\ 0 & t > t_o \end{cases}$$

$$I = \begin{cases} p_m t = I_o(t/t_o) & 0 \le t \le t_o \\ p_m t_o = I_o & t \ge t_o \end{cases}$$

It will be convenient to express our results in terms of the dimensionless variables

$$\lambda = p_m/p_s \qquad \text{and} \qquad \nu = \delta/(I_o^2 a^2/mM_o) \tag{3.21}$$

where p_s is the static collapse pressure, δ the central deflection,

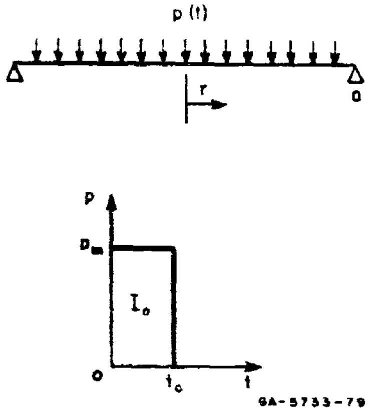

FIG. 3.10 CIRCULAR PLATE PROBLEM

a the plate radius, m the mass of plate per unit area, and M_o the fully plastic moment per unit length of polar coordinate line. Instead of the symbols M_r and M_θ for the radial and circumferential bending moments, we shall use M and N. This will permit the consistent use of subscripts r and t to denote partial differentiation.

We recall that in Section 3.5 the static collapse pressure and the associated velocity field were found to be

$$p_s = 6M_o/a^2 \tag{3.22}$$

and

$$w_t = V(1 - r/a) \tag{3.23}$$

When a rectangular pulse is applied with a pressure slightly in excess of the static collapse pressure, the inertia forces are small so that it is reasonable to assume the velocity distribution (3.23) with $V = V(t)$. From the point of view of the motion of a radius or diameter and the analogous motion of a simply supported beam, the velocity distribution (3.23) will give rise to a mechanism which we shall call mechanism 1.

3.7.1 Mechanism 1, Phase 1 ($0 \le t \le t_o$)

The velocity distribution (3.23) implies that the whole plate is plastic and governed by regime AB of Fig. 3.11c, with A at the center and B at the support, as shown in Fig. 3.11a. Consequently we have

$$0 \le M \le M_o \qquad N = M_o \tag{3.24}$$

Introducing now the equation of motion (see Section 3.4)

$$(Mr)_r - N = -\int_0^r (p - mw_{tt})r\,dr \qquad (3.25)$$

substituting N from (3.24), w_{tt} from (3.23), and integrating twice with respect to r leads to

$$M = M_o - p_m r^2/2 + m\dot{V}r^2(2 - r/a)/12 \qquad 0 \le t < t_o \qquad (3.26)$$

At the support $M(a,t) = 0$ so that, with the use of (3.22), expression (3.26) gives the central acceleration as

$$\dot{V} = 2(p_m - p_s)/m \qquad (3.27)$$

With the initial conditions $w(0,r) = w(0,r) = 0$, and hence $V(0) = 0$, successive time integrations of (3.27) give the central velocity and deflection as

$$V = 2(p_m - p_s)t/m$$

$$\delta = (p_m - p_s)t^2/m \qquad (3.28)$$

This phase of the motion ends at the same time as the pulse, at time t_o. At this time the deflection expression, in terms of the dimensionless variables λ and ν of (3.21), becomes

$$\nu_o = (1 - 1/\lambda)/6\lambda \qquad (3.29)$$

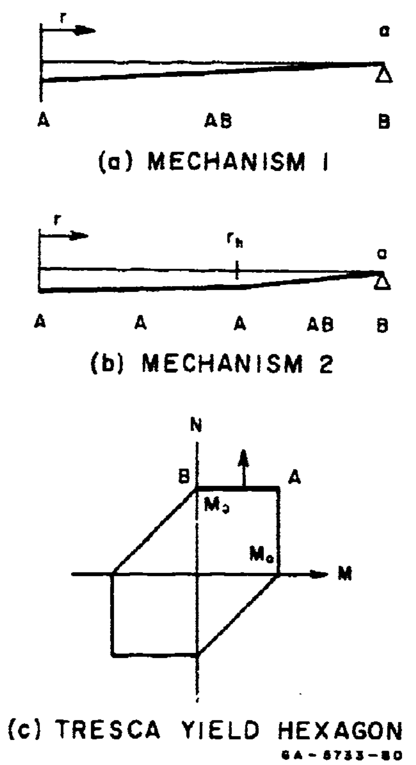

FIG. 3.11 MECHANISMS AND PLASTIC REGIMES. (a) Mechanism 1, (b) Mechanism 2, (c) Tresca yield hexagon

Before considering the next phase of motion the expression (3.26) must be examined to see if any restrictions have to be imposed in order that the moment M satisfies the yield condition (3.24). As we shall presently see, a restriction is indeed necessary and takes the form of a bound on the pressure p_m, as in similar beam problems. This is to be expected because we assumed inertia forces small enough not to change the static collapse mechanism and, if the pressure is high enough, this assumption can no longer be reasonable.

By substituting the central acceleration expression (3.27) in (3.26), we find that moment can be represented in the form

$$M/M_o = 1 - \lambda\rho^2 + (\lambda - 1)\rho^2(2 - \rho) \qquad (3.30)$$

where, for brevity, we have let $\rho = r/a$. The derivative of (3.30) with respect to ρ is $\rho[(\lambda - 1)(4 - 3\rho) - 2\lambda]$, which is zero at $\rho = 0$ and less than zero for all ρ in $0 < \rho \leq 1$ if $1 < \lambda < 2$. Hence if λ is in the range $1 < \lambda < 2$, the moment decreases monotonically from $M = M_o$ at the center to $M = 0$ at the support and thereby satisfies the yield condition (3.24). As λ is increased through $\lambda = 2$, the sign of the second derivative with respect to ρ changes from negative to positive at $\rho = 0$, so that M changes from a maximum to a minimum. Thus, whenever $\lambda > 2$, the yield condition is violated in the neighborhood of the plate center. This suggests that a central area of plate undergoes translatory motion when $\lambda > 2$. This will be taken up under mechanism 2 below.

3.7.2 Mechanism 1, Phase 2 ($t_o < t < t_2$)

During the remaining motion no pressure is being applied. The radial bending moment and central acceleration, from (3.26) and (3.27) with $p_m = 0$, are

$$M = M_o + m\dot{V}r^2 (2 - r/a)/12 \qquad (3.31)$$

$$\dot{V} = -2p_s/m \qquad (3.32)$$

Noting that $V(t_o) = 2(p_m - p_s)/t_o/m$, integrating (3.32) gives for the central velocity

$$V = 2(p_m t_o - p_s t) \tag{3.33}$$

The time t_2 when motion ceases, obtained by setting $V(t_2) = 0$ in (3.33), is $t_2 = (p_m/p_s)t_o = \lambda t_o$. By integrating (3.33) from $t = t_o$ to $t = t_2$ the central deflection acquired during this phase of motion, in terms of λ and ν of (3.21), is found to be

$$\nu_2 - \nu_o = (1 - 1/\lambda)^2/6 \tag{3.34}$$

Thus with ν_o determined by (3.29) the total central deflection is

$$\nu_2 = (1 - 1/\lambda)/6 \qquad 1 < \lambda < 2 \tag{3.35}$$

Again, to ensure that the radial bending moment satisfies the yield condition (3.24), we substitute (3.32) into (3.31). Then we have

$$M/M_o = 1 - \rho^2(2 - \rho)$$

which shows that the moment monotonically decreases from $M = M_o$ at $\rho = 0$ to $M = 0$ at $\rho = 1$.

3.7.3 Mechanism 2, Phase 1 ($0 \le t < t_o$

I. Section 3.7.1 it was found plausible (whenever $\lambda > 2$) to consider a mechanism in which a finite central portion of plate undergoes translatory motion; the tendency of the bending moment diagram to flatten out near the center as $\lambda \to 2$ from below suggests this mechanism. The plastic regimes are A in the central region bounded by a hinge circle of some radius $r = r_h$ with regime A, AB in the outer annulus, and B at the support. Figure 3.11b shows mechanism 2 and the distribution of plastic regimes.

From the flow law, continuity of velocity at $r = r_h$, and the support condition $w_t(a, t) = 0$, the velocity field of mechanism 2 is

$$w_t = \begin{cases} V & 0 \le r \le r_h \\ \left(\dfrac{a - r}{a - r_h}\right)V & r_h < r \le a \end{cases} \tag{3.36}$$

An assumption of the mechanism is that the hinge circle is stationary while a rectangular pulse is being applied. Note that

$$w_{tr} = \begin{cases} 0 & 0 \le r \le r_h \\ -V/(a - r_h) & r_h < r \le a \end{cases}$$

is discontinuous at $r = r_h$, which is consistent with the definition of a hinge circle.

For the central region $0 \le r < r_h$, the equation of motion is simply

$$m\dot{V} = p_m \qquad \text{or} \qquad mV = I \tag{3.37}$$

If we substitute $p = p_m$, w_{tt} from (3.36), and $N = M_o$, in the equation of motion (3.25), carry out the first integration on the right-hand side, integrate the resulting equation from r_h to r in the range $r_h < r < a$ using the continuity condition $M = M_o$ at $r = r_h$, and simplify the algebra we are led to the result

$$M/M_o = 1 - \lambda(r - r_h)^3(r + r_h)/2a^2r(a - r_h) \qquad r_h \le r \le a \tag{3.38}$$

Now making use of the support condition $M(a, t) = 0$, (3.38) yields

$$\lambda = 2a^3/(a - r_h)^2(a + r_h) \qquad \lambda > 2 \tag{3.39}$$

which, when substituted back into (3.38), gives

$$M/M_o = 1 - a(r - r_h)^3(r + r_h)/r(a - r_h)^3(a + r_h) \qquad r_h \le r \le a \tag{3.40}$$

From (3.39), as $\lambda \to \infty$, $r_h \to a$ which says that when an ideal impulse (infinite pressure, zero duration) is applied the hinge circle is at the support. In the next phase, which describes the motion after the pressure has been removed, we shall see that the hinge circle diminishes to a point at the plate center, so for an ideal impulse the initial location is the support circle and it immediately starts to decrease. For a given value of λ, (3.39) gives the following cubic equation for $\rho_h = r_h/a$:

$$\rho_h^3 - \rho_h^2 - \rho_h + (1 - 2/\lambda) = 0 \qquad \lambda > 2 \tag{3.41}$$

The question now arises as to whether a restriction on λ is necessary to ensure that the radial moment expressed by (3.40) obeys the yield condition $0 \le M \le M_o$ of the plastic regime AB. It is readily shown by differentiating (3.40) that $M_r \le 0$ for all values of r in the range $r_h \le r \le a$, with $M_r = 0$ only at $r = r_h$. Consequently, M decreases monotonically from $M = M_o$ at $r = r_h$ to $M = 0$ at $r = a$ for all $\lambda > 2$, and no restriction on λ is required.

This phase ends with the pulse at time $t = t_o$. From (3.37), the central deflection at this time, in terms of the variable λ and ν of (3.21), is

$$\nu_o = 1/12\lambda \tag{3.42}$$

3.7.4 Mechanism 2, Phase 2 ($t_o < t < t_1$)

With the removal of the pressure the central portion of the plate moves at a constant velocity $V_o = I_o/m$. If the plastic hinge were to remain stationary, the plate would retain its kinetic energy with no dissipation by plastic work. Clearly this is not possible, so the plastic hinge circle is assumed to diminish and eventually become a point at the plate center. Thus we are led to the velocity field

$$
w_t = \begin{cases} V_o & 0 \le r \le r_h(t) \\ \dfrac{a - r}{a - r_h(t)} \cdot V_o & r_h(t) \le r \le a \end{cases} \qquad (3.43)
$$

Substituting $p = 0$, w_{tt} from (3.43), and $N = M_o$ into the equation of motion (3.25), carrying out the first integration on the right-hand side, integrating the resulting equation from r_h to r in the range $r_h < r < a$ using the continuity condition $M = M_o$ at $r = r_h$, and simplifying the algebra leads to the equation

$$
2(M/M_o - 1)a^2 r(a - r_h)^2 + \lambda t_o \dot{r}_h (r - r_h)^2 [r^2 - 2r(a - r_h) - r_h(4a - 3r_h)] = 0 \qquad (3.44)
$$

Use of the support condition $M(a,t) = 0$ in (3.44) gives

$$
\dot{r}_h = -2a^3/\lambda t_o (a - r_h)(a + 3r_h) \qquad (3.45)
$$

Noting that $\lambda t_o = I_o/p_s$, we see from (3.45) that for an ideal impulse the initial velocity of the hinge circle is infinite (as $\lambda \to \infty$, $r_h \to a$).

The location of the plastic hinge can be found by integrating (3.45) and using (3.41) to give the initial location. This procedure results in the following cubic for $\rho_h = r_h/a$:

$$
\rho_h^3 - \rho_h^2 - \rho_h + (1 - 2t/\lambda t_o) = 0 \qquad \lambda > 2 \qquad (3.46)
$$

Substituting the hinge velocity $\dot{r}_h$ from (3.45) back into (3.44) gives for the bending moment distribution the expression

$$
M/M_o = 1 + a(r - r_h)^2 [r^2 - 2r(a - r_h) - r_h(4a - 3r_h)]/r(a - r_h)^3 (a + 3r_h)
$$

$$
r_h \le r \le a
$$

We can show that M monotonically decreases from $M = M_o$ at $r = r_h$ to $M = 0$ at $r = a$ for all $\lambda > 2$, so that no restrictions are required.

This phase of motion ends at a time t_1 when the hinge circle reaches the plate center. Hence by substituting $\rho_h = 0$ into (3.46), we have $t_1 = \lambda t_o/2$. From $t = t_o$ to $t = t_1$ the velocity of the plate center is V_o, a constant. Thus the central deflection acquired during this phase is $I_o(t_1 - t_o)/m$ which, in terms of λ and ν, is

$$\nu_1 - \nu_o = (1 - 2/\lambda)/12 \qquad \lambda > 2$$

and since $\nu_o = 1/12\lambda$ by (3.42), we have

$$\nu_1 = (1 - 1/\lambda)/12 \qquad \lambda > 2 \qquad (3.47)$$

The remaining motion takes place by mechanism 1.

3.7.5 Mechanism 1, Phase 3 ($t_1 < t < t_2$)

After the hinge circle becomes a point at the plate center, the whole plate is in plastic regime AB, as it was throughout motion when the pressures were in the range $p_s < p_m < 2p_s$.

The acceleration $\dot{V}$ of the center is determined by (3.32) and, after integration with $V(t_1) = I_o/m$ and $t_1 = I_o/2p_s$, the velocity of the center is found to be

$$V = 2(I_o - p_s t)/m \qquad (3.48)$$

Motion ceases at a time $t_2 = I_o/p_s = 2t_1$, determined by (3.48) with $V(t_2) = 0$. The increase in central deflection, found by integrating (3.48) from t_1 to t_2, is (in terms of ν)

$$\nu_2 - \nu_1 = 1/24 \qquad \lambda > 2$$

and hence with ν_1 given by (3.47)

$$\nu_2 = (3/2 - 1/\lambda)/12 \qquad \lambda > 2 \qquad (3.49)$$

As $\lambda \to \infty$ with I_o held constant, an ideal impulse is approached which, according to (3.49), produces a central deflection of

$$\nu_2 = 1/8 \qquad \lambda = \infty \qquad (3.50)$$

3.7.6 Relationship among Pressure, Impulse, and Central Deflection

Figure 3.12 shows the relationship among pressure, impulse, and central deflection in the form of a graph of λ versus ν obtained from formulas (3.35) and (3.49). For convenience, these formulas are written on Fig. 3.12. The graph bears a strong resemblance to the corresponding curves for clamped and simply supported beams, as can be seen from Figs. 2.16 and 2.17 (curve C). For a fixed impulse, the central deflection δ increases monotonically with the pressure, tending to an asymptote at $\nu = 1/8$ representing the ideal impulse case. At low pressures the deflection is extremely sensitive to a change in pressure. For example, increasing the value of λ from 1.1 to 2.0 increases by 5-1/2 times the value of δ. At high pressures the deflection is insensitive to a change of pressure. In fact at $\lambda = 8$ about 92% of the deflection due to an ideal impulse of magnitude I_o is attained.

Figure 3.13 is a pressure-impulse diagram and is constructed as follows. For a rectangular pulse we have $\delta = (I_o^2 a^2/mM_o)\nu(\lambda)$, where $\nu(\lambda)$ is (3.35) or (3.49), and for an ideal impulse I_1 we have $\delta_1 = (I_1^2 a^2/mM_o)\nu_1$, where $\nu_1 = 1/8$ by (3.50). Let the two deflections be equal. Then we have $(I_o/I_1)^2 = \nu_1/\nu(\lambda)$ so that

$$\left(\frac{I_o}{I_1}\right)^2 = \begin{cases} 3\lambda/4(\lambda - 1) & 1 \le \lambda \le 2 \\ 3\lambda/(3\lambda - 2) & 2 \le \lambda \end{cases} \qquad (3.51)$$

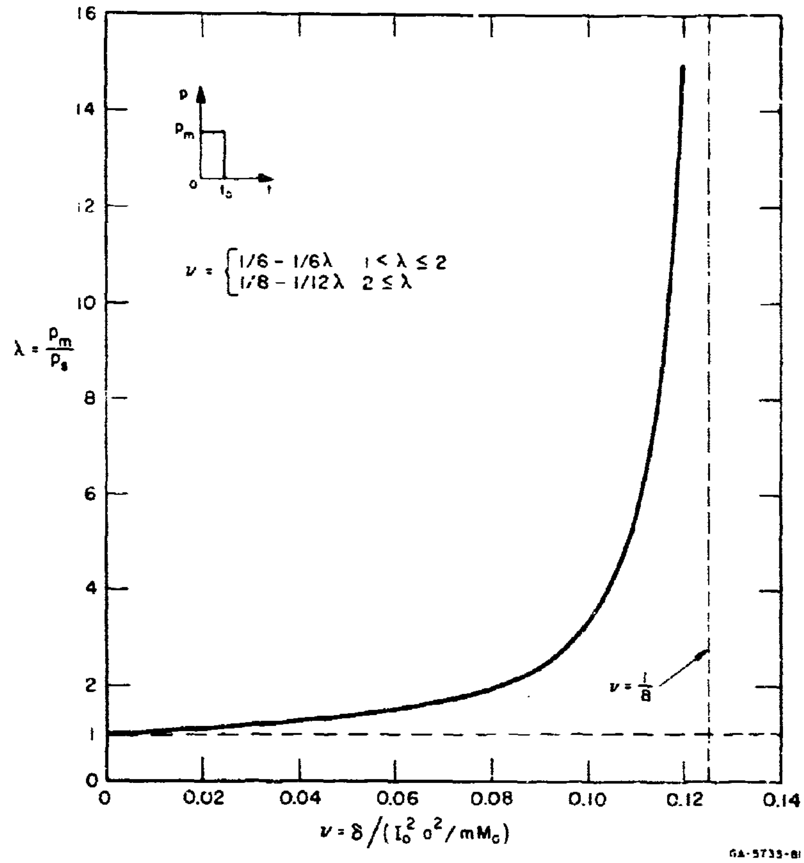

FIG. 3.12 PRESSURE-IMPULSE-CENTRAL DEFLECTION RELATIONSHIP FOR SIMPLY SUPPORTED PLATE

The curve in Fig. 3.13, obtained from (3.51), shows how the pressure and impulse of a rectangular pulse have to be varied to maintain a given central deflection δ. The curve is similar in form to that for simply supported and clamped beams, as can be seen from Fig. 2.23 (curve C). The asymptotes $I_o/I_1 = 1$ and $\lambda = 1$ represent the limiting cases of ideal impulsive and static loading. It is interesting to observe that whenever $\lambda > 6$ the impulse giving the same deflection as an ideal impulse is less than 6% larger than the ideal impulse.

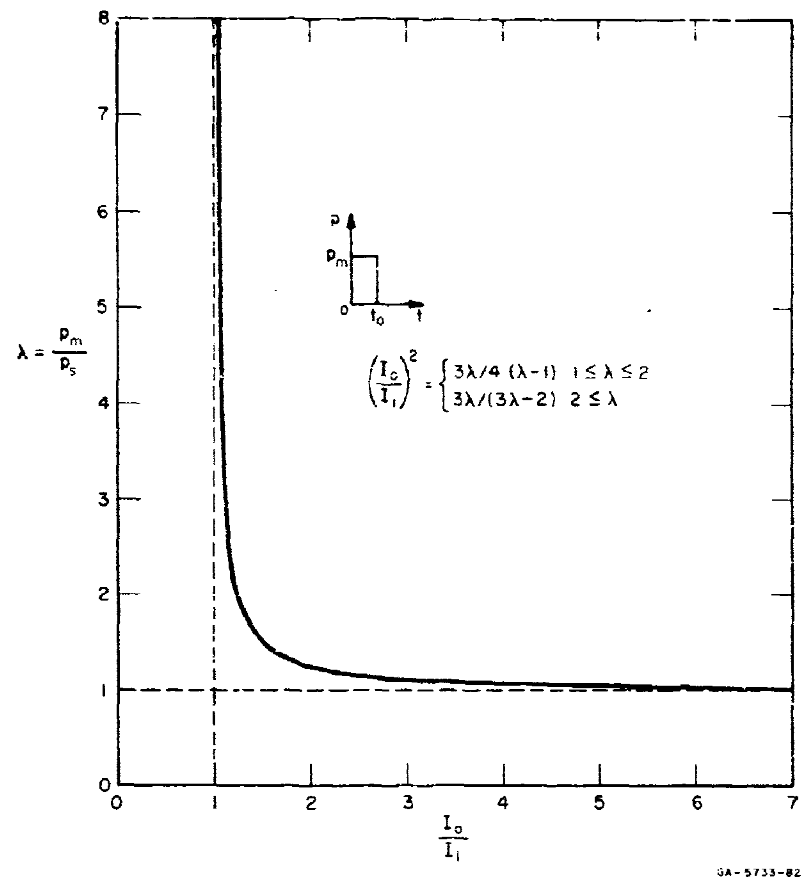

FIG. 3.13 PRESSURE-IMPULSE DIAGRAM FOR SIMPLY SUPPORTED PLATE

3.8 Clamped Circular Plate Subjected to a Rectangular Pulse

Finding the response of a clamped circular rigid-plastic plate to a rectangular pulse uniformly distributed over its entire area is far more difficult than finding the response when the plate is simply supported. Closed form solutions giving the variation of central deflection with pressure and impulse are not obtained as they were in Section 3.7, because the velocity fields are far more complicated. We recall from Section 3.6 that even finding the static collapse pressure requires the solution of a transcendental equation. To obtain the solution therefore, numerical analysis is employed.

As shown in Fig. 3.14, the pulse has an instantaneous rise to a pressure p_m which remains constant until a time t_o when it instantaneously falls to zero. The pressure and impulse functions meeting this description are

$$p = \begin{cases} p_m & 0 \le t < t_o \\ 0 & t > t_o \end{cases}$$

$$I = \begin{cases} p_m t = I_o(t/t_o) & 0 \le t \le t_o \\ p_m t_o = I_o & t \ge t_o \end{cases}$$

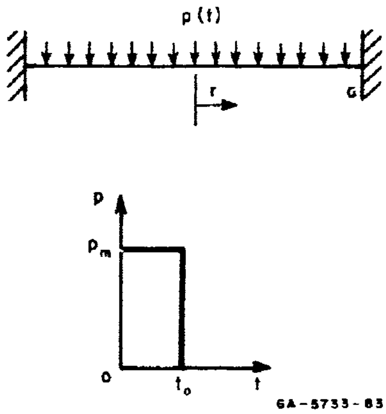

FIG. 3.14 CIRCULAR PLATE PROBLEM

3.8.1 Mechanisms of Deformation

In Section 3.6 it is established that the static collapse pressure is

$$p_s = 6M_o/r_s^2 \tag{3.52}$$

where $r_s/a \doteq 0.73$ is the solution of the equation

$$5 + \ln(a/r_s)^2 = 3(a/r_s)^2$$

a being the plate radius. The associated velocity field (3.20) can be expressed in the form

$$w_t = \begin{cases} V(1 - \sigma\,\rho/\rho_s) & 0 \le \rho \le \rho_s \\ V\,\sigma\,\ln(1/\rho) & \rho_s \le \rho \le 1 \end{cases} \tag{3.53}$$

where $\rho = r/a$, $\rho_s = r_s/a$, and $1/\sigma = \ln(1/\rho_s) + 1$. V is the indeterminate velocity of the plate center.

When the pressure is slightly greater than the static collapse pressure p_s, it is reasonable to assume that the dynamic mode of collapse has a velocity field similar to (3.53) because inertia forces are still small. The only difference in the velocity fields is that, instead of the dimensionless radius ρ_s, we shall require a new radius $\rho_1(t)$, which depends on the pressure and time. However, in the first phase of motion covering the period during which the constant pressure is being applied, we shall assume that ρ_1 is constant at a value which depends on the pressure. In the second phase, which covers the remaining motion, ρ_1 will be taken as a function of time having as its initial value the constant value in phase 1. Thus we have the following velocity field:

$$w_t = \begin{cases} V(1 - \sigma\,\rho/\rho_1) & 0 \le \rho \le \rho_1(t) \\ V\,\sigma\,\ln(1/\rho) & \rho_1(t) \le \rho \le 1 \end{cases} \tag{3.54}$$

where

$$1/\sigma = \ln(1/\rho_1) + 1 \tag{3.55}$$

and c_1 is understood to remain constant while the pressure is acting. The motion of a radius or diameter in accordance with (3.54) and (3.55) will resemble a mechanism. We shall call it mechanism 1. The distribution of plastic regimes associated with this mechanism is shown in Fig. 3.15. As in section 3.7, M and N are the radial and circumferential bending moments; they are positive when they cause tension on the underside of the plate.

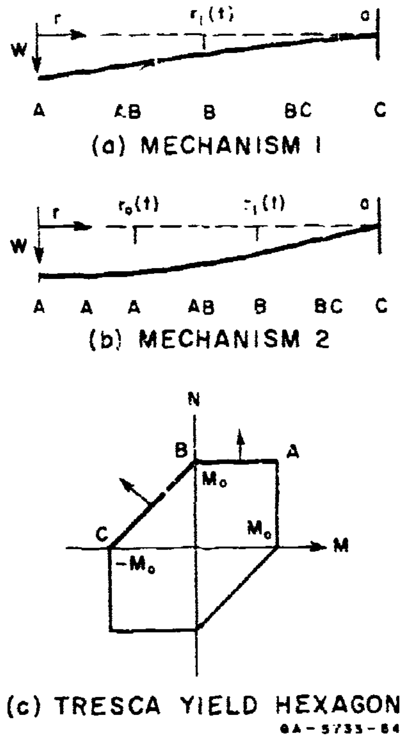

FIG. 3.15 MECHANISMS AND PLASTIC REGIMES. (a) Mechanism 1, (b) Mechanism 2, (c) Tresca yield hexagon

The assumption of small inertia forces makes it predictable at the outset that the velocity field (3.54) will not be applicable for all pressures. We shall see that the upper bound for the pressure causing deformation by mechanism 1 is $p_m \approx 2p_s$. At this pressure, an inflection point in the bending moment diagram occurs at the plate center; slightly higher pressures bring about a change from a maximum moment to a minimum, thereby causing the yield condition to be violated in the neighborhood of the plate center. As in the case of beams and simply supported circular plates, this behavior suggests that whenever $p_m > 2p_s$ a finite central portion of plate acquires a uniformly distributed velocity. This mechanism, called mechanism 2, has the distribution of plastic regimes shown in Fig. 3.15 with the following velocity field:

$$w_t = \begin{cases} V & 0 \le \rho \le \rho_0(t) \\ V\left[1 - \sigma(\rho - \rho_0)/c_1\right] & \rho_0(t) \le \rho \le \rho_1(t) \\ V\,\sigma\,\ln(1/\rho) & \rho_1(t) \le \rho \le 1 \end{cases} \qquad (3.56)$$

where

$$1/\sigma = \ln(1/\rho) + (1 - \rho_o/\rho_1) \qquad (3.57)$$

The plastic regime A now occupies a finite circular area, the circumference of which forms a plastic hinge circle of radius $\rho_o(t)$. While the constant pressure ($p_m > 2p_s$) is acting, both ρ_o and ρ_1 are assumed to remain at a constant value which depends on the pressure. Upon removal of the pressure they are no longer constant. The hinge circle reduces to a central point and thereafter deformation concludes by mechanism 1.

Starting from the equation of motion (Section 3.4)

$$(Mr)_r - N = -\int_o^r (p - m w_H) r dr \qquad (3.58)$$

we shall now derive the equations governing motion by mechanisms 1 and 2. The resulting equations are applicable to general blast pulses but will be solved only for the special case of a rectangular pulse.

3.8.2 Governing Equations for Mechanism 2

When the peak pressure of a blast pulse is large enough to cause deformation by mechanism 2, the acceleration to be substituted in (3.58) is obtained by differentiating (3.56) and (3.57) with respect to time. The circumferential component is eliminated by using the yield condition of Fig. 3.15 in conjunction with the distribution of plastic regimes. Due to the three properties $M = M_o$ in $0 \le r \le r_o$, $M(r_1,t) = 0$, and $M(a,t) = -M_o$, integration of (3.58) leads to the following three equations:

$$V' = \lambda e^{2\xi_s}/2 \qquad (3.59)$$

$$V'(\xi + \eta)\eta\,[2\xi(3 - 3\eta + \eta^2) + \eta(6 - 8\eta + 3\eta^2)] - V\xi'\eta^2[\xi(6 - 8\eta + 3\eta^2)$$

$$+ \eta(1 - \eta)(4 - 3\eta)] - V\eta'\eta^2[2\xi(3 - 2\eta) + \eta(4 - 3\eta)] \qquad (3.60)$$

$$= \lambda e^{2(\xi_s - \xi)}\eta(3 - 3\eta + \eta^2) - 1\, e^{2\xi}(\xi + \eta)^2$$

$$V'(\xi + \eta)[3e^{2\xi} - 3 - 2\xi(3 - 3\eta + 3\eta^2 - \eta^3)] - V\xi'[3e^{2\xi} - 3 - 2\xi$$

$$\left\{3 - \eta^2(1 - \eta)(3 - 2\eta)\right\} - 2\xi^2(3 - 6\eta + 6\eta^2 - 2\eta^3)]$$

$$- V\eta'[3e^{2\xi} - 3 - 2\xi(3 - 3\eta^2 + 2\eta^3) - 6\xi^2(1 - \eta)^2] \qquad (3.61)$$

$$= [3\lambda e^{2(\xi_s - \xi)}(e^{2\xi} - 1)/2 - (1 + \xi)]e^{2\xi}(\xi + \eta)^2$$

The new dimensionless variables that have been introduced in the derivation of (3.59), (3.60), and (3.61) are defined by

$$\xi = \ln(1/\rho_1) \qquad \eta = 1 - \rho_o/\rho_1 \qquad \lambda = p/p_s \qquad \xi_s = \ln(1/\rho_s) \qquad (3.62)$$

The primes denote differentiation with respect to the variable τ' where

$$\tau' = 12M_o t/ma^2$$

For a rectangular pulse of pressure p_m, we have $\lambda = p_m/p_s$.

3.8.3 Governing Equations for Mechanism 1

Whenever the peak pressure is low enough to cause deformation by mechanism 1, the acceleration to be substituted in (3.58) is obtained by differentiating (3.54) and (3.55) with respect to t. N is eliminated by means of the yield condition used in conjunction with the distribution of plastic regimes. Then, after integration of (3.58), satisfying the conditions $M(r_1,t) = 0$ and $M(a,t) = 0$ gives the following two equations:

$$V'(\xi + 1)(2\xi + 1) - V\xi'\xi = [\lambda e^{2(\xi_s-\xi)} - 1]e^{2\xi}(\xi + 1)^2 \qquad (3.63)$$

$$\begin{aligned} &V'(\xi + 1)(3e^{2\xi} - 3) - 4\xi) - V\xi'(3e^{2\xi} - 3 - 6\xi - 2\xi^2) \\ &= [3\lambda e^{2(\xi_s-\xi)}(e^{2\xi} - 1)/2 - (1 + \xi)]e^{2\xi}(\xi + 1)^2 \end{aligned} \qquad (3.64)$$

Alternatively, (3.63) and (3.64) are obtainable from (3.60) and (3.61), which govern mechanism 2, by setting $\eta = 1(\rho_o = 0,\ r_o = 0)$ and $\eta' = 0$.

3.8.4 Rectangular Pulse--Mechanism 2, Phase 1 ($0 < t < t_o$)

Specializing to a rectangular pulse, a solution of (3.59), (3.60), and (3.61), is obtainable if we assume that ξ and η are constants while the load is applied. Thus we set $\xi' = \eta' = 0$ in (3.60) and (3.61), and substitute V' from (3.59). Note that $\lambda = p_m/p_s$ is a constant for a rectangular pulse. Equations (3.60) and (3.61) now become

$$2(\xi + \eta) = \lambda e^{2(\xi_s-\xi)}\eta^3(2 - \eta) \qquad (3.65)$$

$$\begin{aligned} 2(\xi + \eta)(1 + \xi) = \lambda e^{2(\xi_s-\xi)}&[3e^{2\xi}(\xi - 1 + \eta) \\ &+ \xi(3 - 6\eta + 6\eta^2 - 2\eta^3) + 3(1 - \eta)] \end{aligned} \qquad (3.66)$$

The lower bound of λ causing deformation by mechanism 2 can be found by substituting $\eta = 1$ ($\rho_o = 0$) in (3.65) and (3.66). In this way, we obtain

$$\lambda e^{2\xi_s} = 2(\xi + 1)e^{2\xi} \qquad (3.67)$$

where ξ is determined by the equation

$$3\xi e^{2\xi} = 1 \qquad (3.68)$$

From (3.67) and (3.68), $\lambda \approx 2$ and $\xi = 0.216$ ($\rho_1 = 0.805$).

For a given value of $\lambda > 2$, (3.67) and (3.68) fix the initial values of ξ and η, and hence of ρ_o and ρ_1.

The pulse ends at a time $t = t_o$ ($\tau' = \tau_c'$) and, if the velocity of the plate center at this time is V_o, integration of (3.59) gives

$$V_o = 1/2\ \lambda e^{2\xi_s}\ \tau_o' = I_o/m$$

Now $V = p_m t/m$; therefore, by integration, the central deflection δ_o at time t_o is

$$\nu_o = 1/12\ \lambda e^{2\xi_s} = \rho_s^2/12\lambda \qquad (3.69)$$

where we have introduced the dimensionless deflection

$$\nu = \delta/(I_o^2 a^2/mM_o)$$

3.8.5 Rectangular Pulse--Mechanism 2, Phase 2 ($t_o < t < t_1$)

When $t > t_o$ no pressure is acting, so that $\lambda = 0$ and hence, from (3.59), $V' = 0$. Thus the central region of the plate, $0 \le r \le r_o(t)$, moves at a constant velocity $V_o = I_o/m$. It is evident from (3.60) and (3.61) that ξ and η can no longer be treated as constants. Introducing now a new dimensionless time,

$$\tau = 12M_o(t - t_o)/ma^2V_o = 12M_o(t - t_o)/I_oa^2$$

(3.60) and (3.61) become

$$\begin{aligned}\xi'[\xi(6 - 8\eta + 3\eta^2) + \eta(1 - \eta)(4 - 3\eta)] + \eta'[2\xi(3 - 2\eta)\\ + \eta(4 - 3\eta)] = e^{2\xi}(\xi + \eta)^2/\eta^2\end{aligned} \qquad (3.70)$$

$$\xi'[3e^{2\xi} - 3 - 2\xi\left\{3 - 2\eta^2(1 - \eta)(3 - 2\eta)\right\} - 2\xi^2(3 - 6\eta + 6\eta^2 - 2\eta^3)]$$

$$+ \eta'[3e^{2\xi} - 3 - 2\xi(3 - 3\eta^2 + 2\eta^3) - 6\xi^2(1 - \eta)^2] = e^{2\xi}(\xi + \eta)^2(\xi + 1) \tag{3.71}$$

where the primes denote differentiation with respect to τ.

The numerical technique is described in detail in Refs. 5 and 11 but, briefly, it consists of putting (3.70) and (3.71) in the form $d\xi/d\eta = -P(\xi,\eta)/Q(\xi,\eta)$ and, starting from the initial values of ξ and η obtained from (3.65) and (3.66), computing the trajectory in the (ξ,η) plane (method of isoclines) until $\eta = 1$. The duration of phase 2 is found by summing the increments $\Delta\xi/\xi'$ along the trajectory. If phase 2 ends at time t_1, the central deflection occurring in phase 2 is $\delta_1 - \delta_o = V_o(t_1 - t_o)$. In terms of ν and τ, we have

$$\nu_1 - \nu_o = \tau_1/12 \tag{3.72}$$

with ν_o given by (3.69).

3.8.6 Rectangular Pulse--Mechanism 1, Phase 3 ($t_1 < t < t_2$)

The equations governing the final phase of motion, obtained by setting $\eta = 1$, $\eta' = 0$, and $\lambda = 0$, in (3.60) and (3.61), are

$$\zeta'(\xi + 1)(2\xi + 1) - \zeta\xi'\xi = -(\xi + 1)^2e^2\xi \tag{3.73}$$

$$\zeta'(\xi + 1)(3e^{2\xi} - 3 - 4\xi) - \zeta\xi'(3e^{2\xi} - 3 - 6\xi - 2\xi^2) = -(\xi + 1)^3e^{2\xi} \tag{3.74}$$

where $\zeta = V/v_o$ and primes denote differentiation with respect to τ.

From (3.73) and (3.74), we find that

$$\zeta = \left(\frac{\xi + 1}{\xi_1 + 1}\right) \exp\left[-\int_{\xi_1}^{\xi} \frac{(1 - \xi)d\xi}{4 + 7\xi + 2\xi^2 - 3e^{2\xi}}\right] \tag{3.75}$$

where ξ_1 is the value of ξ and the end of phase 2.

Motion ceases when $V = 0$ or $\zeta = 0$ and this occurs when $\xi = \xi_2 \approx 0.478$, which is the solution of $4 + 7\xi + 2\xi^2 - 3e^{2\xi} = 0$. Let τ_2 be the value of τ when motion ceases. Then

$$\tau_2 - \tau_1 = \int_{\xi_1}^{\xi_2} \frac{d\xi}{\xi} = \int_{\xi_1}^{\xi_2} \frac{(3e^{2\xi} - 4\xi - 6\xi - 3)\zeta\, d\xi}{e^{2\xi}(\xi + 1)(4 + 7\xi + 2\xi^2 - 3e^{2\xi})} \tag{3.76}$$

Finally, let the central deflection by δ_2 when $\tau = \tau_2$. Then

$$\delta_2 - \delta_1 = \frac{I^2 a}{12M_o} \int_{\tau_1}^{\tau_2} V\, d\tau$$

and hence

$$\nu_2 - \nu_1 = \frac{1}{12} \int_{\xi_1}^{\xi_2} \frac{(3e^{2\xi} - 4\xi^2 - 6\xi - 3)\zeta^2 d\xi}{e^{2\xi}(\xi + 1)(4 + 7\xi + 2\xi^2 - 3e^{2\xi})} \tag{3.77}$$

where ν_1 is given by (3.72) and ζ by (3.75).

3.8.7 Rectangular Pulse--Mechanism 1, Phase 1 ($0 < t < t_o$

When the pressure lies between p_s and $2p_s$, the equations governing the motion during phase 1 are

$$V'(2\xi + 1) = \left[\lambda e^{2(\xi_s - \xi)} - 1\right] e^{2\xi}(\xi + 1) \tag{3.78}$$

$$V'(3e^{2\xi} - 3 - 4\xi) = \left[3\lambda e^{2(\xi_s - \xi)}(e^{2\xi} - 1)/2 - (\xi + 1)\right] e^{2\xi}(\xi + 1) \tag{3.79}$$

where the primes denote differentiation with respect to τ'. These equations can be obtained by setting $\eta = 1$, $\eta' = 0$, and $\xi' = 0$ in (3.60) and (3.61).

Eliminating V' between (3.78) and (3.79) gives

$$\left[3\lambda e^{2(\xi_s-\xi)}(e^{2\xi}-1)/2-(\xi+1)\right](2\xi+1)$$
$$=\left[\lambda e^{2(\xi_s-\xi)}-1\right](3e^{2\xi}-3-4\xi) \tag{3.80}$$

which determines ξ, and hence ρ_1, for each λ. Substituting this value of ξ into (3.78) and integrating gives the velocity

$$V=\left[\lambda e^{2(\xi_s-\xi)}-1\right]e^{2\xi}(\xi+1)\tau'/(2\xi+1) \tag{3.81}$$

A further integration gives the central deflection at time t_o as

$$\delta_o=\frac{ma^2}{12M_o}\int_0^{\tau_o'}V(\tau')d\tau'$$

which leads to the result

$$\nu_o=\left[1-1/\lambda e^{2(\xi_s-\xi)}\right](\xi+1)/6\lambda e^{2(\xi_s-\xi)}(2\xi+1) \tag{3.82}$$

3.8.8 Rectangular Pulse--Mechanism 1, Phase 2

This phase of motion is essentially the same as the phase 3 motion described in Section 3.8.6. According to (3.81), the central velocity when the pressure is removed is

$$V_o=2I_o\left[1-1/\lambda e^{2(\xi_s-\xi)}\right](\xi+1)/m(2\xi+1)$$

Let $\zeta = V/V_o$, as was done earlier, and let motion cease when $\tau=\tau_2$. Then ζ and $\tau_2-\tau_1$ (where $\tau_1=\tau_o=2/\lambda e^{2\xi_s}$) are again represented by (3.75) and (3.76) and, in place of (3.77), we have

$$\nu_2 - \nu_o = \left[1 - 1/\lambda e^{2(\xi_s - \xi)}\right]^2 \left[(\xi+1)^2/3(2\xi+1)^2\right] \int_{\xi_1}^{\xi_2} \frac{(3e^{2\xi} - 4\xi^2 - 6\xi - 3)\xi^2 d\xi}{e^{2\xi}(\xi+1)(4+7\xi+2\xi^2-3e^{2\xi})} \tag{3.83}$$

where ν_o is given by (3.82), $\xi_2 = 0.478$, and ξ_1 is the solution of (3.80).

3.8.9 Relationship among Central Deflection, Pressure, and Impulse

Figure 3.16 gives a curve of λ versus ν which shows the relationship among the final central deflection δ, the pressure p_m, and the impulse per unit area I_o for a clamped plate. Whenever $\lambda > 2$ the curve is obtainable from (3.69), (3.72), and (3.77): whenever $1 < \lambda < 2$ is is obtainable from (3.82) and (3.83). Also shown in Fig. 3.16, for comparison, is the λ versus ν curve for a simply

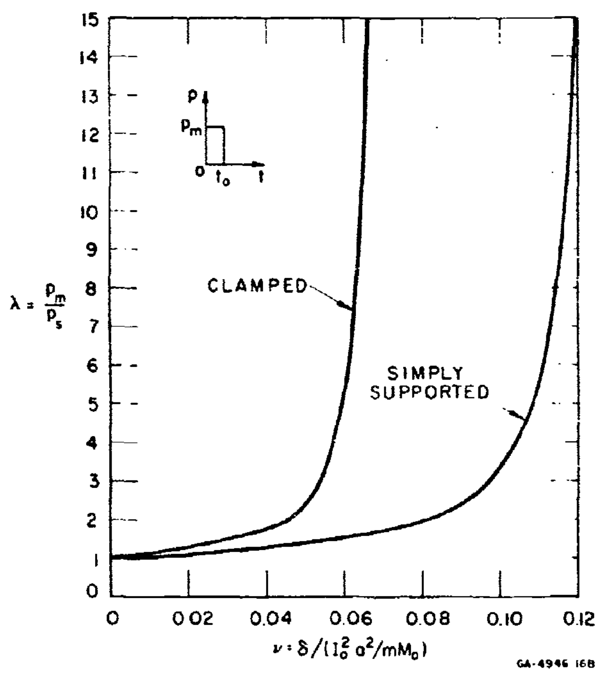

FIG. 3.16 PRESSURE-IMPULSE-CENTRAL DEFLECTION RELATIONSHIP FOR CLAMPED AND SIMPLY SUPPORTED PLATES

supported plate (taken from Fig. 3.12). In using Fig. 3.16 it should be noted that $p_s = 6M_o/r_s^2$ for clamped plates and $p_s = 6M_o/a^2$ for simply supported plates. The former is 1.875 times the latter.

Figure 3.17 is a pressure-impulse diagram which shows how the pressure and impulse must be varied to provide the same central deflection of a clamped plate. In other words, points on the curve define a family of rectangular pulses, each member of which produces the same central deflection of a clamped plate. (The corresponding curve for a simply supported plate, shown in Fig. 3.13, lies almost on top of the curve in Fig. 3.17.) The coordinates have been rendered dimensionless by using $\lambda = p_m/p_s$ and I_o/I_1, where I_1 is the ideal impulse producing the same central deflection as each member of the family of rectangular pulses. The formula giving the central deflection due to an ideal impulse is that given in Ref. 4, namely $\delta_1 = 0.07\ I_1^2a^2/mM_o$ or $\nu_1 = 0.07$.

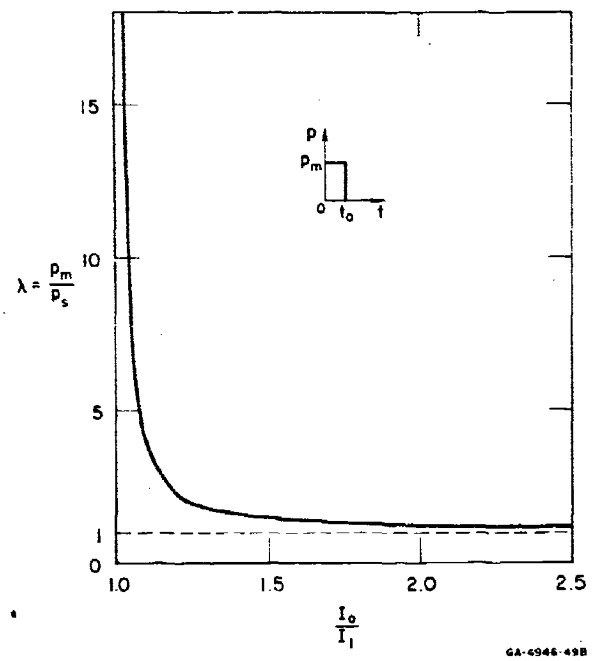

FIG. 3.17 PRESSURE-IMPULSE DIAGRAM FOR CLAMPED PLATES

From Figs. 3.16 and 3.17, the following conclusions are drawn:

1. For a given impulse, the central deflection δ increases monotonically with the pressure p_m, becoming a maximum equal to δ_1 above when the pressure is infinite (ideal impulse).

2. Again, for a given impulse value, rectangular pulses with $p_m > 6p_s$, $(\lambda > 6)$, produce deflections of simply supported and clamped plates which are respectively over 85 and 90% of the deflection caused by an ideal impulse (see Fig. 3.16).

3. For a given central deflection, Fig. 3.17 shows that as the pressure is decreased from infinity to a value corresponding to $\lambda \approx 6$, the increase in impulse necessary to maintain that deflection is less than 7%. Larger increases are necessary as λ decreases further, especially in the range $1 < \lambda < 2$.

3.9 Circular Plates under Uniformly Distributed Impulses: Comparison of Theory and Experiment

In this section we shall describe experiments, present results, and compare them with the corresponding predictions of the bending theory of rigid-plastic plates with a view to establishing the usefulness of the theory. In the experiments, each simply supported and each clamped circular plate is subjected to an impulse (pulses of extremely short duration) uniformly distributed over the entire area. The permanent central deflections and, for a few of the simply supported plates, the shape are compared with the results of the rigid-plastic theory using an ideal impulsive loading (zero duration). The theoretical results are extracted from Refs. 4 and 5.

In Section 2.12 a similar correlation for beams pointed out that the rigid-plastic theory was sufficiently accurate for many engineering applications. Five series of beam experiments were performed and for each series the average ratio of experimental to theoretical central deflection was found (see Table 2.4). These five averages fell between 0.67 and 0.77. However, to ensure a minor role for elastic effects, it was necessary that the ratio R of kinetic energy input to elastic strain energy capacity be greater than 2 to 3. We shall also see that for plates, correlation of the final central deflection ratios is satisfactory, but now large deflections cause a limitation. Deterioration of agreement becomes pronounced when the ratio of predicted deflection to plate radius exceeds values around 1/3. The deterioration is due to membrane forces unaccounted for by the theory. If the deflections are small enough, the elastic energy becomes significant, but the limited experimental data available do not establish a lower bound on R for good agreement. However, in one of the three series of experiments reported here R was as small as 4 and correlation was still satisfactory.

3.9.1 Theoretical Results

After being subjected to a uniformly distributed impulse, the final axisymmetric shape of a simply supported circular plate of rigid-plastic material obeying the Tresca yield condition and associated flow law is[4]

$$w = I^2a^2(1 - r/a)[3 + 2r/a + (r/a)^2]/24mM_o \tag{3.84}$$

which gives, for the central deflection, the formula

$$\delta = I^2a^2/8mM_o \tag{3.85}$$

In (3.84) and (3.85), I and m are the impulse and mass per unit area, a is the plate radius, and M_o is the fully plastic moment per unit arc length.

When the plate is clamped against rotation the central deflection is

$$\delta = 0.56\ I^2a^2/8mM_o \tag{3.86}$$

Before turning to the experiments, the expression will be derived for the ratio R between the kinetic energy input, which equals the plastic work done, and the elastic strain energy capacity of the plate. Let the maximum elastic bending moment per unit length by M_e. Then $M_e = \sigma_o d^2/6$, where σ_o is the yield stress and d is the plate thickness. If this moment is applied uniformly around the circumference of the plate, a state of pure bending exists. This is the state of maximum bending strain energy which, per unit area, is $M_e^2/(1 + \nu)D$, where ν is Poisson's ratio and $D = Ed^3/12(1 - \nu^2)$ is the flexural rigidity, E being Young's modulus. The kinetic energy delivered per unit area is $I^2/2m$, so the energy ratio is $R = 3I^2E/2\sigma_o^2 d^2(1 - \nu)$, where $\rho = m/d$ is the mass density.

3.9.2 Description of Experiments

The simply supported plate experiments were performed with plates of 6061-T6 aluminum and 1018 cold-rolled steel, all nominally 1/4-inch thick and 8-1/2 inches in diameter. They were simply supported on a heavy steel annulus at a diameter of 8 inches. Figures 3.18 and 3.19 show the experimental arrangement. The impulse was generated by sheet explosive rolled to a uniform thickness and cut out to form a disk 8 inches in diameter. This was placed over a similar disk of solid neoprene attenuator nominally 1/8-inch thick which in turn was layed centrally over the plate. The neoprene was used to reduce the high peak

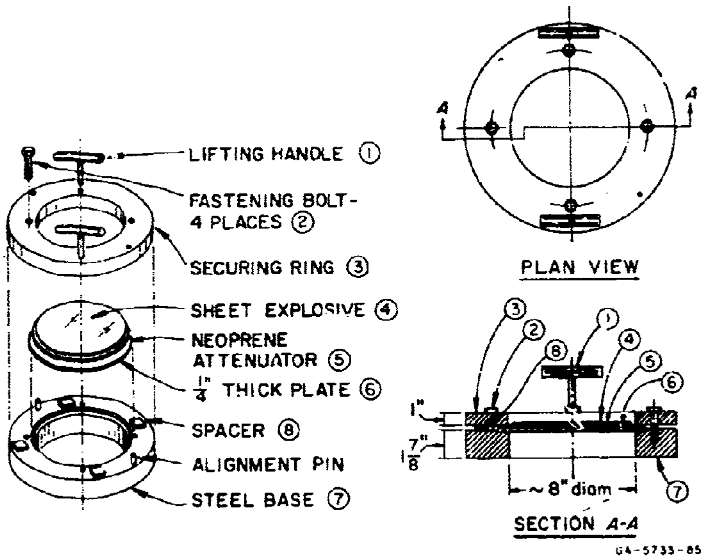

FIG. 3.18 EXPERIMENTAL SET-UP (arranged for simply supported plates)

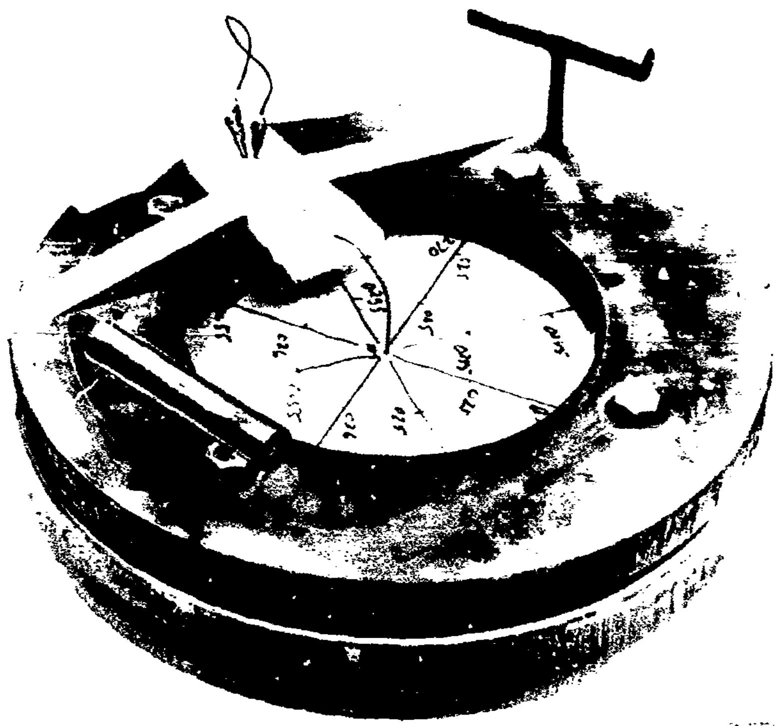

FIG. 3.19 EXPERIMENTAL ARRANGEMENT

pressure in the shock wave from the explosive in order to eliminate plastic waves in the plate, possible changes in material properties, and spalling. A five-grain mild fuse was used to detonate the explosive. The detonation velocity (0.28 in/μsec) is supersonic relative to the maximum plate velocity (0.21 in/μsec), and the initiation point is at the center of the plate, so it is assumed, by analogy with beam results,[12] that simulation of an ideal impulse simultaneously applied over the whole plate is satisfactory. As can be seen in Figs. 3.18 and 3.19, a steel annulus was placed over the supporting annulus to control the plate as it rebounded. Sufficient clearance was provided between the two annuli by means of spacers to prevent the edge of the plate striking the upper annulus as it deforms plastically.

The clamped plate experiments were performed with plates of 6061-T6 aluminum, all nominally 1/4-inch thick and 9-3/4 inches in diameter. Using the two steel annuli shown in Figs. 3.18 and 3.19, with inner diameters of 8 inches, the plates were clamped to prevent rotation but not radial displacements. Around the rim of each plate at 3/4-inch spacing, 5/8-inch-long slots were cut so that during deformation circumferential membrane forces in the annular portion of plate outside the 8-inch-diameter circle were suppressed. The slots can be seen in Fig. 3.20, which shows two plates after impulsive loading (one sectioned along a diameter).

FIG. 3.20 CLAMPED PLATES AFTER IMPULSIVE LOADING

For the explosive-attenuator-plate configuration described above, the impulse imparted was obtained by firing free plates in front of a double-flash X-ray unit. The rigid-body displacement in the predetermined time between radiographs gives the plate velocity. It was found that for each plate material the velocity imparted was proportional to the thickness of explosive over a range from 15 to 60 mils, the range of interest in the plate deformation experiments. This procedure thus provided a simple linear calibration curve of impulse versus explosive thickness. The constant slope of this curve is expressible as impulse per unit volume of explosive with units dyne sec/cm^2/mil or dyne sec/cm^3 and is given the symbol I_o. Values of I_o for the aluminum and steel plates are listed in Table 3.2.

Table 3.2

PROPERTIES

Material	Modulus (lb/in^2) E	Yield Stress (lb/in^2) σ	Mass Density ($lb\ sec^2/in^4$) ρ	Plate Depth (inch) d	Plate Radius (inches) a	Impulse Constant ($dyne\ sec/cm^3$) I_o
Al. 6061-T6	10×10^6	42,000	0.000253	0.251	4	2.5×10^5
C.R. steel 1018	30×10^6	~9,000	0.000732	0.241	4	2.7×10^5

The plate materials were chosen because of the small strain-hardening moduli and because they are believed to be insensitive to strain rate (especially the 6061-T6 aluminum alloy).

To determine the yield stress, an average value was taken of static tensile tests with specimens cut with and across the grain. Each stress-strain curve was replaced by two straight lines, the slope of the strain-hardening portion being obtained by curve fitting to about 3% strain. The ordinate of their point of intersection was taken as the yield stress.

In addition to permanent central deflections, changes in thickness at the center and near the support was measured. In a few cases deflections along a radius were measured to give a plate profile. The deflection measurements will be compared with the predictions of formulas (3.84), (3.85), and (3.86).

3.9.3 Experimental Results and Observations

Table 3.2 contains the materials, properties, and the impulse constants I_o mentioned above. Tables 3.3 and 3.4 contain the results of experiments with simply supported and clamped plates, respectively. The symbol δ_{ex} stands for the experimental central deflection and δ_{th} stands for the theoretical central deflection according to (3.85) or (3.86). The right-hand column of Tables 3.3 and 3.4 show the central deflection ratios δ_{ex}/δ_{th} which are used as a measure of the accuracy of the rigid-plastic theory. Figures 3.21 and 3.22, showing the variation of the central deflections with impulse, assist the comparison of theoretical and experimental values.

Figures 3.23 and 3.24 provide a comparison of theoretical and experimental shapes for a few simply supported plates. Figure 3.25 shows the profiles of several clamped plates; the theoretical profile is not explicitly available in the literature.

Table 3.3

EXPERIMENTAL RESULTS FOR SIMPLY SUPPORTED PLATES

Material	Experiment No.	Impulse I (lb sec/in^2)	Impulse I (dyne sec/cm^2)	Energy Ratio* R	δ_{ex}/a	δ_{th}/a	δ_{ex}/δ_{th}
Al. 6061-T6	1	0.317	21,900	76.5	0.421	1.195	0.352
	2	0.289	19,900	63.7	0.312	0.994	0.314
	3	0.288	19,900	63.3	0.344	0.989	0.348
	4	0.283	19,500	61.2	0.333	0.956	0.348
	5	0.244	16,800	45.2	0.253	0.706	0.358
	6	0.240	16,600	44.1	0.268	0.688	0.389
	7	0.240	16,600	44.1	0.261	0.688	0.380
	8	0.240	16,600	43.8	0.264	0.684	0.387
	9	0.221	15,200	37.1	0.253	0.579	0.437
	10	0.219	15,100	36.7	0.243	0.573	0.425
	11	0.192	13,200	28.1	0.199	0.438	0.455
	12	0.191	13,200	27.7	0.222	0.433	0.514
	13	0.184	12,700	25.8	0.188	0.403	0.467
	14	0.149	10,300	16.9	0.155	0.264	0.588
	15	0.144	9,900	15.8	0.152	0.247	0.615
	16	0.142	9,800	15.3	0.127	0.239	0.533
	17	0.141	9,700	15.1	0.147	0.235	0.625
	18	0.139	9,600	14.6	0.134	0.228	0.588
	19	0.136	9,400	14.1	0.122	0.221	0.551
	20	0.123	8,500	11.6	0.098	0.181	0.541
	21	0.118	8,100	10.6	0.116	0.165	0.700
	22	0.108	7,400	8.9	0.099	0.139	0.715
C.R. steel 1018	1	0.505	34,800	61.7	0.261	0.629	0.414
	2	0.501	34,600	60.8	0.251	0.620	0.410
	3	0.450	31,000	49.0	0.224	0.500	0.448
	4	0.436	30,100	46.1	0.215	0.471	0.456
	5	0.414	28,600	41.4	0.211	0.423	0.498
	6	0.359	24,800	31.3	0.193	0.319	0.603
	7	0.349	24,100	29.5	0.175	0.301	0.582
	8	0.344	23,700	28.7	0.167	0.292	0.571
	9	0.331	22,800	26.6	0.152	0.271	0.563
	10	0.314	21,600	23.9	0.135	0.243	0.553
	11	0.312	21,500	23.6	0.143	0.241	0.595
	12	0.272	18,800	17.9	0.114	0.183	0.623
	13	0.258	17,800	16.1	0.097	0.164	0.590
	14	0.215	14,800	11.2	0.077	0.114	0.674
	15	0.157	10,800	6.0	0.032	0.061	0.519
	16	0.156	10,800	5.9	0.031	0.060	0.507
	17	0.156	10,800	5.9	0.036	0.060	0.595
	18	0.153	10,600	5.6	0.045	0.058	0.786
	19	0.123	8,500	3.7	0.024	0.038	0.625
	20	0.121	8,300	3.6	0.025	0.036	0.676

*Value of Poisson's ratio is taken to be $\nu = 0.3$.

Table 3.4

EXPERIMENTAL RESULTS FOR CLAMPED PLATES

Material	Experiment No.	Impulse I (lb sec/in^2)	Impulse I (dyne sec/cm^2)	Energy Ratio R	δ_{ex}/a	δ_{th}/a	δ_{ex}/δ_{th}
Al. 6061-T6	1	0.268	18,500	55.0	0.264	0.491	0.536
	2	0.238	16,400	43.6	0.230	0.389	0.591
	3	0.238	16,400	43.6	0.229	0.389	0.589
	4	0.228	15,700	39.9	0.221	0.357	0.619
	5	0.228	15,700	39.6	0.216	0.354	0.610
	6	0.217	14,600	34.4	0.207	0.307	0.674
	7	0.202	14,000	31.4	0.185	0.281	0.658
	8	0.196	13,500	29.4	0.181	0.263	0.688
	9	0.180	12,400	24.7	0.154	0.220	0.700
	10	0.170	11,700	22.2	0.144	0.198	0.727
	11	0.162	11,200	20.1	0.134	0.180	0.744
	12	0.144	10,000	16.0	0.112	0.143	0.783
	13	0.144	9,900	15.8	0.108	0.141	0.766

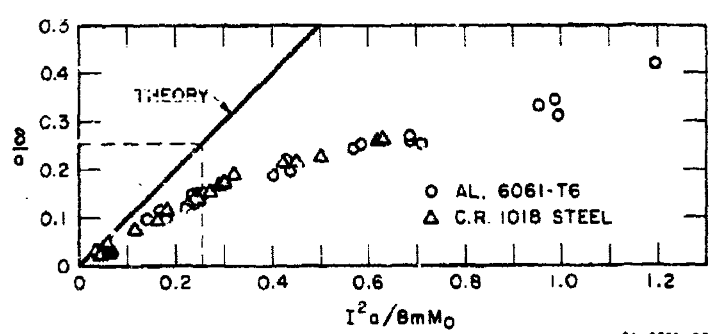

FIG. 3.21 CENTRAL DEFLECTION-IMPULSE RELATIONSHIP FOR SIMPLY SUPPORTED PLATES

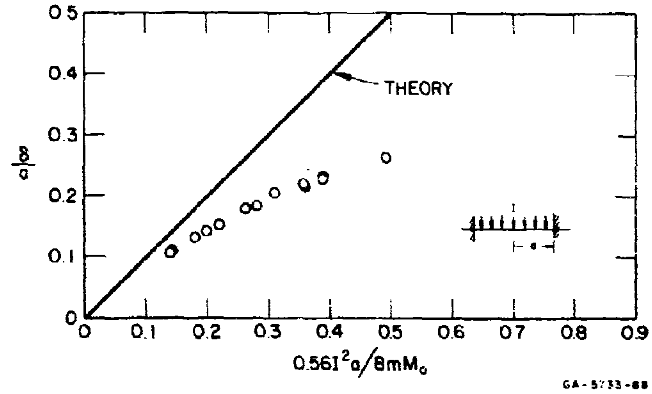

FIG. 3.22 CENTRAL DEFLECTION–IMPULSE RELATIONSHIP FOR CLAMPED PLATES

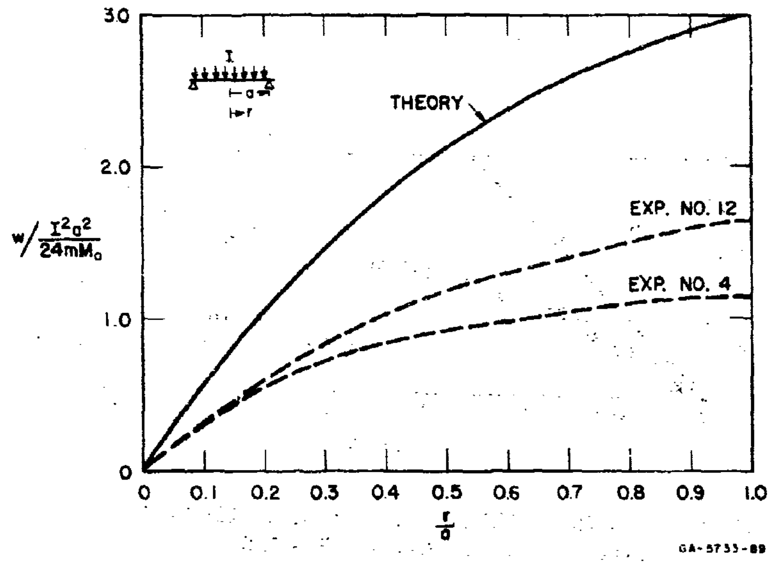

FIG. 3.23 DEFLECTION CURVES FOR SIMPLY SUPPORTED PLATES — Al. 6061–T6

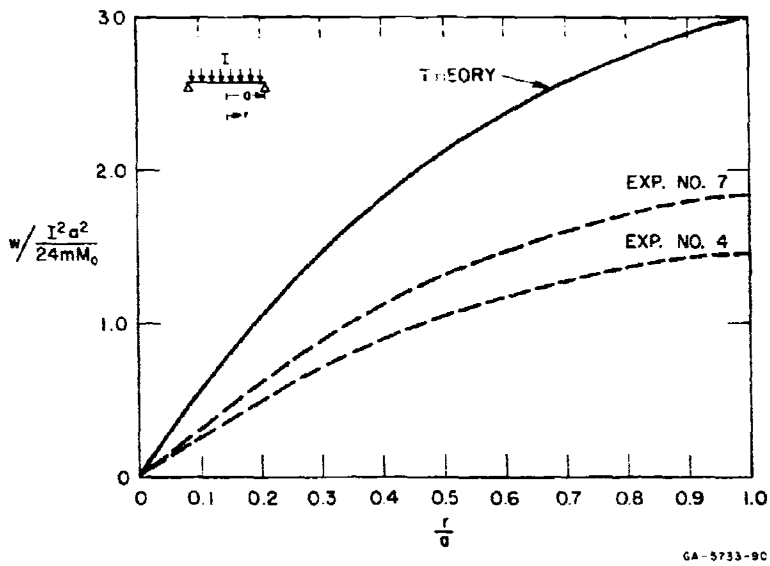

FIG. 3.24 DEFLECTION CURVES FOR SIMPLY SUPPORTED PLATES — C.R. 1018 STEEL

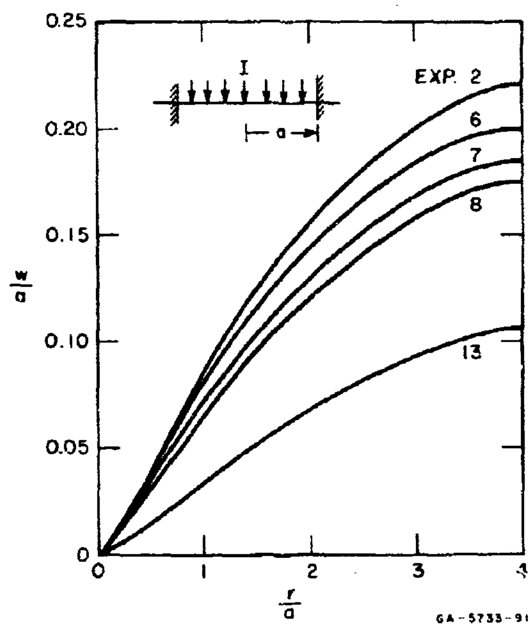

FIG. 3.25 CLAMPED PLATE PROFILES — Al. 6061–T6

Measurements of the plate thickness indicate thinning at the centers and thickening at the supports. In the series of simply supported aluminum plates, the extent of thinning increased gradually with increasing impulse to 8% at the maximum impulse. Thickening increased similarly to 6%. In the series of simply supported steel plates, the corresponding maximum values were 4% and 4%. In the series of clamped aluminum plates, the maximum values were 9% and less than 1%. The thickness changes are indications of membrane forces increasing with central deflection.

The main observation to be made is that within certain limits to be described, the rigid-plastic theory does serve as a reasonable first-order theory. The lower limit of the useful range is determined by the energy ratio R, which gives a measure of elastic effects. In the present series of experiments, minimum values of R are 9 and 4 for the simply supported aluminum and steel plates, and $R = 16$ for the clamped aluminum plates. At these values correlation is at its best, although for steel a leveling off of correlation is detectable between $R = 11$ and $R = 4$ (unfortunately the scatter is worst in this region). A reasonable guide for the lower limit of the range of applicability of the theory may be taken as $R = 4$. For the upper limit a suitable criterion is a maximum value for the ratio of the theoretical central deflection to the plate radius (a measure of the "cone angle"), suggested here as $\delta_{th}/a \approx 1/3$. Whenever $\delta_{th} < 1/3$ Tables 3.3 and 3.4 show that $\delta_{ex}/\delta_{th} > 0.5$.

It is interesting to compare Figs. 3.21 and 3.22 with Figs. 2.28 and 2.29 for beams. The main difference is that when the central deflections become large (say, $\delta_{th}/a > 1/3$) correlation deteriorates rapidly for plates but remains satisfactory for beams. This is due to the increasing significance with deflection of the plate membrane forces.

Figures 3.23 and 3.24 indicate a satisfactory prediction of the deflected shape of a simply supported plate except at the center where a discontinuity of slope is predicted. Although no theoretical shape is readily available for clamped plates, the theory[5] does predict a discontinuity of slope at the support due to the action of a stationary plastic hinge circle. The experimental evidence of a "discontinuity" of slope at the support (that is, a very rapid change of slope) is given by Figs. 3.23 and 3.24.

REFERENCES

1. Hopkins, H. G. and W. Prager, "The Load Carrying Capacities of Circular Plates," J. Mech. and Phys. of Solids 2, 1-13, 1953.

2. Hopkins, H. G. and W. Prager, "On the Dynamics of Plastic Circular Plates," Zeitschrift fur Angewandte Mathematik and Physik 5, 317-330, 1954.

3. Florence, A. L., "Clamped Circular Rigid-Plastic Plates under Central Blast Loading," Int. Journ. Solids and Structures 2, 319-335, 1966.

4. Wang, A. J., "The Permanent Deflection of a Plastic Plate under Blast Loading," J. Appl. Mech. 22, 375-376, 1955.

5. Wang, A. J. and H. G. Hopkins, "On the Plastic Deformation of Built-in Circular Plates under Impulsive Loading," J Mech. and Phys. of Solids 3, 22-37, 1954.

6. Shapiro, G. S., "On a Rigid-Plastic Annular Plate under Impulse Load," Prikl. Mat. Mekh. 23, 172-175, 1959.

7. Florence, A. L., "Annular Plate under a Transverse Line Impulse," AIAA Journ. 3, 1726-1732, 1965.

8. Florence, A. L., "Circular Plate under a Uniformly Distributed Impulse," Int. Journ. Solids and Structures 2, 37-47, 1966.

9. Hodge, P. G., Jr., Plastic Analysis of Structures, McGraw-Hill Book Co., Inc., New York, 1959.

10. Hodge, P. G., Jr., Limit Analysis of Rotationally Symmetric Plates and Shells, Prentice-Hall, Inc., Englewood Cliffs, New Jersey, 1963.

11. Florence, A. L., "Clamped Circular Rigid-Plastic Plates under Blast Loading," J. Appl. Mech. 33, 256-260, 1966.

12. Florence, A. L., "Traveling Force on a Timoshenko Beam," J. Appl. Mech. 32, 351-358, 1965.

CHAPTER 4

DYNAMIC ELASTIC AND PLASTIC PULSE BUCKLING OF BARS

by

H. E. Lindberg

4.1 Introduction

For about a century it has been recognized that structures, particularly those made from high-strength alloys, must be designed to resist static buckling from high compressive stresses. However, buckling from dynamic loads has received serious attention only since World War II, and only within the last 10 years has a basic understanding of buckling under explosive loads been developed. This development followed closely the introduction of high-speed electronic and photographic instrumentation to observe such buckling, which can occur in a small fraction of a millisecond. The present chapter gives the fundamentals of dynamic buckling using a simple pinned bar to give the theory in its simplest possible form. In Chapter 5 this theory is applied to cylindrical shells under radial pressure pulses.

Physical evidence of dynamic buckling can take on very different aspects, depending upon the nature of the applied load. This is illustrated in Fig. 4.1, which shows two identical simple columns subjected to axial loads with differing time histories. In the column on the left the peak load is less than the static buckling load, but it oscillates at a critical frequency that induces large growth of lateral vibrations. The critical relation between the load frequency Ω and the natural frequency ω of the bar is $\Omega = 2\omega$. In the column on the right, the load is much greater than the static buckling load but it is applied for only a short time. Under such a load the bar deforms monontonically into a very high order pattern with no oscillations. The critical condition in this case is a duration of load application sufficiently long to produce plastic bending strains or excessively large displacements.

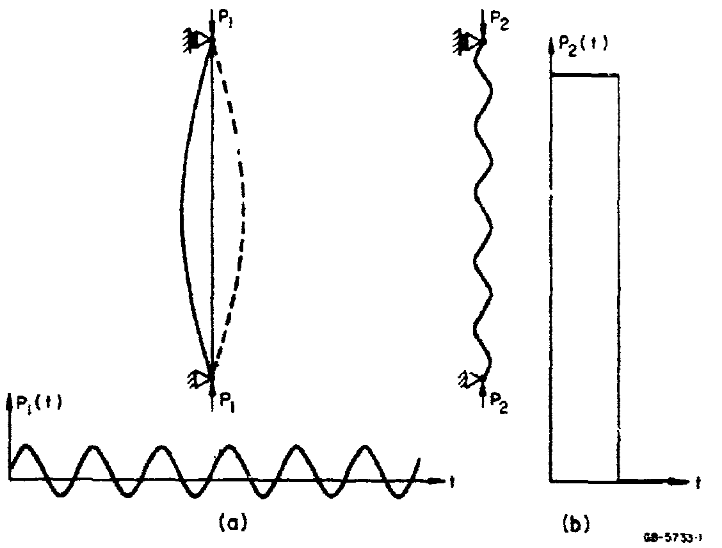

FIG. 4.1 VIBRATION BUCKLING AND PULSE BUCKLING

In the mathematical formulation of both of these problems, the underlying feature is the appearance of a parameter involving the load that multiplies the lateral displacement. Thus, dynamic buckling can be defined as dynamic response of structural systems induced by time-varying parametric loading. Both problems in Fig. 4.1 fall within this definition. However, problems involving parametric oscillations, as in the bar on the left, have a somewhat longer historical background than problems involving monotonic parametric growth, as in the bar on the right. Consequently, the terms dynamic buckling and dynamic stability were first associated with oscillation problems. This association was accentuated by the appearance in 1956 of a book by V. V. Bolotin[1] in which he defined "the theory of the dynamic stability of elastic systems as the study of vibrations induced by pulsating parametric loading." However, as more work is done on buckling from single pulses, the term dynamic buckling is taking on the more general definition adopted here.

Nevertheless, it is still useful to divide dynamic buckling problems into two groups, corresponding to the two examples in Fig. 4.1, because to a large extent oscillation problems are associated with conventional vibration analysis, while single pulse problems are associated with impact and explosive loads. These two types of buckling can therefore be appropriately called vibration buckling and pulse buckling. Chapters 4 and 5 are concerned almost entirely with pulse buckling. A detailed account of vibration buckling is given in the book by Bolotin.

Since pulse buckling is so very different from static buckling, before the detailed theory is given it is illustrative to examine the forms of buckling to be considered. Several structural elements buckled from pulse loads are shown in Fig. 4.2. A common feature in all these examples is that the buckling is in very high order modes. This is a consequence of the extremely high membrane stresses induced by intense pulse loads. The first three examples (Figs. 4.2a, b, c) are of very thin structures in which plastic bending has taken place in a pattern established by initial dynamic elastic buckling motion. The thin strip in Fig. 4.2a was buckled from a 40,000-psi elastic stress wave eminating from a jaw gripping the left end. The thin cylinder (radius-to-thickness ratio a/h = 480) in Fig. 4.2b was rolled from sheet metal of the same thickness as the strip in Fig, 4.2a and was subjected to an impulsive radial pressure which produced a hoop stress approximately equal to the compressive stress applied to the thin strip. The wavelengths of the buckles are about the same as in the buckled strip. These lengths correspond to harmonics having from 50 to 100 waves around the circumference. Figure 4.2c shows a similar thin cylinder (a/h = 550) photographed while buckling from an elastic impact at the lower end which gave an axial stress 1.5 times the classical static buckling stress. The axial wavelengths of the buckles are an order of magnitude smaller than those in large deflection static buckling, and the circumferential-to-axial aspect ratio of the buckles near the impacted end averages about 3:1 compared to about 1:1 in static buckling.

The other three examples of buckling in Fig. 4.2 show the forms which result when the compressive stress is beyond the yield stress and buckling takes place during plastic flow. The solid aluminum rod in Fig. 4.2d was impacted at its left end at a velocity of about 500 ft/sec.

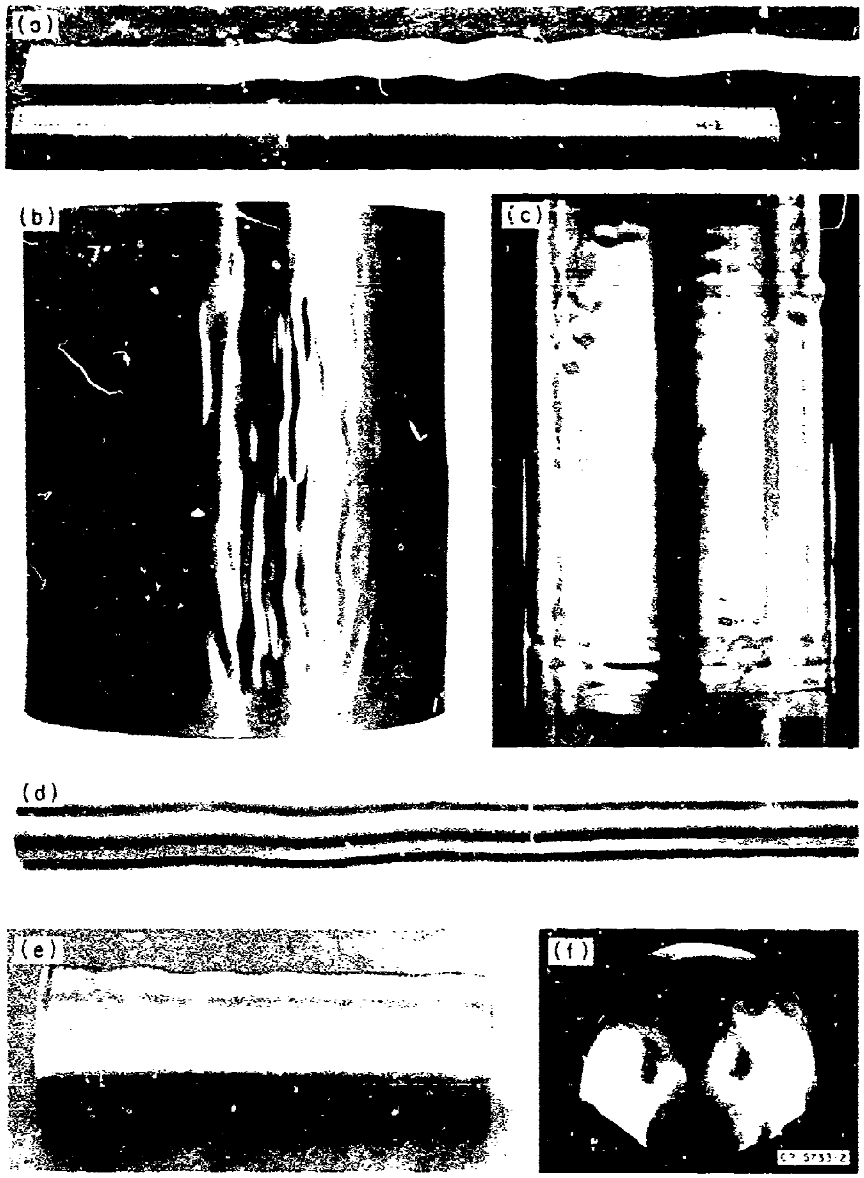

FIG. 4.2 EXAMPLES OF DYNAMIC PULSE BUCKLING

The buckles here are much shorter in comparison to the lateral dimension of the bar than those in the elastically buckled strip in Fig. 4.2a. This is because during plastic flow resistance to flexure is governed by the tangent modulus, which is of the order of 100 times smaller than the elastic modulus. Figure 4.2e shows a relatively thick ($a/h \approx 5$) cylindrical shell buckled in an axisymmetric pattern, again during dynamic axial plastic flow. The hemispherical shell in Fig. 4.2f was subjected to an intense impulsive external pressure causing dynamic plastic flow in two dimensions. Over the top of the hemisphere the shell is buckled into a dimpled pattern from the combined flow. Around the edges, where the flow is similar to that in a cylindrical shell, under radial impulse, a one-dimensional wave pattern again appears.

These examples demonstrate that dynamic forms of buckling can be very different from static forms. The corresponding theories must therefore reveal the mode of buckling in addition to predicting the pulse amplitude and impulse that produce buckling. The theories developed in the following pages are motivated by experimental observations and are compared to experimental results. Simply supported bars are treated first in order to give the essential concepts in their simplest form. To relate the dynamic and static problems, static elastic and plastic theories are summarized before the dynamic theory is given. In Chapter 5 the dynamic concepts are applied to cylindrical shells under radial pressure pulses.

4.2 Equations of Motion

The simplest problem in elastic buckling is that of a simply supported uniform bar under axial compression, as in Fig. 4.3. The bar is of length L and supports an axial compressive force P. Its cross section is uniform with axial distance x, measured from one end.

Deflection y is taken positive downward, and is measured from an unstressed initial deflection $y_o(x)$. An element of length dx between two cross sections taken normal to the original (undeflected) axis of the beam is shown in Fig. 4.3b. The shearing force V and bending moment M acting on the sides of the element are taken positive in the directions shown. The inertia force acting on the element is $\rho A(\partial^2 y/\partial t^2)dx$, where ρ is density of the bar, A is the area of the cross section, and t is time.

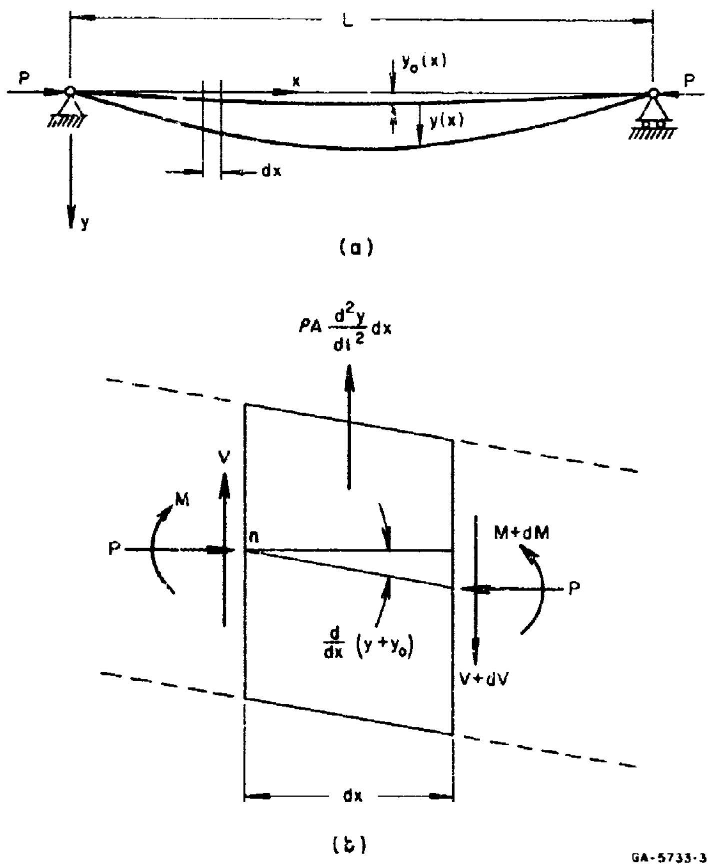

FIG. 4.3 BAR NOMENCLATURE AND ELEMENT OF LENGTH

The basic equations for the analysis of bar buckling are derived from dynamic equilibrium of the element in Fig. 4.3b and the moment-curvature relation for the bar. Summing forces in the y direction gives

$$- V - \rho A \frac{\partial^2 y}{\partial t^2} dx + (V + dV) = 0$$

or

$$\rho A \frac{\partial^2 y}{\partial t^2} = \frac{dV}{dx} \qquad (4.1)$$

Taking moments about point n and neglecting rotary inertia of the element results in

$$M - \rho A \frac{\partial^2 y}{\partial t^2} dx \frac{dx}{2} + (V + dV)dx - (M + dM) + P \frac{\partial}{\partial x} (y + y_o)dx = 0$$

Terms of second order are neglected, reducing this equation to

$$V = \frac{\partial M}{\partial x} - P \frac{\partial}{\partial x} (y + y_o) \qquad (4.2)$$

If the effects of shear deformations and shortening of the beam axis are neglected, the curvature of the bar axis is related to the bending moment by

$$EI \frac{\partial^2 y}{\partial x^2} = - M \qquad (4.3)$$

in which E is Young's modulus and I is the moment of inertia of the bar section, assumed symmetric about the xy plane (otherwise the bar would twist in addition to bending). The differential equation for the deflection of the beam axis is found by differentiating (4.2) and then eliminating V by means of (4.1) and M by means of (4.3) twice differentiated. The result is

$$EI \frac{\partial^4 y}{\partial x^4} + P \frac{\partial^2}{\partial x^2} (y + y_o) + \rho A \frac{\partial^2 y}{\partial t^2} = 0 \qquad (4.4)$$

4.3 Static Elastic Buckling of a Bar

For static buckling, the inertia term is neglected and (4.4) becomes

$$EI \frac{d^4 y}{dx^4} + P \frac{d^2 y}{dx^2} = - P \frac{d^2 y_o}{dx^2}$$

or, substituting $k^2 = P/EI$,

$$\frac{d^4 y}{dx^4} + k^2 \frac{d^2 y}{dx^2} = - k^2 \frac{d^2 y_o}{dx^2} \qquad (4.5)$$

If we consider first a bar with no initial deflection, we need only the general solution to the homogeneous equation (with $y_o(x) = 0$). This solution is

$$y = A \sin kx + B \cos kx + Cx + D \qquad (4.6)$$

For a simply supported bar the deflection and bending moment are zero at the ends and the boundary conditions are

$$y = \frac{d^2 y}{dx^2} = 0 \quad \text{at} \quad x = 0 \quad \text{and} \quad x = L \qquad (4.7)$$

Applying these to (4.6) gives

$$B = C = D = 0 \quad , \quad \sin kL = 0$$

and therefore

$$kL = \pm n\pi$$

where n is an integer. Using the definition of k, this becomes an equation for P.

$$P_n = \frac{\pi^2 EI}{L^2} \cdot n^2 \tag{4.8}$$

Thus, with no initial deflection, only discrete values of P give a nontrivial solution, and the magnitude A of the deflection is undetermined.

Before discussing these solutions further, let us treat the bar having an initial shape $y_o(x)$. The solution for the perfectly straight bar suggests that $y_o(x)$ should be expressed by the Fourier sine series

$$y_o(x) = \sum_{n=1}^{\infty} a_n \sin \frac{n\pi x}{L} \tag{4.9}$$

The coefficients in this series are found from

$$a_n = \frac{2}{L} \int_o^L y_o(x) \sin \frac{n\pi x}{L} \, dx \tag{4.10}$$

Substituting (4.9) into (4.5) gives the following differential equation for the imperfect bar.

$$\frac{d^4 y}{dx^4} + k^2 \frac{d^2 y}{dx^2} = k^2 \frac{n^2 \pi^2}{L^2} a_n \sin \frac{n\pi x}{L} \tag{4.11}$$

To find a particular solution, we take

$$y_P = \sum_{n=1}^{\infty} A_n \sin \frac{n\pi x}{L} \tag{4.12}$$

When this is substituted into (4.11), the coefficients A_n are found to be

$$A_n = \frac{-k^2 a_n}{k^2 - n^2 \pi^2 / L^2} = \frac{- Pa_n}{P - P_n} \tag{4.13}$$

The complete solution is then

$$y = A \sin kx + B \cos kx + Cx + D - \sum_{n=1}^{\infty} \frac{Pa_n}{P - P_n} \sin \frac{n\pi x}{L} \qquad (4.14)$$

Since P, and hence k, is arbitrary, application of the boundary conditions (4.7) gives $A = B = C = D = 0$ and the general solution is simply

$$y = -\sum_{n=1}^{\infty} \frac{Pa_n}{P - P_n} \sin \frac{n\pi x}{L} \qquad (4.15)$$

From this solution we see that the deflection becomes arbitrarily large as P approaches the critical loads P_n given by (4.8). However, the dynamic solution given in subsequent sections shows that the motion is unstable for <u>any</u> load greater than the lowest critical load P_1, which, from (4.8), is given by

$$P_1 = \frac{\pi^2 EI}{L^2} \qquad (4.16)$$

In the neighborhood of $P = P_1$ the first term dominates the deflection. Neglecting the higher terms, the midspan deflection for $P < P_1$ is given approximately by

$$\delta = y(L/2) \approx \frac{-Pa_1}{P - P_1} \qquad (4.17)$$

Figure 4.4a gives a plot of deflection δ from (4.17) versus end load P. On the basis of this formula, Southwell[2] suggested that the critical load P_1 could be extracted from test data by plotting δ/P versus δ. In this form, (4.17) becomes

$$\frac{\delta}{P} = \frac{1}{P_1} (\delta + a_1) \qquad (4.18)$$

which gives the straight line in Fig. 4.4b. The inverse of the slope gives the critical load P_1 and the δ intercept gives the coefficient a_1 as shown.

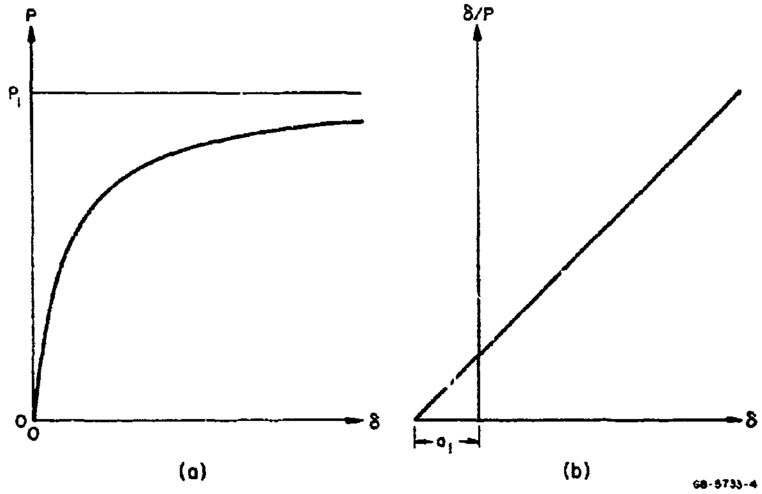

FIG. 4.4 FORCE-DEFLECTION CURVE AND SOUTHWELL PLOT FOR SMALL DEFLECTION ELASTIC BUCKLING

If the bar is treated as initially perfectly straight but subjected to an eccentrically placed load, the Southwell procedure can still be used to determine the critical load. Consider, for example, that the load is displaced from the centroidal axis by an amount ε, equal at both ends. This can be treated as a bar having an initial displacement given by

$$y_o(x) = \varepsilon \qquad x \neq 0,\ L$$
$$= 0 \qquad x = 0,\ L \tag{4.19}$$

Substituting this displacement into (4.10), the coefficient of the first term in its Fourier expansion is

$$a_1 = \frac{4\varepsilon}{\pi} \tag{4.20}$$

Thus, for P in the neighborhood of P_1 the Southwell plot is as described previously, and the δ intercept is now $4\varepsilon/\pi$. If the bar is considered to have both an initial shape and some eccentricity, (4.18) becomes

$$\frac{\delta}{P} = \frac{1}{P_1}\left[\delta + \left(a_1 + \frac{4\varepsilon}{\pi}\right)\right] \quad (4.21)$$

For real columns, in which both a_1 and ε are small and difficult to measure, there is therefore no way of telling in a Southwell plot how much of the deflection is caused by load eccentricity and how much is caused by an initial deflection. In experiments run near the turn of the century,[3-5] it was found that the experimental buckling deflections could be calculated,* on the average, using values of equivalent eccentricity given by

$$\varepsilon = 0.06\, r^2/c \quad (4.22)$$

where r^2/c is the core radius of the cross section, r being the radius of gyration and c being the distance from the elastic axis to the outermost fiber. For a rectangular bar of depth h, this gives $\varepsilon = 0.01\, h$. In long columns, it is reasonable to assume that initial imperfections in shape become more important and these can be expected to depend on the length of the column. On this basis, Salmon[6] found that, although equivalent imperfections from a large collection of experimental results scattered by an order of magnitude at any given length, both the average amplitude of the imperfections and the range of amplitudes increased in proportion to the length of the bars. For the longer columns, almost all imperfections were in the band

$$0.0001 < \frac{a_1}{L} < 0.001 \quad (4.23)$$

Several authors have proposed that imperfections depending on both the core radius and the column length can be expected to be present.

*For short columns, these calculations take into account plastic deformation, discussed in the next section.

They suggest that a conservative estimate for an equivalent deflection including both types of imperfections can be taken as

$$a_1 = 0.1\, r^2/c + \frac{L}{750} \tag{4.24}$$

In the dynamic problems in subsequent sections, we will see that the range of normalized imperfections found in static buckling give reasonably good agreement with values observed in dynamic buckling.

4.4 Static Plastic Buckling of Bars

If we consider a sequence of simply supported bars of fixed cross section but with decreasing length, the maximum load each bar can sustain before elastic buckling, from (4.16), increases as $P_1 = \pi^2 EI/L^2$. The corresponding stress is

$$\sigma_c = \frac{P_1}{A} = \pi^2 E\left(\frac{r}{L}\right)^2 \tag{4.25}$$

where the slenderness ratio L/r is the ratio between the bar length and the radius of gyration of the cross section. As this ratio becomes smaller, the compressive buckling stress from (4.25) increases and eventually approaches the yield stress σ_y of the bar material. Thus we would expect plastic effects to become important at slenderness ratios smaller than about

$$\frac{L}{r} = \pi\left(\frac{E}{\sigma_y}\right)^{1/2} = \frac{\pi}{\left(\epsilon_y\right)^{1/2}} \tag{4.26}$$

where ϵ_y is the yield strain. For example, 6061-T6 aluminum has a yield stress near $\sigma_y = 40{,}000$ psi which, with $E = 10 \times 10^6$ psi, gives a yield strain of 0.004. From (4.26), plastic behavior would be expected to become important in this material for slenderness ratios smaller than $L/r = 50$. For structural steel, $\sigma_y = 45{,}000$ psi, $E = 30 \times 10^6$ psi, and therefore $\epsilon_y = 0.0015$, and so plastic effects must be considered for slenderness ratios as large as $L/r = 80$. Generally speaking, bars or columns with $L/r > 100$ are called slender columns and buckling is predicted quite well by the elastic theory. Columns with $L/r < 50$ are called short columns, and plastic effects must generally be considered.

In addition to reducing the load that the bar could otherwise carry, plastic deformations change the basic character of the load-deflection curve. This is illustrated in Fig. 4.5, which gives load-deflection curves (in terms of average stress across the bar) calculated for a simply supported steel column having several values of load eccentricity.[7] In contrast to the monotonic increase in load with deflection typical of elastic buckling (Fig. 4.4), the plastic buckling curves exhibit a maximum value of load. A further increase in deflection is accompanied by a decrease in load. Thus, there is a range of loads below the maximum which have two equilibrium deflections, the smaller one being stable and the larger one unstable. Near the maximum, it is possible for small disturbances to cause the deflection to move from the stable to the unstable branch and hence to still larger displacements. Such sudden jumps in displacement are actually observed in plastic buckling experiments and account for the wide scatter in observed plastic buckling loads compared to those in elastic buckling. Figure 4.5 shows that small changes in imperfections, represented here by load eccentricity, can cause significant changes in the critical load.

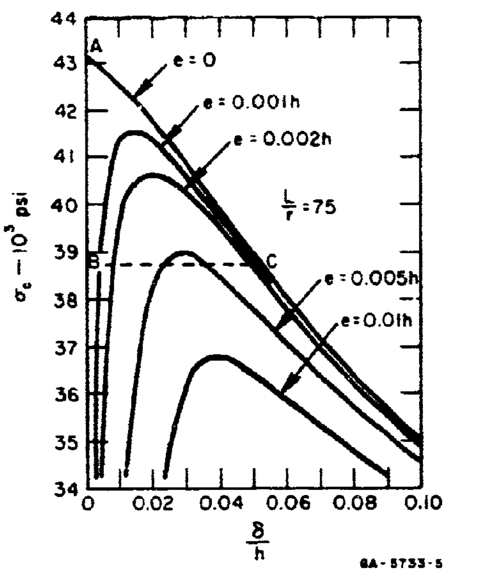

FIG. 4.5 COMPRESSIVE STRESS-DEFLECTION CURVES FOR PLASTIC BUCKLING

To develop a theory for plastic buckling, we must return to the relationship between bending moment and curvature and examine the influence of axial force and plastic strains on this relationship. As in elastic buckling, plane cross sections are assumed to remain plane as the bar bends so that axial strains vary linearly across the bar. An element of bar under this assumption with its neutral axis bent to a radius of curvature ρ is shown in Fig. 4.6. In the absence of compressive forces, the strain at a fiber located a distance z from the neutral axis is

$$\varepsilon = \frac{z}{\rho} \tag{4.27}$$

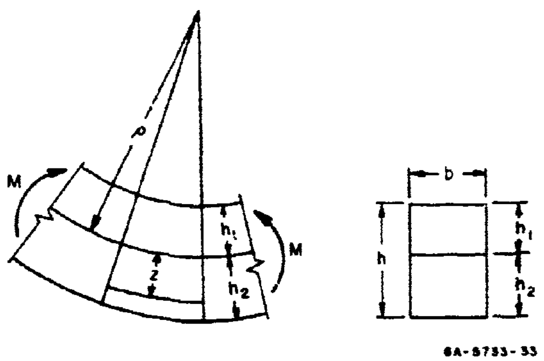

FIG. 4.6 ELEMENT OF FLEXED BAR

If, in addition to the bending moment M which produces this curvature, the section also sustains an axial compressive force P, each fiber is additionally compressed so that the total strain is

$$\varepsilon = \frac{z}{\rho} + \varepsilon_c \tag{4.28}$$

The resulting stress distribution across the section is given in Fig. 4.7, in which it is assumed that the stress-strain curve is the same as in a simple tension-compression test.

In the following, let us consider a simple rectangular bar of depth h and width b. To find the relation between the strain quantities ε_c and $\Delta = h/\rho$ and the loads P and M, the stress distribution across the section must be integrated. The compressive load P is

$$P = -b \int_{-h/2}^{h/2} \sigma dz \tag{4.29}$$

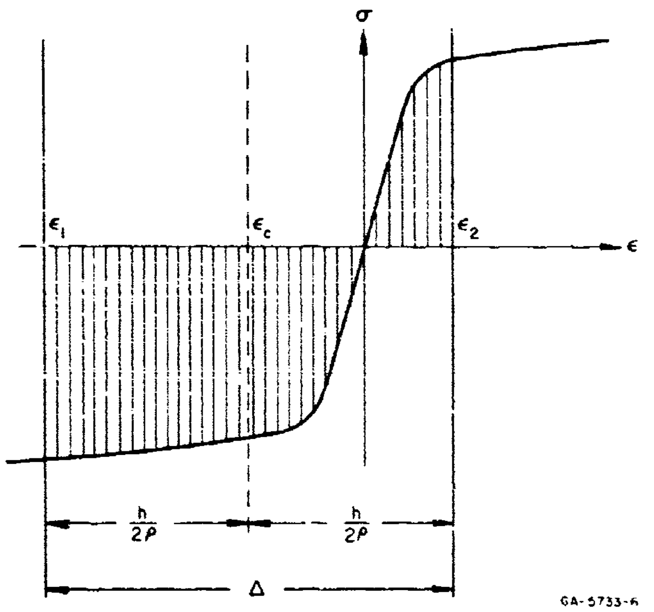

FIG. 4.7 STRESS DISTRIBUTION UNDER PLASTIC THRUST AND FLEXURE

Since σ is known as a function of strain ϵ, it is convenient to change the variable of integration in (4.29), using (4.28) in the form

$$z = \rho(\epsilon - e_c) \quad , \quad dz = \rho d\epsilon \tag{4.30}$$

In terms of strain, (4.29) is then

$$P = - b\rho \int_{\epsilon_1}^{\epsilon_2} \sigma d\epsilon = - \frac{bh}{\Delta} \int_{\epsilon_1}^{\epsilon_2} \sigma d\epsilon \tag{4.31}$$

This integral represents the net area under the shaded portion of the stress-strain curve in Fig. 4.7, multiplied by an appropriate quantity to give total force, positive when compressive.

The bending moment about the ce oidal axis is

$$M = b \int_{-h/2}^{h/2} \sigma y\,dy \tag{4.32}$$

which, using (4.30) and $\Delta = h/\rho$ and $I = bh^3/12$, becomes

$$M = b\rho^2 \int_{\epsilon_1}^{\epsilon_2} (\epsilon - \epsilon_o)\sigma d\epsilon = \frac{12I}{\rho\Delta^3} \int_{\epsilon_1}^{\epsilon_2} (\epsilon - \epsilon_o)\sigma d\epsilon \tag{4.33}$$

This integral is the first moment of the shaded area of the stress-strain diagram (Fig. 4.7) about the vertical dotted axis. Equation (4.33) can be represented in the form

$$M = \frac{E''I}{\rho} = E''I \frac{d^2v}{dx^2} \tag{4.34}$$

where

$$E'' = \frac{12}{\Delta^3} \int_{\epsilon_1}^{\epsilon_2} (\epsilon - \epsilon_o)\sigma d\epsilon \tag{4.35}$$

If the material is elastic, then $\sigma = E\epsilon$ and (4.35) gives $E'' = E$ so that the moment-curvature relation (4.34) reduces to the elastic form given in (4.3).

Load deflection curves such as those in Fig. 4.5 are generated using the load-strain relations just developed. This must be done numerically, because even for the simplest nonlinear stress-strain law no analytical expressions can be written to allow direct calculation of deflection for a given load. Instead, the bar is broken up into a number of longitudinal segments of length Δx. Values for ϵ_1 and ϵ_2 at the center of the bar are chosen and from these P, M, and the radius of curvature ρ are calculated. Since P and M are known, the sum δ_o of the central deflection plus eccentricity is calculated from $\delta_o \equiv \delta + e = M/P$. Then, assuming the element Δx is a circular arc of radius ρ, the displacement and moment at the next element toward the support are calculated. These are used, with a curve of M vs. h/ρ at constant P (generated using (4.31) and (4.33)), to calculate ρ for the next element. Proceeding in this way to the pinned support, the total deflection δ between the center of the bar and the support is calculated. Finally, the eccentricity corresponding to the originally assumed ε_1 and ε_2 at the center of the bar is $\epsilon = \delta_o - \delta$. This procedure is repeated for many values of ε_1 and ε_2 until curves can be drawn of P vs. δ for various ϵ as in Fig. 4.5.

Bounds for the maximum possible buckling load for a perfectly straight bar having no load eccentricity (corresponding to point A in Fig. 4.5) can be obtained very simply. To find these bounds we need be concerned only with small perturbations in displacement of the perfectly straight bar under thrust. It is assumed that up to the point of buckling the increasing stress is uniform throughout the section. The upper bound is found by assuming the load is constant as the influence of a flexural perturbation is examined. The lower bound is found by assuming that the load continuously increases as the flexural perturbation is applied. Arguments that these procedures yield upper and lower bounds have been given by Shanley.[8]

If we treat the load as constant as the perturbation in flexure is allowed, the small bending stresses, superimposed on the direct stresses from the compressive load, are distributed through the cross section as depicted in Fig. 4.8b. At the fiber on the concave side of the bar the compressive strain increases and moves out along the loading curve from point A to point B in Fig. 4.8a. For small strain increments, this increase in compressive stress can be associated with the tangent modulus E_t. In the fiber on the convex side of the bar, the strain increment is tensile and is accompanied by unloading, from point A to point C in Fig. 4.8a, along the elastic modulus E. Since the compressive load is assumed constant, the net force from the flexural stress distribution in Fig. 4.8b must be zero. For the rectangular cross section being considered here, this condition gives

$$E_t h_1^2 = E h_2^2 \tag{4.36}$$

In terms of the total depth $h = h_1 + h_2$, we then obtain

$$h_1 = \frac{h\sqrt{E}}{\sqrt{E} + \sqrt{E_t}} \quad , \quad h_2 = \frac{h\sqrt{E_t}}{\sqrt{E} + \sqrt{E_t}} \tag{4.37}$$

Taking the first moment of the area in Fig. 4.8b, the bending moment M for the rectangular cross section of width b is

$$M = \frac{Eh_1}{\rho} \frac{h_1}{2} \frac{2}{3} hb = \frac{bh^3}{12\rho} \frac{4E\, E_t}{\left(\sqrt{E} + \sqrt{E_t}\right)^2} \tag{4.38}$$

This equation is analogous to Eq. (4.3) for elastic bending (noting that $1/\rho \approx d^2y/dx^2$) with the elastic modulus E being replaced by a reduced modulus E_r given by

$$E_r = \frac{4E\, E_t}{\left(\sqrt{E} + \sqrt{E_t}\right)^2} \tag{4.39}$$

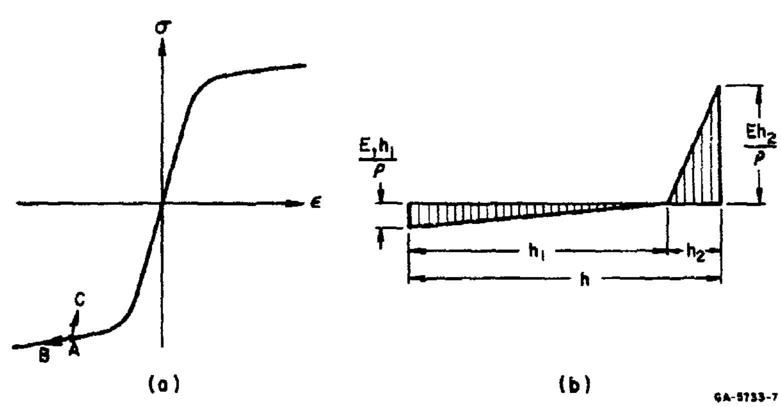

FIG. 4.8 MOMENT-PRODUCING STRESSES FOR FLEXURE UNDER CONSTANT THRUST

Thus, in place of (4.3), the moment curvature relation is now

$$M = \frac{E_r I}{\rho} = -E_r I \frac{d^2y}{dx^2} \tag{4.40}$$

The remaining equations are the same as in elastic buckling, so that for a simply supported bar the critical load is given by (4.16) with E replaced by E_r:

$$P_r = \frac{\pi^2 E_r I}{L^2} \tag{4.41}$$

This theory is called the von Karman reduced modulus theory. From the derivation of E_r it can be seen that the reduced modulus depends not only on the material properties but also on the shape of the cross section. For example, in an idealized I beam, in which it is assumed that one-half of the cross section is concentrated in each flange, the reduced modulus is

$$E_r = \frac{2E\ E_t}{E + E_t} \tag{4.42}$$

If, instead of taking the load to be constant as the bar flexes, it is assumed that the load is steadily increased as in a testing machine, a lower effective modulus is obtained. In the initial stages of buckling the increase in load produces a strain which overrides the decrease in strain on the convex side of the column. Thus all points throughout the cross section lie on the loading stress-strain curve, as depicted in Fig. 4.9a. The state at the centroidal axis is at point A, and points B and C, corresponding to the outer fibers on the concave and convex sides of the column, lead and lag point A because of the flexure. All three points move out along the stress-strain curve as the motion proceeds. In this case the effective modulus is simply E_t and the buckling load for a simply supported column of any cross section is

$$P_t = \frac{\pi^2 E_t I}{L^2} \tag{4.43}$$

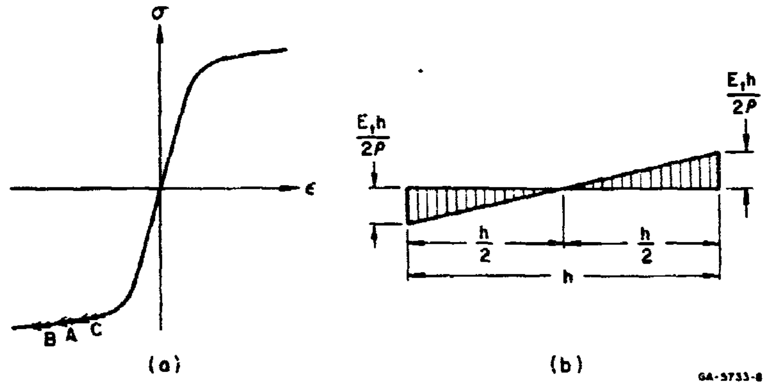

FIG. 4.9 MOMENT-PRODUCING STRESSES FOR FLEXURE UNDER INCREASING THRUST

This theory is called the Shanley tangent modulus theory. Since E_t is always smaller than E_r, Shanley proposed that it be used as a conservative estimate for plastic buckling. Critical loads calculated using E_t agree well with data from experiments run on circular and rectangular aluminum bars[9,10] with L/r ranging from 20 to 100. Since for many engineering metals both E_r and E_t decrease rapidly with very little increase in stress, the difference in critical loads from the two theories is usually small.

4.5 Dynamic Elastic Buckling of a Simply Supported Bar

The static buckling considered in the preceding sections was concerned with the steady load that can be safely carried by a column or bar. If, instead, a load is suddenly applied and then removed, as in striking a nail, the maximum load can far exceed the static buckling load without inducing objectionably large strains or deflections. On the other hand, oscillatory forces such as from reciprocating or unbalanced machinery, even while producing loads smaller than the static buckling load, can nevertheless produce objectionably large deflections if the frequency of oscillation bears a critical relation to the natural frequency of the column. Both of these problems involve dynamic buckling.

As discussed in the introduction, the impact of a nail is a pulse buckling problem, whereas a column under an oscillatory load is a vibration buckling problem. In the remainder of this chapter we will examine several examples of elastic and plastic pulse buckling of bars.

In the pulse problem loads can be applied with no appreciable buckling right up to and beyond the elastic limit, provided only that they are applied for a short enough time. Because of this feature in the dynamic problem, rather than asking for the maximum load that can be carried, we specify a load and ask for the response. Knowing how the buckling grows with time, the maximum duration for which the given load can safely be applied is then determined. In Chapter 5 this procedure will be applied to more general problems in which the load varies continuously with time.

Consider first a simply supported bar under a compressive load P, uniform throughout its length as shown in Fig. 4.3. The force P may be much larger than the critical Euler load P_1 but, for the present, the average compressive stress is assumed to be within the elastic limit. To keep the bar from buckling during application of the load P, imagine that it is supported all along its length by lateral constraining blocks.* Then, at time $t = 0$, the blocks are suddenly removed and buckling motion begins. The motion is governed by Eq. (4.4), repeated here.

$$EI \frac{\partial^4 y}{\partial x^4} + P \frac{\partial^2}{\partial x^2} (y + y_o) + \rho A \frac{\partial^2 y}{\partial t^2} = 0 \qquad (4.44)$$

After dividing through by EI, it is convenient to introduce the parameters

$$k^2 = \frac{P}{EI} , \quad r^2 = \frac{I}{A} , \quad c^2 = \frac{E}{\rho} \qquad (4.45)$$

*In practice, the load is suddenly communicated to the bar by an axial stress wave (or waves). Effects of these waves are small as will be seen in Section 4.3.

The first two parameters have already appeared in the static problem. The new parameter, appearing because of the dynamic inertia term, is the wave speed of longitudinal stress waves in the bar.[11] Using these quantities, the equation of motion (4.44) becomes

$$\frac{\partial^4 y}{\partial x^4} + k^2 \frac{\partial^2 y}{\partial x^2} + \frac{1}{r^2 c^2} \frac{\partial^2 y}{\partial t^2} = - k^2 \frac{\partial^2 y_o}{\partial x^2} \tag{4.46}$$

As in the static problem, the boundary conditions of zero moment and displacement at the ends of the bar give

$$y = \frac{\partial^2 y}{\partial x^2} = 0 \quad \text{at} \quad x = 0 \quad \text{and} \quad x = L \tag{4.47}$$

The solution to (4.46) subject to boundary conditions (4.47), as in the static problem, can be expressed by a Fourier sine series in x. Thus, we assume a product solution

$$y(x,t) = \sum_{n=1}^{\infty} q_n(\tau) \sin \frac{n\pi x}{L} \tag{4.48}$$

The initial displacement $y_o(x)$ is also expressed in series form by

$$y_o(x,t) = \sum_{n=1}^{\infty} A_n \sin \frac{n\pi x}{L} \tag{4.49}$$

where the coefficients can be found from

$$A_n = \frac{2}{L} \int_o^L y_o(x) \sin \frac{n\pi x}{L}\, dx \tag{4.50}$$

Equations (4.48) and (4.49) are now substituted into (4.46) to give the following equation of motion for the Fourier coefficients $q_n(t)$:

$$\left(\frac{n^4\pi^4}{L^4} - k^2 \frac{n^2\pi^2}{L^2}\right) q_n + \frac{1}{r^2 c^2} \ddot{q}_n = k^2 \frac{n^2\pi^2}{L^2} A_n \tag{4.51}$$

which, rearranging to the more standard form, becomes

$$\ddot{q}_n + \frac{r^2c^2n^2\pi^2}{L^2}\left(\frac{n^2\pi^2}{L^2} - k^2\right)q_n = r^2k^2c^2 \cdot \frac{n^2\pi^2}{L^2} A_n \qquad (4.52)$$

One of the principal points of the theory of dynamic buckling to be discussed in this volume appears here. The nature of the solutions to Eq. (4.52) depends upon the sign of the coefficient of q_n. If $n\pi/L < k$, this coefficient is negative and the solutions are hyperbolic; if $n\pi/L > k$, this coefficient is positive and the solutions are trigonometric. Thus, if the mode numbers n are sufficiently large, $n > kL/\pi$, the displacements are trigonometric and therefore bounded. However, over the lower range of mode numbers, $n < kL/\pi$, the hyperbolic solutions grow exponentially with time and have the potential of greatly amplifying small initial imperfections. These modes are therefore called the "buckling modes."

The mode number $n = kL/\pi$, separating the trigonometric and hyperbolic solutions, gives a wavelength corresponding to the wavelength of static buckling under the given load P; no matter how long the duration of load application, if $n > kL/\pi$ the motion remains bounded, while for any $n < kL/\pi$ the motion diverges. To see more clearly this relation to a static problem, recall first that from Eq. (4.48) the deflection curve of the bar is a sine wave with n half-waves. For $n = kL/\pi$ this curve is given by sin kx. One half-wave of this deflection curve, corresponding to the buckle shape of a simple pinned Euler column, therefore occupies a distance from the left support given by

$$kx_{st} = \pi$$

or

$$x_{st} = \pi/k \qquad (4.53)$$

Using the definition $k^2 = P/EI$, this relation gives

$$P = \frac{\pi^2 EI}{x_{st}^2} \tag{4.54}$$

This is identical to Eq. (4.16) for the static buckling of an Euler column of length x_{st} under the load P.

The dynamic equation also demonstrates the statement made in Section 4.3 that loads greater than $P_1 = \pi^2 EI/L^2$ give unstable motion. This follows from the observation already made that the motion is unstable if the coefficient of q_n in (4.52) is negative, that is, if

$$\frac{n^2\pi^2}{L^2} - k^2 < 0 \tag{4.55}$$

Since $k^2 = P/EI$ is positive, this quantity is most negative for $n = 1$. Using $n = 1$ in Eq. (4.55), the left-hand side is negative for all $P > \pi^2 EI/L^2$ and the motion is unstable as previously stated.

For the dynamic problems of present interest here, $P >> \pi^2 EI/L^2$ and many modes are unstable. Thus the mode numbers of the buckling modes are very high and the wavelengths of the buckling are so short that the total length of the bar becomes relatively unimportant. In fact, in experiments to be described later, dynamic buckling is produced by impact at one end of the bar and, because of the finite speed of axial wave propagation, buckling occurs before any signal is received from the opposite end. In this problem the total length of the bar has no significance at all. We should therefore seek a characteristic length other than the length of the bar. Because the nature of the motion changes at the static Euler wavelength $x_{st} = \pi/k$, it is quite natural to use $1/k$ as the characteristic length in the x-direction, along the bar. Similarly, it is natural to normalize lateral deflections with respect to the radius gyration, r of the cross section. The ratio between these lengths is a significant parameter and will be denoted by s:

$$s^2 = r^2k^2 = \frac{r^2P}{EI} = \frac{P}{AE} = \varepsilon \tag{4.56}$$

Thus the wavelength of the buckling varies inversely with the square root of the strain ϵ due to the compressive load P. This will be discussed more fully later.

To incorporate these lengths into the equation of motion, we introduce the nondimensional variables

$$w = \frac{y}{r} \quad , \quad \xi = kx = \frac{sx}{r} \quad , \quad \tau = \frac{s^2ct}{r} \tag{4.57}$$

Using these, Eq. (4.44) becomes

$$w'''' + w'' + \ddot{w} = w_o'' \tag{4.58}$$

where primes indicate differentiation with respect to ξ and dots differentiation with respect to τ. Boundary conditions (4.47) become

$$w = w'' = 0 \quad \text{at} \quad \xi = 0 \quad \text{and} \quad \xi = \ell = \frac{sL}{r} \tag{4.59}$$

and the product form of solution is now expressed by

$$w(\xi, \tau) = \sum_{n=1}^{\infty} g_n(\tau) \sin \frac{n\pi\xi}{\ell} \tag{4.60}$$

Similarly, the initial displacements are

$$w_o(\xi) = \sum_{n=1}^{\infty} a_n \sin \frac{n\pi\xi}{\ell} \tag{4.61}$$

where

$$a_n = \frac{2}{\ell} \int_o^{\ell} w_o(\xi) \sin \frac{n\pi\xi}{\ell} \, d\xi \tag{4.62}$$

A wave number η is introduced by

$$\eta = \frac{n\pi}{\ell} \tag{4.63}$$

and finally (4.60) and (4.61) are substituted into (4.58) to give the equations of motion for the Fourier coefficients $g_n(\tau)$:

$$\ddot{g}_n + \eta^2 (\eta^2 - 1) g_n = \eta^2 a_n \qquad (4.64)$$

This equation corresponds to (4.52); in the new notation the transition from hyperbolic to trigonometric solutions occurs at $\eta = 1$.

The general solution to (4.64) is

$$g_n(\tau) = C_n \cosh p_n\tau + D_n \sinh p_n\tau - \frac{a_n}{1 - \eta^2} \qquad \text{for} \quad \eta < 1$$

$$(4.65)$$

$$g_n(\tau) = C_n \cos p_n\tau + D_n \sin p_n\tau - \frac{a_n}{1 - \eta^2} \qquad \text{for} \quad \eta > 1$$

where

$$p_n = \eta \left|(1 - \eta^2)\right|^{1/2}$$

Substituting these into (4.60), the general solution for the lateral displacement is

$$w(\xi, \tau) = \sum_{n=1}^{N} \left(C_n \cosh p_n\tau + D_n \sinh p_n\tau - \frac{a_n}{1 - \eta^2} \right) \sin \frac{n\pi\xi}{\ell}$$

$$(4.66)$$

$$+ \sum_{n=N+1}^{\infty} \left(C_n \cos p_n\tau + D_n \sin p_n\tau - \frac{a_n}{1 - \eta^2} \right) \sin \frac{n\pi\xi}{\ell}$$

where N is the largest integer for which $\eta < 1$.

The bar is assumed to be initially at rest. Also, recall that w is measured from the initial displacement w_o so that the initial conditions are

$$w(\xi, 0) = \dot{w}(\xi, 0) = 0 \qquad (4.67)$$

Applying these to (4.66) yields $D_n = 0$ and $C_n = a_n/(1 - \eta^2)$. The final solution is then

$$w(\xi, \tau) = \sum_{n=1}^{\infty} \frac{a_n}{1 - \eta^2} \left[\begin{matrix} \cosh \\ \cos \end{matrix} \; p_n \tau - 1 \right] \sin \frac{n\pi\xi}{\ell} \tag{4.68}$$

in which the hyperbolic form is taken for $\eta < 1$ and the trigonometric form for $\eta > 1$.

Equation (4.68) shows quantitatively the exponential growth of the buckling terms. The ratio between the Fourier coefficients a_n of the initial displacement and the coefficients $g_n(\tau)$ in the buckling bar will be called the <u>amplification function</u> and in this problem is given by

$$G_n(\tau) = \frac{g_n(\tau)}{a_n} = \frac{1}{1 - \eta^2} \left[\begin{matrix} \cosh \\ \cos \end{matrix} \; p_n \tau - 1 \right] \tag{4.69}$$

A plot of this function, treating η as a continuous variable, is given in Fig. 4.10 for several values of nondimensional time τ. It is apparent that as time increases, a narrow band of wavelengths is amplified having wave numbers centered at somewhat less than $\eta = 1$. To find the wave number of the most amplified mode for late times, we differentiate (4.69) for $\eta < 1$.

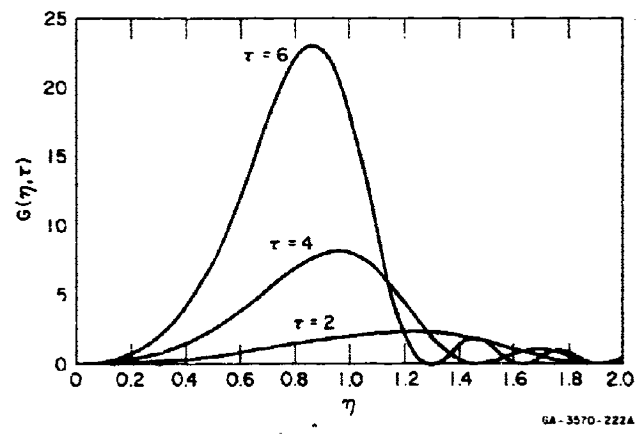

FIG. 4.10 AMPLIFICATION FUNCTION

$$\frac{dG_n}{d\eta^2} = \frac{(1 - 2\eta^2)}{2\eta^2(1 - \eta^2)^2} p_n\tau \sinh p_n\tau + \frac{1}{(1 - \eta^2)^2} (\cosh p_n\tau - 1) \tag{4.70}$$

Setting this to zero yields

$$1 - \frac{1}{2\eta^2} = \frac{1}{p_n\tau} \cdot \frac{\cosh p_n\tau - 1}{\sinh p_n\tau} \tag{4.71}$$

For times sufficiently large that significant amplification has occurred, $\cosh p_n\tau - 1 \approx \sinh p_n\tau$ and (4.71) is approximated by

$$\eta_{cr}^2 = \frac{1}{2} \quad \frac{p_n\tau}{p_n\tau - 1} \tag{4.72}$$

To a lessor approximation, for large τ such that $p_n\tau >> 1$, the wave rumber of the most amplified mode is therefore

$$\eta_{cr} \approx \frac{1}{\sqrt{2}} = 0.707 \tag{4.73}$$

Using this to obtain an estimate for $p_{cr} = \eta_{cr}(1 - \eta_{cr}^2)^{1/2} \approx 1/2$, a better estimate for η_{cr}, from (4.72) is

$$\eta_{cr} \approx \frac{1}{\sqrt{2}} \cdot \sqrt{\frac{\tau}{\tau - 2}} \tag{4.74}$$

For example, at $\tau = 6$, Eq. (4.74) gives $\eta_{cr} = 0.866$, which is about 22% larger than the value in (4.73). At $\tau = 10$, the estimate in (4.73) is only about 12% low. Thus, for practical purposes, the wavenumber of the most amplified mode can be taken as $\eta_p = 1/\sqrt{2}$. This will be called the "preferred" mode of buckling. The corresponding wavelength is found from

$$\eta_p \xi_p = 2\pi \quad , \quad \text{or} \quad \xi_p \equiv \lambda_p = 2\pi\sqrt{2} \tag{4.75}$$

In dimensional units, from (4.57), this length is

$$x_p = \frac{r}{s} \xi_p = \frac{2\pi\sqrt{2}}{\sqrt{\epsilon}} r = 8.88 \ r/\sqrt{\epsilon} \tag{4.76}$$

A graph of the maximum amplification plotted against τ is given in Fig. 4.11. Beyond $\tau = 4$, growth is very rapid; at $\tau = 12$ initial imperfections are amplified by more than 400. These results suggest that a bar under very high compression will buckle into wavelengths near $8.88\ r/\sqrt{\epsilon}$ at nondimensional times between 4 and 12. Better estimates for critical buckling times are given in succeeding sections.

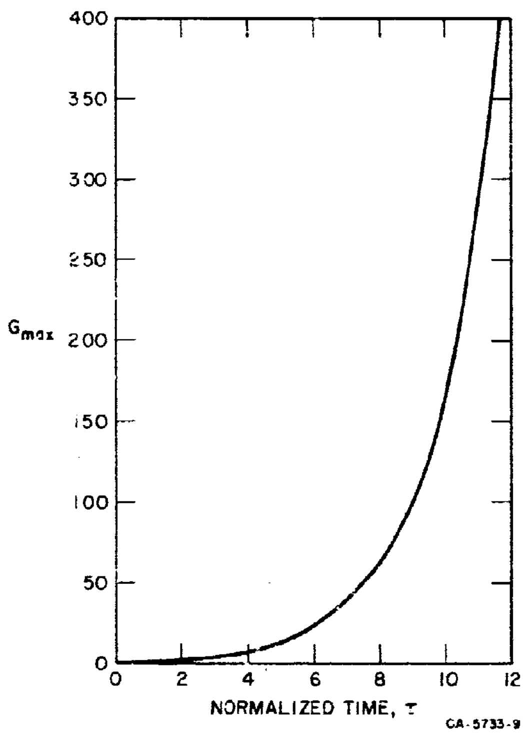

FIG. 4.11 MAXIMUM AMPLIFICATION vs. TIME

4.6 Dynamic Elastic Buckling under Eccentric Load

As an example, consider a bar eccentrically loaded as in Fig. 4.12. For this problem, the initial deflection is taken as

$$\begin{aligned} w_o(\xi) &= \delta/r & \xi &\neq 0,\ell \\ w_o(\xi) &= 0 & \xi &= 0,\ell \end{aligned} \tag{4.77}$$

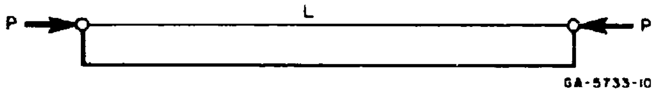

FIG. 4.12 ECCENTRICALLY LOADED BAR

Expanding into the Fourier sine series

$$w_o(\xi) = \sum_{n=1}^{\infty} a_n \sin \frac{n\pi\xi}{\ell} \tag{4.78}$$

the coefficients are found using formula (4.62), which yields

$$\begin{aligned} a_n &= \frac{4\delta}{n\pi r} && n \quad \text{odd} \\ a_n &= 0 && n \quad \text{even} \end{aligned} \tag{4.79}$$

From (4.68), the buckled shape is given by

$$w(\xi, \tau) = \sum_{n=1,3}^{\infty} \frac{4\delta}{n\pi r} \cdot \frac{1}{1 - \eta^2} \left[\begin{matrix} \cosh \\ \cos \end{matrix} \; p_n\tau - 1 \right] \sin \frac{n\pi\xi}{\ell} \tag{4.80}$$

To evaluate this sum, recall that

$$\eta = \frac{n\pi}{\ell} \; ; \quad \text{and for} \quad n \quad \text{odd,} \quad \Delta\eta = \frac{2\pi}{\ell} \tag{4.81}$$

Then

$$\frac{4\delta}{n\pi r} = \frac{4\delta}{\eta\ell r} = \frac{4\delta}{r\eta} \cdot \frac{1}{2\pi} \cdot \frac{2\pi}{\ell} = \frac{2\delta}{\pi r\eta} \Delta\eta \tag{4.82}$$

and (4.80) can be written

$$w(\xi, \tau) = \frac{2\delta}{\pi r} \sum_{n=1,3\ldots}^{\infty} \frac{1}{\eta(1 - \eta^2)} \left[\begin{matrix} \cosh \\ \cos \end{matrix} \; p_n\tau - 1 \right] \sin \eta\xi \, \Delta\eta \tag{4.83}$$

If we assume that the bar is very long compared to the wavelengths of the buckling, $\Delta\eta \to d\eta$ and η can be treated as a continuous variable. The sum (4.83) can then be replaced by the integral*

$$w(\xi, \tau) = \frac{2\delta}{\pi} \int_0^{\infty} \frac{1}{\eta(1 - \eta^2)} \left[\begin{matrix} \cosh \\ \cos \end{matrix} \; p_n\tau - 1 \right] \sin \eta\xi \, d\eta \tag{4.84}$$

A plot of the function

$$f(\eta, \tau) = \frac{1}{\eta(1 - \eta^2)} \left[\begin{matrix} \cosh \\ \cos \end{matrix} \; p_n\tau - 1 \right] \tag{4.85}$$

in the integrand is given in Fig. 4.13 for $\tau = 6$. To obtain an approximate analytical expression for the integral in (4.84), we replace this curve by the triangle of height A in Fig. 4.13, where $A(\tau) = f(1/\sqrt{2}, \tau)$.

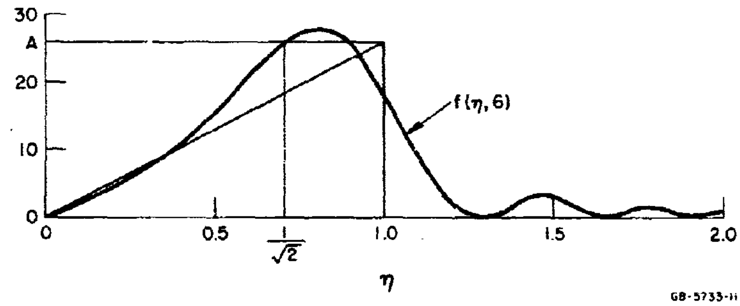

FIG. 4.13 FOURIER COEFFICIENTS (transform) OF BUCKLED SHAPE

Then

$$w(\xi, \tau) \approx \frac{2\delta}{\pi} \int_0^1 A(\tau)\eta \sin \eta\xi d\eta = \frac{2\delta A(\tau)}{\pi\xi^2} \left[\sin \eta\xi - \eta\xi \cos \eta\xi\right]_0^1$$

$$= \frac{2\delta A(\tau)}{\pi\xi^2} (\sin \xi - \xi \cos \xi) \tag{4.86}$$

*This is merely a plausible argument, but the result is correct, as can be confirmed by using a Fourier integral representation from the start. Converting from a sum to an integral here can be done because the function multiplying $\sin \eta\xi$ in the integrand dies off for large η such that there is no difficulty with $\sin \eta\xi$ oscillating in the interval $\Delta\eta = 2\pi/\ell$. For a more rigorous discussion see Ref. 12.

where

$$A(\tau) = \frac{1}{\frac{1}{\sqrt{2}}\left(1 - \frac{1}{2}\right)} \left[\cosh \tau/2 - 1\right] \qquad (4.87)$$

The function

$$W(\xi) = \frac{1}{\xi^2} (\sin \xi - \xi \cos \xi) \qquad (4.88)$$

which gives the approximate shape of the buckling bar, is plotted in Fig. 4.14. The wavelengths between peaks are slightly greater than 2π near the support and approach 2π away from the support.

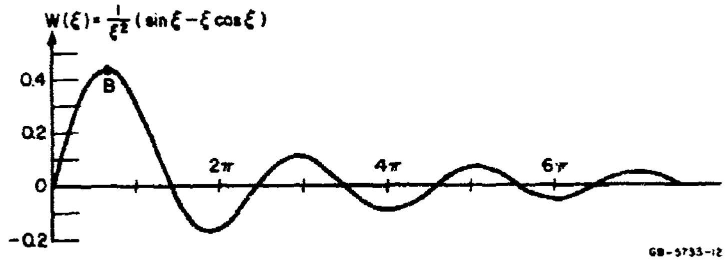

FIG. 4.14 APPROXIMATE BUCKLED SHAPE OF BAR UNDER SUDDENLY APPLIED ECCENTRIC LOAD

This discussion gives an estimate for the buckled shape of a bar under idealized eccentric thrust, and also shows how the amplitude of the buckled form grows with time. Specification of a criterion for failure by dynamic buckling, however, depends on the particular structural problem at hand. For example, if the bar is a push rod used to measure rapid displacements, large deflections within the elastic limit could constitute failure. On the other hand, in a rod used as a hammer, large displacements are probably not objectionable so long as the motion remains elastic and the rod returns to its initial shape.

To give a concrete example, let us calculate the duration of load application required to produce a combined bending-compressive stress equal to the yield stress. The maximum bending stress occurs at point B in Fig. 4.14 where the curvature $W'' = 0.235$ and is a maximum. In general, the compressive bending stress in the inner fiber, for a rectangular bar of height h, is

$$\sigma_b = \frac{M\frac{h}{2}}{I} = \frac{Eh}{2}\frac{\partial^2 y}{\partial x^2} = \frac{Eh}{2}\frac{s^2}{r^2} rw'' = \sqrt{3}\ Es^2 w'' \qquad (4.89)$$

Using (4.86) with $W'' = -0.235$ and the time variation from (4.87), the bending stress at B is

$$\sigma_b = \sqrt{3}\ Es^2 \frac{2\delta A(\tau)}{\pi r}(-.235) = -0.732\frac{\delta}{r}\sigma_c\left[\cosh\left(\frac{\tau}{2}\right) - 1\right] \qquad (4.90)$$

where σ_c is the compressive impact stress.

The threshold of buckling is defined by the total stress $\sigma_b + \sigma_c$ reaching the yield stress σ_y. Using σ_b from (4.90), this condition gives the following relation between the compressive stress σ_c and the time τ_{cr} at which first yield occurs:

$$\left(\frac{\sigma_c}{\sigma_y}\right)^{-1} = 1 + 0.732\frac{\delta}{r}\left[\cosh\left(\frac{\tau_{cr}}{2}\right) - 1\right] \qquad (4.91)$$

A graph of τ_{cr} versus σ_c/σ_y from (4.91) is given in Fig. 4.15 for several values of eccentricity δ, with δ expressed in terms of depth h of a rectangular bar for later comparison to experiment. The values chosen range over an order of magnitude, from $\delta = 0.00316\ h$ to $\delta = 0.0316\ h$. The mid value $\delta = 0.01\ h$ is a representative value found from static experiments, as given by Eq. (4.22). We shall see that the dynamic buckling experiments in Section 4.8 suggest that the static data do indeed give equivalent imperfections in the appropriate range for the dynamic problem.

Also given is a curve of the amplification G_p (from (4.69) with $\eta = 1/\sqrt{2}$) required to produce first yield for an eccentricity $\delta = 0.01\ h$. Similar curves for $\delta = 0.00316\ h$ and $\delta = 0.0316\ h$ are omitted for clarity. This curve shows that for small values of impact

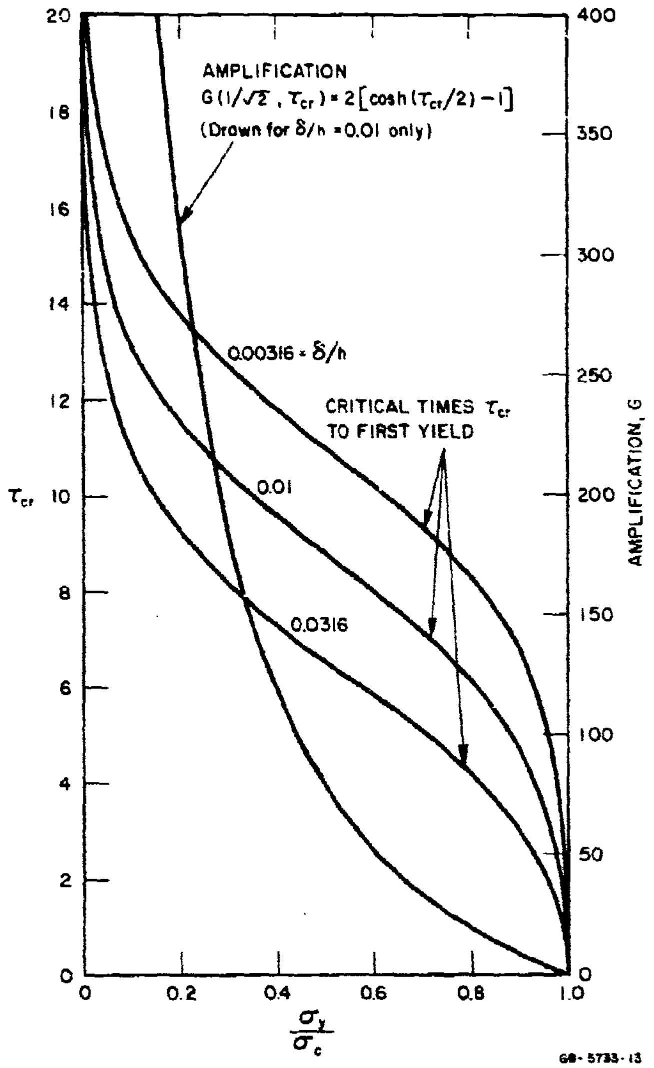

FIG. 4.15 CRITICAL BUCKLING TIMES TO FIRST YIELD FOR BAR UNDER ECCENTRIC LOAD

stress the amplification must be very large to produce yield. This results because the bending contribution must be larger and also because the wavelength of the buckling is longer. Under these conditions, depending on the practical application, large buckling deformations may constitute buckling before the yield stress is reached, thus placing an upper limit on τ_{cr}. However, with the yield definition of buckling here, τ_{cr} approaches infinity (as does the length of the bar) as P approaches zero. At the other end of the curves, as the impact stress approaches the yield stress, the amplification required to produce first yield is quite small (less than 10 for $\sigma_c/\sigma_y = 0.9$). Also, in a real material the yield stress is not sharply defined and, more important, the tangent modulus begins to fall rapidly as the material yields so that the elastic modulus in the present buckling formulation is inappropriate. Thus, application of the curves in Fig. 4.15 has little meaning for real materials beyond about $\sigma_c/\sigma_y = 0.9$. Buckling in this range of loads is considered in Section 4.9.

To obtain a physical interpretation of the curves, we observe that in physical units nondimensional time τ corresponds to the impulse of the applied load. Thus, from the definition of τ in Eq. (4.57), this impulse is

$$Pt = \frac{AEr}{c}\tau \tag{4.92}$$

and the critical impulse to cause first yield from buckling is

$$I_{cr} = \frac{AEr}{c}\tau_{cr} \tag{4.93}$$

Also, the applied load can be expressed by

$$P = A\sigma_c = A\sigma_y\left(\frac{\sigma_c}{\sigma_y}\right) \tag{4.94}$$

Thus the curves in Fig. 4.15 can be interpreted as giving the combinations of load amplitude P and load impulse I that produce threshold buckling. Load points above the curves give more severe buckling, while load points below the curves give no permanent buckling deformations. We shall see in Chapter 5 that amplitude-impulse curves of this type can be applied to more complex structures, such as a cylindrical shell under lateral pressure.

4.7 Dynamic Elastic Buckling with Random Imperfections

Another form of imperfection, more uniquely concerned with the dynamic problem, is suggested by experiments to be described later in which rubber strips were buckled over a wide range of dynamic thrusts. It was found that the strips buckled into wavelengths which varied randomly at each thrust, with a mean and standard deviation both inversely proportional to the square root of the thrust as suggested by Eq. (4.76). These results are consistent with the assumption that random imperfections in the strips are amplified by the buckling motion so that the resulting buckled form, although still random, has statistics determined by the buckling amplification function given by Eq. (4.69) and in Fig. 4.10.

Several methods of representing a random function have been described by Rice[13] in the study of filtering electrical noise. In the electrical problem, the function represents the variation of current with time, $I = I(t)$. In the buckling problem here, the random function represents the variation of lateral displacement with distance along the bar, $w = w(\xi)$. Thus there is an analogy between the two problems, with electrical current being associated with mechanical displacement, and time in the electrical problem being associated with axial position in the mechanical problem. In the electrical problem, a noise signal $I_o(t)$, having Fourier components $a_n(\omega_n)$, is fed into a filter having an attenuation characteristic $F(\omega_n)$. The output signal is $I(t)$, having Fourier components $A_n(\omega_n) = F(\omega_n)a_n(\omega_n)$. In the mechanical problem, the "input" is the initial displacement $w_o(\xi)$, having Fourier components $a_n(\eta)$, and the "output" is the buckled form $w(\xi)$, having Fourier components $g_n(\eta) = G(\eta, \tau)a_n(\eta)$. The mechanical problem contains one added variable, time τ, so that the amplification characteristic also depends on time as indicated by $G_n(\tau)$ in Eq. (4.69), which is denoted here by $G(\eta, \tau)$. However, at each instant the analogy is quite close. The only difference is that in the electrical problem the process is stationary, that is, the currents continue indefinitely in time and the statistics are taken to be independent of time. In the buckling problem, the boundary conditions at the ends of the bar must be met so that the statistics depend also on the position ξ , the variable analogous to time. If the buckle wavelengths are very short compared to the length of the bar, however, one would expect that some distance from the end of the bar its effect diminishes and the assumption of white noise would be acceptable. With this assumption the two problems are completely analogous and all the theory available for the electrical problem can be used here.

It is not necessary to assume that the random imperfections are stationary; this assumption merely makes the mathematics simpler. Before this is done, consider a random form of imperfection which does satisfy the boundary conditions of simple supports at $\xi = 0$ and $\xi = \ell$. These imperfections are given by

$$w_o(\xi) = \sum_{n=1}^{\infty} a_n \sin \eta\xi \tag{4.95}$$

where

$$\eta = \frac{n\pi\xi}{\ell}$$

and N will be specified later. The coefficients a_n are random normal, having mean value zero and standard deviation $\sigma(\eta)$. The normal or Gaussian probability distribution is shown in Fig. 4.16. It is further assumed that σ is constant over all wavenumbers of interest, then

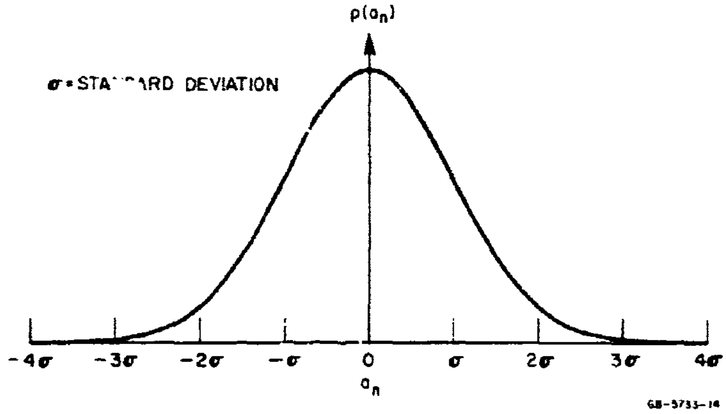

FIG. 4.16 ASSUMED NORMAL DISTRIBUTION OF FOURIER COEFFICIENTS OF INITIAL IMPERFECTIONS

Eq. (4.95) is called (nonstationary) white noise. In order that $w_o(\xi)$ remain bounded, σ must ultimately die off for large η. Since our central concern is in the buckled shape $w(\xi)$ after the Fourier coefficients have been amplified by $G(\eta, \tau)$, and Fig. 4.10 shows that for $\eta \tilde{>} 2$ the amplification is very small, harmonics with $\eta > 2$ can safely be neglected. Thus, in the initial deflections given by (4.95) we merely specify that $\sigma(\eta)$ dies off in some unspecified manner for $\eta > 2$ and is constant for $0 < \eta \bar{<} 2$. This is the usual assumption justifying the use of white noise as a filter input.

Since the concept of white noise can be applied only when associated with a process passing a finite band of wavenumbers, we must defer any examples of random functions until after the amplification function with its inherent cut-off has been applied to give the buckled shapes. This function, repeated from Eq. (4.69), is

$$G(\eta, \tau) = \frac{1}{1-\eta^2}\left[\begin{matrix}\cosh \\ \cos\end{matrix}\; p(\eta)\tau - 1\right] \tag{4.96}$$

where

$$p(\eta) = \left|\eta\,(1-\eta^2)\right|^{1/2}$$

and the hyperbolic form is taken for $\eta < 1$. The buckled form is given by

$$w(\xi, \tau) = \sum_{n=1}^{N} a_n G(\eta, \tau) \sin \eta\xi \tag{4.97}$$

where N is the largest value of n for which $\eta < 2$.

With a cutoff characteristic now applied, examples can be given of the functions characteristic of buckling from random imperfections. Figure 4.17 gives two examples of buckled forms calculated from Eq. (4.96) using a length $\ell = 50\pi$, which is 25 complete Euler lengths and very long compared to the highly amplified wavelength $\lambda_p = 2\pi\sqrt{2}$ corresponding to $\eta = 1/\sqrt{2}$. With this choice for ℓ, $N = 100$. The procedure was to select 100 random numbers from a population having a

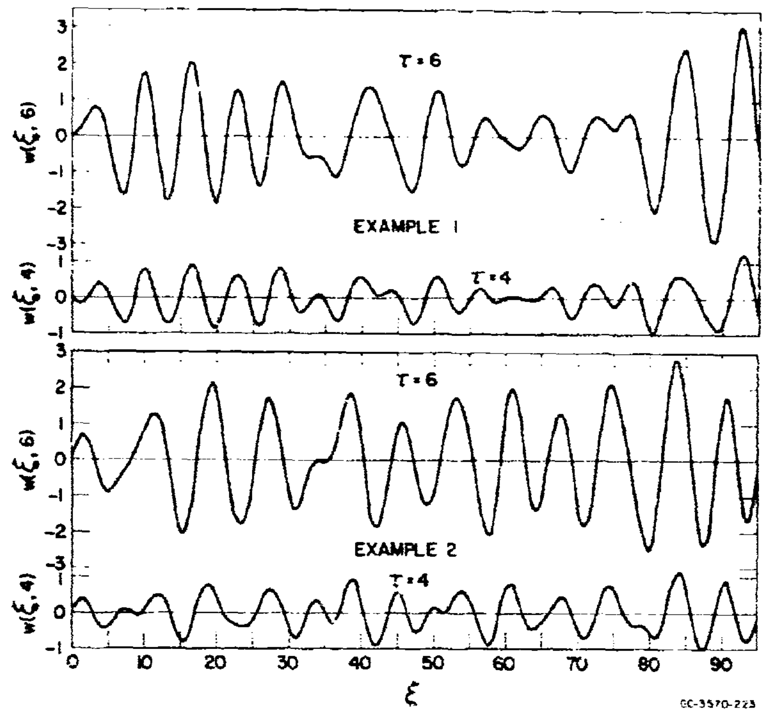

FIG. 4.17 TWO EXAMPLES OF BUCKLED FORMS FROM RANDOM IMPERFECTIONS

Gaussian distribution as in Fig. 4.16, with $\sigma = 1$. These were then used as the coefficients a_n in Eq. (4.96) and the summation was taken over 100 modes, corresponding to $0 < \eta \leq 2$. Higher harmonics would have had a negligible effect as already mentioned because of the rapid decrease of $G(\eta, \tau)$ with η for $\eta > 2$.

In each example in Fig. 4.17 (i.e., for each set of 100 random coefficients) the buckled shape is plotted at $\tau = 4$ and $\tau = 6$. In both examples, there are more crests (waves) at $\tau = 4$ than at $\tau = 6$. This is a consequence of the shift in the peak of the amplification function in Fig. 4.10 from $\eta \approx 1$ at $\tau = 4$ to $\eta \approx 0.8$ at $\tau = 6$. At still later times little further change in the number of crests would be expected because, as discussed in Section 4.5, the point of maximum amplification cannot shift below $\eta = 1/\sqrt{2} \approx 0.707$.

Another feature exhibited in these examples is typical of buckled forms from white noise: although they consist of a random assemblage of harmonics, they exhibit a surprisingly regular pattern of waves. The average wavelength of this pattern depends, of course, on the region of amplification defined by the amplification function. In fact, an amplification function which is square in shape, constant for $\eta < 2$ and zero for $\eta > 2$, would give a wave pattern similar to those shown in Fig. 4.17. This is exactly the waveform of the imperfection $w_o(\xi)$ corresponding to the computational procedure used in generating the curves in Fig. 4.17, but it is not the waveform of the "actual" imperfection, whose Fourier components do not cut off abruptly at $\eta = 2$. This is the reason that numerical examples had to be deferred to the discussion of buckled shapes; any specification of a cut-off wavenumber already implies filtered noise.

The only way of quantitatively describing buckled shapes such as in Fig. 4.17 is to give statistics of the features of interest. The most easily measured quantity in experiments is the buckled wavelengths, so statistics of wavelengths will be calculated for later comparison to experiment. Direct calculation of these statistics is beyond the means of currently available analysis except for a special case to be given later. Instead, the statistics are calculated by the Monte Carlo method; a large sample of random buckled forms is generated numerically by the procedure just described and the resulting data are plotted directly in the form of a probability distribution (histogram) for the feature of interest. To determine the distribution of wavelengths, 65 random buckled shapes as in Fig. 4.17 were calculated, each with a different set of 100 random values for a_n. Wavelengths in each buckled shape were then measured for $\tau = 6$ and the histogram in Fig. 4.18a was prepared. The wavelengths were measured between alternate zero crossings for the first three waves from the support $\xi = 0$, not counting the support as a crossing. Separate histograms were also prepared for the first, second, and third waves individually and no significant differences were found, indicating that the end support does not seriously affect the

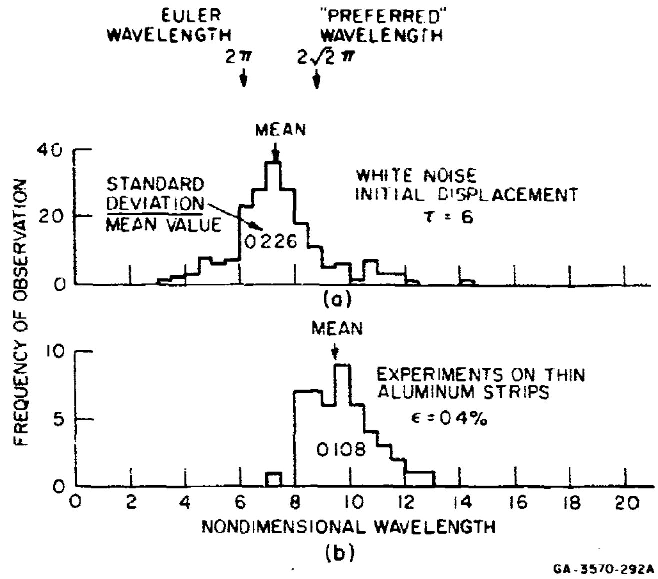

FIG. 4.18 THEORETICAL AND EXPERIMENTAL HISTOGRAMS OF BUCKLED WAVELENGTHS

wavelengths even a small distance from the support. Many more computations would have to be added before this would approximate the probability distribution, but the main features of the distribution are apparent. The mean wavelength is $\lambda_m = 7.4$, which lies between the Euler wavelength $\lambda_e = 2\pi = 6.28$ and the "preferred" wavelength $\lambda_p \approx 2\pi\sqrt{2} = 8.88$, as shown. The standard deviation of the wavelength is $\sigma_\lambda = 1.7$ and the ratio of standard deviation to mean wavelength is $\sigma_\lambda/\lambda_m = 0.23$.

Figure 4.18b gives a histogram prepared from experiments on about 50 aluminum strips buckled under axial impact as described in Section 4.8. The mean value of the buckled wavelengths is somewhat larger than in the theoretical histogram ($\lambda_m = 9.5$ compared to $\lambda_m = 7.4$ in Fig. 4.18a) and the spread in wavelengths is somewhat smaller. The narrower spread possibly results because part of the initial imperfection was in the form of an eccentric impact, which tends to produce a fixed wavelength as described in Section 4.6. However, the general features of the observed distribution are adequately represented by the white noise theory. More extensive experimental examples are given in Section 4.8.

An analytical expression for the mean wavelength directly in terms of the amplification function $G(\eta, \tau)$ can be given if it is assumed that the buckling displacements are stationary, i.e., if the end conditions are neglected as discussed earlier. With this assumption the initial imperfections can be represented by stationary white noise as follows:

$$w_o(\xi) = \sum_{n=1}^{N} a_n \sin(\eta\xi + \varphi_n) \tag{4.98}$$

This form is similar to Eq. (4.95) except that here the Fourier components are added in random phase, with the phase angles φ_n uniformly distributed (with equal probability) in the interval $0 \le \varphi_n \le 2\pi$. The buckled displacements are then

$$w_o(\xi) = \sum_{n=1}^{N} a_n G(\eta, \tau)\sin(\eta\xi + \varphi_n) \tag{4.99}$$

With the standard deviation of a_n constant, it is reasonably simple to demonstrate[13] that the mean wavelength between alternate zero crossings in the buckled form is

$$\lambda_m(\tau) = 2\pi \left[\frac{\int_0^\infty G^2(\eta, \tau)d\eta}{\int_0^\infty \eta^2 G^2(\eta, \tau)d\eta} \right]^{1/2} \tag{4.100}$$

No analytical expression has yet been found for the standard deviation of wavelengths, even with the stationary process assumption (Slepian[14] discusses the current status of this perennial problem in information theory).

For the complicated $G(\cdot\ ,\tau)$ in Eq. (4.96), no closed form expressions for the integrals in Eq. (4.100) were found. Instead, the integrals were evaluated numerically over the region $0 < r < 2$ of significant amplification for several values of τ. The resulting mean wavelengths are plotted against τ in Fig. 4.19. The mean wavelength increases monotonically with τ, but in the region $\tau \gtrsim 6$ of significant amplification (see Fig. 4.11) the increase is very small. At $\tau = 6$, Fig. 4.19 gives $\lambda_m = 7.4$ which is the same result found in Fig. 4.18 for buckles satisfying the pinned end conditions. Also plotted is the wavelength corresponding to the most amplified mode, given approximately by Eq. (4.74) for large τ. The mean and most amplified wavelengths are very close together and have very nearly the same variation with τ. For large τ, both approach the preferred wavelength $\lambda_p = 2\pi\sqrt{2}$.

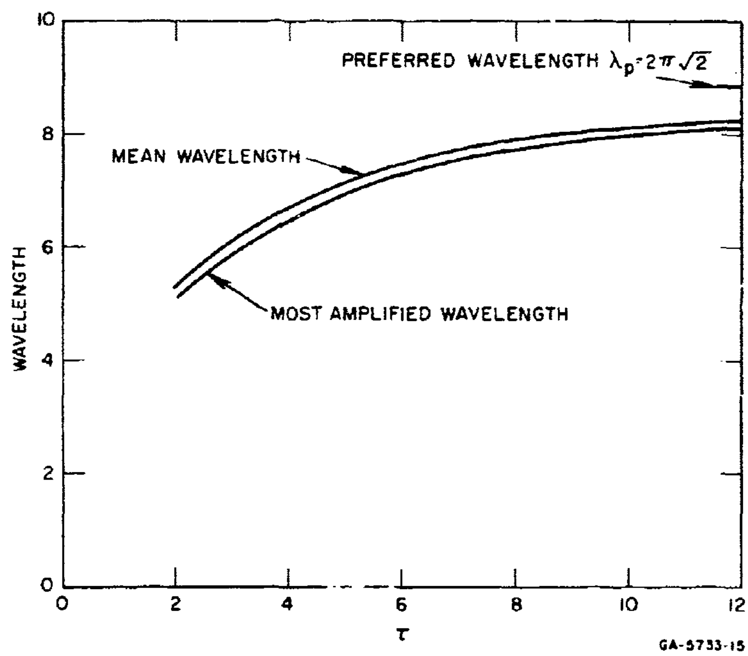

FIG. 4.19 MEAN AND MOST AMPLIFIED WAVELENGTHS vs. TIME

These results suggest that, if it is reasonable to assume that random imperfections are present in a bar as described, then the bar will buckle over the entire compressed length and the wavelength of the buckles will be reasonably well characterized by the preferred wavelength $\lambda_p = 2\pi\sqrt{2}$. To calculate a threshold of buckling, one can make the simplifying assumption that the motion consists of response in only the preferred wavelength, with an assumed single equivalent imperfection at this wavelength. This will now be done.

As in static buckling, imperfections can be divided into two types, one type having amplitudes proportional to the thickness of the bar and the other having amplitudes proportional to the wavelength of the buckling. In the following, both types will be considered and it will be shown that the resulting critical times τ_{cr} for buckling do not depend strongly upon which type is assumed.

We treat first imperfections having amplitudes proportional to the buckle wavelength λ_p and denote the coefficient of this Fourier component by A_p, in physical units. Thus we assume

$$A_p = \beta L_p \tag{4.101}$$

where L_p is the preferred half-wavelength (the buckled shape of an Euler column) under the applied load $\dot{P}$, corresponding to a half-wavelength $\lambda_p/2$ in nondimensional units. In dimensionless form these quantities, using (4.57), are expressed by

$$a_p = \frac{A_p}{r}, \quad \frac{\lambda_p}{2} = \frac{sL_p}{r}, \quad \lambda_p = 2\pi\sqrt{2} \tag{4.102}$$

and the imperfection is now given by

$$a_p = \frac{\beta}{s}\frac{\lambda_p}{2} = \frac{\pi\sqrt{2}\,\beta}{s} \tag{4.103}$$

The criterion for buckling is taken as in Section 4.6 on eccentric impact; a critical time τ_{cr} is determined such that the bending stress plus the direct stress due to P reaches the yield stress.

The bending stress, from Eq. (4.89), is

$$\sigma_b = \sqrt{3}\, Es^2 w'' \tag{4.104}$$

The idealized buckled shape is simply a sine wave, given from Eqs. (4.96) and (4.97) as

$$w(\xi,\tau) = \frac{a_p}{1-\eta^2}\left[\cosh \mu(\eta_p)\tau - 1\right]\sin \eta_p \xi \tag{4.105}$$

with $\eta_p = 1/\sqrt{2}$. Differentiating (4.105) and substituting the result into (4.104) gives the peak bending stress, at $\sin \eta_p \xi = 1$, as

$$\sigma_b = \sqrt{3}\, Es^2 \cdot a_p \left[\cosh \frac{\tau}{2} - 1\right] \tag{4.106}$$

which, using a_p from (4.103), becomes

$$\sigma_b = \pi\sqrt{6}\, \beta\, Es \left[\cosh \frac{\tau}{2} - 1\right] \tag{4.107}$$

Finally, we use $s^2 = \sigma_c/E$ and the buckling criterion $\sigma_b + \sigma_c = \sigma_y$ to obtain

$$\frac{1 - \sigma_c/\sigma_y}{\sqrt{\sigma_c/\sigma_y}} = \pi\beta\sqrt{\frac{6}{\epsilon_y}}\left[\cosh \frac{\tau_{cr}}{2} - 1\right] \tag{4.108}$$

This equation is the counterpart of Eq. (4.91) for buckling from eccentric impact. An essential difference is that here the critical curves for buckling depend not only on the imperfection amplitude β but also on the yield strain ϵ_y. This results from taking the imperfections proportional to the buckle wavelengths.

Curves of τ_{cr} versus σ_c/σ_y from Eq. (4.108) are given in Fig. 4.20 for $\epsilon_y = 0.005$, a representative value for engineering metals.

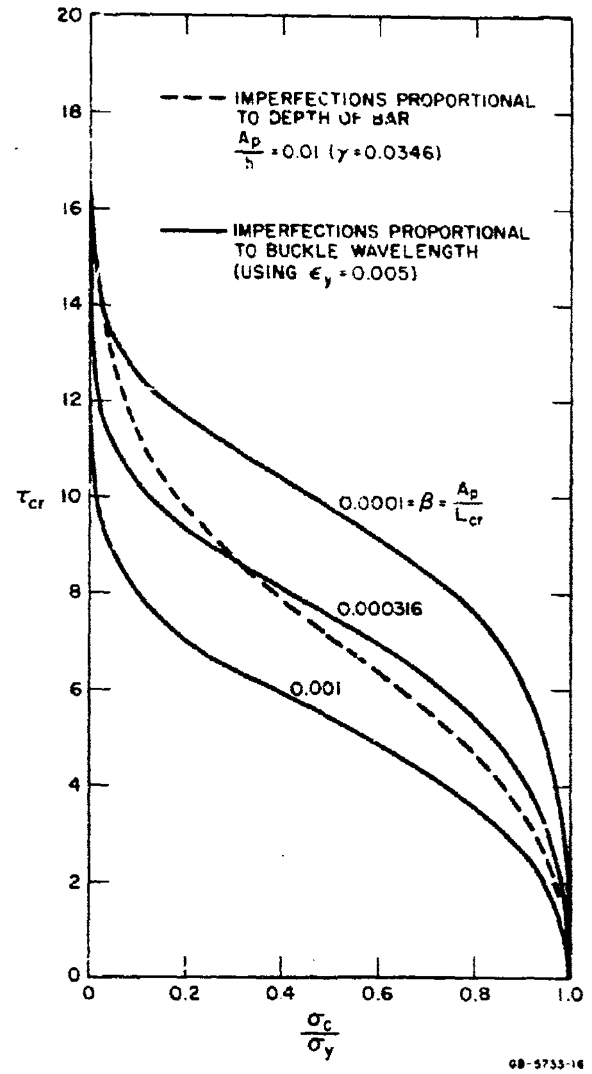

FIG. 4.20 CRITICAL TIMES TO FIRST YIELD FOR BUCKLING IN "PREFERRED" MODE

Values of β are taken from 0.0001 to 0.001, corresponding to the range of imperfection amplitudes observed in static buckling as given in Eq. (4.23). The curves are quite similar to those in Fig. 4.15 for eccentric impact except that the critical times τ_{cr} change more slowly with σ_c/σ_y (i.e., the curves are more nearly horizontal for intermediate values of σ_c/σ_y). Also, τ_{cr} does not shoot up to very large values until σ_c/σ_y is very small. These observations can be made by comparing the solid curves (imperfections proportional to wavelength) to the dashed curve (which has the same functional form as in the curves for eccentric impact).

Critical buckling times for imperfections proportional to the depth of the bar are found in essentially the same way. The equivalent imperfection amplitude in the preferred mode is then given by

$$A_p = \gamma r \tag{4.109}$$

Using this in place of Eq. (4.101) and applying the same procedure as for imperfections proportional to wavelength, the expression for τ_{cr} becomes

$$\left(\frac{\sigma_c}{\sigma_y}\right)^{-1} = 1 + \sqrt{3}\,\gamma \left[\cosh \frac{\tau_{cr}}{2} - 1\right] \tag{4.110}$$

This is exactly the same functional form as found for eccentric impact, with the constant 0.732 δ/r replaced by $\sqrt{3}\,\gamma = \sqrt{3}\,A_p/r$. Again, τ_{cr} depends only on σ_c/σ_y and not on the magnitude of the yield strain ε_y.

As for imperfections proportional to wavelength, we take as estimates for γ the values found appropriate in static buckling. For a rectangular bar of depth h, the static empirical formula (4.24) gives the conservatively large value $\gamma = 0.1\ r/(h/2) = 0.058$. In Fig. 4.20 the dashed curve is a plot of Eq. (4.10) for a somewhat smaller value ($\gamma = 0.0346$, corresponding to $A_p/h = 0.01$) to give an intermediate value for comparison to the solid curves. This comparison shows that the values of τ_{cr} calculated for either type of imperfections (with representative values for both taken from static buckling) give very nearly the same result. More important, we shall see in the next section that these curves compare favorably with observed thresholds of dynamic buckling.

4.8 Experiments on Dynamic Elastic Buckling of Bars

In practice, the most directly applicable physical problem for the preceding theory is the impact of a long bar against a massive target. We consider that the bar is originally stress free and moving toward the wall with velocity V as shown in Fig. 4.21a. Since to a good approximation the target can be considered to be a rigid wall, on impact the left end of the bar immediately comes to rest. Adjacent particles to the right subsequently come to rest as a stress wave of magnitude σ propagates to the right at the bar sound velocity c. When the stress wave has passed a distance x_σ into the bar, the impulse applied by the end load at the rigid wall must be equal to the initial momentum of the length x_σ brought to rest by the stress wave. This condition is expressed by

$$\sigma A \cdot \frac{x_\sigma}{c} = \rho A x_\sigma \cdot V$$

or

$$\sigma = \rho c V \qquad (4.111)$$

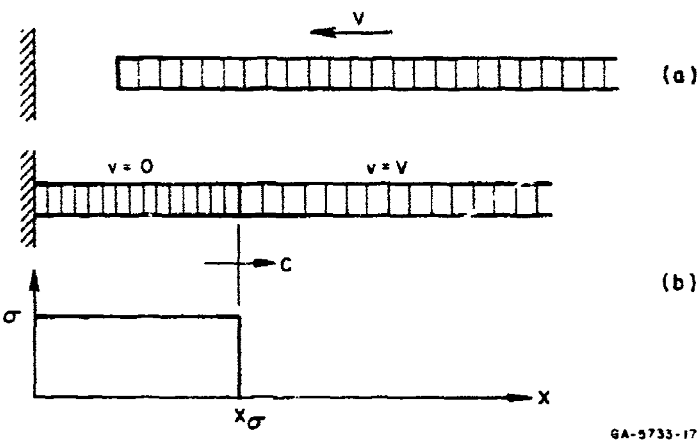

FIG. 4.21 AXIAL STRESS WAVE IN A BAR IMPACTING A RIGID WALL

This situation is conveniently produced experimentally by using a tensile testing machine.[15] The initial velocity V is produced by first pulling the bar to a tensile stress σ. Prior to applying the tension a notch is filed in the bar near the upper jaw with its depth adjusted so that fracture occurs at the notch when the stress in the remainder of the bar is near the desired stress σ. After fracture, a (compressive) relief wave travels down the bar at velocity c, leaving the bar stress-free behind the wave and traveling at velocity $V = \sigma/\rho c$ by the same argument just made for axial impact. When the wave arrives at the lower jaw it reflects, again as a compressive wave. Since the rod is completely stress-free and traveling at velocity V at the instant of this reflection, formula (4.111) can again be used, giving a compressive stress equal to the initial tensile stress σ. In actual fact the stress rises to this value in a finite time comparable to the time for stress waves to cross the bar and communicate the notch fracture to the full cross section.

4.8.1 Framing Camera Observations

An example[16] of a strip buckled by this procedure is given in Fig. 4.22. The strip is made of 6061-T6 aluminum with a

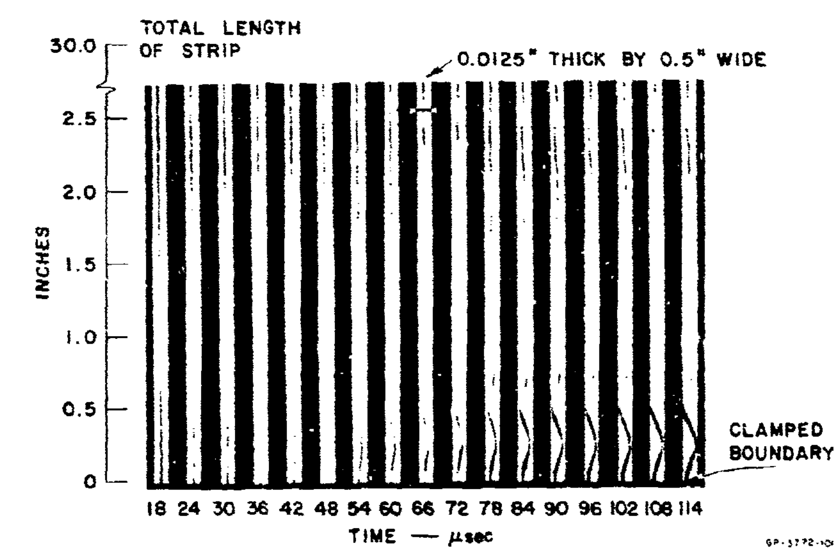

FIG. 4.22 ALUMINUM STRIP BUCKLING WITHIN A 40,000-psi AXIAL STRESS WAVE (time measured from compressive reflection at lower jaw)

0.5 x 0.0125-inch cross section and a length of 30 inches between notch and lower jaw. The photographs show only a few inches of the strip just above the lower jaw. The magnitude of the compressive wave was approximately 40,000 psi, between 10 and 20 percent below the yield stress. It was photographed by an ultrahigh-speed framing camera at a framing rate giving 6 microseconds between frames. In the figure, at 18 μsec after the arrival of the compressive wave the strip appears straight, but careful measurements show that it is slightly buckled even at this early time. At 24 μsec the deflection is perceptible in the printed reproduction here and at later times the developing buckles are clearly visible. All the buckles remain nearly fixed in position and merely grow in amplitude, just as in the idealized eccentric impact example. The lowermost buckle continues to grow throughout the time shown, but the upper buckles oscillate beyond 70 μsec because the very large deflection of the lower buckles reduces the thrust by allowing the remainder of the bar to move toward the jaw. The rapidity of the buckling is demonstrated by the lateral velocity of the crest of the lowermost wave, calculated to be 75 fps. The wavelength of the lower buckle is about 0.47 inch, very close to the value of 0.50 inch calculated for the preferred wavelength λ_p from the theory.

4.8.2 Streak Camera Observations--Effects of the Moving Stress Wave

The theory, of course, is not strictly applicable to the impact problem because it assumes that the thrust is uniform throughout the length of the bar. In impact, the thrust is applied by the moving axial stress wave and at each instant only the distance enveloped by the wave is under compression. To observe possible effects of this moving wave, and also to observe early exponential buckling growth as predicted by the theory, another experimental arrangement[17] was used to amplify the tiny early motion. Instead of observing the buckling directly in an edge-on view as in Fig. 4.22, the strip was polished on one side and the reflected image of a series of light sources was viewed with a streak camera as shown in Fig. 4.23. The shift in position of the light source is proportional to the product of the small change in slope of the strip at the point in which the image forms and the distance between the light source and the strip. With this method, deflections of the order of 50 millionths of an inch were easily resolved and the exponential growth was observed.

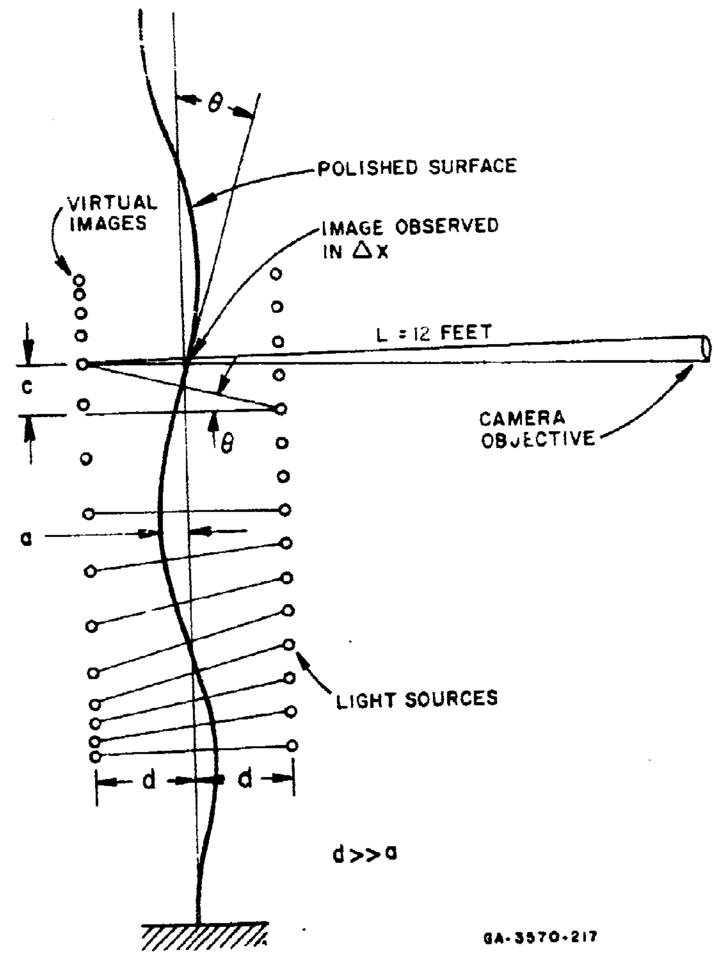

FIG. 4.23 OPTICAL LEVER METHOD OF OBSERVING BUCKLING SLOPE

A plot of peak displacement versus time (assuming the buckle was a simple sine wave at the observed 0.65-inch wavelength) is shown in Fig. 4.24 for one such experiment. The magnitude of the stress wave in this experiment was approximately 30,000 psi and the cross section of the aluminum strip was 0.50 x 0.0116 inch. The experimental points are peak displacements $A(t)$ measured from the initial (unmeasured) displacement A_o. The lower smooth curve passing through these points is a theoretical curve calculated under the assumption that the growth is

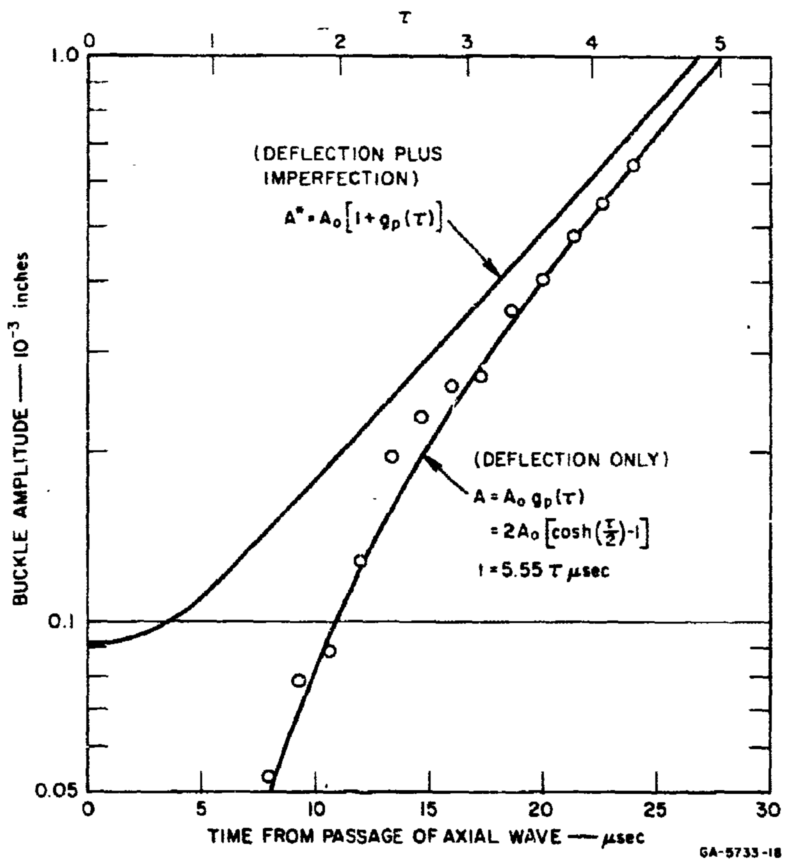

FIG. 4.24 EXPERIMENTAL (points, for deflection only) AND THEORETICAL (curves) BUCKLE AMPLITUDE vs. TIME (matched at 22 μsec)

adequately represented by the preferred mode. Taking $\eta_p = 1/\sqrt{2}$ in Eq. (1.69), the amplitude of this mode is

$$A(\tau) = 2A_o \left[\cosh(\tau/2) - 1\right] \tag{4.112}$$

Using $\epsilon = 0.003$, $c = 0.20$ in/µsec, and $r = 0.0116/\sqrt{12}$ inch in Eq. (4.57) gives $\tau = 0.18\ t$, with t in µsec. The Fourier coefficient A_o of the equivalent initial imperfection was adjusted to 9.1×10^{-5} inch to fit the experimental data as shown. The upper curve is the calculated total amplitude $A_o + A(\tau)$.

This experiment demonstrates that the observed buckling consists of exponential growth which can be calculated quite adequately by the simple theory. The simple uniform thrust theory is adequate, even though the thrust is applied by a moving stress wave, because the stress wave has moved a large distance along the bar before significant buckling displacements appear. For example, in Fig. 4.24, the peak amplitude of the buckling is only about 0.001 inch (giving a bending stress of 4600 psi, well within the elastic limit) at 30 µsec after passage of the axial stress wave. At 30 µsec the stress wave has propagated about 6 inches along the bar, about 10 times the observed wavelength of 0.65 inch.

However, the high magnification of the optical lever did reveal that the axial impact produced very high frequency bending vibrations superimposed on the buckling motion. On the original streak camera record an oscillation was observed* having a period of 3.1 µsec (320 kc/s) and a peak-to-peak amplitude of about 5×10^{-6} inch. The oscillations appeared to be a wave train propagating along the bar from the impact at the lower jaw at a phase velocity of 0.075 inch/µsec, giving a wavelength of (0.075) (3.1) = 0.23 inch. These oscillations had little effect on the buckling, apparently because of this short wavelength and because their period was so short compared to the buckling

*These were observed on all three experiments performed.

motion (3.1 μsec corresponds to $\Delta\tau = 0.55$). Thus we can conclude that effects dependent upon the moving axial stress front had a negligible effect on the buckling.

The argument concerning the distance the axial stress wave has traveled during the buckling motion can be stated analytically. From the theory, we have seen that whether we assume the imperfections are local in nature, as in eccentric impact, or consist of a general random form of imperfections, the wavelength of the buckles is always quite close to the wavelength $\lambda_p = 2\pi\sqrt{2}$ of the preferred mode. Also, the magnification of the buckling motion depends only on τ, all other essential parameters having been included in its definition. It seems reasonable to assume that effects of the axial stress wave will be small as long as significant magnification takes place only after the axial wave has passed several buckle wavelengths along the bar. Without specifying a numerical value, we assume that the buckled form is unalterably determined (e.g., the buckled deformations are much larger than the initial imperfections) at a critical time τ_{cr}. Using the definition τ in Eq. (4.57) gives for the corresponding real time

$$t_{cr} = \frac{r}{s^2 c} \tau_{cr} \tag{4.113}$$

Real time t can be expressed in terms of the number N of preferred wavelengths L_p through which the axial stress wave passes at velocity c, giving

$$t = \frac{L_p N}{c} = \frac{2\pi\sqrt{2}\, r}{cs} N \tag{4.114}$$

Putting this into expression (4.113) for critical time and using the definition of s in Eq. (4.57) gives

$$N_{cr} = \frac{\tau_{cr}}{2\pi\sqrt{2}} \cdot \frac{1}{\sqrt{\epsilon}} \tag{4.115}$$

This suggests that neglect of axial wave effects depends only on the compressive strain of the axial thrust. In metals this strain is very small within the elastic limit and, as we have observed, elastic buckling is adequately represented by the constant thrust theory.

4.8.3 Experiments on Rubber Strips--Statistical Observations

Since formula (4.115) suggests that axial wave front effects, if any, would be more pronounced at large compressive strains, confidence in the theory would be enhanced for metals if it could be demonstrated experimentally that the theory is acceptable in a material which can withstand large elastic compressive strains. Pure gum rubber is such a material and experiments have been performed using this material to strains up to about 15%.[17]

The apparatus for these experiments, in Fig. 4.25, is very simple and can be used for classroom demonstrations. A strip of pure gum rubber 0.0375 x 0.50 inch in section and about 1 foot long was looped over one end of a rigid support bar and secured by means of masking tape as shown, with extra layers of tape wound above and below the rubber strip so that its end was separated from the support and cover bar. The cover bar is shown above this assembly in the photograph. A strip of emery cloth has been glued to it and saturated with chalk dust.

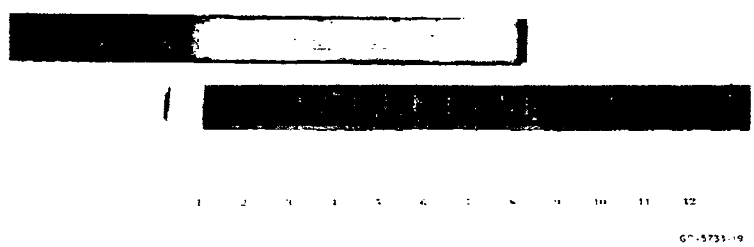

FIG. 4.25 APPARATUS AND TYPICAL RECORD FOR BUCKLING RUBBER STRIPS

To perform an experiment, the free end of the strip was held between thumb and forefinger, the cover bar placed over the strip, chalked side down and not touching the strip, and then the strip was stretched to a specified strain and released. The wrinkled strip impacted the chalk bar with sufficient velocity that a well-defined line was left on the strip at the crest of each wave, as shown. The positions of these lines were easily measured to an accuracy of 0.01 inch.

To examine the applicability of the random noise assumption for imperfections, in addition to the applicability of the constant thrust theory, many experiments were performed so that statistical distributions could be prepared. Figure 4.26 gives histograms of the measured wavelengths for several values of initial tensile elongation. These data were taken from tests on 18 strips, each tested at all the strains, from smallest to largest strain in order to minimize any perturbations caused by the wrinkling of a previous test. Buckling at a strain greater than 25% is rather violent and leaves the strip with a definite bias toward the corresponding wavelength. The number of waves observed in each test varied from 2 to 3 at 3% strain up to 12 at 16% strain. The same strip tested repeatedly at the same strain gave an almost identical wave pattern each time, consistent with our mathematical model in which the imperfections are assumed random but fixed for any given bar. Data from only the first test at each strain were used for the histograms. Each histogram has a total of 65 observations so they can be compared directly.

It is significant that the general shape of all histograms is the same and that the ratio between the standard deviation and mean value is nearly constant over the entire range of strains, as shown in Fig. 4.26. This demonstrates that the statistics are inherent in the buckling process and are not the result of errors in measurement. It also indicates that the strips had no preferred wavelength characteristic of a manufacturing process. If these distributions are compared with the distribution in Fig. 4.18, calculated assuming that initial imperfections can be represented by white noise, we see that the white noise assumption gives a very good description of the observed buckling.

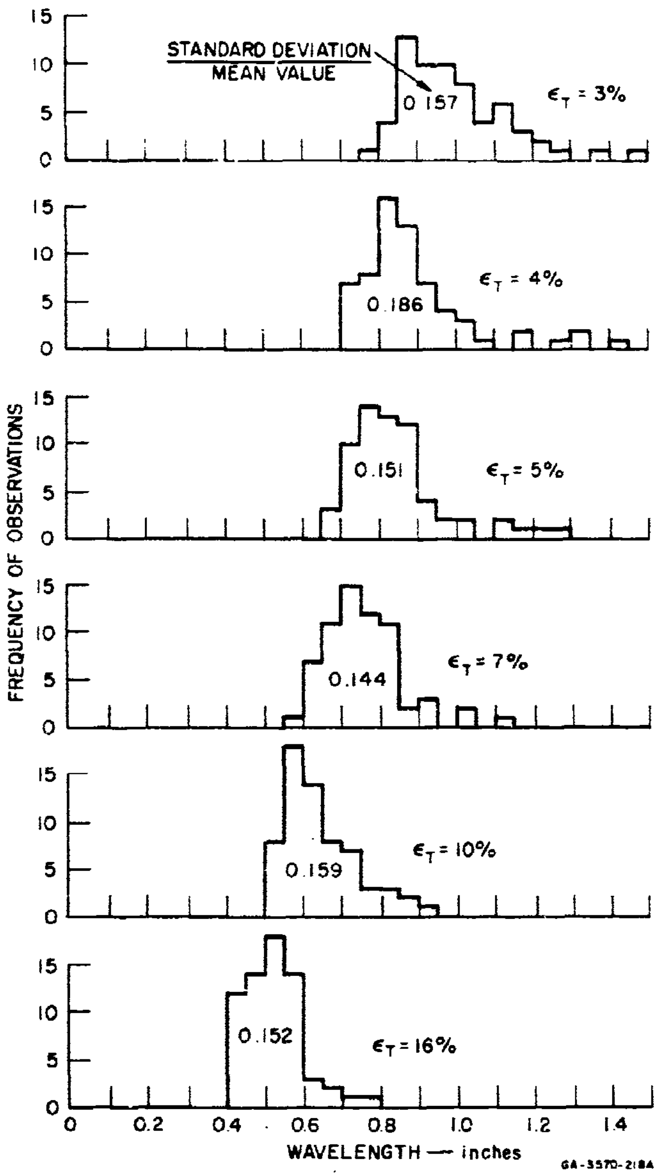

FIG. 4.26 HISTOGRAMS OF OBSERVED BUCKLE WAVELENGTHS FOR SEVERAL INITIAL TENSILE STRAINS

To compare the observed wavelengths with the uniform thrust theory, the large strains involved must be taken into account. Only the final compressive strain resulting from the initial tensile strain is needed, so the corrections can be obtained without reference to the details of large strain-wave propagation. It is sufficient to assume that the rubber behaves elastically so that the potential energy stored in compression equals the initial potential energy in tension. Tensile stress-strain tests were performed on sample strips which showed that true stress was linear with elongation out to at least 100% with a Young's modulus of 285 psi. Thus the initial tensile force F in the strip is given by

$$F = E\epsilon \frac{A_o}{1 + \epsilon} \tag{4.116}$$

where A_o is the unstressed cross-sectional area of the strip and $\epsilon = (\ell - \ell_o)/\ell_o$ is the elongation. The initial stored energy at uniform tensile elongation ϵ_T is equal to the work done by the end force $F(z)$,

$$U_T = \int_o^{\ell - \ell_o} F(z)dz = EA_o\ell_o \int_o^{\epsilon_T} \frac{\epsilon d\epsilon}{1 + \epsilon} = EA_o\ell_o \log_e(1 + \epsilon_T) \tag{4.117}$$

where z is in the position of the moving end of the strip. Similarly, the compressive energy stored in the strip is

$$U_c = - EA_o\ell_o \log_e(1 - \epsilon_c) \tag{4.118}$$

expressed so that the compressive strain ϵ_c is a positive quantity. Equating these energies, the compressive strain is simply

$$\epsilon_c = \frac{\epsilon_T}{1 + \epsilon_T} \tag{4.119}$$

Further, the increased thickness h from the unstressed thickness h_o, assuming the rubber is incompressible, is

$$h = \frac{h_o}{(1 - \epsilon_c)^{1/2}} \tag{4.120}$$

The last correction to be made accounts for the wrinkles being formed at axial strain ϵ_c but measured when the strip has returned to zero strain. The ratio of the observed wavelength ℓ_r to the wavelength while under compression is, by the definition of ϵ_c,

$$\frac{\ell_r}{\ell_c} = \frac{1}{1 - \epsilon_c} \tag{4.121}$$

The wavelength of the "most amplified" mode in dimensionless coordinate ξ is $\lambda_p = 2\sqrt{2}\,\pi$. Using this with Eqs. (4.57) and $r = h/\sqrt{12}$, the wavelength of the most amplified mode while the strip is under compression is

$$\ell_{pc} = \pi \left(\frac{2}{3}\right)^{1/2} \frac{h}{\epsilon_c^{1/2}} \tag{4.122}$$

After the strip has relaxed, this preferred length would be elongated according to (4.121). Using (4.122) in (4.121) with (4.119) and (4.120) the elongated length is given by

$$\ell_{pr} = \pi \left(\frac{2}{3}\right)^{1/2} \frac{(1 + \epsilon_T)^2}{\epsilon_T^{1/2}} h_o \tag{4.123}$$

In Fig. 4.27 the observed wavelengths of Fig. 4.26 are plotted against this preferred length, the circled points giving the mean values and the bars extending one standard deviation above and below the circles. The mean values fall very close to a straight line through the origin, and the ends of the standard deviation bars are also closely bounded by straight lines. These observations suggest that Eq. (4.123) gives the proper form of variation with strain. However, the ratio between observed and preferred wavelengths (the slope of the line through the circles) is 1.70 here as compared to only 1.07 for the aluminum experiments given in Fig. 4.18. This difference is attributed to strain-rate effects in the rubber. If, for example, these effects are lumped into an effective dynamic compressive modulus k times the static tensile modulus, the preceding theory gives a slope of 1.00 for k = 2.

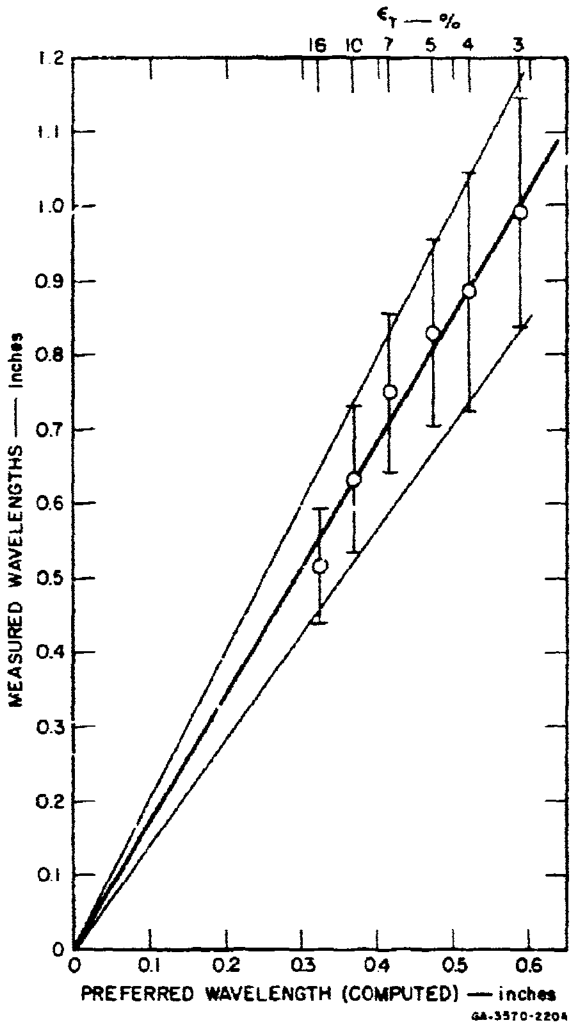

FIG. 4.27 MEASURED vs. THEORETICAL WAVELENGTHS (bars extend one standard deviation above and below mean value)

Although the foregoing interpretation of the discrepancy between the aluminum and rubber experiments is somewhat speculative, the smooth variation of measured wavelength with strain strongly supports the conclusion that lateral motion immediately behind the axial-stress front has a negligible effect on the wrinkle formation and that a constant-thrust theory can be used with confidence. The main effect of the traveling thrust is that the duration of the thrust decreases as one moves away from the struck end, and this could easily be accounted for by simply assigning a different duration to each wrinkle. This conclusion should also be applicable to more complicated structures, such as cylindrical shells under axial impact. For large deflections, it might prove necessary also to compute a new thrust for each wave, reduced owing to lateral deflections in preceding waves.

4.8.4 Buckling Thresholds in Aluminum Strips

To obtain estimates of equivalent imperfections to be used in estimating thresholds of pulse buckling, experiments were run on thin 6061-T6 aluminum strips using a tensile testing machine as described previously. Tests were run on strips 1/2 and 1/4 inch wide and 0.0124 and 0.025 inch thick.* The initial tensile stress (and reflected compressive stress) was nominally adjusted to 0.4 and 0.7 times the yield stress of 42,000 psi by appropriately sized fracture notches in the strips. Duration of the thrust at the lower jaw was varied by varying the length L between the notch and lower jaw, the duration being $2L/c$. For each combination of strip width, thickness, and compressive stress, tests were run at increasing lengths until plastic buckles appeared. These were observed by sighting down the shiny finish of the strips, a simple procedure with high resolution. The dimensionless time τ, from its definition in Eq. (4.57), is

$$\tau = \frac{\epsilon_c c}{r} \cdot \frac{2L}{c} = \frac{2\epsilon_c L}{r} \tag{4.124}$$

*Two widths were tested at each thickness to examine the effect of fracture time on buckling. It was found that possible effects were masked by changes in critical loads caused by random variations in imperfections.

Figure 4.28 gives a plot from tests at many combinations of axial stress and duration, with open points representing tests in which no buckling was observed and solid points tests in which buckling was observed. The upper points (longer duration, buckling) are all solid and

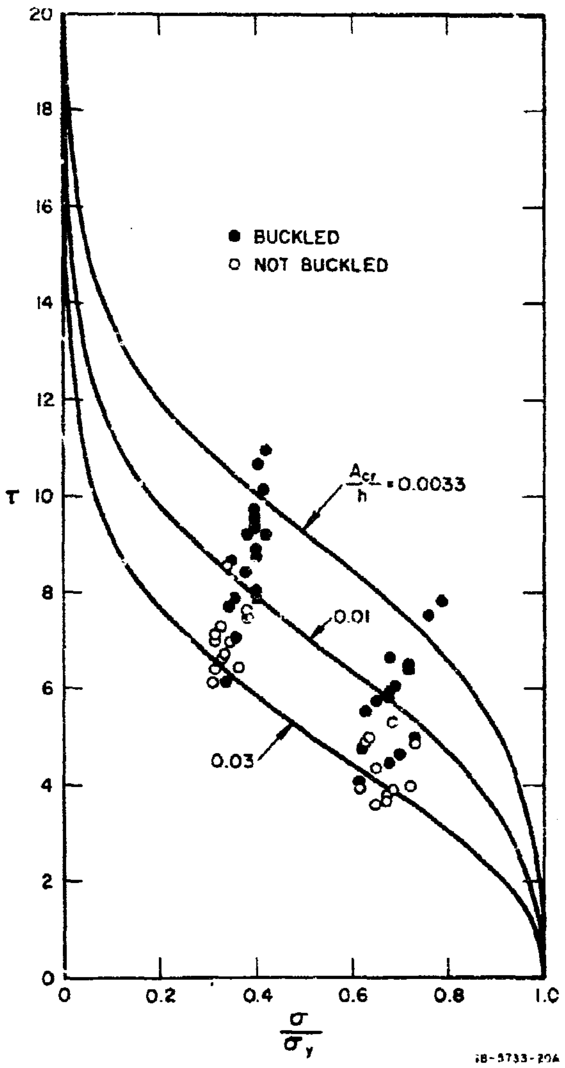

FIG. 4.28 COMPARISON OF OBSERVED BUCKLING TO CRITICAL CURVES FOR IMPERFECTIONS IN PREFERRED MODE PROPORTIONAL TO STRIP THICKNESS

the lower points (shorter duration, no buckling) are nearly all open, as would be expected. At intermediate durations buckling and no-buckling points are intermingled as a result of the random nature of the imperfections. Also given on the same graph are theoretical curves similar to the dotted curve in Fig. 4.20 for assumed imperfections in the preferred mode proportional to strip thickness. The experimental transition band of intermingled points between no buckling and buckling follows the trend of the theoretical curves, with equivalent imperfections in the experiments ranging from about 0.01 to 0.03 times the thickness of the bar.

The most severe buckles generally appeared at the jaw or one plastic hinge from the jaw, as would be expected because of the longer duration of thrust near the jaw and the possibility of eccentric loading (see Fig. 4.14). As often as not, however, 3 or 4 plastic hinges were observed, suggesting that random imperfections throughout the bar were at least as important as eccentric loading. Buckling a few wavelengths away from the jaw, of course, had to take place in a somewhat shorter time, thus increasing the equivalent imperfections above those implied in Fig. 4.28. However, this effect is small because the wavelength of the buckling is small compared to $2L$, as discussed in relation to Eq. (4.115). Thus we can conclude that random imperfections in these tests were equivalent to single imperfections in the preferred mode of from 1 to 3% of the strip thickness.

4.9 Dynamic Plastic-Flow Buckling

In all the preceding theory the axial stress was much greater than the static Euler buckling stress, but was nevertheless assumed to be within the elastic range. Even if the stress exceeds the yield stress, however, the mathematics of the elastic theory can still be used. For this treatment it is assumed that the axial stress increases as buckling takes place, as in the Shanley hypothesis in Fig. 4.9. Thus, buckling flexure is accompanied by moments proportional to the tangent modulus E_t

and the equation of motion is the same as Eq. (4.4) in elastic buckling with E replaced by E_t.

$$E_t I \frac{\partial^4 y}{\partial x^4} + p \frac{\partial^2}{\partial x^2}(y + y_o) + \rho A \frac{\partial^2 y}{\partial t^2} = 0 \qquad (4.125)$$

Similarly, if dimensionless variables w, ξ, and τ are introduced using Eq. (4.57), with the following modifications,

$$\tau = \frac{s^2 c_p t}{r} \quad , \quad c_p^{\,2} = \frac{E_t}{\rho} \quad , \quad s^2 = \frac{p}{AE_t} = \frac{\sigma_y}{E_t} \qquad (4.126)$$

the equation of motion (4.125) becomes

$$w'''' + w'' + \ddot{w} = - w_o'' \qquad (4.127)$$

which is identical to Eq. (4.58). In Eq. (4.126) it has been assumed that the small increase in p beyond yield can be neglected and that E_t is constant.

The mathematics for the plastic problem is therefore identical to that in the elastic problem, yielding a "preferred" mode with wavelength $\xi_p = 2\pi\sqrt{2}$, and resulting in large growth for $5 < \tau < 10$. In physical units, of course, these quantities are much different in the plastic problem. Using the definition $\xi = sx/r$ from Eq. (4.57), we see from Eq. (4.126) that the ratio of preferred wavelengths in the plastic and elastic problems is

$$\frac{\lambda_{\text{plastic}}}{\lambda_{\text{elastic}}} = \left(\frac{\sigma}{\sigma_y}\frac{E_t}{E}\right)^{1/2} \qquad (4.128)$$

For many engineering metals the elastic modulus is about 100 times the tangent modulus, so that buckles formed during plastic flow have wavelengths at least an order of magnitude smaller than in elastic buckling. The buckling times are also an order of magnitude smaller, as is seen by comparing the definitions of τ in Eq. (4.57) and (4.126), giving

$$\frac{t_{\text{plastic}}}{t_{\text{elastic}}} = \frac{\sigma}{\sigma_y}\left(\frac{E_t}{E}\right)^{1/2} \qquad (4.129)$$

As in elastic buckling, the most directly applicable physical problem for the plastic-flow buckling theory is axial impact of a bar against a massive target. From Eq. (4.111), impact velocities that result in plastic flow are greater than

$$V = \frac{\sigma_y}{\rho c} = c\ \epsilon_y \tag{4.130}$$

where ϵ_y is yield strain and c is elastic wave velocity. For aluminum, magnesium, and steel, c is near 16,000 ft/sec and a typical yield strain is 0.005. In these metals plastic flow buckling therefore occurs for velocities greater than about 80 ft/sec; at smaller velocities the initial buckling is elastic. Since E_t does not decrease abruptly at yield, there is a small transition in velocity over which buckle wavelengths and times decrease by an order of magnitude. The transition zone is narrow, however, because

$$V = \int_0^{\epsilon_c} \left(\frac{E_t}{\rho} \right)^{1/2} d\epsilon \tag{4.131}$$

(the generalization of Eq. (4.130) to a continuously changing modulus[18]) increases slowly beyond yield. Inclusion of a continuously changing modulus in the buckling theory is given in the next chapter for cylindrical shells subjected to radial impulse.

REFERENCES

1. Bolotin, V. V., Dynamic Stability of Elastic Systems, Holden-Day, Inc., San Francisco, 1964 (translated from Russian edition, 1956).

2. Southwell, R. V., Proc. Roy. Soc., London, Series A, 135, p. 601, 1932.

3. Marston, A., Trans. ASME 39, p. 108, 1897.

4. Jensen, C., Engineering 85, London, p. 433, 1908.

5. Lilly, W. E., ASCE 76, New York, p. 258.

6. Salmon, "Columns," London, 1921. Salmon's data and a more complete discussion of equivalent imperfections is given in Timoshenko and Gere, Theory of Elastic Stability, 2nd ed., McGraw-Hill Book Co., New York.

7. Von Karman, T., Forschungsarb 81, Berlin, 1910.

8. Shanley, F. R., J. Aeronaut. Sci. 14, p. 261, 1947.

9. Templain, R. L., R. G. Strum, E. C. Hartmann, and M. Holt, Aluminum Research Laboratories, ALCOA, Pittsburg, 1938.

10. Van den Broek, J. A., The Engineering Journal (Canada), December 1945.

11. Kolsky, H., Stress Waves in Solids, Dover Publications, New York, 1963, pp. 41-47.

12. Churchill, Fourier Series and Boundary Value Problems, McGraw-Hill Book Co., New York 1941 pp. 85-90.

13. Rice, S. O., "Mathematical Analysis of Random Noise," in N. Wax, Selected Papers on Noise and Stochastic Processes, Dover Publications, New York, 1954.

14. Slepian, D., "Contributions to Signal and Noise Theory," IEEE Trans. on Information Theory IT-9, pp 229-233, 1963.

15. Gerard, G. and H. Becker, "Column Behavior under Conditions of Impact," J. Aeronaut. Sci. 19, pp 58-65, 1952.

16. Lindberg, H. E., "Buckling of a Very Thin Cylindrical Shell Due to an Impulsive Pressure," J. Appl. Mech. 31, Trans. ASME 86, Series E, pp 267-272, June 1964.

17. Lindberg, H. E., "Impact Buckling of a Thin Bar," J. Appl. Mech. 32, Trans. ASME 87, Series E, pp 315-322, 1965.

18. Von Karman, T. and P. Duwez, "The Propagation of Plastic Deformation in Solids," J. Appl. Phys. 21, pp 987-994, October 1950.

19. Abrahamson, G. R. and J. N. Goodier, "Dynamic Flexural Buckling of Rods within an Axial Plastic Compression Wave," J. Appl. Mech. 33, 2, pp. 241-247, June 1966.

20. J. N. Goodier, "Dynamic Buckling of Rectangular Plates in Sustained Plastic Compressive Flow," to be published in the Proceedings of a symposium on Plasticity to be held at Cambridge University Engineering Laboratory, April 1968.

CHAPTER 5

DYNAMIC PULSE BUCKLING OF CYLINDRICAL SHELLS UNDER TRANSIENT LATERAL PRESSURES

by

H. E. Lindberg

5.1 Introduction

Cylindrical shells subjected to transient lateral pressures (produced, for example, by blast waves) often fail by dynamic pulse buckling. Three examples of dynamically buckled shells are given in Fig. 5.1, the only difference between them being the peak pressure and duration of the applied load. The shell on the left was subjected to an impulsive pressure (duration short compared to the shell response time) and has buckled into a very high order wave pattern with $n = 45$ waves around the circumference. The shell in the center was subjected to a quasi-impulsive pressure (duration comparable to the shell response time) and has several buckles around the circumference, corresponding to $n = 13$ The shell on the right was subjected to a quasi-static pressure (duration long compared tc the shell response time) and has buckled into $n = 7$, very close to the static pattern for this shell. This chapter

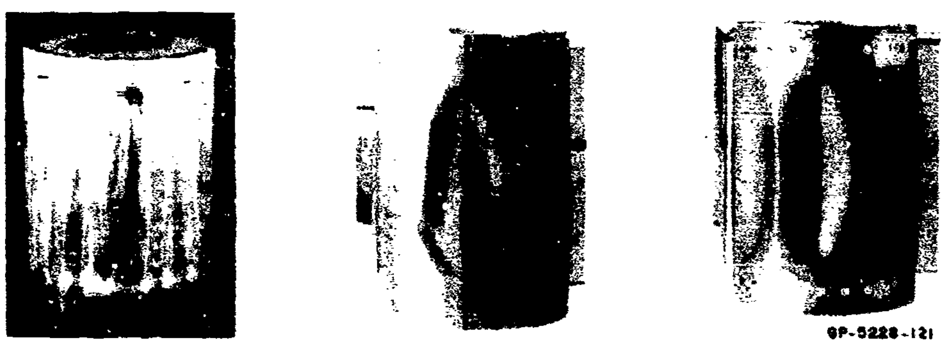

(a) IMPULSIVE LOAD $n \simeq 45$ (b) QUASI-IMPULSIVE LOAD $n \simeq 13$ (c) QUASI-STATIC LOAD $n \simeq 7$

FIG. 5.1 IDENTICAL SHELLS BUCKLED FROM PULSE LOADS OF VARIOUS DURATIONS (6061-T6 aluminum, $a/h = 100$, $L/D = 1$)

is concerned with buckling over the entire range of load durations, from ideal impulses to durations so long that the buckling is essentially static.

At each extreme of pulse duration the analysis becomes relatively simple, and theories for the extremes have been given in the literature. For very short durations the load is characterized entirely by the impulse, and the wavelength of the buckling is so short that the length of the shell is unimportant. Thus two parameters, load duration and shell length, are eliminated from the problem and the solutions become particularly simple. These are given by Abrahamson and Goodier[1] for relatively thick shells and by Lindberg[2] for very thin shells.

For very long durations the load is characterized entirely by peak pressure and, although the length of the shell must be considered, it is shown here that inertia forces can be neglected and the solution is again relatively simple. This is a classical static buckling problem and is given in several standard texts, for example Ref. 3. Between these extremes, pressure, duration, shell length, and inertia forces must all be considered. No previous investigations of this problem are known to the authors. The present analysis treats this problem and contains the simple theories as special cases.

The problem taken is that of a simply-supported cylindrical shell subjected to external surface pressures uniform around the circumference.* The time variations of pressure considered are triangular and exponential in shape, as shown in Fig. 5.2. However, it is postulated that the most significant load characteristics are peak pressure and impulse.† Therefore, in the theory to follow, loads that cause buckling

*Applicability of the solution to asymmetric loads is discussed later.

†Abrahamson[4] has shown that the response of a wide variety of structures to blast-type loads is most conveniently summarized in terms of the peak pressure and impulse of the load.

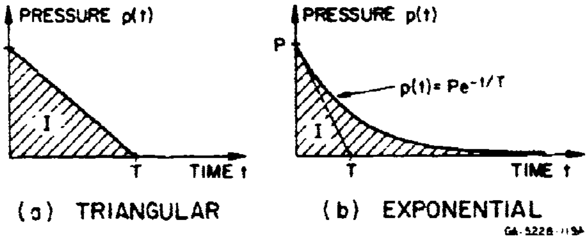

FIG. 5.2 PULSE SHAPES

are characterized by these quantities, and for each type of shell a "critical curve" for buckling is generated in the pressure-impulse plane as shown in Fig. 5.3. Impulse (per unit surface area) for the triangular pulse is $I = PT/2$, where T is pulse duration, and for the exponential pulse is $I = PT$, where T is the pulse time constant as shown in Fig. 5.2.

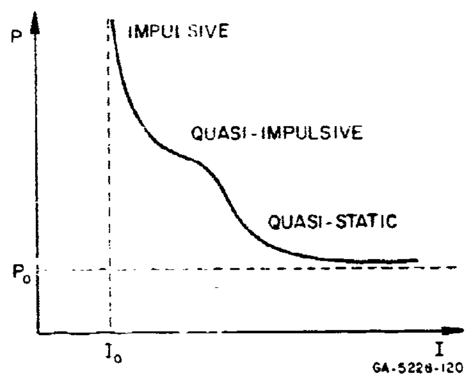

FIG. 5.3 PULSE REGIONS AND SCHEMATIC CRITICAL CURVE FOR BUCKLING IN THE PRESSURE-IMPULSE PLANE

5.2 Idealized Models

Loads that produce the types of buckling in the three shells in Fig. 5.1 fall into three corresponding load regions indicated in Fig. 5.3. Since the response of the shell differs widely from one region to another, the analysis is based on three corresponding models--a "tangent modulus" model for impulsive loads, an "elastic" model for quasi-static loads, and a "strain-reversal" model for a narrow range of quasi-impulsive loads for which neither of the other models is applicable.

Under impulsive loads it has been found that, except in very thin shells, buckling occurs only when the load is sufficiently intense to produce membrane plastic flow. In the early motion buckling takes place with no strain reversal and is therefore governed by the tangent modulus, hence the name for this model. Fortunately, as shown in Fig. 5.1a, the buckling is in high order modes; thus the effects of the ends are unimportant beyond a few wavelengths from the ends and, in the tangent modulus model, the shell will be treated as infinitely long. The analysis will follow that given in Ref. 5 except that finite pulse durations will be considered.

Under quasi-static loads buckling occurs in lower order modes, directly dependent on the length of the shell as shown in Fig. 5.1c. However, for most metal shells of present interest, this buckling takes place at pressures sufficiently low that the early buckling growth is elastic, hence the name for this model. Static elastic theory is simply extended to the dynamic problem by including radial inertia terms.

Under quasi-impulsive loads the membrane stress can be plastic as under impulsive loads, but significant buckling deformation takes place only after several oscillations in the hoop mode. To treat this buckling a strain reversal model is used which considers nonlinear stress variations across the section, influenced by both the membrane and flexural motion. This requires that the cross section be divided into laminates, and the resulting theory becomes more complex. Since it serves mainly to support the general character of the critical curves derived by the simpler theories, only the results from this analysis are presented here.

5.3 Equations of Motion

5.3.1 Tangent Modulus Model

The notation adopted is shown in Fig. 5.4. With time denoted by t and angular position on the cylinder denoted by θ, we are concerned in this model with radial displacements $w(\theta,t)$, measured positive inward from an initial unstressed deformation $w_i(\theta)$, in an infinitely long shell. The equations of motion for this problem are derived by Abrahamson and Goodier.[1] Under impulsive or nearly impulsive radial pressure, the shell elements initially move inward nearly uniformly to a smaller radius, inducing plastic circumferential membrane strains. The fundamental assumption is that during the early buckling motion the circumferential strain across the section is dominated by this membrane plastic flow, and therefore flexural motion is accompanied by bending moments proportional to the instantaneous tangent modulus; the strains in both the inner and outer fibers continue to move along the plastic stress-strain curve, but one lags behind the other because of the flexure. In the present problem we wish to treat a continuously varying tangent modulus E_t, so the notation in Ref. 5 is used. Constant shell and material parameters are defined by

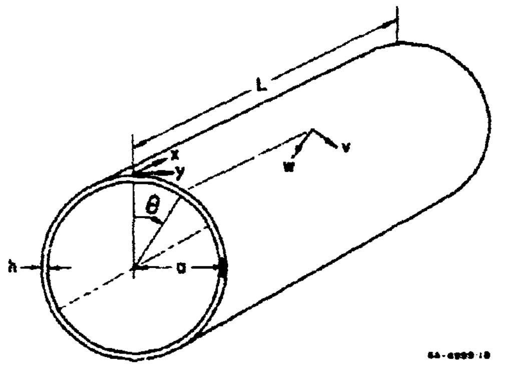

FIG. 5.4 COORDINATES AND SHELL NOMENCLATURE

$$\alpha^2 = \frac{h^2}{12a^2} \quad , \quad c^2 = \frac{E}{\rho} \tag{5.1}$$

where a is the shell radius, h its wall thickness as shown in Fig. 5.4,

E is Young's (elastic) modulus, and ρ is mass density. Dimensionless forms of the displacement and time variables are defined by

$$u = \frac{w}{a} \quad , \quad u_i = \frac{w_i}{a} \quad , \quad \tau = \frac{ct}{a} \tag{5.2}$$

and a dimensionless form of the external pressure p^*, including small nonsymmetric perturbations, is given by

$$p(\theta,\tau) = \frac{a}{Eh} p^*(\theta,\tau) \tag{5.3}$$

With this nomenclature, the equation of motion, from Ref. 5, is

$$\ddot{u} + \frac{\alpha^2 E_t}{E} \frac{\partial^4 u}{\partial\theta^4} + \left[\frac{\alpha^2 E_t}{E} + \frac{\sigma_\theta}{E}\right] \frac{\partial^2 u}{\partial\theta^2} + \frac{\sigma_\theta}{E} (1 + u) = p - \frac{\sigma_\theta}{E} \left(u_i + \frac{\partial^2 u_i}{\partial\theta^2}\right) \tag{5.4}$$

in which dots indicate differentiation with respect to τ and σ_θ is the circumferential membrane stress.

For simplicity, we will treat only the cos $n\theta$ terms in the initial shape and pressure imperfections so that the displacements and pressure can be expanded in the series

$$u_i(\theta) = \sum_{n=1}^{\infty} \delta_n \cos n\theta \tag{5.5}$$

$$u(\theta,\tau) = u_o(\tau) + \sum_{n=1}^{\infty} u_n(\tau) \cos n\theta \tag{5.6}$$

$$p(\theta,\tau) = p_o(\tau) + \sum_{n=1}^{\infty} p_n(\tau) \cos n\theta \tag{5.7}$$

Substituting these into (5.1) and equating the coefficients of each term in the series gives

$$\ddot{u}_o + \frac{\sigma_\theta}{E} (1 + u_o) = p_o \tag{5.8}$$

$$\ddot{u}_n + (n^2 - 1)\left[\frac{\alpha^2 E_t}{E} n^2 - \frac{\sigma_\theta}{E}\right] u_n = p_n + \frac{\sigma_\theta}{E} (n^2 - 1)\delta_n \tag{5.9}$$

The shell is taken at rest in the initial unstressed condition, giving initial conditions

$$u_n(0) = \dot{u}_n(0) = 0 \quad , \qquad n = 0, 1, 2, \ldots \qquad (5.10)$$

The normalized amplitude u_o of the hoop mode is the membrane strain ε_o so that u_o is small and omitted compared to unity in Eq. (5.8), giving a linear equation. Simple analytic solutions for u_o for the triangular and exponential pulses in Fig. 5.2 were obtained by replacing the actual stress-strain curve by two straight lines, one at the elastic slope E and the other at an average strain-hardening modulus E_h . For the flexural motion, however, E_t appears as a coefficient in Eq. (5.9) and a continuous variation of E_t was used. With $u_o(\tau) = \varepsilon_o(\tau)$ known, σ_θ and E_t were taken as functions of time from the stress-strain curve,* inserted into Eq. (5.9), and the motion of the flexural modes were found by numerical integration. The material properties used are given in Appendix A.

5.3.2 Elastic Model

The governing equations of motion for the elastic model are obtained using Donnell's equations[6] with the addition of inertia terms. As in the static buckling analysis of cylindrical shells, the uniform radial deformation is assumed to be independent of the length and end conditions, but it is required that the superimposed flexural deformations satisfy the end constraints. This assumption allows the equation of motion to be separated into individual uncoupled equations for each mode.

---

*As in Ref. 5, for convenience we neglect the Poisson effect $(1 - \nu^2)$ and take σ_θ and E_t in both the elastic and plastic range directly from available simple tension experiments rather than from circumferential compression tests under appropriate axial constraint.

The equation of equilibrium in the radial direction is

$$D\nabla^4 w + N_x \frac{\partial^2}{\partial x^2}(w + w_i) + \frac{2N_{x\theta}}{a}\frac{\partial^2}{\partial x \partial\theta}(w + w_i) + \frac{N_\theta}{a^2}\frac{\partial^2}{\partial\theta^2}(w + w_i)$$

$$+ \frac{N_\theta}{a} + \rho h \frac{\partial^2 w}{\partial t^2} - p^* = 0 \tag{5.11}$$

where N_x, $N_{x\theta}$, N_θ are the membrane forces with the sign convention chosen so that compression is considered positive, D is the flexural rigidity of the shell wall, and ∇^2 the Laplacian operator:

$$D = \frac{Eh^3}{12(1 - \nu^2)} \quad , \qquad \nabla^2 = \frac{\partial^2}{\partial x^2} + \frac{\partial^2}{a^2 \partial\theta^2} \tag{5.12}$$

The force N_θ is taken as the sum of two parts, one caused by the uniform radial deformation and the other caused by flexural deformations; thus

$$N_\theta = \frac{Eh}{1 - \nu^2}\frac{w_o}{a} + \frac{\partial^2 F}{\partial x^2} \tag{5.13}$$

where F is a stress function for the membrane forces produced by flexural deformations and w_o is the uniform radial deformation. The membrane forces N_x and $N_{x\theta}$ are assumed to be independent of the uniform radial motion, and for the flexural motion are given in the usual manner in terms of F :

$$N_x = \frac{\partial^2 F}{a^2 \partial\theta^2} \quad , \qquad N_{x\theta} = - \frac{\partial^2 F}{a \partial\theta \partial x} \tag{5.14}$$

The compatibility condition between the midsurface strains then requires that

$$\nabla^4 F = \frac{Eh}{a}\frac{\partial^2 w}{\partial x^2} \tag{5.15}$$

The use of a stress function in the manner shown satisfies static equilibrium in the x and y directions but neglects the small in-plane inertia forces.

It is convenient to introduce the nondimensional quantities

$$\xi = \frac{x}{a} \quad , \quad u = \frac{w}{a} \quad , \quad u_i = \frac{w_i}{a} \quad , \quad \ell = \frac{L}{a} \quad , \quad \tau = \frac{ct}{a} \qquad (5.16)$$

and express u, u_i, and p^* in the series forms

$$u(\xi,\theta,\tau) = u_o(\tau) + \sum_{n=1}^{\infty} u_n(\tau) \cos n\theta \sin \frac{\pi\xi}{\ell} \qquad (5.17)$$

$$u_i(\xi,\theta) = \sum_{n=1}^{\infty} \delta_n \cos n\theta \sin \frac{\pi\xi}{\ell} \qquad (5.18)$$

$$p^*(\xi,\theta,\tau) = \frac{Eh}{a(1-\nu^2)} \left[p_o(\tau) + \sum p_n(\tau) \cos n\theta \sin \frac{\pi\xi}{\ell} \right] (5.19)$$

Representing the radial deformation by Eq. (5.17) assumes simple support conditions for the flexural motion, as well as restricting the deformation to a half-wave in the axial direction. The latter assumption is based on experience with static buckling and experimental results of dynamic buckling. Although the assumption of simple supports is not representative of the actual test conditions in the present program, results from the simple support theory agree reasonably well with the experiments. To comply with the assumed form of the displacement, the initial shape imperfections and pressure perturbations are also taken to vary sinusoidally in the axial direction, as given in Eqs. (5.18) and (5.19).

Using Eqs. (5.16) and (5.17) in (5.15) yields

$$\frac{1}{a^4}\left(\frac{\partial^2}{\partial\xi^2} + \frac{\partial^2}{\partial\theta^2}\right)^2 F = -\frac{Eh}{a^2} \sum_{n=1}^{\infty} \frac{\pi^2}{\ell^2} u_n \cos n\theta \sin \frac{\pi\xi}{\ell}$$

from which it can be concluded that, for simple supports, F is of the form

$$F = \sum_{n=1}^{\infty} \alpha_n u_n \cos n\theta \sin \frac{\pi\xi}{\ell} \tag{5.20}$$

where α_n are constants.

Using Eqs. (5.13 - 5.19), taking F in the form of Eq. (5.20), and dropping all second-order terms in u_n, the equilibrium equation (5.15) can be separated to give

$$\ddot{u}_o + u_o = p_o \tag{5.21}$$

and

$$\ddot{u}_n + \left[\alpha^2\left(n^2 + \frac{\pi^2}{\ell^2}\right)^2 + \frac{\left(1 - \nu^2\right)\left(\frac{\pi}{\ell}\right)^4}{\left(n^2 + \frac{\pi^2}{\ell^2}\right)^2} - n^2 u_o\right] u_n \tag{5.22}$$

$$= p_n + n^2 u_o \delta_n \qquad n = 1,2,3\ldots$$

The shell is taken initially at rest with zero displacement as in Eq. (5.10).

Equation (5.21) is solved analytically, and the resulting expression for u_o is substituted into Eq. (5.22) but, as for the tangent modulus model, the resulting equations for the flexural modes must be integrated numerically, since no analytical solution is apparent.

For a static pressure the derivatives with respect to time vanish and Eq. (5.21) gives $u_o = p_o$. Substituting this into Eq. (5.22), the coefficient of u_n vanishes at a critical pressure for each mode number given by

$$\left(p_o\right)_{cr} = \frac{1}{n^2}\left[\alpha^2\left(n^2 + \frac{\pi^2}{\ell^2}\right)^2 + \frac{\left(1 - \nu^2\right)\left(\frac{\pi}{\ell}\right)^4}{\left(n^2 + \frac{\pi^2}{\ell^2}\right)^2}\right] \tag{5.23}$$

The smallest of these critical pressures is the static collapse pressure which, for $\nu = 0.3$, is given approximately by

$$p_o = 0.92E \left(\frac{a}{L}\right)\left(\frac{h}{a}\right)^{5/2} \tag{5.24}$$

This is the result presented in Ref. 6 and is valid for

$$100 \lesssim Z \lesssim 10\left(\frac{a}{h}\right)^2$$

in which $Z = (1 - \nu^2)^{1/2} L^2/ah$.

5.4 Amplification Functions and Critical Curves for Buckling

The governing equations of motion for both the tangent modulus and elastic models exhibit the same general features, a single equation to determine the motion of the uniform hoop mode, and for each flexural mode an equation that contains the hoop membrane force as a coefficient. The equations can be put in the form

$$\ddot{u}_o + \frac{N_\theta}{Eh}(1 - \nu^2) = p_o \tag{5.25}$$

and

$$\ddot{u}_n + (\omega_n^2 - \beta_n N_\theta)u_n = p_n + \beta_n N_\theta \delta_n \tag{5.26}$$

where ω_n are the (no-load) bending frequencies and β_n are constants.

The major feature of the solutions is that for a sufficiently large value of N_θ the coefficient of u_n in Eq. (5.26) becomes negative over a range of n and the solution becomes hyperbolic in character rather than oscillatory; these are the buckling modes, and the hyperbolic growth can lead eventually to permanent flexural deformations. The general problem is to determine the pressure-impulse levels that cause a particular flexural mode or group ~ flexural modes to grow to magnitudes sufficiently large to exceed a specific buckling criterion.

To demonstrate the type of growth that occurs in each of the load regions in Fig. 5.3, consider an example of a shell subjected to triangular pressure pulses. The shell is made of 6061-T6 aluminum with $a/h = 100$ and $L/D = 1$. The general procedure was to integrate the equations of motion as described, which yields an amplification $u_n(t)/\delta_n$ for each flexural mode.* These were then plotted against n, giving an amplification function for each combination of peak pressure and impulse (load point). Example curves are given in Fig. 5.5.

For impulsive loads high amplification does not occur until the hoop strains are in the plastic range, giving high values of σ_θ/E_t. These high values make the coefficient of u_n in Eq. (5.9) negative for a wide range of n, and most negative (at each instant) for $n = (\sigma_\theta/2\alpha^2 E_t)^{1/2}$. This is reflected in Fig. 5.5a by a broad amplification function, extending to mode numbers as high as $n = 150$ and having a maximum at $n = 95$. Thus, under impulsive loads the shell has a strong tendency to buckle into a high order pattern and, as postulated, shell length has little effect.†

To calculate loads at a threshold of buckling it has been shown[7] that it is reasonable to assume that random imperfections are present at all wavelengths. Thus, the dominant modes of buckling are selected by the amplification function, and buckling can be said to be eminent when the peak amplitude reaches a critical value. In this chapter, buckling thresholds are calculated on the basis of an amplification of 1000. Although this value was selected rather arbitrarily, it will be shown that the change in load over a range of amplifications from 100 to 10,000 is small for most practical applications.

---

*Only perturbations δ_n in shape are treated here. In Appendix B it is demonstrated that these are likely to dominate over perturbations in pressure.

†A more extensive discussion of this type of buckling is given by Abrahamson and Goodier[1] under the simplifying assumption that σ_θ and E_t are constant.

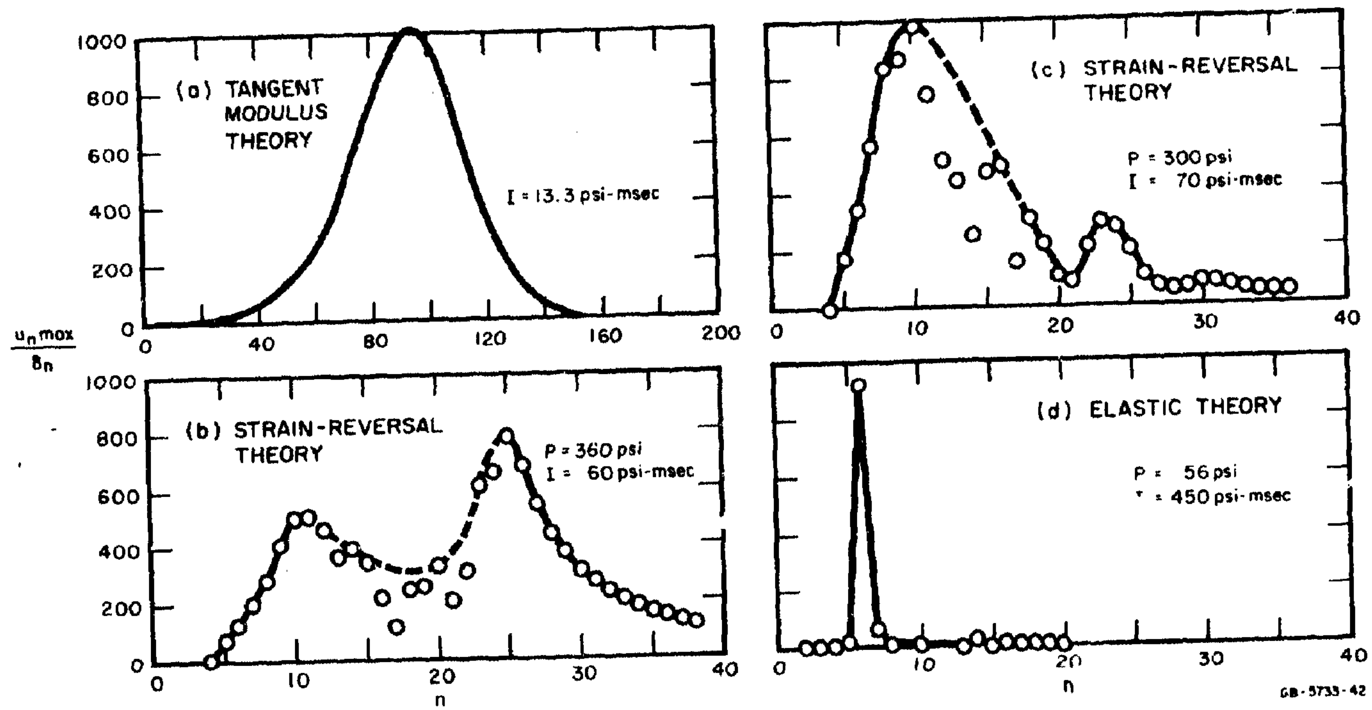

FIG. 5.5 TYPICAL AMPLIFICATION FUNCTIONS FOR (a) IMPULSIVE, (b) AND (c) QUASI-IMPULSIVE, AND (d) QUASI-STATIC LOADS. (All for triangular pulses and 6061-T6 aluminum shell with a/h = 100, L/D = 1.)

Using this criterion, a critical curve for buckling was calculated in the impulsive range using the tangent modulus theory. This is the upper curve in Fig. 5.6. The curve is hyperbolic in shape, approaching a critical impulse for high pressures and a critical pressure for large impulses. The mode number of maximum amplification increases with peak pressure as shown by the numbers on the curve. Approximate formulas for such curves are given later

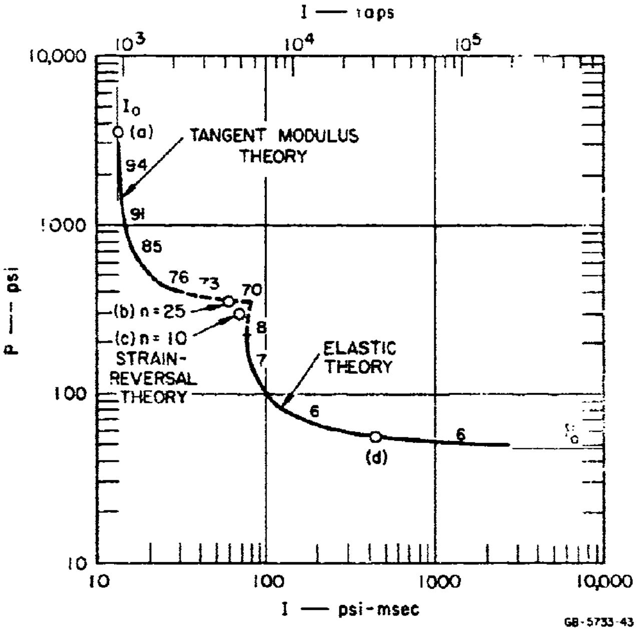

FIG. 5.6 CRITICAL CURVE FOR BUCKLING OF SHELL IN FIG. 5.5

At the other extreme, under a quasi-static load having a low pressure and long duration, results from the elastic model, given in Fig. 5.5d, show that very large amplification is confined to $n = 6$, the static buckling mode for this shell. As the duration of the load is increased still further, the minimum peak pressure that gives large amplification approaches the static pressure as given by Eq. (5.24) even though the pressure pulse rises instantaneously to its peak value.

The sudden rise causes overshoot and oscillation in the hoop mode, but any energy transferred from this oscillation to the buckling mode must be made through a series of many oscillations in the buckling mode. This type of Mathieu instability[8] cannot cause large plastic deformations of the type observed in the experiments because the kinetic energy in the membrane oscillation is finite and, if the flexural oscillations are sufficiently large to cause plastic strains, the energy would be extracted in small amounts at each oscillation. Instead, the dominant buckling growth is caused by the psuedo-static component $u_o = p_o(\tau)$ of the membrane motion about which the hoop mode oscillates. Experiments[9] show that buckling takes place with little or no oscillation and is essentially a single growth to large deformations. Because of the observations, throughout the present analysis only modes exhibiting hyperbolic-type growth are considered to be significant for buckling.

A critical curve for buckling (amplification = 1000) under quasi-static loads was calculated using the elastic model and appears as the lower hyperbola-shaped curve in Fig. 5.7. As in the tangent modulus curve, the mode number of the most amplifide mode increases with increasing peak pressure. Pressures greater than about half the static yield pressure result in hoop strains beyond the elastic limit, but the dotted curve is extended to higher pressures assuming that the material remains elastic. This extension meets the curve from the tangent modulus theory in a cusp-like intersection and there is a sudden jump in the mode number of the most amplified mode in going from the elastic branch to the tangent modulus branch. Although the theory is not strictly applicable near this cusp, application of the strain-reversal theory shows that a cusp still persists and that there is a jump in mode number.

Amplification functions from the strain reversal theory applied near the cusp (as shown by the points in Fig. 5.6) are given in Figs. 5.5b and c. These show the reason for the jump in mode number. Because load points in this region have high enough peak pressures to induce plastic flow in the hoop mode, and also have durations long enough to allow growth of the low order "elastic" modes, large growth takes place in both high and low order modes. Thus two maxima appear in the

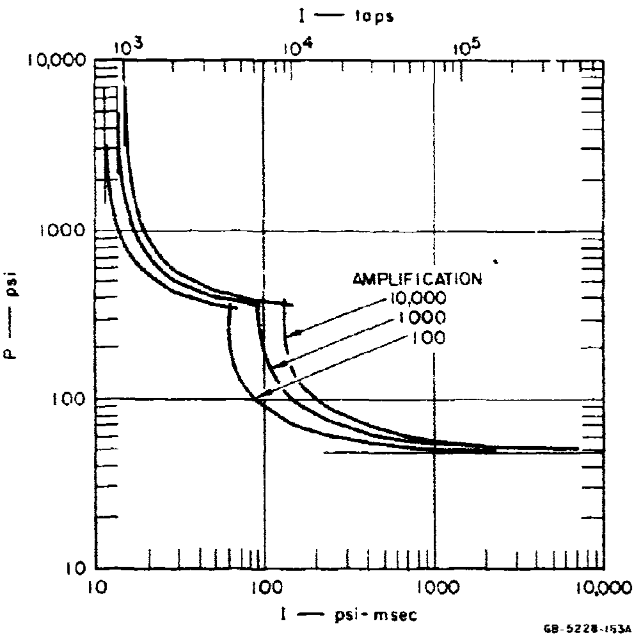

FIG. 5.7 CRITICAL CURVES FOR BUCKLING AMPLIFICATIONS OF 100, 1000, AND 10,000 (Exponential pulses, same shell as Fig. 5.5)

amplification function and a small change in load point changes the absolute maximum from a high order to a low order mode, or vice-versa. This is illustrated by the large shift in relative amplification in going from a peak pressure of 360 psi and impulse of 60 psi-msec (Fig. 5.5b) to a slightly smaller peak pressure of 300 psi and larger impulse of 70 psi-msec (Fig. 5.5c). The amplifications of intermediate modes fluctuate because in this range of loads buckling takes place during a few oscillations of the hoop mode and small changes in phase between the hoop and flexural modes significantly affect the amplification, although the overall growth is exponential in nature.

Since the general behavior of the complete critical curve for buckling in Fig. 5.6 is adequately described by using only the simpler tangent modulus and elastic theories, no detailed discussion of the strain reversal model is given in this report. Development of a more complete elastic-plastic theory is still in progress.

To examine the influence of the magnitude of the amplification buckling criterion, critical curves were calculated as described above for amplifications of 100, 1000, and 10,000. These are given in Fig. 5.7, which shows that over most of the load range the curves differ by less than ±15%. The maximum difference, in the quasi-impulsive range, is a factor of 1.6 between the 100 and 1000 amplification curves. Thus, although buckling from pulse loads cannot be described with the accuracy of an eigenvalue problem in static buckling, the hyperbolic growth makes exact specifications of a critical amplification of secondary importance.

5.5 Effects of Parameter Variations on Critical Curves

Before giving approximate formulas for determining critical buckling curves, the numerical integration procedure is used to generate example curves which demonstrate the effects of variations in pulse shape, radius-to-thickness ratio, and length-to-diameter ratio.

5.5.1 Pulse Shape

Figure 5.8 gives a comparison between critical curves calculated for exponential and triangular pulse shapes. The maximum difference between the curves (measured along a line at 45^{o}) is 35% and occurs in the knee of each branch. This difference is not significant in many applications and we can conclude that changes in pulse shape are of secondary importance.

5.5.2 Radius-to-Thickness Ratio

Figure 5.9 gives critical curves for $L/D = 1$ with a/h ranging from 24 to 250; each curve is normalized to I_o and P_o for the given a/h. The major effect of increasing a/h is an upward movement of the intersection between the tangent modulus and elastic branches, resulting in a broader range of quasi-impulsive response for the thinner (higher a/h) shells. These same curves are repeated in Fig. 5.10 without the normalization to show the broad range of pressures and impulses involved.

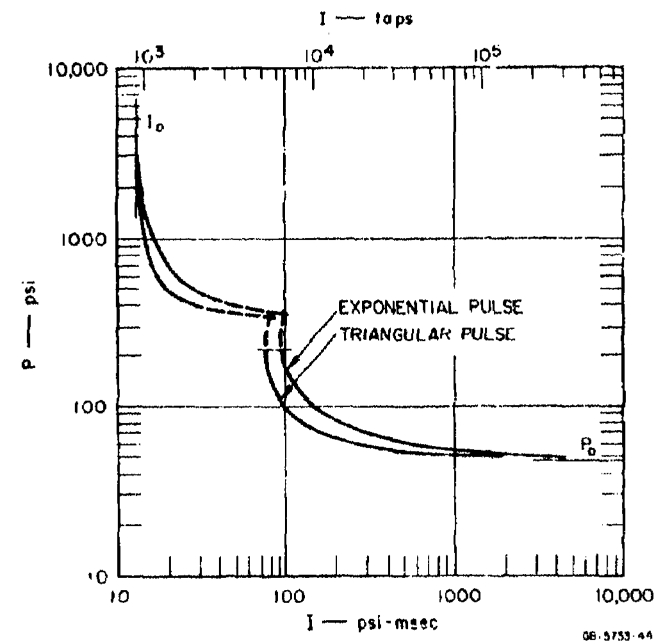

FIG. 5.8 EFFECT OF PULSE SHAPE ON CRITICAL CURVES FOR BUCKLING (same shell as Fig. 5.5)

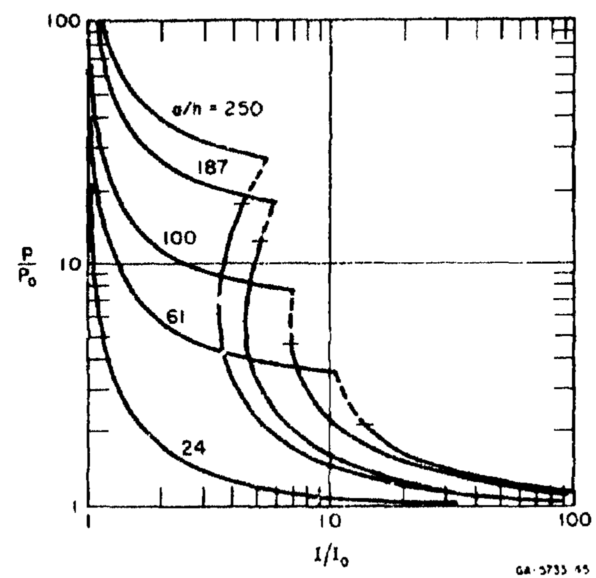

FIG. 5.9 EFFECT OF a/h ON CRITICAL CURVES FOR BUCKLING (exponential pulses, 6061-T6 aluminum, L/D = 1, curves normalized to P_o and I_o for each shell)

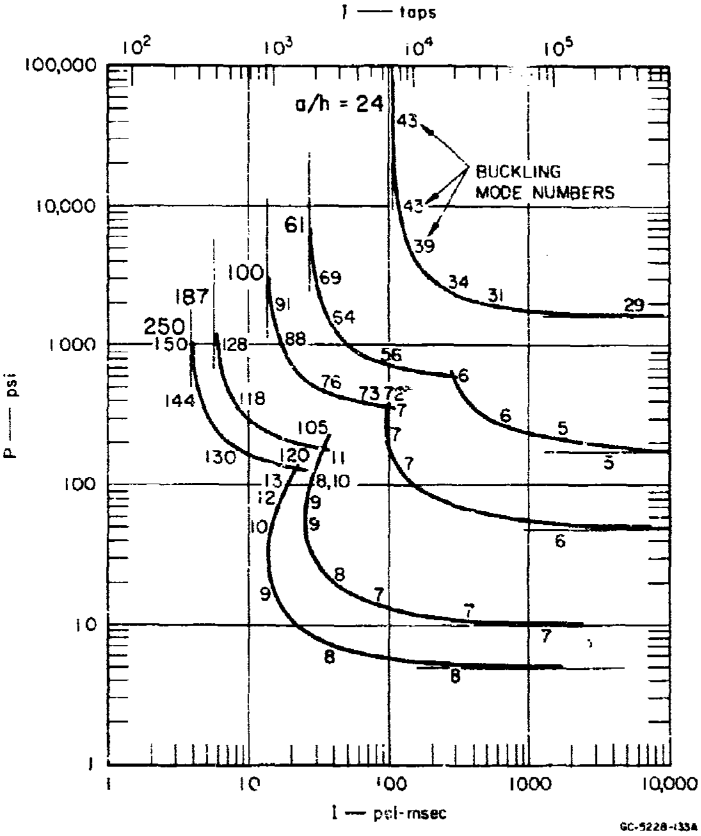

FIG. 5.10 EFFECT OF a/h ON CRITICAL CURVES FOR BUCKLING
(Same as Fig. 5.9, but without normalization for D = 6 inches)

5.5.3 Length-to-Diameter Ratio

Variations in L/D affect only the elastic branch, as shown in Fig. 5.11. Thus the main effect of increasing L/D is to lower the quasi-static pressure asymptote P_o, giving a broader range of quasi-impulsive loads as for thin cylinders. The impulse "asymptote" of the elastic branch does not change significantly because the mode numbers in this region are sufficiently high that end effects are secondary.

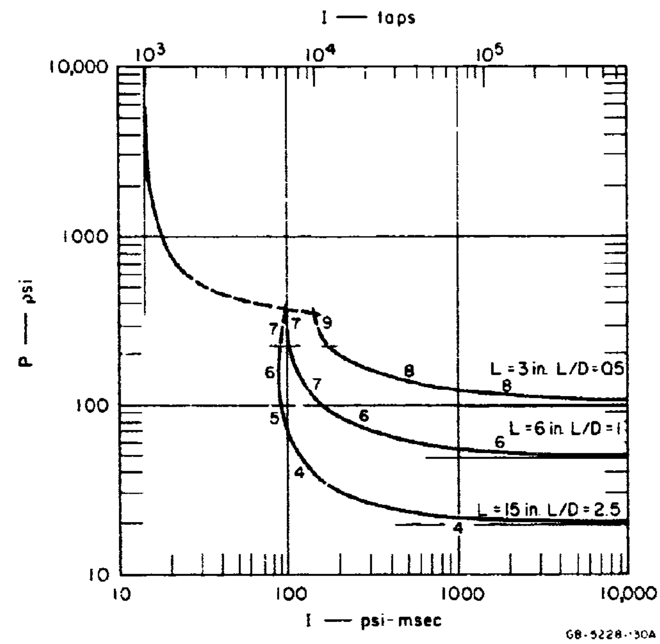

FIG. 5.11 EFFECT OF L/D ON CRITICAL CURVES FOR BUCKLING (exponential pulses, 6061-T6 aluminum, D = 6 inches, a/h = 100)

5.6 Approximate Formulas for Critical Curves

The general form of the critical buckling curves in the preceding examples is given in Fig. 5.12 and can be described by a few approximate formulas based on the results of the numerical integration. The curves consist of two branches, one from each model, each of which can be approximated to an accuracy of about 20% by simple hyperbolas of the form

$$\left(\frac{P}{P_A} - 1\right)\left(\frac{I}{I_A} - 1\right) = 1 \tag{5.27}$$

where P_A and I_A are the asymptotic values of the hyperbola. For the

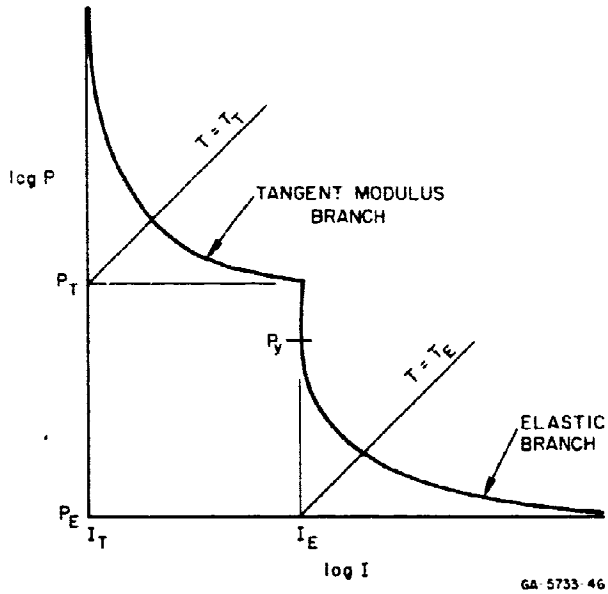

FIG. 5.12 CHARACTERIZATION OF CRITICAL CURVES FOR BUCKLING

tangent modulus branch these asymptotes are given by*

$$P_T = \frac{3}{4}\,\sigma_y\,\frac{h}{a} \tag{5.28}$$

$$I_T = \left(\frac{96}{K}\right)^{1/4} a\left(\rho\sigma_y\right)^{1/2}\left(\frac{h}{a}\right)^{3/2} \tag{5.29}$$

where K is the slope beyond yield of a plot of σ/E_t versus compressive hoop strain for the shell material.† For the elastic branch, from Eq. (5.24) and observation of the numerical results, the asymptotes are given by

$$P_E = 0.92E\left(\frac{a}{L}\right)\left(\frac{h}{a}\right)^{5/2} \tag{5.30}$$

$$I_E = 5\ \rho c a\left(\frac{h}{a}\right)^2 \tag{5.31}$$

*The formula for P_T is an empirical observation of the numerical integration; a derivation of I_T is given in Appendix C.

†See Appendix A.

The lines at 45 degrees in the log-log plot of Fig. 5.12 define a characteristic time I_A/P_A for each branch which can be compared directly, for example, with the characteristic time $T = I/P$ for an exponential pulse. From Eqs. (5.28) and (5.29), the characteristic time for the tangent modulus branch is

$$T_T = \left(\frac{96}{K}\right)^{1/4} \frac{4a}{3c} \varepsilon_y^{-1/2} \left(\frac{h}{a}\right)^{1/2} \tag{5.32}$$

However, in the numerical examples it was found that variations in K moved the horizontal pressure asymptote slightly from the value given in Eq. (5.28) in such a way as to compensate for the small variation of T_T with K given in Eq. (5.32). Thus, a better expression of T_T with K in the range $10 < K < 60$, typical of many engineering metals, is simply

$$T_T = 2 \frac{a}{c} \varepsilon_y^{-1/2} \left(\frac{h}{a}\right)^{1/2} \tag{5.33}$$

Similarly, from Eqs. (5.30) and (5.31), the characteristic time for the elastic branch is

$$T_E = 5.5 \frac{L}{c} \left(\frac{a}{h}\right)^{1/2} \tag{5.34}$$

From Fig. 5.12 we see that if the time constant T of the applied pulse is much shorter than T_T , the load appears impulsive to the shell, and if T is much larger than T_E , the load appears quasi-static. Loads with durations near or between T_T and T_E are quasi-impulsive, and both pressure and impulse are important to the response. As shells become longer and thinner, T_T and T_E become more widely separated (see Figs. 5.9 - 5.11) and the range of quasi-impulsive loads increases. Conversely, for short, thick shells, the tangent modulus and elastic curves move closer together and only a small range is quasi-impulsive.

5.7 Buckling from Asymmetric Loads

In all the experiments in the present investigation, and in many practical applications, the load is applied by a blast wave passing laterally across the shell. For moderately short duration blast waves (in the quasi-impulsive and somewhat into the quasi-static range in Fig. 5.3), the load is dominated by the diffraction phase and can be approximated by[9]

$$p(\theta,t) = (p_r - p_i)\cos^2\theta + p_i \qquad -\frac{\pi}{2} \le \theta \le \frac{\pi}{2}$$

$$= p_i \qquad \frac{\pi}{2} \le \theta \le \frac{3\pi}{2} \tag{5.35}$$

where p_r and p_i are reflected and incident pressures, both assumed to have the same exponential decay with time.*

A rigorous treatment of shell buckling under asymmetric loads would be very difficult, particularly since both elastic and plastic-flow buckling must be considered, as we have seen for symmetric loads. However, experiments show that critical pressure-impulse curves from the symmetric load theory give reasonable estimates for buckling under smoothly varying asymmetric loads such as in Eq. (5.35), taking pressure and impulse at the peak load. This is demonstrated for impulsive plastic-flow buckling in Fig. 5.13, which shows two shells, one buckled from a cosine impulse over one side and the other buckled from a uniform impulse of the same peak intensity. Both exhibit the same plastic deformation and buckling in the area of the peak load. Similar examples are given in Ref. 9 for shells subjected to quasi-static loads.

*The small transit time of the shock across the cylinder is neglected, and the pressure on the back surface (away from the oncoming blast) rises slowly instead of sharply as does the front surface pressure in Fig. 5.2. Neither effect has a serious influence on the shell buckling, however, because the buckling is dominated by the front surface pressure.

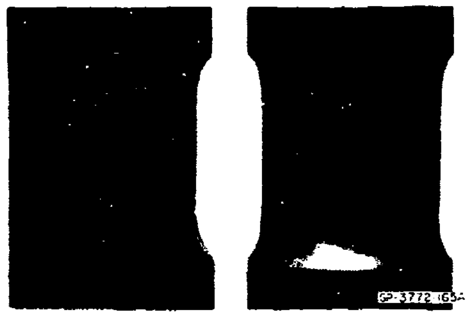

FIG. 5.13 PLASTIC-FLOW BUCKLING FROM ASYMMETRIC (left) AND SYMMETRIC (right) IMPULSIVE LOADS (6061-T6 aluminum, D = 3 inches, L/D = 1, a/h = 24, peak impulse 150 psi-msec for both shells)

The type of response likely to differ most widely under symmetric and asymmetric loads is elastic buckling from impulsive loads, which occurs in very thin shells.[2] Payton's[10] membrane solution for a cosine impulse over one side shows that the peak membrane stress (occurring under the peak impulse I) is about 70% of that in a shell under a uniform impulse I, and the duration of the first positive swing (during which buckling takes place) is also about 70% of the half period of the symmetric (hoop) mode. Thus, since the buckling is in very high order modes and grows in proportion to the product of the peak stress and duration (see Ref. 7), buckling under an asymmetric load requires a peak impulse about twice the impulse under a symmetric load. In moderately thick shells ($a/h \lesssim 100$), however, buckling takes place during plastic flow and the results in Fig. 5.13 suggest that for these shells asymmetric and symmetric buckling impulses will differ by less than the factor of 2 estimated above the impulsive elastic buckling.

Under quasi-static (long) loads, asymmetric and symmetric buckling loads are quite close because the buckling is dominated by the psuedo-static membrane stress, which is proportional to peak pressure. Thus, the essential requirement for similarity in peak buckling load is only that the pressure does not vary significantly over a buckle wavelength. This is true for the smoothly varying pressures and relatively high order buckling modes here. To a better approximation, Almroth's [11] results for static asymmetric buckling show that an average pressure over a buckle wavelength could be used.

5.8 Comparison of Theory and Experiment

Extensive experiments were run on aluminum and magnesium shells with L/D = 1 and radius-to-thickness ratios from 24 to 250. These are described in detail in Ref. 9 and only a few results are given here for demonstration. The shells were made from extruded tubing or rolled sheet stock and were clamped rigidly at each end to heavy plugs. They were subjected to lateral blast loads from explosive spheres and from an explosive shock tube. Pulse shapes and pressure distributions from these loads were measured on rigid models. The measured pulses were very nearly exponential in shape as shown in Fig. 5.2b, and peak pressure varied around the shell approximately as the $\cos^2\theta$ distribution given in Eq. (5.35).

Figure 5.14 gives theoretical and experimental buckling curves for shells with a/h = 100 and a/h = 61. The lower experimental curves give the maximum loads at which no permanent deformation of any type was observed, and the upper experimental curves give loads at which the peak permanent buckling deformation was about 10% of the shell radius. It was a general observation that for quasi-static loads the two experimental curves approached each other very closely; the shells were either undamaged or severely buckled with deformations as large as 50% of the radius. The impulsive end of the no-damage and 10%-buckling curves differed by as much as a factor of 2. Increases in load of about 50% above the buckling curves generally resulted in very severe buckling and tearing.

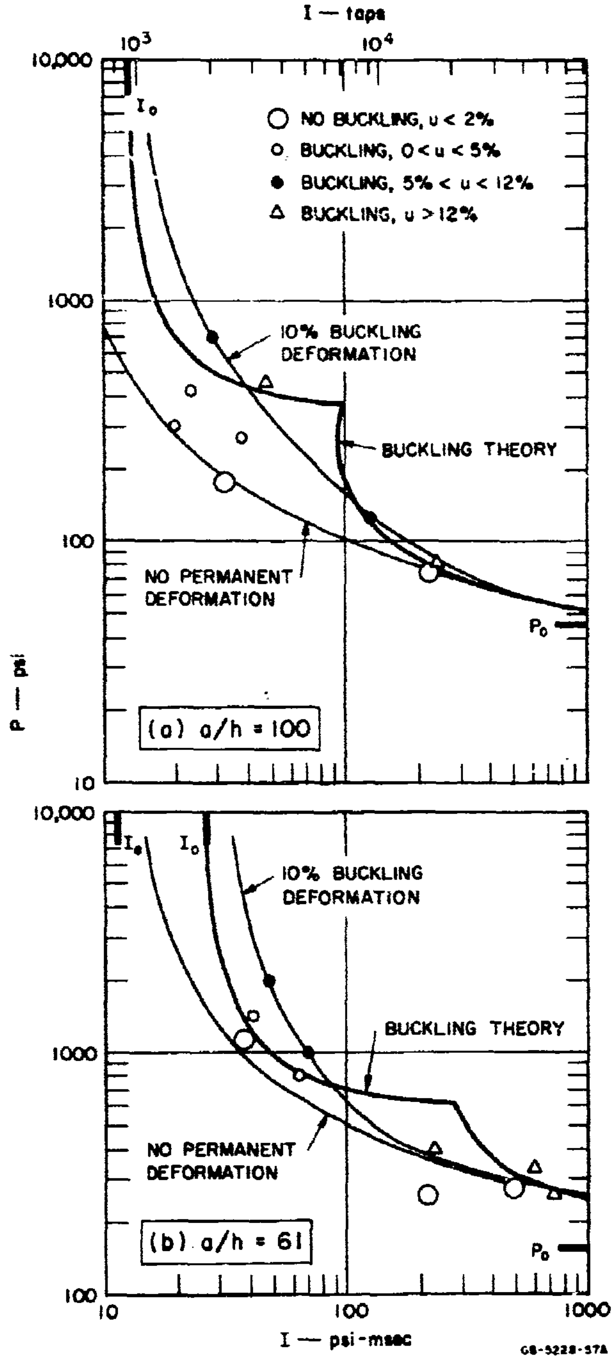

FIG. 5.14 COMPARISON OF THEORETICAL AND EXPERIMENTAL CRITICAL CURVES (exponential pulses, 6061-T6 aluminum, D = 6 inches, L/D = 1)

The theoretical buckling curves in Fig. 5.14 lie within about 30% of the experimental buckling curves over the entire range of pressure and impulse. There was a hint of a cusp-like shape in the experimental curves, but the curves are drawn with a smooth hyperbolic shape because very extensive experiments would be required to justify an inflection. Mode numbers of buckling on the elastic model branch agreed well with observed buckling in this load range. Mode numbers on the tangent modulus branch were sometimes as large as twice the experimental values, partly because of poor material property data and partly because strain reversal was neglected; the strain reversal model gave mode numbers in closer agreement with experiment. These favorable comparisons between theory and experiment demonstrate that the assumptions made in the analysis are reasonable and the theory will be useful in predicting pulse buckling of cylindrical shells.

REFERENCES

1. Abrahamson, G. R. and J. N. Goodier, "Dynamic Plastic Flow Buckling of a Cylindrical Shell from Uniform Radial Impulse," Proceedings of Fourth National Congress of Applied Mechanics 2, 939-950,(1962).

2. Lindberg, H. E., "Buckling of a Very Thin Cylindrical Shell due to an Impulsive Pressure," J. Appl. Mech. 31, 267-272, 1964.

3. Timoshenko, S. P. and J. M. Gere, Theory of Elastic Stability, McGraw-Hill Book Co., Inc., New York, N.Y. (1961).

4. Abrahamson, G. R., "Characterization of Critical Pulse Loads in Structural Dynamics," (submitted for publication).

5. Lindberg, H. E., "Dynamic Plastic Buckling of a Thin Cylindrical Shell Containing an Elastic Core," J. Appl. Mech. 32, 803-812, 1965.

6. Batdorf, S. B., "A Simplified Method of Elastic-Stability Analysis for Thin Cylindrical Shells," NACA Report No. 874, 1947.

7. Lindberg, H E., "Impact Buckling of a Thin Bar," J. Appl. Mech. 32, 315-322, 1965.

8. Goodier, J. N. and I. K. McIvor, "The Elastic Cylindrical Shell under Nearly Uniform Radial Impulse," J. Appl. Mech. 31, 259-266, 1964.

9. Lindberg, H. E., D. L. Anderson, R. D. Firth, and L. V. Parker, "Response of Reentry Vehicle-Type Shells to Blast Loads," Stanford Research Institute Final Report, Contract AF04(694)-655, subcontract LMSC 24-14517, September 30, 1965, LMSC-B130200, Vol. IV-C.

10. Payton, R. G., "Dynamic Membrane Stresses in a Circular Elastic Shell," J. Appl. Mech. 28, 417-420, 1961.

11. Almroth, B. O., "Buckling of a Cylindrical Shell Subjected to Nonuniform External Pressure," J. Appl. Mech. 29, 675-682, 1962.

12. Lindberg, H. E. and R. E. Herbert,"Dynamic Buckling of a Thin Cylindrical Shell under Axial Impact," J. Appl. Mech. 33, 105-112, 1966.

13. Florence, A. L. and J. N. Goodier, "Dynamic Plastic Buckling of Thick Cylindrical Shells in Sustained Axial Compressive Flow," (submitted to J. Appl. Mech.).

APPENDIX A

MATERIAL PROPERTIES USED IN THE CALCULATIONS

In the tangent modulus model the numerical calculations were made using stress-strain data taken from tension tests on longitudinal samples cut from the shell materials. The most important material properties are Young's modulus, yield stress, and the variation of σ/E_t with strain. Figure A.1 gives plots of σ/E_t for several metals and

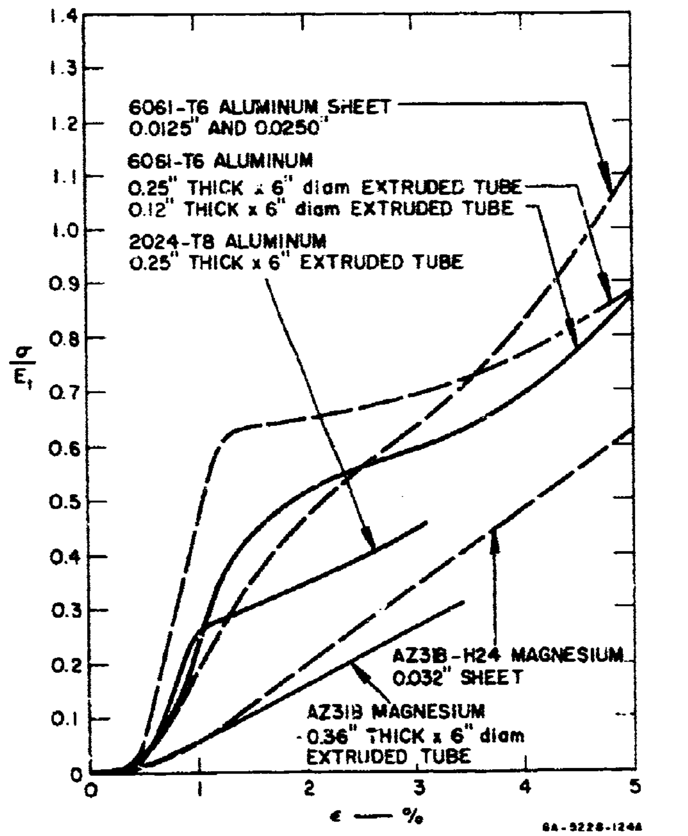

FIG. A.1 MATERIAL TANGENT MODULUS PROPERTIES
(from longitudinal tensile specimens)

shows that for many of them σ/E_t increases approximately linearly with strain beyond yield. Therefore, to the accuracy of the stress-strain data, the calculations were made using the formula

$$\begin{aligned} \sigma/E_t &= \sigma/E = \varepsilon & \varepsilon &\leq \varepsilon_y \\ \sigma/E_t &= K(\varepsilon - \varepsilon_y) + \varepsilon_y & \varepsilon &\geq \varepsilon_y \end{aligned} \qquad \text{(A 1)}$$

where K is the slope taken from Fig. A.1. Values of K and other pertinent properties are given in Table A.1 for the three metals used.

Table A.1

MATERIAL PROPERTIES
(Tensile Test Data)

Material	E (psi)	σ_y (psi)	E_h/E	ν	K	ρ (lb/in^3)
6061-T6 Al.	10×10^6	45,000	0.006	0.3	30	0.098
2024-T8 Al.	11×10^6	66,000	0.033	0.3	35	0.100
AZ31B Mag.	6×10^6	24,000	0.05	0.3	10	0.064

APPENDIX B

RELATIVE IMPORTANCE OF SHELL AND LOAD PERTURBATIONS

To examine the relative importance of shell and load perturbations in triggering buckling, we consider buckling under an ideal impulse I_o and obtain analytic results using the simplified equations studied by Abrahamson and Goodier.[1*] For an ideal impulse the pressure term in Eq. (5.9) is dropped and the initial conditions in Eq. (5.10) are replaced with

$$u_n(0) = 0 \quad , \qquad \dot{u}_n(0) = \frac{\beta_n I_o}{\rho c h} \tag{B.1}$$

where $\beta_n I_o$ is the perturbation of I_o in the n^{th} mode. Treating σ_ϵ and E_t as constants, as in Ref. 1, the solution to Eq. (5.9) with initial conditions (B.1) is

$$u_n = \frac{s^2 \delta_n}{s^2 - n^2}\left[\cosh q_n \tau - 1\right] + \frac{\beta_n I_o}{\rho c h \, q_n} \sinh q_n \tau \qquad n < s \tag{B.2}$$

where

$$s^2 = \frac{\sigma_\theta}{\alpha^2 E_t} \quad \text{and} \quad q_n^{\,2} = \frac{\alpha^2 E_t}{E}(n^2 - 1)(s^2 - n^2) \tag{B.3}$$

For large $q_n \tau$ the maximum displacement due to either shell imperfections δ_n or load imperfections β_n occurs approximately at the maximum value of q_n, given by

$$q_n \Big]_{max} \approx \frac{\sigma_y}{2E_t \alpha}\left(\frac{E_t}{E}\right)^{1/2} \quad \stackrel{\Delta}{=} \quad Q \tag{B.4}$$

---

*No simple solutions are apparent for quasi-impulsive loads and, for quasi-static loads, the effect of imperfection amplitudes is unimportant in the present problem (see Fig. 5.7).

and n is the integer n :est $s/\sqrt{2}$. Using Eqs. (B.1 - B.4) and $n \approx s/\sqrt{2} >> 1$, the ıtio can be formed between the maximum displacement due to shell impe: :ctions and that due to load imperfections, resulting in

$$\frac{u_{shell}}{u_{load}} = \frac{\delta_n}{\beta_n} \frac{\sigma_\theta}{\alpha V_o (\rho E_t)^{1/2}} \cdot \frac{\cosh Q\tau - 1}{\sinh Q\tau} \tag{B.5}$$

where $V_o = I_o/\rho h$ is the initial inward velocity of the shell wall. Finally, we recall from the definition of δ_n in Eqs. (5.2) and (5.5) that the shell imperfections in dimensional units are $w_{in} = a\delta_n$. Since impulse buckling is at very short wavelengths, it is more reasonable to take the imperfections proportional to the wall thickness h. Denoting shell imperfections by $w_{in} = h\gamma_n$ and observing that for large growth $\cosh Q\tau - 1 \approx \sinh Q\tau$, Eq. (B.5) becomes

$$\frac{u_{shell}}{u_{load}} = \frac{\gamma_n}{\beta_n} \frac{\sqrt{12}\,\sigma_\theta}{V_o (\rho E_t)^{1/2}} \tag{B.6}$$

Equation (B.6) can be interpreted directly in terms of the circumferential stress-strain curve for the shell material as shown in Fig. B.1 The initial kinetic energy of the shell wall is equated to the plastic work in membrane strain, neglecting the elastic and strain hardening contributions, giving

$$\frac{1}{2} \rho V_o^2 = \sigma_y \epsilon_{max} = \sigma_y \frac{\sigma_h}{E_t} \tag{B.7}$$

where σ_h is the increment in stress due to strain hardening as shown in Fig. B.1. Using Eq. (B.7) in Eq. (B.6) with $\sigma_\theta = \sigma_y$ as already assumed, we obtain

$$\frac{u_{shell}}{u_{load}} = \left(\frac{6\sigma_y}{\sigma_h}\right)^{1/2} \cdot \frac{\gamma_n}{\beta_n} \tag{B.8}$$

The strain-hardening increment σ_h is much smaller than the yield stress for many engineering materials; thus Eq. (B.8) shows that for these materials shell imperfections are likely to dominate over load imperfections if we can assume that shell imperfections in terms of percent wall thickness are comparable to percent imperfections in load. For example, a 6061-T6 aluminum shell with a/h = 50 buckles at about 1.5% strain with $E_t \approx 100{,}000$ psi, giving $\sigma_h = 1500$ psi. Using this in Eq. (B.8) with $\sigma_y \approx 50{,}000$ psi gives $(6\sigma_y/\sigma_h)^{1/2} = 14$. Thus, if we assume shell imperfections of 1% of the wall thickness (a reasonable value, from observations of bar buckling[7]), the impulse imperfection would have to be 14% of the peak impulse in order to give comparable buckling displacements. Such large load imperfections are very unlikely.

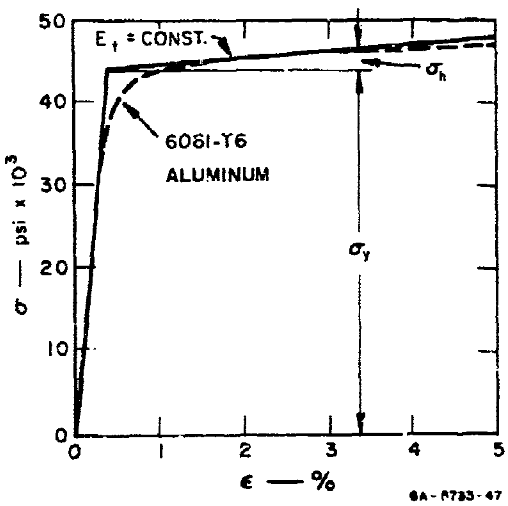

FIG. B.1 STRESS-STRAIN CURVE

APPENDIX C

CRITICAL IMPULSE FOR PLASTIC-FLOW BUCKLING

The simplified solution in Appendix B is also used to give the approximate formula (5.28) for impulsive buckling. The magnitude of u_n in Eq. (B.2) depends mainly on the argument $Q\tau$ of the hyperbolic term, since we are concerned with large amplifications in which exponential growth dominates. Thus, it is reasonable to assume that the buckling criterion of an amplification of 1000 corresponds closely to $Q\tau$ reaching a critical value, i.e.,

$$Q\tau_s = B \tag{C.1}$$

where B is a constant to be determined and τ_s is the nondimensional duration of the inward membrane plastic flow. In real time, this duration is given by

$$t_s = \frac{I_o a}{\sigma_y h} \tag{C.2}$$

in which the material has been assumed to be rigid-plastic. Using the definition $\tau = ct/a$ and combining Eqs. (B.4), (C.1), and (C.2), results in the following expression for the critical impulse I_o:

$$I_o = 2\alpha h \left(\rho\sigma_y\right)^{1/2} \left(\frac{E_t}{\sigma_y}\right)^{1/2} B \tag{C.3}$$

For a material in which E_t is nearly constant Eq. (C.3) suffices. However, for most materials E_t decreases significantly with increasing strain as discussed in Appendix A. In the numerical integration this increase was described by Eq. (A.1), treating σ/E_t as a function of ε and hence of time τ. Since most of the amplification of u_n takes place near the end of the hoop motion (because σ/E_t is increasing) a reasonable approximation to the flexural motion can be found by assuming σ/E_t to be constant at its final value. With this assumption, σ/E_t

from Eq. (A.1) can be used in Eq. (C.3) to find I_o. To eliminate ε from the final expression for I_o, the relation between I_o and final strain ε_s must also be found. This is most easily done by equating the kinetic energy imparted by I_o to the strain energy absorbed in plastic work, which gives

$$I_o^2 = 2\rho h^2 \int_o^{\varepsilon_s} \sigma(\varepsilon) d\varepsilon \tag{C.4}$$

Taking the material to be elastic, perfectly plastic gives

$$I_o^2 = 2\rho h^2 \sigma_y \left(\varepsilon_s - \frac{\varepsilon_y}{2}\right) \tag{C.5}$$

To simplify the final expression for I_o we further assume that the final strain ε_s is large enough that we can take $\varepsilon_s - \varepsilon_y/2 \approx \varepsilon_s - \varepsilon_y$. With this approximation, Eqs. (A.1), (C.3), and (C.5) yield the desired expression for critical impulse:

$$I_o = \left(\frac{2}{3K}\right)^{1/4} B^{1/2} a\left(\rho\sigma_y\right)^{1/2} \left(\frac{h}{a}\right)^{3/2} \tag{C.6}$$

The results of the numerical integration are matched by taking B = 12 which yields Eq. (5.32). Impulses from this formula agree with the numerical integration within 5% for the materials in Table A.1 and $20 < a/h < 200$.

UNCLASSIFIED

Security Classification

DOCUMENT CONTROL DATA - R&D

(Security classification of title, body of abstract and indexing annotation must be entered when the overall report is classified)

1 ORIGINATING ACTIVITY (Corporate author) Poulter Laboratories Stanford Research Institute Menlo Park, California	2a REPORT SECURITY CLASSIFICATION Unclassified 2b GROUP

3 REPORT TITLE

Radiation Damage Study Final Report, Volume XIII - Dynamic Response of Beams, Plates, and Shells to Pulse Loads

4 DESCRIPTIVE NOTES (Type of report and inclusive dates)

Final Report

5 AUTHOR(S) (Last name, first name, initial)

Abrahamson, G. R., Florence, A. L., and Lindberg, H. E.

6 REPORT DATE	7a TOTAL NO OF PAGES	7b NO OF REFS
September 1966	271	56

8a CONTRACT OR GRANT NO. AF04(694)-824, Avco/MSD Subcontract No. b PROJECT NO. 159706	9a ORIGINATOR'S REPORT NUMBER(S) AVMSD-0339-66RR, Vol. XIII
c d	9b OTHER REPORT NO(S) (Any other numbers that may be assigned this report) BSD TR 66-372, Vol. XIII

10 AVAILABILITY/LIMITATION NOTICES

This document may be further distributed by any holder only with specific prior approval of AFBSD.

11 SUPPLEMENTARY NOTES	12 SPONSORING MILITARY ACTIVITY
	Air Force Ballistic Systems Division Norton AFB, California

13 ABSTRACT (Unclassified)

Two types of response are treated, dynamic plastic bending of beams and circular plates under transient lateral loads, and dynamic pulse buckling of bars and cylinders under transient axial thrust or lateral pressure. For each type, the fundamental theory is developed first for the simple beam or bar and then extended to the more complex structural elements. In the bending problems, both simply supported and clamped boundaries are treated. The loads are of the blast type, consisting of a sudden rise to a peak load followed by a decay to zero pressure in an arbitrary duration, including the extremes of an ideal impulse and a step load. Numerical examples are given for rectangular, triangular, and exponential decay shapes. In the buckling problems, simply supported bars under both elastic and plastic thrust are treated for eccentric impact and for bars with random imperfections. Buckling of cylindrical shells is treated for transient lateral blast pressures, again over the entire range of durations. In both the bending and buckling problems, experimental results are given to demonstrate the mechanisms of deformation and the accuracy of the theories in calculating maximum bending deformations or critical buckling loads.

DD FORM 1 JAN 64 1473

UNCLASSIFIED

Security Classification

14 KEY WORDS	LINK A		LINK B		LINK C	
	ROLE	WT	ROLE	WT	ROLE	WT
Dynamic response						
Buckling						
Beams						
Plates						
Shells						
Plastic response						

INSTRUCTIONS

1. **ORIGINATING ACTIVITY:** Enter the name and address of the contractor, subcontractor, grantee, Department of Defense activity or other organization *(corporate author)* issuing the report.

2a. **REPORT SECURITY CLASSIFICATION:** Enter the overall security classification of the report. Indicate whether "Restricted Data" is included. Marking is to be in accordance with appropriate security regulations.

2b. **GROUP:** Automatic downgrading is specified in DoD Directive 5200.10 and Armed Forces Industrial Manual. Enter the group number. Also, when applicable, show that optional markings have been used for Group 3 and Group 4 as authorized.

3. **REPORT TITLE:** Enter the complete report title in all capital letters. Titles in all cases should be unclassified. If a meaningful title cannot be selected without classification, show title classification in all capitals in parenthesis immediately following the title.

4. **DESCRIPTIVE NOTES:** If appropriate, enter the type of report, e.g., interim, progress, summary, annual, or final. Give the inclusive dates when a specific reporting period is covered.

5. **AUTHOR(S):** Enter the name(s) of author(s) as shown on or in the report. Enter last name, first name, middle initial. If military, show rank and branch of service. The name of the principal author is an absolute minimum requirement.

6. **REPORT DATE:** Enter the date of the report as day, month, year, or month, year. If more than one date appears on the report, use date of publication.

7a. **TOTAL NUMBER OF PAGES:** The total page count should follow normal pagination procedures, i.e., enter the number of pages containing information.

7b. **NUMBER OF REFERENCES:** Enter the total number of references cited in the report.

8a. **CONTRACT OR GRANT NUMBER:** If appropriate, enter the applicable number of the contract or grant under which the report was written.

8b, 8c, & 8d. **PROJECT NUMBER:** Enter the appropriate military department identification, such as project number, subproject number, system numbers, task number, etc.

9a. **ORIGINATOR'S REPORT NUMBER(S):** Enter the official report number by which the document will be identified and controlled by the originating activity. This number must be unique to this report.

9b. **OTHER REPORT NUMBER(S):** If the report has been assigned any other report numbers *(either by the originator or by the sponsor)*, also enter this number(s).

10. **AVAILABILITY/LIMITATION NOTICES:** Enter any limitations on further dissemination of the report, other than those imposed by security classification, using standard statements such as:

(1) "Qualified requesters may obtain copies of this report from DDC."

(2) "Foreign announcement and dissemination of this report by DDC is not authorized."

(3) "U. S. Government agencies may obtain copies of this report directly from DDC. Other qualified DDC users shall request through ________________."

(4) "U. S. military agencies may obtain copies of this report directly from DDC. Other qualified users shall request through ________________."

(5) "All distribution of this report is controlled. Qualified DDC users shall request through ________________."

If the report has been furnished to the Office of Technical Services, Department of Commerce, for sale to the public, indicate this fact and enter the price, if known.

11. **SUPPLEMENTARY NOTES:** Use for additional explanatory notes.

12. **SPONSORING MILITARY ACTIVITY:** Enter the name of the departmental project office or laboratory sponsoring *(paying for)* the research and development. Include address.

13. **ABSTRACT:** Enter an abstract giving a brief and factual summary of the document indicative of the report, even though it may also appear elsewhere in the body of the technical report. If additional space is required, a continuation sheet shall be attached.

It is highly desirable that the abstract of classified reports be unclassified. Each paragraph of the abstract shall end with an indication of the military security classification of the information in the paragraph, represented as *(TS)*, *(S)*, *(C)*, or *(U)*.

There is no limitation on the length of the abstract. However, the suggested length is from 150 to 225 words.

14. **KEY WORDS:** Key words are technically meaningful terms or short phrases that characterize a report and may be used as index entries for cataloging the report. Key words must be selected so that no security classification is required. Identifiers, such as equipment model designation, trade name, military project code name, geographic location, may be used as key words but will be followed by an indication of technical context. The assignment of links, roles, and weights is optional.